Epitaxial growth of thin Fe3O4 films on ZnO by PLD : a perspective for spintronics

Ismail Madaci

université PARIS-SACLAY

Croissance épitaxiale de films minces de Fe_3O_4 sur ZnO par PLD : Une perspective pour la spintronique

Epitaxial growth of thin Fe_3O_4 films on ZnO by PLD: A perspective for spintronics

Thèse de doctorat de l'université Paris-Saclay

École doctorale n° 573, interfaces : matériaux, systèmes, usages (INTERFACES)
Spécialité de doctorat : Physique
Graduate School : Sciences de l'ingénierie et des systèmes
Référent : Université de Versailles-Saint-Quentin-en-Yvelines

Thèse préparée dans les unités de recherche **GEMaC (Paris-Saclay, CNRS)**, et **CRHEA (CNRS)**, sous la direction de **Yves DUMONT**, professeur des universités, le co-encadrement de **Olena POPOVA**, ingénieur de recherche, et le co-encadrement de **Philippe VENNEGUES**, ingénieur de recherche

Thèse soutenue à Versailles, le 20 décembre 2023, par

Ismail MADACI

Composition du Jury

Membres du jury avec voix délibérative

Isabelle BERBEZIER Directrice de recherche CNRS, Université d'Aix-Marseille	Présidente
Nathalie VIART Professeure des universités Université de Strasbourg, IPCMS	Rapporteuse & Examinatrice
Bénédicte WAROT-FONROSE Directrice de Recherche CEMES-CNRS, Toulouse	Rapporteuse & Examinatrice
Jean-Baptiste MOUSSY Directeur de recherche CEA Saclay, Université Paris-Saclay	Examinateur

THÈSE DE DOCTORAT

NNT : 2023UPAST170

université PARIS-SACLAY | ÉCOLE DOCTORALE Interfaces: matériaux, systèmes, usages

Titre : Croissance épitaxiale de films minces de Fe_3O_4 sur ZnO par PLD : Une perspective pour la spintronique

Mots clés : Fe_3O_4, dépôt par ablation laser pulsée, ferromagnétisme, couches minces magnétiques, microscopie électronique à transmission

Résumé : Ce travail de doctorat s'inscrit dans le domaine de la science des matériaux pour l'électronique de spin. Notre objectif est de maîtriser la croissance épitaxiale du semi-métal Fe_3O_4, ayant une densité d'états entièrement polarisée, sur des substrats semi-conducteurs en ZnO, possédant une longue cohérence de spin (dans la gamme du micromètre). La combinaison réussie "Fe_3O_4/ZnO" constitue la première fondation nécessaire pour des études physiques sur l'injection de spin dans les dispositifs. Dans ce travail, des réalisations notables ont été obtenues, en particulier les processus réussis de croissance épitaxiale pour Fe_3O_4 sur des substrats ZnO(000±1), indépendamment de la polarité du substrat. Un contrôle précis de la pression partielle d'oxygène pendant le dépôt a permis la synthèse de films minces de Fe_3O_4 purs et stœchiométriques, avec des propriétés magnétiques ressemblant à celles de Fe_3O_4 massif. L'étude a fourni des informations sur l'influence de la température de croissance sur l'interface entre Fe_3O_4 et ZnO, y compris les effets des couches tampon de FeO intentionnellement déposées. De plus, la recherche s'est étendue pour explorer l'impact du désorientation du substrat sur l'aimantation rémanente des films minces de Fe_3O_4. En utilisant des techniques avancées de microscopie électronique en transmission, une analyse complète de la croissance épitaxiale a révélé divers défauts structuraux, fournissant une compréhension approfondie des défis dans ce domaine de recherche.

Title : Epitaxial growth of thin Fe_3O_4 films on ZnO by PLD: A perspective for Spintronics

Keywords : Fe_3O_4, Pulsed Laser Deposition, ferromagnetism, magnetic thin films, Transmission Electron Microscopy

Abstract : This PhD work is inscribed in the research domain of materials science for spin electronics. We aim to master the epitaxial growth of the half-metallic Fe_3O_4, a material with a fully polarized density of states, on ZnO semiconducting substrates, possessing a long spin coherence length (within the micrometer range). The successful combination "Fe_3O_4/ZnO" is the first necessary foundation for physical spin injection studies on devices. In this work notable achievements were realized, particularly the successful epitaxial growth processes for Fe_3O_4 on ZnO(000±1) substrates, regardless of substrate polarity. Precise control of oxygen partial pressure during deposition allowed the synthesis of pure stoichiometric Fe_3O_4 thin films, with magnetization properties closely resembling those of bulk Fe_3O_4. The investigation provided critical insights into the influence of growth temperature on the interface between Fe_3O_4 and ZnO, including the effects of intentionally grown FeO template layers. Furthermore, the research extended to explore the impact of substrate miscut on remanent magnetization of Fe_3O_4 thin films. Utilizing advanced transmission electron microscopy techniques, a comprehensive analysis of epitaxial growth revealed various structural defects, providing an in-depth understanding of the challenges in this area of research.

Résumé

La spintronique est un domaine fascinant de la physique qui explore comment exploiter le spin des électrons, et non seulement leur charge, pour atteindre de nouvelles fonctionnalités qui n'étaient pas accessibles dans l'électronique classique. Elle nous permet d'envisager un avenir où le traitement des données se libère des limites actuelles, ouvrant la voie à des dispositifs de mémoire ultra-rapides, à des solutions de stockage de données plus efficaces et à de nombreuses applications novatrices qui pourraient remodeler notre monde axé sur l'information. Cela inclut non seulement un traitement plus rapide des données, mais aussi des innovations dans les capteurs économes en énergie, contribuant à un avenir durable.

Dans le cadre de cette thèse, nous nous sommes engagés dans une aventure d'exploration de la croissance épitaxiale de films minces magnétiques de Fe_3O_4 sur des substrats semiconducteurs de ZnO. L'objectif était de faire progresser la science et de contribuer aux objectifs globaux du projet "SPINOXIDE", qui se concentre sur la fabrication de photodétecteurs et photoémetteurs à base de spin.

Dans la partie de la croissance de films minces, au cœur de nos réalisations se trouve l'établissement de processus de croissance épitaxiale par dépôt par laser pulsé de films minces de Fe_3O_4 sur des substrats en ZnO(000±1), suivant la relation $Fe_3O_4(111)[10\bar{1}]$ // $ZnO(0001)[11\bar{2}0]$. Nous avons constaté que la polarité du substrat n'a aucun rôle discernable dans l'influence sur les propriétés volumiques des films minces de Fe_3O_4. Cette découverte ouvre des perspectives passionnantes, suggérant que les films minces de Fe_3O_4 peuvent être déposés sur des substrats de ZnO de polarités différentes sans compromettre leur intégrité structurelle.

En ajustant précisément la pression partielle d'oxygène pendant le processus de croissance, nous avons réussi à obtenir des films minces de Fe_3O_4 stœchiométriques. Par exemple, lorsque déposés à 260°C, la pression partielle d'oxygène nécessaire pour obtenir des films minces de Fe_3O_4 purs et stœchiométriques était de $1{,}0 \times 10^{-6}$ Torr. Cet équilibre délicat de stœchiométrie est un point essentiel pour atteindre les propriétés physiques désirées, mettant en lumière la précision de nos démarches.

En approfondissant l'étude des propriétés de ces films minces, nous constatons que les propriétés d'aimantation ressemblent étroitement à celles du Fe_3O_4 massif. Les couches déposées à 400°C se rapprochent exceptionnellement de l'aimantation de saturation du massif, ayant une valeur de 480 ému/cm³. Et même à une température de substrat plus basse (260°C), l'aimantation de saturation reste remarquablement élevée, atteignant 435 ému/cm³.

L'étude de l'interface à l'aide de la microscopie électronique en transmission a révélé que l'interface entre le Fe_3O_4 et le ZnO reste géométriquement plate lorsque la croissance est effectuée à des températures de substrat inférieures à 400°C. Cependant, cette interface prend une forme ondulée lorsque la croissance est effectuée à 500°C, ce qui indique une interdiffusion thermiquement activée entre le film et le substrat à des températures élevées. Une exploration plus approfondie de l'effet de la température de croissance à l'aide du profilage en profondeur SIMS a montré que certaine teneur en Zn peut être détectée dans le film de Fe_3O_4 lorsqu'il est déposé à 400°C, tandis qu'elle est pratiquement absente dans les films à 260°C. Parmi les résultats les plus importants de notre étude, ces derniers soulignent l'importance de notre choix de baisser la température de croissance, créant une interface abrupte à la fois chimiquement et structurellement, et empêchant ainsi efficacement l'interdiffusion, un élément très important dans le domaine de la spintronique.

De plus, de notre réussite dans la croissance de Fe_3O_4, nous avons également réussi à déposer du FeO(111) (wurtzite) pur sur du ZnO(0001) en contrôlant la stœchiométrie de la cible en PLD. Cette réalisation ouvre des possibilités pour l'utilisation du FeO en tant que couche interfaciale. L'interaction entre le Fe_3O_4 et le FeO offre des perspectives passionnantes d'exploration.

Pendant le dépôt de Fe_3O_4, on a observé la présence de FeO tout au début de la croissance grâce à l'analyse RHEED *operando*. Malgré les résultats de l'analyse RHEED suggérant la formation de FeO, des analyses plus poussées à l'aide de la microscopie électronique à transmission en haute résolution (HR-STEM) confirment l'absence de ce composé à l'interface à la fin du processus de croissance, validant ainsi la possibilité de déposer directement du Fe_3O_4 pur sur le substrat ZnO. Cependant, nous avons également exploré la croissance intentionnelle d'une couche de FeO d'1 nm à l'interface entre le Fe_3O_4 et le ZnO. Les images HR-STEM ont révélé que même le FeO déposé intentionnellement est oxydé au cours de la croissance ultérieure de

Fe_3O_4. Il peut être nécessaire d'utiliser une couche de FeO plus épaisse pour stabiliser une couche ultra-mince de FeO à l'interface. Fait intéressant, malgré l'absence du FeO déposé à l'interface, nous avons observé son influence sur les propriétés magnétiques du film final de Fe_3O_4. Cette influence se manifeste par des différences dans l'anisotropie magnétique entre différents échantillons, soulignant l'impact du FeO sur le comportement magnétique des films minces.

De plus, nos investigations de croissance sur du substrat avec un désorientation de 1° ont révélé un impact remarquable du miscut sur l'aimantation rémanente des films minces de Fe_3O_4. La désorientation $[10\bar{1}0]$, en particulier, a présenté l'aimantation rémanente la plus élevée (272 ému/cm³) résultant en Mr/Ms = 60%, mettant en évidence l'importance de la désorientation du substrat dans l'ingénierie du comportement magnétique des films minces de Fe_3O_4.

De plus, nos mesures avancées de microscopie électronique en transmission, comprenant la DF-TEM, HAADF-STEM, et ADF-STEM, nous ont permis de réaliser une analyse approfondie sur les couches de Fe_3O_4(111) épitaxié par PLD sur ZnO(0001). Grâce au GPA (Geométric Phase Analysis), nous avons mis en évidence que la croissance épitaxiale est relaxée, avec une relaxation de contrainte se produisant dans une couche de moins de 5 Å d'épaisseur. Cette relaxation est facilitée par la formation de dislocations de désaccord de maille à l'interface Fe_3O_4/ZnO, présentant une périodicité de 1,74 nm le long de la direction $[1\bar{1}0]$.

Notre analyse a principalement révélé deux catégories de défauts présents dans les couches minces de Fe_3O_4 : les joints de macle et les joints d'antiphase. Il est à noter que ces joints ne s'alignent pas toujours sur des plans de haute symétrie, et peuvent présenter une courbure ou une inclinaison par rapport à l'axe de croissance. En outre, en plus des joints de macle et d'antiphase, nous avons observé des défauts courbés dans les observations en vue plane ADF-STEM qui ne présentent pas les caractéristiques cristallographiques des joints de phase.
Nous avons quantifié une longueur caractéristique de défauts par unité de surface à partir d'images en vue plane HAADF-STEM, mesurant 0,12 nm^{-1} pour les échantillons déposés avec une couche intermédiaire de FeO et 0,10 nm^{-1} pour les échantillons sans celle-ci. L'orientation et la fraction des joints d'antiphase, par rapport à la densité totale estimée des défauts, peuvent différer entre ces deux types d'échantillons.

Les découvertes ci-dessus représentent une avancée significative dans la maîtrise et la compréhension de la croissance hétéroépitaxiale de Fe_3O_4 sur le ZnO, ouvrant la voie au développement de dispositifs spintroniques efficaces à applications pratiques dans le cadre du projet SPINOXIDE.

Acknowledgments

This academic journey was a challenging yet attainable pursuit. I learned valuable lessons and had the privilege of meeting wonderful people I might never have crossed paths with otherwise. These individuals, particularly my dedicated supervisors, Pr. Yves Dumont, Dr. Philippe Vénneguès, and Dr. Olena Popova, deserve my deepest gratitude. Their guidance, mentorship, encouragement, advice, and critical feedback were instrumental in reaching the highest level this thesis could attain, ensuring it would shine brightly among scholarly accomplishments. Their belief in my abilities and unwavering commitment to my growth as a scholar have left an indelible mark on this journey, for which I am profoundly grateful.

I would like to express my gratitude to the members of the academic committee for accepting to evaluate this work. I extend my thanks to Dr. Bénédicte WAROT-FONROSE, Dr. Isabelle BERBEZIER, Dr. Jean-Baptiste MOUSSY, and Pr. Nathalie VIART for their time and dedication in reviewing this thesis. Their kind words, encouragement, and valuable suggestions are greatly appreciated. I am truly delighted and honored to have such esteemed researchers as a part of this committee.

I acknowledge the ANR for their financial support, which made this research possible.

My sincere thanks go out to our collaborators at CRHEA, Dr. Christian Morhain, the coordinator of the SPINOXIDE project, which this thesis is a part of, and Dr. Maud Nemoz, who played a crucial role in the XRD characterizations and contributed significantly to this thesis. Our fruitful discussions, from which I consistently learn new things in science, their investment in this thesis, ongoing support, and kindness have been invaluable.

My sincere thanks to Dr. Alain Lusson, Director of the GEMaC laboratory, for their commitment to the efficient functioning of the laboratory and maintaining a well-operated research environment which has been instrumental to the success of my work.

A special thanks to Dr. Bruno Berini, the responsible for PLD in GEMaC laboratory, for his kindness and continuous help, advice, and support throughout the duration of my thesis. Whenever I consulted him with a problem, we unfailingly found a solution for it.

I express my heartfelt gratitude to everyone who contributed to my research project, whether from near or afar, including Dr. François Jomard and Dr. Ingrid Stenger, Dr. Gaëlle Amiri, who had a profound impact on my thesis with their valuable contributions.

I am thankful to Dr. Ekaterina Chikoidze for my first research experience, which ignited my passion for the PhD journey. Her kindness, support, and meaningful exchange broadened my perspectives, and I'm deeply thankful.

I'd like to express my gratitude to the administration team at GEMaC, particularly Laurence Turpin, and Karen Bremond. Their kindness and assistance with all administrative tasks have been precious.

I would like to extend my gratitude to my colleagues at GEMaC, whose enriching discussions and shared memories have made my academic journey all the more fulfilling. Special appreciation goes to Dr. Mohamed Bouras, Dr. Sumit Kumar, and Dr. Hagar Mohamed who are unforgettable members of GEMaC family, even as they have moved on to new horizons. To Nour El Islam Belamouri, Mamadou Ndiaye, Moussa Mebarki, and Zeyu Chi; your support was invaluable. Together, we have cultivated a vibrant academic environment, and I am honored to have had the opportunity to engage in meaningful discussions, create lasting memories, and benefit from your expertise and camaraderie throughout this journey. Thank you for being an essential part of this academic experience.

Thanks to my beloved family, my parents, dear sisters, and my brother, who have been my lifelong motivation propelling me forward. Words can't fully convey the depth of my gratitude for your constant support and encouragement, I love you all.

Table of contents

List of figures

List of tables

List of acronyms

ADF	Annular Dark Field
AFM	Atomic force microscopy
APB	Anti-Phase Boundary
APD	Antiphase Domain
CVD	Chemical Vapor Deposition
DOS	Density of state
EDS	Energy Dispersive Spectroscopy
FC	Field Cooled
FFT	Fast Fourier Transform
FWHM	Full Width at Half Maximum
GPA	Geometric Phase Analysis
HAADF	High Angle Annular Dark Field
IFFT	The Inverse Fast Fourier Transform
LDA + U	Local Density Approximation + Hubbard U
LSDA + U	Local Spin-Density Approximation + Hubbard U
MBE	Molecular Beam Epitaxy
PLD	Pulsed Laser Deposition
RHEED	Reflection High-Energy Electron Diffraction
ROI	Region Of Interest
RSM	Reciprocal Space Mapping
SAD	Selected Area Diffraction
SIMS	Secondary Ion Mass Spectrometry
STEM	Scanning Transmission Electron Microscopy
TB	Twin Boundary
TEM	Transmission Electron Microscopy
VSM	Vibrating Sample Magnetometer
XPS	X-ray Photoelectron Spectroscopy
XRD	X-ray Diffraction
ZFC	Zero Field Cooled

Introduction

In today's rapidly advancing world of technology, where we constantly crave faster, more powerful devices that don't drain our energy resources, physics and research have become pivotal players in our quest for innovation. Meeting the demand for high-capacity but also energy-efficient devices, is now an imperative, given our ecological concerns. Enter spintronics, a fascinating field of physics that explores how we can leverage the intrinsic spin of electrons, not just their charge, to unlock new possibilities. Spintronics offers a fresh way to approach our technological needs. It enables us to envision a future where data processing breaks free from current limitations, ushering in ultra-fast memory devices, more efficient data storage solutions, and a multitude of novel applications that could reshape our information-driven world. This includes not only faster data processing but also innovations in energy-efficient sensors, facilitating real-time monitoring and contributing to a sustainable future [1].

The promise of spintronics is being actively pursued through the "SPINOXIDE" project, a collaborative initiative funded by the ANR, involving four laboratories: GEMaC in Versailles, CRHEA in Valbonne, LPCNO in Toulouse, and IPCMS in Strasbourg. The primary goal of the "SPINOXIDE" project is to explore the potential of ferrimagnetic oxide with high Curie temperature in conjunction with semiconducting oxide ZnO. The aim is not only to demonstrate efficient electrical spin injection and detection in semiconductors but also to fabricate practical opto-spintronic devices, including spin-photodetectors and spin-light emitters.

Several challenges hinder efficient spin injection and detection in semiconductors. The foremost obstacle is creating a spin-polarized carrier population within the semiconductor. Current approaches involve using diluted magnetic semiconductors, which suffer from low Curie temperatures [2]–[5], or employing ferromagnetic metallic electrodes with a tunnel barrier (commonly MgO) to increase specific contact resistivity at the interface [6]–[9]. However, this approach faces limitations, with polarization injection efficiency of approximately 30%, mainly achieved in GaAs-based spin-LEDs, but often restricted to cryogenic temperatures [10]. This limitation is attributed to the degree of electron polarization in ferromagnetic metals (30-40%). Moreover, the compatibility of metal electrodes with semiconductors is complicated by the formation of unwanted compounds such as oxides at the interface.

At the core of the "SPINOXIDE" project is the exploration of Fe_3O_4, a material that is electrically and chemically compatible with ZnO and holds the promise of addressing the challenge of efficient spin injection and detection at room temperature. This choice is grounded in the exceptional properties of these two materials. The oxide character of Fe_3O_4 makes it perfectly suitable for the combination with ZnO in all-oxide heterostructures. ZnO exhibits one of the longest spin coherence times and spin coherence lengths at room temperature, with a measured spin coherence time of approximately 200 picoseconds and a spin coherence length in the micrometer range [11]. Additionally, Fe_3O_4 boasts a high Curie temperature of 850 K, long spin diffusion length (~100 nm), alongside with its predicted half metallicity at room temperature [12]–[14], making it well-suited for room temperature applications. Most intriguingly, the conduction band of ZnO and the Fermi level of Fe_3O_4 can be aligned [15]. This alignment not only positions Fe_3O_4 as a good spin injector but also as a spin detector, all without the added complexity and additional contact resistance associated with tunnel barriers.

Within the collaborative framework of the "SPINOXIDE" project, my thesis is an integral part of the research efforts conducted between GEMaC and CRHEA laboratories. It is dedicated to the integration of Fe_3O_4 as a thin film onto a ZnO substrate. This work involves the growth of Fe_3O_4 thin films using Pulsed Laser Deposition (PLD), a highly efficient technique that has demonstrated its effectiveness in the growth of oxide materials.

My thesis focuses on three core objectives that are at the heart of advancing toward successful spintronic devices. First, it addresses the challenge of growing highly pure Fe_3O_4 thin films, considering the difficulties associated with eliminating other iron oxide compounds during the deposition process. Second, it aims to approach the bulk properties of Fe_3O_4 by optimizing the volume properties of thin films. This optimization intends to achieve at the same time a well-defined interface when growing Fe_3O_4 thin films on ZnO, crucial for preventing spin depolarization caused by any potential non-magnetic interfacial layers resulting from material interdiffusion. Lastly, my thesis involves a meticulous subnanometer-scale characterization of the grown films. This detailed examination aims to identify and understand defects affecting the Fe_3O_4 physical properties, such as the antiphase boundaries.

This manuscript is structured as follows.

Chapter 1 introduces Fe_3O_4, its structure, properties, and epitaxy, with a special focus on pulsed laser deposition. It also describes the ZnO substrate and critical defects associated with

heteroepitaxy, particularly twinning and antiphase boundaries. At the end of the chapter, a brief description of other iron oxide compounds is given.

In **Chapter 2** we delve into the experimental techniques employed in this thesis and the main tools used throughout this research.

Chapter 3 centers on the *Pulsed Laser Deposition* of Fe_3O_4 thin films on c-oriented ZnO substrates, considering both oxygen and zinc terminations. It presents a rigorous methodology of exploiting the growth parameters for a successful optimization of film growth. The primary objective is to obtain samples with properties that closely align with those of bulk Fe_3O_4. This chapter also includes structural and magnetic characterizations necessary to qualify the quality of the samples.

After the establishment of the appropriate growth conditions for Fe_3O_4 thin films in the preceding chapter, in **Chapter 4** we pay specific attention to the Fe_3O_4/ZnO interface. It covers the early stages of growth, monitored through in-situ RHEED characterizations to investigate the formation of unwanted FeO at the beginning of Fe_3O_4 growth, a phenomenon reported by Müller *et.al* [16]. This chapter also explores the intentional deposition of 1 nm of FeO at the interface; the nature of the magnetic interaction across this layer will be a subobjective of another thesis in SPINOXIDE project. Additionally, in this chapter we investigate the influence of substrate surface on the films by studying the growth of Fe_3O_4 on vicinal substrates with two different miscut orientations.

Chapter 5 places its focus on electron transmission microscopy of Fe_3O_4 thin films. This analysis provides detailed insights into the atomic structure of the thin films and highlights various defects that occur during the growth process. These defects include misfit dislocations, rotational twinning, and antiphase boundaries. The chapter also includes an attempt at a quantitative study of antiphase boundaries to investigate the potential effects of FeO at the interface.

At the end of the manuscript, we provide a **Summary** highlighting the key achievements derived from the study on the integration of Fe_3O_4 on ZnO. Additionally, future **perspectives** are evoked, outlining potential directions for further research in Fe_3O_4 epitaxy and Fe_3O_4/ZnO interface engineering.

1. Generalities and state of the art

1.1. Fe_3O_4: structure and properties

Magnetite, with the chemical formula Fe_3O_4, has been known since ancient times. Aristotle (384 – 322 BC) and Thales of Miletus (624 – 547 BC) were among the early observers who recognized the unique properties of this magnetic stone, which was extracted from mines in the Magnesia region of Asia Minor. As centuries passed, magnetite gained significant importance in scientific inquiries and technological advancements. William Gilbert's experiments in 1600, for instance, investigated the phenomenon now recognized as the ferromagnetic phase transition. Furthermore, magnetite played a pivotal role in a groundbreaking invention that transformed maritime navigation—the compass—which was first employed by the Chinese in the 11^{th} century. However, despite its extensive historical significance and usage, development of comprehensive understanding of magnetite's properties, particularly when employed as thin films, remains an ongoing pursuit.

1.1.1. Crystalline structure of Fe_3O_4

Fe_3O_4 has an inverse spinel structure at room temperature (space group Fd-3m) [17]. The spinel family of compounds are materials having the chemical formula AB_2O_4. The spinel structure is based on a face centered cubic (FCC) oxygen "compact" sublattice, in which A^{2+} cations occupy one of the eight tetrahedral interstitial sites that we call "A site", while the B^{3+} cations occupy octahedral sites or "B site". The particularity of an *inverse spinel* structure is the inversed distribution of A^{+2} and half of the B^{3+} cations over A and B sites.

The unit cell of magnetite contains 32 anions of oxygen composing the FCC oxygen sublattice, inside which half of Fe^{3+} occupy eight of the 64 available tetrahedral sites (A sites). The rest eight of Fe^{3+} in addition to the eight Fe^{2+} cations occupy together 16 of the 32 available octahedral sites (B sites). The magnetite is characterized by distortion of the oxygen sublattice given by the parameter u=0.379 [18], which should be 0.375 in the case of ideal FCC [19].

At room temperature, the lattice parameter of bulk Fe_3O_4 is measured as 8.396 Å [20], [21]. A perspective view of the unit cell of Fe_3O_4 revealing the complexity of this structure is presented in **Figure 1.1**.

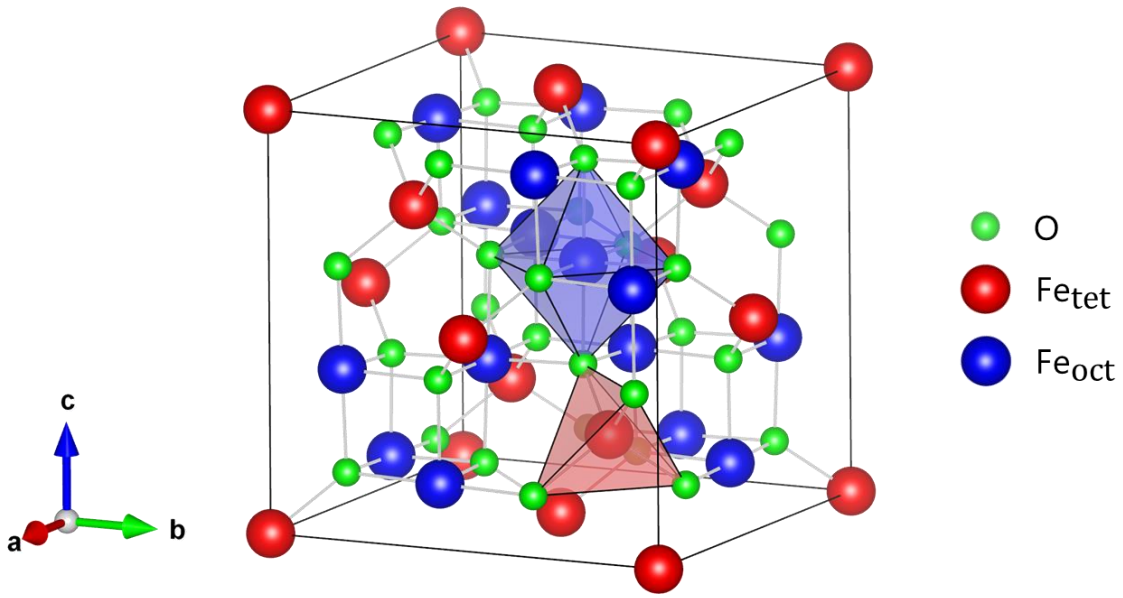

Figure 1.1 *Schematic representation of the Fe_3O_4 unit cell*

The epitaxial growth of Fe_3O_4 on (0001)-oriented ZnO substrate follows the (111) orientation as we will demonstrate in the next chapters. **Figure 1.2** displays the (111) atomic plane stacking of the magnetite, viewed along $[1\bar{1}0]$. It can be described as the stacking of six types of atomic planes displayed in **Figure 1.3**, and that we cite starting from the oxygen plane as follows:

1. A plane of oxygen forming a hexagonal lattice
2. A plane of Fe cations in the octahedral sites forming a Kagome lattice
3. Another plane of oxygen shifted with respect to the first one along $[11\bar{2}]$ to form the FCC lattice of oxygen (with the distortion mentioned above)
4. A plane of Fe cations of tetrahedral sites as a hexagonal lattice
5. A plane of Fe cations of the octahedral sites in a hexagonal lattice, shifted along $[11\bar{2}]$ with respect to the previous plane
6. A plane of Fe cations of tetrahedral sites in a hexagonal lattice shifted along $[11\bar{2}]$ with respect to the previous one

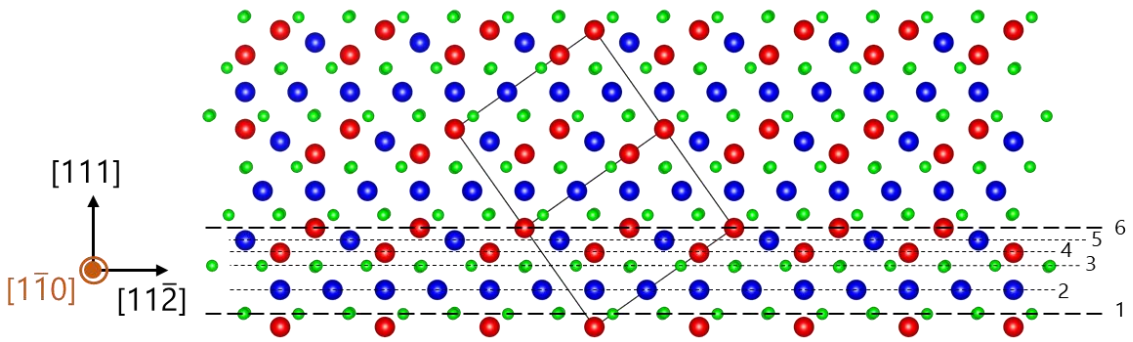

Figure 1.2 *(111) atomic plane stacking of Fe_3O_4 viewed along [1$\bar{1}$0] direction. Green spheres represent oxygen atoms, red spheres represent iron (Fe) atoms in tetrahedral sites, and blue spheres represent Fe atoms in octahedral sites. Black continuous lines delineate a unit cell of Fe_3O_4*

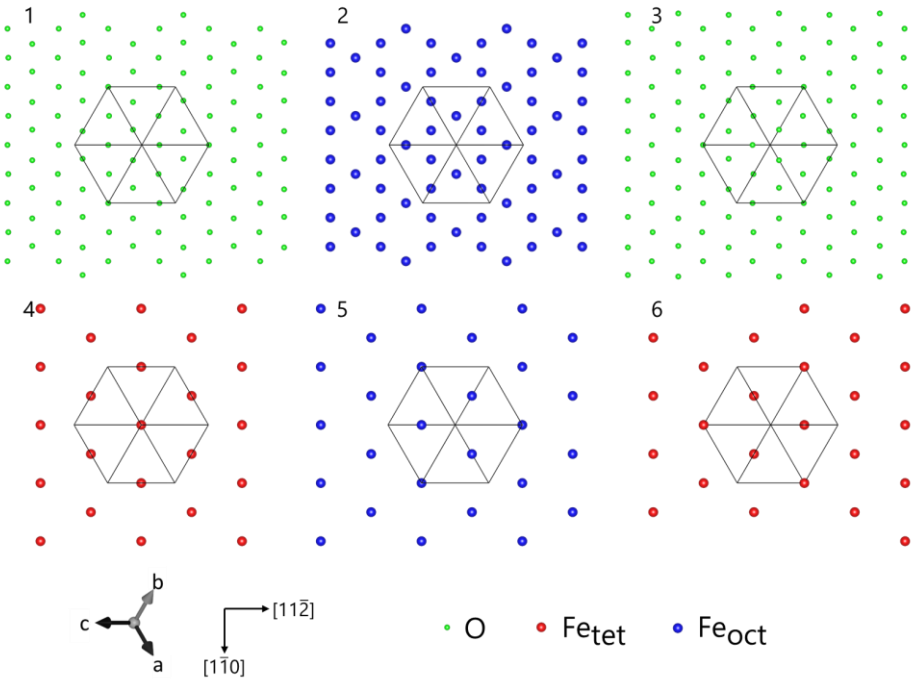

Figure 1.3 *projection of the six (111) atomic planes of Fe_3O_4 along [111] (top view of the planes (111)). The black hexagon is the projection of the cub representing the unit cell on the plane (111)*

1.1.2. Magnetism of Fe_3O_4

Magnetite, Fe_3O_4, was initially described by Néel as an example of a ferrimagnetic material [22], although a microscopic origin of the magnetic couplings was not provided. To understand its magnetic properties, it's necessary to describe the electron configuration and its effect on the Fe_3O_4 magnetization. Fe cations in magnetite have unpaired electrons in the *3d* orbitals, so according to Hund's rule, the obtained electron distribution is shown in **Figure 1.4**. The magnetic order in Fe_3O_4 is a result of several magnetic interactions, including three super-exchange interactions (SE) and one double-exchange (DE). The cations in Fe_3O_4 are separated

by a distance of 3Å, making direct interactions impossible. Instead, magnetic interactions involve oxygen as an intermediate. The e_g of Fe orbitals overlap with oxygen *p* orbitals of σ symmetry, while the t_{2g} orbitals overlap with oxygen *p* orbitals of π symmetry [23], [24].

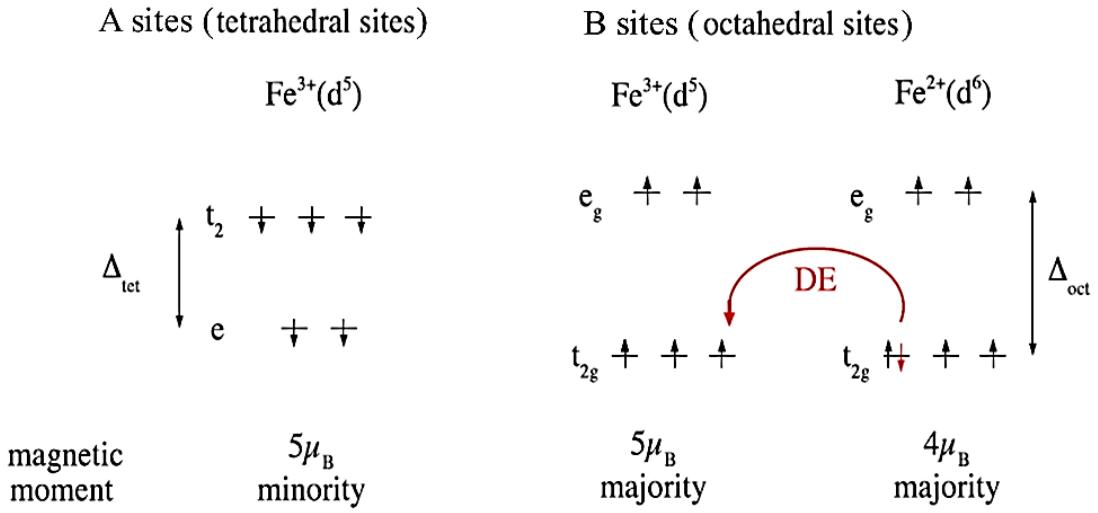

Figure 1.4 *diagram of electron configuration in Fe 3d orbitals in the Fe_3O_4 and the resulting magnetic moment. Figure from [25]*

The A-B exchange interaction is through super-exchange due to the absence of mixed valence on the A site. The Fe_A-O-Fe_B triplet experiences a strong antiferromagnetic super-exchange with an angle of 123° (see **Figure 1.5**). The Fe_A-O-Fe_A triplet also exhibits antiferromagnetic coupling but is masked by interactions between A and B sites due to the larger atomic distances involved, as the distance between A sites equals 3.64 Å and between oxygen and second neighboring A is 3.42 Å.

The Fe_B-O-Fe_B triplet is weakly ferromagnetically coupled at an angle of approximately 90°. The exchange case between Fe_B is not clearly defined due to mixed valence in the B sites, making it difficult to distinguish double-exchange from super-exchange; however, it is reported in literature that the most important interaction is the double-exchange interaction between of the mixed valence Fe_B-Fe_B doublet. The exchange coefficients for Fe_3O_4, as reported in the literature, are provided in **Table 1.1**. The divergences in values are due to the different hypotheses made for the determination of these exchange interactions from experimental results, i.e., whether to consider three iron sublattices when making a distinction between Fe cations of different valence in the B sites or two sublattices when assuming only the two A and B sites sublattices regardless of the mixed valence of Fe_B cations.

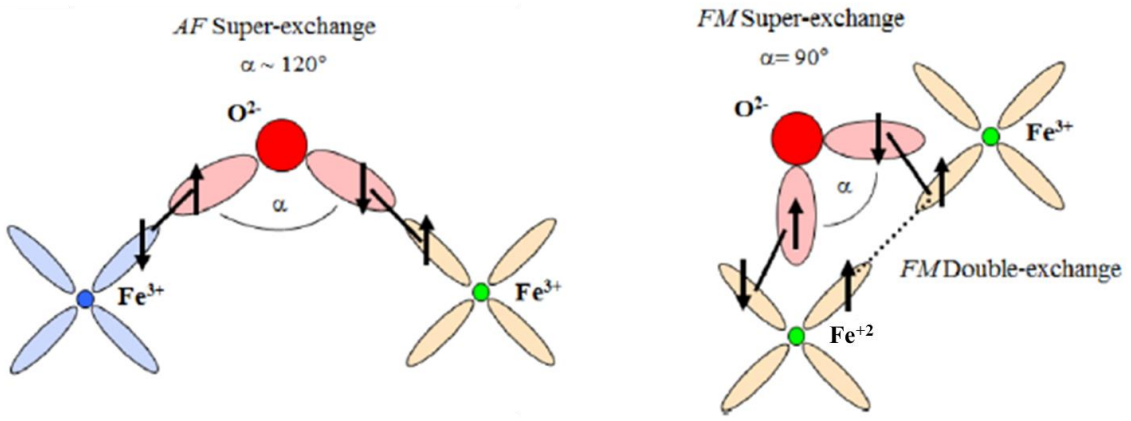

Figure 1.5 *schematic representation of the exchange interactions in Fe_3O_4 , adopted from [26], on the left super-exchange interaction between Fe_A and Fe_B, on the right super-exchange and double-exchange interactions between Fe_B and Fe_B*

Table 1.1 *exchange constants in the Fe_3O_4 from literature*

Reference	Method	J_{AA}(°K)	J_{AB}(°K)	J_{BB}(°K)
[22]	1/χ(T)	-17.7	-23.4	+0.5
[27]	Neutrons	0	-19.5	+5.7
[28]	1/χ(T) et Ms(T)	-21	-28 ~ -23.8	-13.2 ~ 48.4
[29]	Neutrons	-18.1	-27.6	+3
[30]	Mössbauer	-11 -11	-22 -2	+3 -
[31]	*ab-initio* *ab-initio* avec approximation	-2.1 -1.27	-33.42 -33.88	9.63 7.31
[32]	Ms(T)	0	-11.7	-14.7

The competition between exchange interactions results in a ferromagnetic alignment of spins belonging to the same type of site and antiferromagnetic alignment between different sites. Consequently, Fe_3O_4 exhibits a ferrimagnetic order, as shown in **Figure 1.4**. The net spin moment of Fe^{3+} (Fe^{2+}) cations corresponds to S=5/2 (S=2 respectively), leading to an expected saturation moment of $4\mu_B$ per unit chemical formula of Fe_3O_4. The actual observed value is around 4.1μB (~ 480 emu.cm^{-3} at room temperature). Additionally, contributions from oxygen ions and orbital angular momentum of ions may account for the slight difference between estimation and measurement [22], [33]. The relative orientation of spins between iron ions in A and B sites leads to a ferrimagnetic order along the easy magnetization axis [111]. The

magnetic anisotropy of Fe_3O_4 is relatively weak, with K_1 having a value of -1.1×10^5 erg.cm^{-3} [29].

Below Verwey transition (T_V), the easy magnetization axis becomes [100], leading to a variation in coercivity from around 300 Oe at 300K [34] to a range of 1000-1200 Oe at T_V. This change in coercivity at Tv is due to change of crystallographic structure and consequently the magnetic anisotropy [35]. To keep in mind, the coercivity of Fe_3O_4 strongly depends on the sample nature (poly- or single-crystalline) and the presence of defects.

1.1.3. Verwey transition

The Verwey transition is an intriguing characteristic of Fe_3O_4. When the magnetite is cooled below a specific temperature known as the Verwey temperature ($T_V \sim 120$K), it undergoes a first-order metal-insulator transition [36]. However, it is important to note that this transition is somewhat inaccurately termed a metal-insulator transition since magnetite does not strictly belong to either category. In addition to changing its structural symmetry from cubic to monoclinic at T_V, other alterations in physical properties become apparent. One such change is a discontinuity in the magnetization curve concerning temperature (**Figure 1.6(a)**) when crossing the Verwey temperature [37]. Furthermore, there is a demonstrated shift in the direction of the easy magnetization axis: from [111] for $T > T_V$ to [100] for $T < T_V$ [38]. Accompanying this transformation is a peak in the specific heat (**Figure 1.6(b)**) [39], as well as thermal expansion [40], leading to a change in the material's structure.

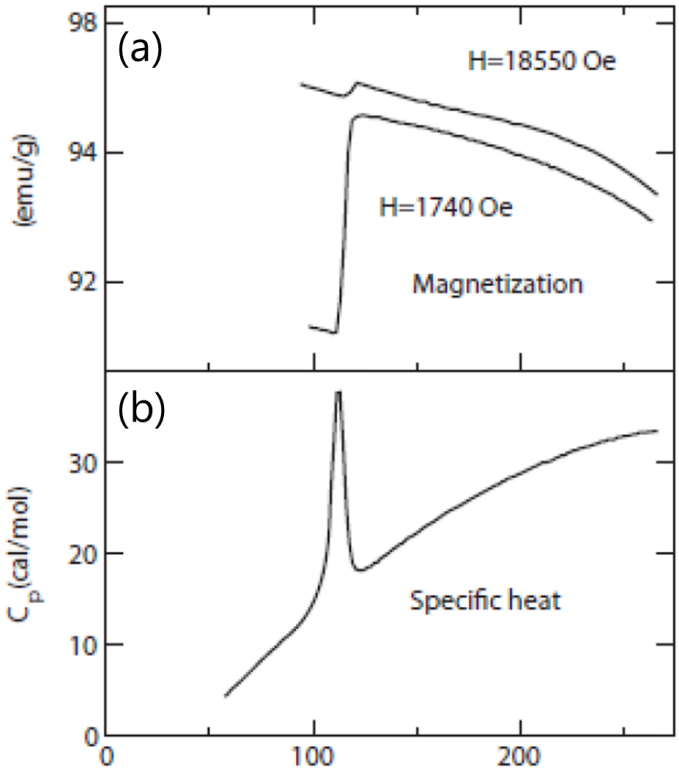

Figure 1.6 *Verwey transition manifestation as: (a) jump in magnetization at ~ 125K from reference[37], (b) pic of the specific heat of Fe_3O_4, from the reference [41]*

Determining the precise structural modification remains challenging, but it is believed that the structure at low temperatures is monoclinic with the space group Cc [42]. The Verwey transition is considered to be first order in the sense of Landau, particularly for stoichiometric single crystals. Nevertheless, it is crucial to emphasize that the Verwey transition involves both an electrical and a structural change. And as accompanying a phase transition, the value of T_V is very sensitive to parameters influencing local or long-distance order.

Numerous investigations on single crystals have revealed that the Verwey transition is highly sensitive to structural defects, non-stoichiometry, and potential doping of the samples. The relationship between the T_V transition temperature and the composition of the prepared single crystals is shown in **Figure 1.7**.

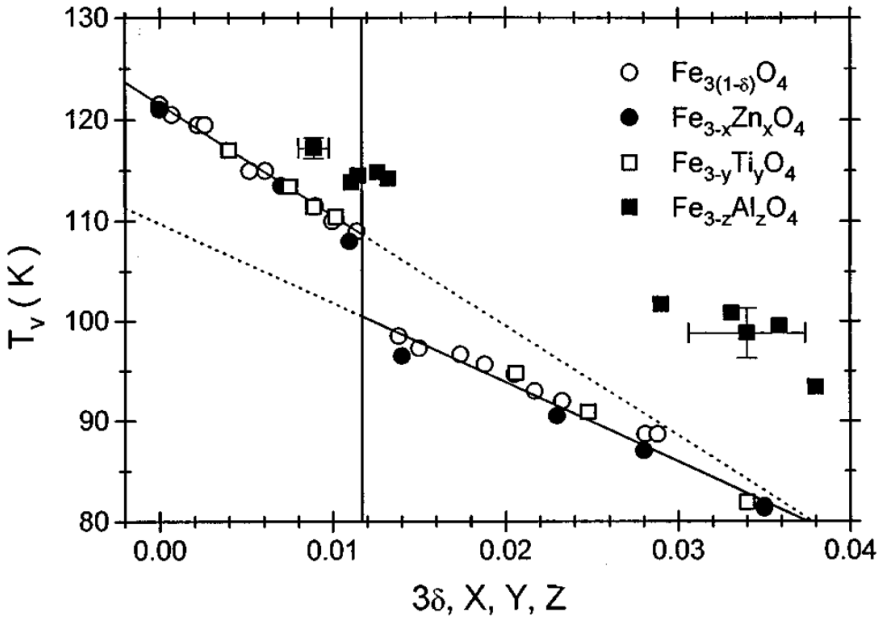

Figure 1.7 *Verwey transition temperature dependence on the off stoichiometry coefficient (δ), Zn (x), Ti (y), and Al (z) contents, from [43]*

T_V is found to be an affine function of the sub-stoichiometry [44], with zinc, titanium, or aluminum doping affecting the transition temperature (although the trend is less clear in the case of aluminum doping) [43]. For small deviations from ideal magnetite, the Verwey transition remains first order according to Landau's classification, but it becomes second order beyond critical values $3\delta_c$, x_c and y_c of approximately 0.012. As a result, the transition temperature decreases from 120K to around 110K as the deviation from stoichiometry changes from 0 to δ_c (δ represents the measure of non-stoichiometry in Fe). Thus, measuring the variation in T_V can serve as an indirect method of determining the iron non-stoichiometry of Fe_3O_4.

1.1.4. Half-metallicity of Fe_3O_4

Magnetite has a considerably high Curie temperature (T_C = 858 K) and is of considerable importance in spintronics due to its assumed half-metallic nature, as calculated from its band structure [45]–[47] as shown in **Figure 1.8** [46]. According to these calculations, only minority spin carriers are present at the Fermi level.

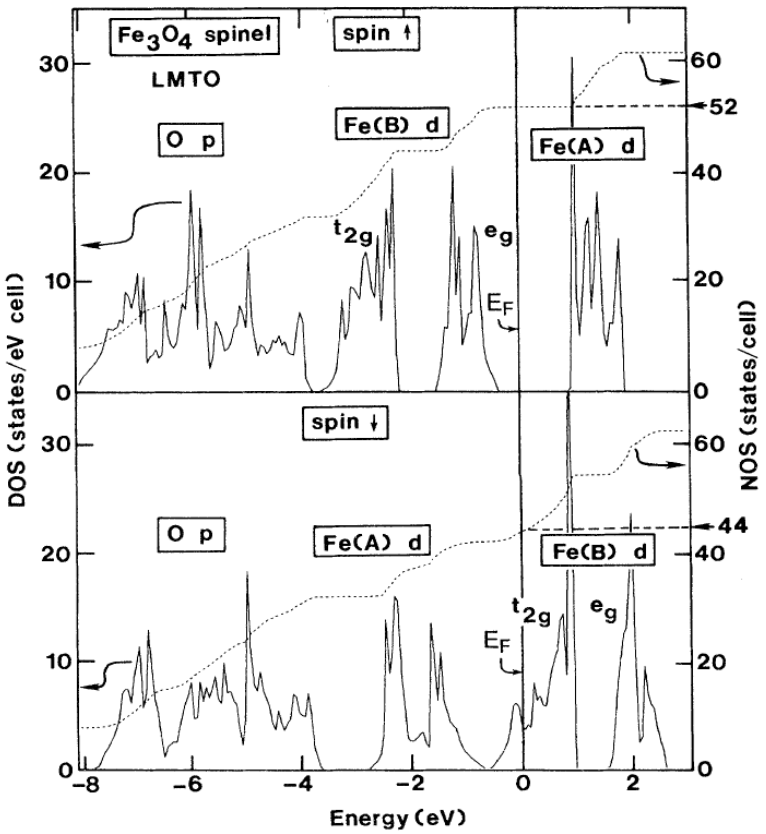

Figure 1.8 *Spin-projected one-electron DOS and number of states in magnetite [46], showing that at the Fermi level only carriers with a minority spin are present*

It's important to note that these simulations neglect electronic correlation effects, which are incorporated as an empirical parameter in the LDA+U and LSDA+U methods [48]. Describing a material in terms of bands becomes challenging when electrons are localized. Nevertheless, such calculations have been accurate for manganites [49].

Fe_3O_4's electronic structure has been the subject of extensive research efforts, and it remains a topic of intense debate [46], [47], [50], [51]. Additionally, transport occurs through electron jumps between B sites, where an incoming electron transforms an Fe^{3+} ion into Fe^{2+}. The extra electron then assumes a fivefold degenerate state, with crystal field splitting the *d* orbitals into a t_{2g} triplet and an e_g doublet. Cullen and Callen developed a spinless Hamiltonian to describe transport properties [52].

They also propose that the triplet orbital further splits into a doublet or a singlet, with the singlet being the lowest energy state. The distinction between an Fe^{2+} ion and an Fe^{3+} ion depends on whether the singlet orbital is doubly occupied or not. The double-exchange mechanism ensures that the electron's spin remains conserved during each jump, leading to a ferromagnetic

coupling between cations in B sites as shown in **Figure 1.9**. As a result, all transporting electrons carry the same spin, thus defining Fe_3O_4 as a half-metal.

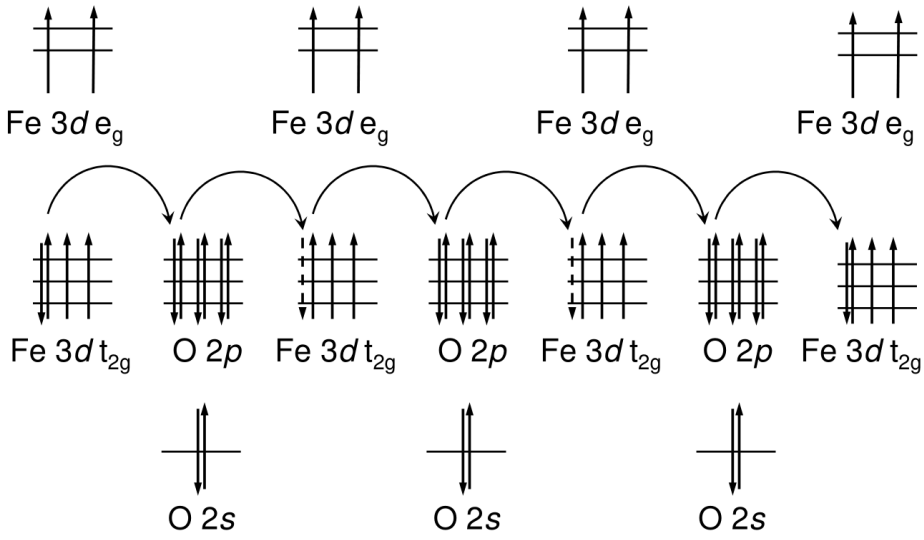

Figure 1.9 *Conduction by hopping between cations at B sites, through oxygen anions, and the double-exchange process [48]*

Validating the half-metallic nature of Fe_3O_4 through photoemission experiments is challenging, with measurements indicating spin polarization at the Fermi level ranging from -80% to 16% according to [12], [53]–[56]. In most cases, the spin polarization at the Fermi level is negative. It's worth noting that photoemission measurements are highly sensitive to surface conditions, and the obtained values are influenced by surface defects, potentially affecting half-metallicity, as suggested by Tobin *et al.* [55].

Furthermore, the half-metallicity of magnetite has been demonstrated through tunneling spectroscopy experiments [57], as well as transport experiments [58], both yielding a spin polarization of around 53%. The discrepancy in experimental values can be attributed to the different nature of the measurement techniques used.

1.2. Epitaxy of Fe_3O_4 thin films

In the context of spintronics, emphasis is placed on the integration of Fe_3O_4 in thin layers on semiconductor or insulating substrates. Various techniques of epitaxial growth have been used for this purpose. Most of the studies have used Molecular Beam Epitaxy (MBE) due to its efficiency of growth control of thin layer at the atomic scale, especially in 2D growth mechanisms. Two approaches were followed: (i) direct oxidation of iron during the growth where the oxidizing atmosphere is molecular oxygen, atomic oxygen, or NO_2 [21], [59]–[65];

or (ii) post oxidation of pure iron deposited on the substrate under vacuum [66], [67] (generally on non-oxide substrates). Although not as widely used as MBE, the Pulsed Laser Deposition finds use in the growth of Fe_3O_4 thin films as it was employed to deposit samples of high crystalline quality and bulk-like properties on different substrates [68]–[74]. RF-sputtering also was employed for this aim, for example for the growth on the Si(001) and MgO(001) substrates [75]–[77]. Over the past almost three decades, among substrates, MgO is most extensively used in existing publications due to its specific study as a tunnel barrier for spin injection and its small lattice mismatch with Fe_3O_4.

PLD growth of Fe_3O_4

Since the employed technique in this thesis is PLD, we will cite here some results obtained for the growth of Fe_3O_4 using this technique. As we mentioned above, PLD was employed to grow Fe_3O_4 on various substrates such as $SrTiO_3$, ZnO, Al_2O_3, Si, MgO, and GaAs.

Hamie et al. [72] grew Fe_3O_4 on $SrTiO_3$ substrate under $P_{O_2} = 1.5 \times 10^{-5}$ Torr at temperatures ranging from 360 °C to 595 °C. At the lowest temperatures, the film showed poor crystallization, and by increasing the substrate temperature, good crystallinity was obtained. However, at 595 °C, the film changed from epitaxial growth to polycrystalline growth. The lowest lattice deformation was measured for growth with a substrate temperature of 510 °C. The films exhibited the Verwey transition and saturation behavior close to the bulk ones.

Xuelian et al. [78] conducted a comparative study of Fe_3O_4 growth by PLD on different substrates: single crystalline substrates {Al_2O_3(0001), Si(001), SiO_2(110)}, polycrystalline ZnO, and amorphous glass. They substrates were heated from room temperature to 550°C under $P_{O_2} = 2 \times 10^{-8}$ Torr. Single phase Fe_3O_4 thin films could be obtained, which was confirmed by XPS and Raman spectroscopy. However, the measured structural and magnetic properties strongly depended on the substrates for a given temperature. Samples grown at RT were amorphous while those of 150°C were polycrystalline. For $T_s = 350$°C, (111) textured Fe_3O_4 films could be obtained and for higher substrate temperature ($Ts \geq 500$°C) other iron oxides appeared.

Zhou et al. [79] studied the PLD growth of Fe_3O_4 on Si(001) substrates at 350°C, where only granular growth could be obtained. TEM analysis revealed the formation of an amorphous layer of SiO_2 at the interface under the used conditions.

Master et al. [80] carried out the growth of Fe_3O_4/ZnO bilayers at 450°C under $P_{O_2} = 1 \times 10^{-4}$ Torr. The Fe_3O_4 films were highly (111) oriented parallel to the (0001) planes of ZnO. Annealing at 550°C led to an enhancement of the saturation magnetization from 310 emu.cm^{-3} in the as-deposited films to 390 emu.cm^{-3} after annealing, which is still lower than the bulk saturation magnetization. This was explained by the presence of antiphase boundaries (APBs, will be discussed in the next section).

The growth at room temperature was not successful in obtaining pure magnetite, as reported by Paramês et al. on Si(001) substrates [81]. Various iron oxides were present in the samples in addition to magnetite. The growth of magnetite at relatively low temperature (T_s = 200°C) was also investigated by Paramês et al. [74] on Al_2O_3(0001) and (T_s = 300°C) on GaAs(001). On the sapphire substrate, the film was preferentially (111)-oriented with a small contribution of (311) planes observed in the X-Ray diffraction pattern. For GaAs, the film was randomly oriented, similar to growth on Si(001) at room temperature. The saturation magnetization was measured around 315 emu.cm^{-3} for the Al_2O_3 substrate and 210 emu.cm^{-3} for GaAs, which was enhanced by reducing the growth temperature to 200°C.

Muller et al. [82] investigated the growth of Fe_3O_4 on ZnO(0001) substrate at 390°C, that gave epitaxial (111)-oriented magnetite thin films. However, a value of saturation magnetization was measured only as 370 emu.cm^{-3}. The most important observation in this work is that the growth of Fe_3O_4 starts with the growth of FeO or FeO-like structures (using XPS and RHEED analysis). A surplus of oxygen was necessary to achieve the stoichiometry of Fe_3O_4, which is richer in oxygen than FeO. Furthermore, after a certain thickness, it was necessary to reduce the oxygen pressure inside the growth chamber to prevent the oxidation of the film into Fe_2O_3.

Table 1.2 lists the growth conditions used in the above cited references and the results obtained for the best samples in the presented works.

By observing the presented results and divergences in the growth conditions from one study to another, these researches have highlighted the potential of pulsed laser deposition for producing Fe_3O_4 thin films on various substrates. However, these varying outcomes also reveal the need for a deeper exploration and precise investigation of growth parameters to achieve significantly improved results. In particular, our focus in the upcoming chapters will be on optimizing the growth process to reduce as much as possible the growth temperature temperatures while ensuring the highest quality of Fe_3O_4 thin film growth.

Table 1.2 *PLD growth conditions and the obtained results in the references cited in the text*

Ref	Substrate	Target / Laser fluence	Temperature (°C)	Oxygen partial pressure (Torr)	Results
[72]	$SrTiO_3$ (001)	α-Fe_2O_3 / J.cm^{-2}	360 – 595	1.5×10^{-7}	M_S = 470 emu.cm^{-3}
[78]	Si (001)	α-Fe_2O_3 / --	300°C	1.0×10^{-6}	M_S = 440 emu.cm^{-3}
[79]	Si (001)	α-Fe_2O_3 / --	350°C	--	Columnar growth
[80]	Al_2O_3 (0001)	α-Fe_2O_3 / --	450°C	2.0×10^{-6}	M_S = 310 emu.cm^{-3} *Annealing* 500°C ➔ M_S = 390 emu.cm^{-3}
[81]	Si (001)	Fe_3O_4 / 2 – 7 J.cm^{-2}	RT	6.0×10^{-4}	Polycrystalline film
[74]	Al_2O_3 (0001)	Fe_3O_4 /2 J.cm^{-2}	200	6.0×10^{-4} [O]:[Ar] = 4:1	Contribution of (311) orientation M_S = 315 emu.cm^{-3}
[82]	ZnO (0001)	Pure Fe / 4 J.cm^{-2}	390 °C	1.8×10^{-5} to 7.1×10^{-6}	Oxygen variation is necessary to stabilize Fe_3O_4 single phase M_S = 372 emu.cm^{-3} (400 emu.cm^{-3} MgO)

1.3. The ZnO substrate

Zinc oxide, a binary compound semiconductor, naturally occurs as the mineral "zincite" and adopts the hexagonal wurtzite lattice structure. In this arrangement, zinc atoms almost align with the "hexagonal close packed" structure (see **Figure 1.10**). Each oxygen atom resides within a tetrahedral group of four zinc atoms, all oriented along the hexagonal axis. The lattice constants for this structure are given as a = 3.24 Å and c = 5.19 Å [83]. The wurtzite structure features a hexagonal unit cell with two lattice parameters, a and c, related by c/a = 1.66. It comprises two interpenetrating hexagonal close-packed (hcp) sub-lattices, each hosting one type of atom displaced with respect to the other along the three-fold c-axis by an amount of u = 3/8 = 0.375 in fractional coordinates (in an ideal wurtzite structure). Each sub-lattice contains four atoms per unit cell, with one type surrounded by the other type in a tetrahedral arrangement. However, real ZnO crystals deviate from the ideal configuration due to changes in the c/a ratio [83].

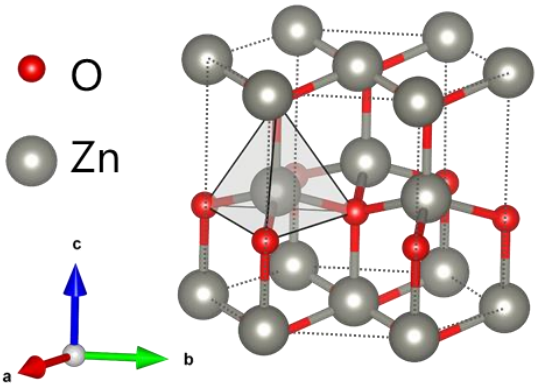

Figure 1.10 *Schematic representation of the ZnO wurtzite structure*

Due to the differing electronegativities of zinc and oxygen, the bonding between these elements exhibit characteristics of both covalent and ionic nature. This results in an inherent polarization within the crystal lattice along the c-axis. As illustrated in **Figure 1.11** When the polarization vector points toward the crystal surface, it forms what we call the $(000\bar{1})$ polar surface(bottom in the **Figure 1.11**). In contrast, the other side is called (0001) polar surface. These two types of surfaces are expected to exhibit distinct physical and chemical properties as both polar surfaces reveal dissimilar accumulation layers at their surface [84]. Measurements of the valence band edges using photoemission spectroscopy showed an approximately 190 meV greater band bending for the Zn-terminated surface, leading to a higher electron accumulation. This discrepancy between the two terminations could result in difference in the interfacial electrical resistance and, consequently, different efficiencies in spin injection. This aspect will be further explored in the SPINOXIDE project. The growth on Fe_3O_4 on both polar surfaces of ZnO will be discussed in Chapter 3.

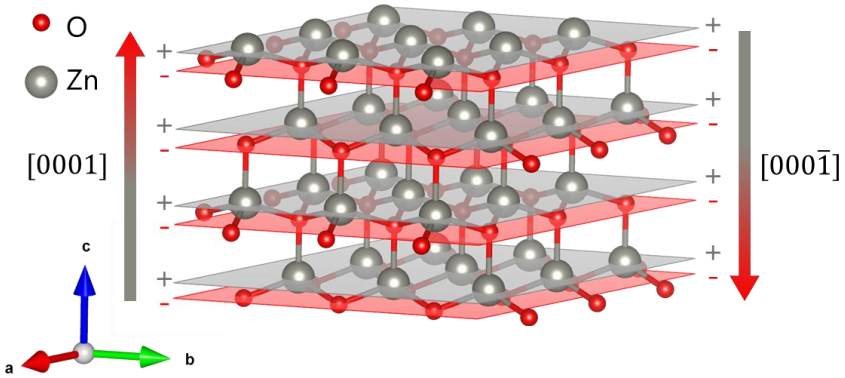

Figure 1.11 *alternation of Zn and O atomic planes along c-axis of ZnO*

Zinc oxide exhibits a band gap of 3.44 eV at low temperatures and 3.37 eV at room temperature [85]. Comparatively, the band gap values for wurtzite GaN are 3.50 eV and 3.44 eV,

respectively [86]. These properties make ZnO well-suited for optoelectronic applications in the blue/UV region, including light-emitting diodes, laser diodes, and photodetectors [87]–[91]. Furthermore, ZnO exhibits one of the longest spin coherence times and spin coherence lengths at room temperature. This is particularly pertinent to SPINOXIDE project, which aims to explore its potential application in opto-spintronic devices. A spin coherence time of approximately 200 picoseconds at room temperature, with a spin coherence length in the micron range, was measured in n-type ZnO using optical orientation experiments [11]. The extended spin lifetimes can be attributed to the exceptionally low spin-orbit coupling in wide-band gap ZnO, which is roughly 100 times smaller than that of GaAs [92].

The combination of Fe_3O_4/ZnO offers several advantages. Mainly, the chemical compatibility inherent in using an all-oxide structure can circumvent issues related to unwanted oxidation often encountered in metal growth processes. Moreover, through tuning the interface chemistry (doping), achieving both ohmic and Schottky contacts at the interface between Fe_3O_4 and ZnO is possible [15].

The growth of Fe_3O_4 on ZnO presents several complexities. Firstly, Fe_3O_4 has a lattice parameter of $a_{Fe_3O_4}$ = 8.396 Å, while ZnO has a_{ZnO} = 3.249 Å. Fe_3O_4 grows following the (111) orientation on the (0001)-oriented ZnO, resulting in a large lattice mismatch of 8.6%. This significant mismatch can give rise to various defects that can adversely affect both the interface quality and the structural properties (and consequently the electronic properties) of the resulting thin film. These defects may include dislocations, misfit dislocations, strain-induced structural anomalies, as well as defects associated with the formation of multiple crystalline domains, such as twinning and antiphase boundaries, which can reduce Fe_3O_4 magnetization.

Secondly, there is the possibility of unwanted iron oxides forming (which lack magnetization, and the half-metallic nature of Fe_3O_4) at the film/substrate interface or within the film volume. The main focus of Chapter 3 is dedicated to overcoming this challenge in order to precisely control the stoichiometry of Fe_3O_4 thin films through the control of the oxygen partial pressure in PLD which demonstrated its efficiency in oxide growth [74], with controlled stoichiometry.

1.4. Epitaxial defects

1.4.1. Anti-phase boundaries in Fe_3O_4

Magnetite thin film often showed an anomalous magnetic behavior which deviates from the bulk character. This behavior was attributed by Margulies et al. [93] to the presence of the

so-called “Anti-Phase Boundaries” (APBs) defects, for which he suggested the antiferromagnetic coupling across the APB. Following works by Celotto et al. [94] evidenced the relationship between the magneto-transport properties of the samples and the density of APBs which varies with the sample thickness.

1.4.1.1. Nature of Antiphase Boundaries

Antiphase boundaries are two-dimensional defects that occur when there is a misalignment of atomic planes in the crystal lattice of Fe_3O_4. The growth of Fe_3O_4 thin films typically begins with the formation of isolated nuclei or islands on the substrate surface. These nuclei then continue to grow in size and thickness as more material is deposited. During this initial stage, individual islands are separated by gaps or terraces.

As the deposition process continues, the islands grow laterally and eventually begin to coalesce (merge) due to the diffusion of adatoms on the substrate surface. The coalescence occurs when adjacent islands come into contact with each other and share common crystallographic planes. However, when these islands originate from different nucleation events or have slightly different crystallographic orientations, their lattice structures may not align perfectly at the interface. This misalignment results in the formation of antiphase boundaries along the plane where the islands coalesce with shifted plane stacking as illustrated in **Figure 1.12** (same colors as in **Figure 1.2** are used to present atoms). While there is a shift in the cation sublattice, the oxygen sublattice remains undisturbed. It is very important to underline that the shift of the APB presented in **Figure 1.12** isn’t perpendicular to the (111) atomic plane, but it is following ¼[110] (the scheme is a projection where only the perpendicular component of the shift is observable). An illustration of similar APB in our samples will be presented in Chapter 5.

APBs were consistently observed in Fe_3O_4 thin films, regardless of the substrate material or the growth technique employed. These boundaries were detected in films grown using various physical and chemical vapor deposition techniques, including MBE, PLD, and CVD [95]–[97]. Moreover, they were present on diverse substrates such as $SrTiO_3$, MgO, α-Al_2O_3, Pt, ZnO, and $MgAl_2O_4$ [21], [98]–[100]. Several investigations of the atomic structure and the possible shifts between the Anti-Phase Domains (APD) suggested that the most stable APBs are the ones having a shift of ¼<110> and laying in the planes $(1\bar{1}0)$ (or equivalent) [48], [94], [101].

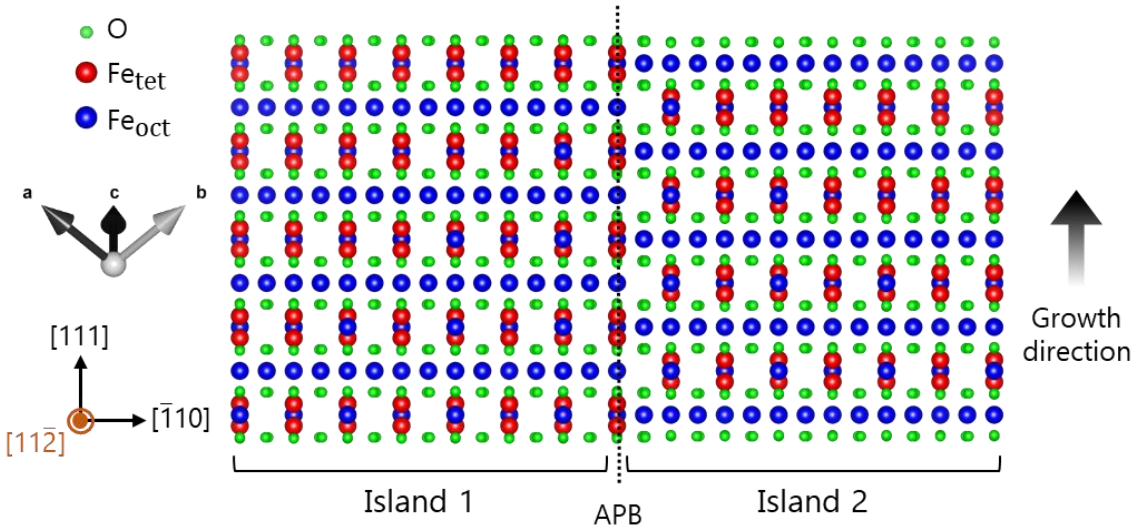

Figure 1.12 *Schematic representation of an APB in the ($\bar{1}$10) plane, indicated by a black dotted line, characterized by a ¼[110] translation vector between one domain (right of the APB) and the other (left of the APB)*

1.4.1.2. Effect of Anti-Phase Boundaries on Fe_3O_4 magnetization

The arrangement of cations at an APB has distinct bond lengths and bond angles compared to the ideal material, which leads to the emergence of new exchange interactions at the boundary that do not exist in Fe_3O_4 ideal single crystals. As a result, an enhanced antiferromagnetic interaction occurs between iron Fe sites on the tetrahedral sublattice Fe_{tet}, while the interaction between irons on the tetrahedral and octahedral sublattices Fe_{tet}-Fe_{oct} is significantly reduced. Additionally, a very strong antiferromagnetic interaction is observed between Fe sites on the octahedral sublattice Fe_{oct} [93]. Consequently, both intra-sublattice spin couplings dominate and exhibit an antiferromagnetic alignment at the APB, resulting in a spin canting that is different from the ferromagnetic spin arrangement found inside the domains. However, the magnetic moments at the APB can only be aligned in very large magnetic fields, leading to magnetization values lower than the bulk magnetization in finite fields, and a slow approach to saturation. Furthermore, depending on the local magnetic coupling, the APBs might behave as sites for pinning and nucleation of domain walls [102].

Margulies et al. [93] demonstrated that the approach to saturation magnetization resembles a model of a one-dimensional chain of ferromagnetically coupled spins with additional antiferromagnetic coupling at the APB. This one-dimensional model was initially discussed by Zijlstra [102] and Dieny et al. [103]. The model describes the competition between the Zeeman energy in the domains and the new exchange energy at the APB, neglecting the magneto-crystalline anisotropy. In this context, APBs are treated analogously to Bloch walls. However,

the width of the APBs is controlled by the external magnetic field rather than the magneto-crystalline field. The slow approach to saturation magnetization, M_S, can be mathematically described by the equation (1.1):

$$M = M_s(1 - b/H^{1/2}) \quad (1.1)$$

where the parameter b quantifies the difficulty of saturating the film and is proportional to the APB density (ρ). This approach to saturation law has been applied by other researchers, such as Hibma et al. [62] and Bataille et al. [99], [104]. Bataille et al. extended the model to consider two APBs per chain and found that for small APB separations, the inner anti-phase domain (APD) becomes magnetized in the opposite direction. They also observed that for fields below a critical value, the magnetization inside each single domain becomes homogeneous. The extended model is consistent with the weaker dependency of the saturation approach on the APB density, described as $b(\rho) = \rho^{1/3}$. Although the one-dimensional model oversimplifies the system, the approach to saturation law in equation (1.1) still exhibits reasonable agreement with experimental data and is widely used by many researchers.

1.4.2. Twinning

The formation of rotational domains can occur during heteroepitaxial growth when the surface of the film and the surface of the substrate have different rotational symmetries at the heterointerface, leading to a symmetry mismatch. When considering a substrate with a Cn symmetry and a film with a Cm symmetry, the minimum number of rotational domains that can be formed is given by the equation (1.2) [105]:

$$N_{RD} = {}^{lcm(n,m)}/_{m} \quad (1.2)$$

where *lcm* represents the least common multiple, and n, m ∈ {1, 2, 3, 4, 6} [106]. **Figure 1.13** provides a schematic representation of the potential epitaxial domain configurations of an epilayer with C_m symmetry that can be arranged on a substrate with C_n symmetry. These rotational domains share the same growth axis direction but differ in their in-plane azimuthal orientations.

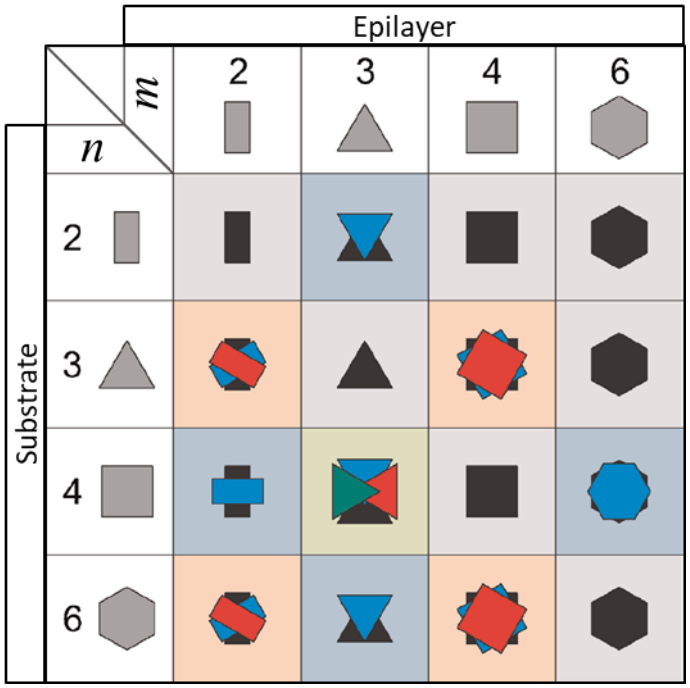

Figure 1.13 *schematic representation of the rotational domains of an m-fold symmetry epilayer on an n-fold symmetry substrate, reprinted from [107]*

In the case of growing Fe_3O_4 on a ZnO substrate, the growth follows to the epitaxial relationship $(111)_{Fe_3O_4}//(0001)_{ZnO}$, as will be demonstrated in Chapter 3. The ZnO surface exhibits a six-fold rotational symmetry, while the (111) surface of Fe_3O_4 exhibits three-fold symmetry; typically, resulting in the growth of two domains rotated by 180° relative to each other. This phenomenon is known as rotational twinning.

Crystal twinning is considered a defect, or more precisely, the twin boundary (TB) since it can lead to a perturbed atomic arrangement across the twin boundary, potentially affecting the physical properties of the resulting film. This is particularly significant for magnetic coupling across the TB in the case of Fe_3O_4 [108]. Twin boundaries form when rotated domains (one with respect to the other) resulting from different nucleation islands coalesce. These twins are assumed to have equivalent energetic favorability on an ideal 2D substrate surface [109]. Introducing a substrate miscut can be a means to favor the nucleation of one domain over the other (explored in Chapter 4).

1.5. Other iron oxides

Depending on the ratio [O]:[Fe], iron has several oxides with different crystalline structure as illustrated in **Figure 1.14**, among which the most known are:

(i) ***Wüstite FeO**:* the less oxidized iron oxide phase, in which the ratio of oxygen to iron is 1:1. It has a rock salt structure (space group *Fm-3m*, a = 4.30 Å). Below 200K it's an antiferromagnetic compound.

(ii) ***Maghemite γ-Fe_2O_3**:* a ferrimagnetic oxide with a magnetization $M_{\gamma\text{-}Fe_2O_3}$ that is approximately 80% of the magnetite magnetization $M_{Fe_3O_4}$, and an estimated Curie temperature of around 985 K [80]. It crystalizes in a cubic structure with lattice parameter very close to the one of the magnetite a = 8.35 Å. It can be described as a fully oxidized magnetite or defective magnetite with only Fe^{3+} cations, where the distribution of iron vacancies over the octahedral positions may result in different symmetries such as the space group Fd-3m for random distribution, the space group $P4_132$ for partially ordered distribution, and the space group $P4_32_12$for ordered distribution. Maghemite is stable only at high temperatures; it inverts to Hematite (α-Fe_2O_3) at temperatures as low as 550 K [110] and, in some reports, as low as 800 K [111], [112].

(iii) ***Hematite α-Fe_2O_3**:* it is the most stable iron oxide which belongs to the space group *R-3c* having corundum structure (a = 5.03 Å, c = 13.74 Å). Up to 680°C the hematite is characterized by a canted antiferromagnetic order between the Fe^{3+} cations resulting in a very small magnetization (< 2 emu/cm^3).

As mentioned before, the difference among the above iron oxides primarily lies in the ratio of [Fe]:[O], which controls the stoichiometry of the iron oxide phases, and consequently, their physical properties. Being able to control this ratio is extremely important for achieving the growth of the pure Fe_3O_4 phase.

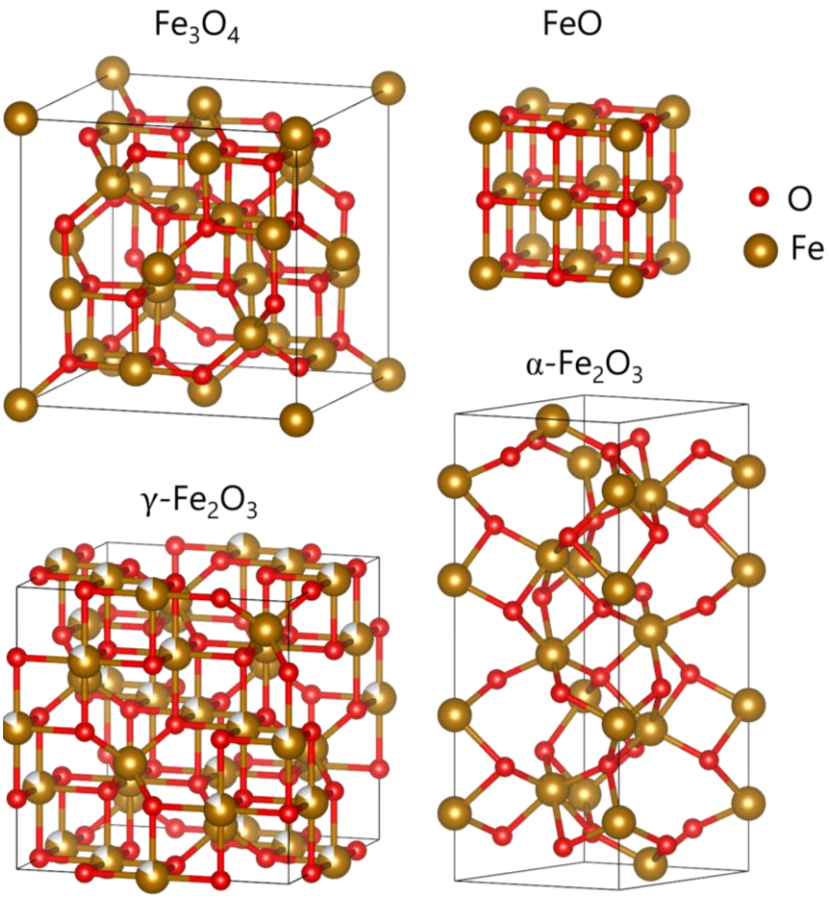

Figure 1.14 *crystalline structure of different iron oxides; in the figure, maghemite is presented as iron-defective magnetite ($Fe_{3-1/3}O_4$)*

2. Experimental techniques

2.1. Pulsed laser deposition

Back in 1987, PLD acquired its famous reputation as an efficient growth technique for complex materials after the successful growth of high-temperature superconducting thin films of $YBa_2Cu_3O_7$ by D. Dijkkamp et al. [113], but the first experiences were over 20 years earlier when the first film was grown by H.M. Smith and A.F. Turner in 1965, just a few years after the invention of the laser [114]. Nowadays, PLD is used for the growth of ***oxides***, nitrides, and metals, which present interesting properties for electronics and spintronics, such as superconductivity, ferroelectricity, ferromagnetism, and piezoelectricity [115]–[118], and more recently as multi-ferroicity [119]–[121].

In this section, we will present the principle of pulsed laser deposition, the growth parameters, the growth and nucleation modes of crystalline thin films, and the advantages of this technique.

2.1.1. Principle

The standard PLD system consists of a pulsed laser and vacuum chamber holding a target and a heated substrate as illustrated in the schematic representation in **Figure 2.1**. In an oversimplified description of the PLD process, when the laser radiation is focused on the target, the absorbed electromagnetic energy heats the surface of the target locally. If the energy is sufficiently high, it allows evaporation, plasma formation, and exfoliation of the heated area in the form of a "plume". This latter contains is a mixture of energetic electrons, atoms, ions, molecules, and possibly micron-sized particles. Under vacuum, the plasma plume extends perpendicularly to the target with those elements reaching the surface of the substrate where the deposition happens. In a geometry where the laser spot is fixed, the target is rotated continuously with an added translation movement to ensure a homogeneous ablation of the whole surface of the target. Facing the target, the substrate is also rotated for a homogeneous coverage by deposited material. The distance target-substrate is optimized in a way not to exceed the plume length *Lp* $(\propto E/P_0)^{1/3\gamma}$, where E is the energy of the laser pulse, P_0 is the background pressure, and γ is the average ratio of specific heats for elements in the plume [122]. However, when this distance increases in the limit of *Lp*, a merge of the plume elements can occur during the flight to the substrate as was reported by Nishikawa *et al.* [123].

Different *in situ* characterization techniques can be coupled to the PLD chamber to characterize and control the growth, such as Reflection high-energy electron diffraction, emission spectroscopy, spectroscopic ellipsometry etc., and the set of these facilities is piloted numerically.

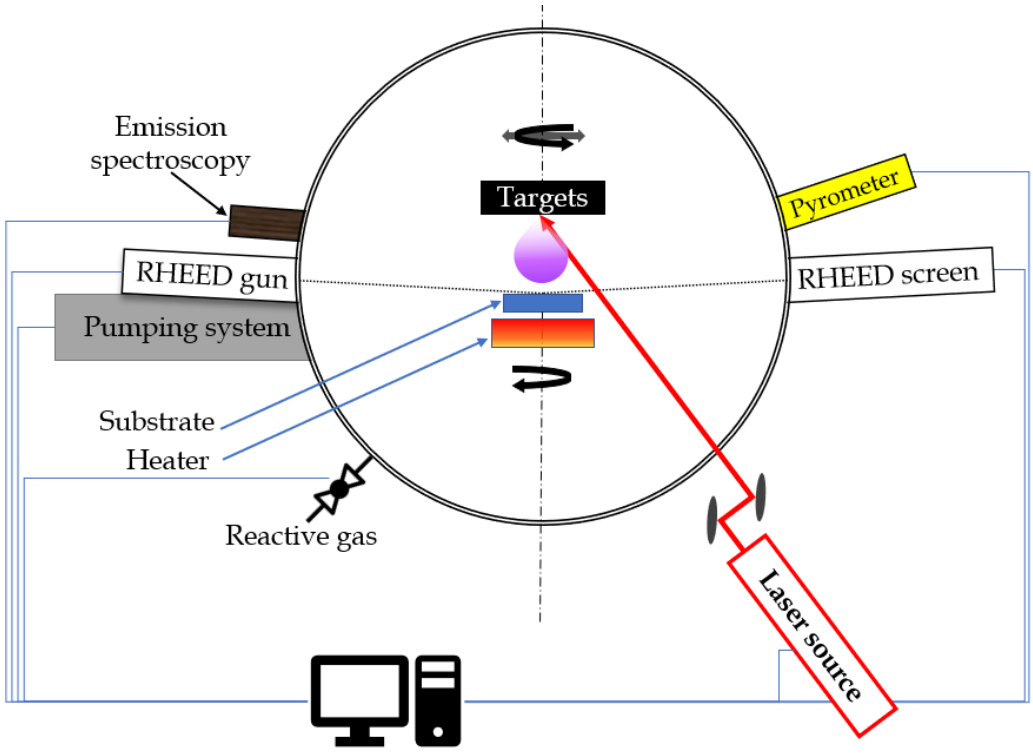

Figure 2.1. *schematic representation of standard PLD equipment, as the one in GEMaC*

The properties of the films grown by PLD depend directly on the substrate, the target stoichiometry, and the growth parameters.

Substrate

The nature of the substrate can modify the structural properties of the film, favoring an amorphous, polycrystalline, textured, or epitaxial growth. In the case of epitaxial growth, the lattice mismatch between the desired film and the substrate is defined as $\varepsilon = (a_f - a_s)/a_s$ with a_f and a_s being the lattice parameters of the film and the substrate for the given epitaxial relationship, respectively.

Target stoichiometry

The target must contain the chemical elements of the thin film that we want to deposit with precise proportions. PLD targets are generally made by powder compacting and sintering.

Compared to other growth techniques, the specificity of the PLD is the congruent material transfer process; in other words, the stoichiometry of the precursor material (target) is preserved

except for some volatile elements (with respect to other targeted elements) such as for example oxygen and bismuth. The loss of such elements can be compensated either by the growth under reactive O_2 in the case of oxides or the preparation of targets with an excess of the concerned elements.

In this work, two targets were used. The first and primary target was employed for growing Fe_3O_4 thin films with a stoichiometry of Fe_2O_3. This target was fabricated in the GEMaC laboratory. The second target was primarily used for growing FeO template layers with a stoichiometry of Fe_3O_4. The latter is a commercial target requiring synthesis in an oxygen-reduced atmosphere

2.1.2. Growth parameters

2.1.2.1. Substrate temperature

The substrate in PLD setup can be heated by radiative, resistive, or laser heating. The prevalent method is the radiative heating, which allows more flexibility of substrate movement and a large area heating. The substrate temperature affects, in the first place, the crystallinity of the grown films. Hence, low growth temperature results in an amorphous or/and polycrystalline structure deposition, while high temperature favors epitaxial growth. Nevertheless, very high temperatures increase the re-evaporation rate of the adsorbed atoms and might induce an interdiffusion between the film and the substrate.

2.1.2.2. Laser parameters

The laser beam is the source of energy that allows the extraction of material from the target to be deposited on the substrate, so the wavelength of the laser must be absorbed by the target. Short pulses are used to ensure an efficient ablation and to avoid thermal fusion during absorption. The most employed in PLD are Nd:YAG (1064 nm, 532 nm, 355 nm, and 266 nm) and excimer lasers (KrF 248nm).

The energy delivered to the target must be sufficient to break atomic bonds and trigger off the evaporation, here we talk about the laser *fluence* or the density of energy per surface unit (J/cm^2) that can be varied either by changing the laser power or the focalization of the beam on the target surface. With each laser pulse, a small amount of material is deposited on the substrate (up to 0.01 nm per pulse for $5J/cm^2$ [124]), so at a given fluence, the high pulse repetition increases the growth rate.

Laser-induced desorption and ablation occur as a consequence of the initial electronic excitation undergoing a conversion into kinetic energy that drives nuclear motion. This leads to the

expulsion of atoms, ions, and molecules from the surface of the target. The rate and specific dynamics of this conversion process are critically dependent on electron-lattice interactions inherent to the laser-irradiated solid. These interactions involve various phenomena, such as the scattering of free electrons by phonons, phonon emission, localized lattice rearrangements, and alterations in atomic configurations. The latter category includes crucial processes, including self-trapping of holes and excitons, formation of defects, and subsequent reactions involving these defects. Additionally, electronic interactions between defects and lattice ions can initiate surface decomposition. Following or accompanying the electron-lattice interaction, secondary electronic processes occur [125]. These processes involve photoabsorption by free electrons, successive excitations of self-trapped excitons and electronic defects, transient modifications in optical absorption as the surface layer or near-surface bulk disintegrates, photoemission, ionization of neutral species prompted by the incident laser irradiation, generation of a laser-induced ablation plasma, as well as photoacoustic and photothermal phenomena. **Figure 2.2** shows a schematic diagram of electronic processes leading to laser ablation.

Under the pulsed illumination of the laser, it's inevitable to form large particles, droplets, and to exfoliate the target due to the so called "subsurface heating" or "hydrodynamic sputtering". Fähler et *al.* suggest the energy densities should not be very high in order to reduce the number of the small droplets [126]. In practical point of view, a compromise has to be found between a fluence threshold of ablation and too high fluence generating too many droplets. Other growth parameters such as for example oxygen pressure, off-center deposition or film-substrate distance can be used to improve film morphology.

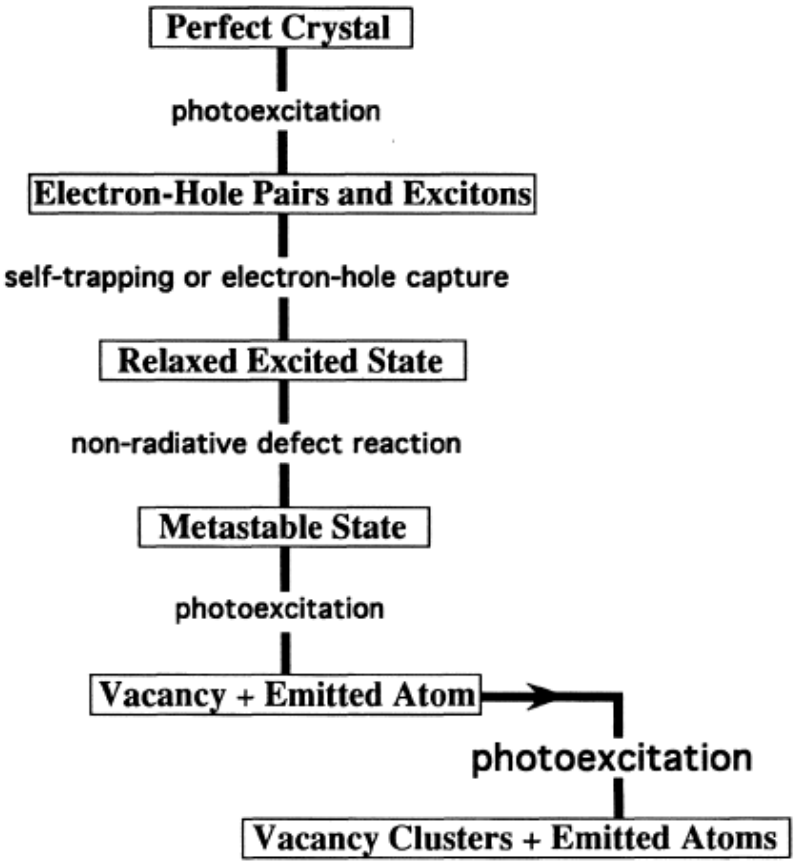

Figure 2.2 *diagram illustrating electronic processes leading to laser ablation, taken from [125]*

2.1.2.3. Growth atmosphere

The PLD can be performed under ultra-high vacuum in the case of metal thin films [127], or under reactive gas; oxygen in the case of oxides for example. The partial pressure of oxygen can be adjusted through the use of a mixture with inert gas (Xe, Ar…).

The kinetic energy of the ablated elements can be increased by increasing the laser fluence, it can exceed 100eV for ions, and in the order of the electron volt for the neutral particles in the case of high fluences on metals (~ 8 J/cm²) [128], [129], but this increase changes slightly the film properties [130]. A much more remarkable effect is when the kinetic energy is lowered using an inert gas, where the phenomena can be described by scattering of a dense cloud of ablated material moving through a diluted gas [130], also the shock between the plasma plume and the surrounding gas limits the plasma expansion and reduces the particles velocity. The decrease of the ablated material kinetic energy using an inert gas can be exploited in order to avoid the ion implantation inside the substrate.

Growth of Oxides

In the case of oxides, the background oxygen plays a crucial role in oxidizing the deposited film. Chan et al. [131] have demonstrated, using ^{18}O, that increasing the oxygen background pressure results in an increased oxygen content in the grown film. Several gases can be used as oxidizing sources, such as O_2, NO_2, or ozone. The oxidation of the grown thin film results from the interaction between the background gas and the plasma and the direct exchange between the film and the background gas. However, activated oxygen (generated after the interaction of the background gas and the plasma) exhibits a higher oxidizing power than molecular background oxygen [132].

Additionally, the background gas is not the sole source of oxygen in PLD growth. Two other sources should be considered: the target and the substrate. The target serves as a source of activated oxygen. As for the substrate, the outward diffusion of oxygen may contribute to the oxidation process, as observed by Schneider *et al.* [133] when SrTiO3 films were grown on substrates containing ^{18}O. Higher growth temperatures led to increased ^{18}O content in the $SrTiO_3$ grown films. It should be noted that the effect of substrates is much more pronounced under low oxygen background pressures.

2.1.3. Film nucleation mode

The pulsed laser deposition of thin films can be described in three steps: (1) evaporation of the target and plasma formation, (2) material transfer with the adiabatic expansion of the plasma, (3) nucleation and growth of clusters formed by the adsorbed adatoms at the surface of the substrate. Several phenomena are possible within the last step such as atomic surface diffusion, adsorption, re-evaporation, and interdiffusion into the substrate [134] (**Figure 2.3**).

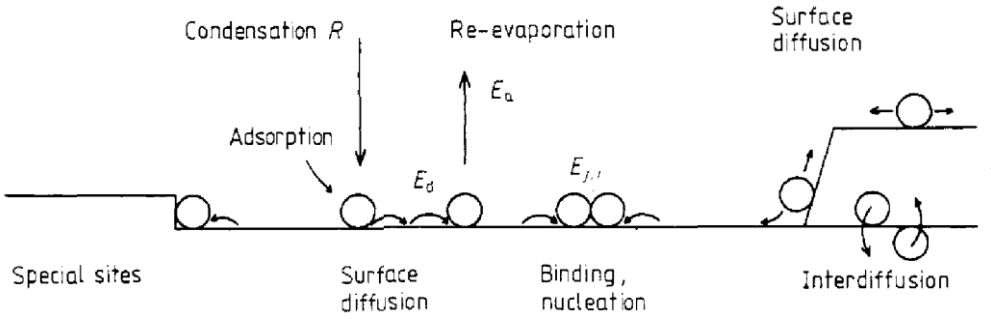

Figure 2.3 *schematic representation of the possible atomistic processes during growth and nucleation on a surface (from [134])*

Depending on the thermodynamics relating the surface energies and the interface film-substrate energy, the modes of nucleation can be classified into: three-dimensional island growth

(Volmer-Weber), layer-by-layer growth (Frank-van der Merwe), and the growth of full 2D monolayer followed by 3D island growth (Stranski–Krastanov). The three modes are illustrated in **Figure 2.4**, θ represents the overlayer coverage in monolayers (ML).

Volmer-Weber growth mode: in this mode, film growth begins with forming separated clusters of atoms, which will capture new arriving adatoms to form 3D islands. The coalescence of islands ensures the coverage of the substrate with the film. This type of growth takes place when the bounds between the film atoms are stronger than the bounds between the film and the substrate atoms.

Frank-van der Merwe growth mode: known also as layer-by-layer growth, in this mode, the substrate is fully covered with the first monolayer of the film before the formation of the second monolayer, and the rest of the monolayers subsequently follow the same growth mechanism. It's described as the ideal growth model. It occurs when the bounding energy between the film atoms is equal to or less than the bounding energy between the atoms of film and the substrate. It also requires a perfect lattice matching between the film and the substrate, the reason why this mode is often observed in homoepitaxial growth [135].

Stranski-Krastanov growth mode: the film grows initially in fully 2D layer-by-layer mode up to certain critical thickness, then clusters appear and the growth undergo the 3D mode. The transition from 2D to 3D mode is not completely explained, but hypothesis relates that to the release of elastic energy stored in the film due the film-substrate lattice mismatch [136].

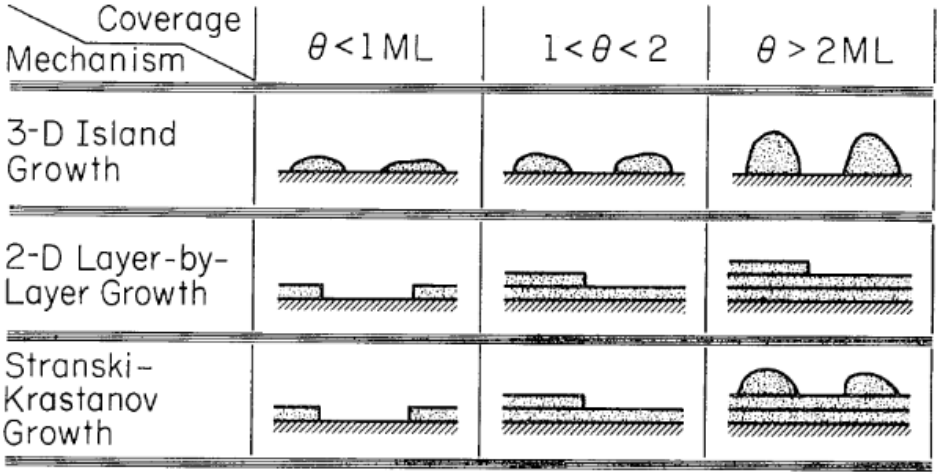

Figure 2.4 *schematic representation of the film growth modes where θ represents the overlayer coverage in monolayers (ML) [136]*

2.1.4. Advantages of the PLD

As mentioned before, PLD growth allows epitaxial growth of different kinds of materials with several advantages, among which we cite:

(i) In general, congruent cation transfer between the target and the deposited film. For ternary or more compounds, a special attention has to be put onto element transfer ratio of lighter element or more volatile element. Respectively examples are oxygen for metal transition functional oxides, and bismuth in ferrites oxides.

(ii) The pulsed nature of the PLD process allows for the adjustment of laser parameters, such as pulse rate and laser energy, for each utilized target

(iii) High kinetic energy of particles that can reach more than 100eV, which can be increased by increasing the laser fluence, and can be decreased using a background gas.

(iv) Inside the PLD chamber we can load many targets regarding their small size and separation of the energy source (laser), which allows combinatory growth and multilayer deposition with adequate conditions for each layer.

(v) Possibility to adjust, via oxygen partial pressure control, the degree of oxidation in complex functional materials, where fine oxygen stoichiometry tunes the target physical properties.

(vi) PLD as usual low-pressure physical deposition process, with steel chamber with many branches, many *in-situ*, working *operando*, characterizations could be developed, such as emission spectroscopies, electron diffractions, ellipsometry.

2.1.5. PLD setup of GEMaC laboratory

The growth setup used in this thesis is an ultra-high vacuum chamber equipped with KrF and Nd:YAG lasers. The vacuum limit reaches 10^{-9} Torr at room temperature, with a slight increase at higher temperatures. The laser used to grow Fe_3O_4 thin films is the Nd:YAG which provides a wavelength of 355 nm and a power of 1 W (at the target surface), allowing it to reach high fluences when focused on the target. The laser beam is guided using an optical system composed of mirrors and a sliding lens, to a quartz window through which it is focused on the target. The lenses on the optical path are used to adjust the laser fluence. The quartz porthole is periodically changed/cleaned to avoid laser beam absorption due to eventual material depositions on the quartz, which can degrade its transmittance.

Eight targets are placed inside the growth chamber and can be automatically brought to the work position. When the target is in the ablation position, it is continuously rotated and

vertically translated during the growth to ensure homogeneous ablation of its surface. In contrast, the other seven targets are protected with a metallic shutter to avoid contamination by the redeposition of other elements on them. The substrate is placed on a rotating holder vertically face-oriented to the target at a distance of 5 cm and heated by the radiation of a ceramic heater set around 5mm behind. The temperature of the substrate is measured using a Williamson PRO DW2434-C dual-wavelength pyrometer, a thermocouple placed on the ceramic heater, and an infrared camera. It is important to underline that the temperatures recorded using the thermocouple are always higher than the values measured with the pyrometer and the camera, which is an evident consequence of the lower efficiency of the radiation heating (the thermocouple measured the actual temperature of the heater and not the temperature of the substrate surface). However, we performed calibration measurements to determine the accurate temperature of the substrate surface. A protocol consists of heating some metals and alloys with precisely known melting points to their respective melting points, thereby allowing us to ascertain the exact temperature.

As the PLD growth is usually oxygen deficient, it is possible to introduce oxygen or a desired mixture of oxygen with Argon or Nitrogen gas through a system of flowmeters with different flows.

To monitor the growth and the crystallinity of the grown films, we use a STAIB Instruments *in situ* Reflection High Energy Electron Diffraction (RHEED) instrument that will be described in the next section.

Two other accessories connected to the chamber are an *in situ* ellipsometer (SENTECH SE850) to measure the thickness and the optical indexes of the grown layers and an optical emission spectrometer (Ocean Optics) used to characterize the plasma plume and notably to analyze its chemical composition.

A more detailed description of the growth chamber is available in the reference [137].

2.2. Reflection high-energy electron diffraction (RHEED)

Reflection high-energy electron diffraction (RHEED), is a vacuum-compatible technique based on electron-matter interaction. It allows a direct access to several information such as the crystallinity of the grown sample, the growth mode, real-time phase transition, surface roughness, surface reconstruction, and the epitaxial relationships between the film and the substrate. RHEED consists of an incident beam of highly accelerated electrons, generally under 10 keV- 40 keV, hitting the sample surface with a grazing angle θ_i between 0.1° and 3°.

The diffracted electrons are collected on a fluorescent screen placed at a distance L_s from the interaction point. **Figure 2.5** illustrates the geometry of RHEED technique.

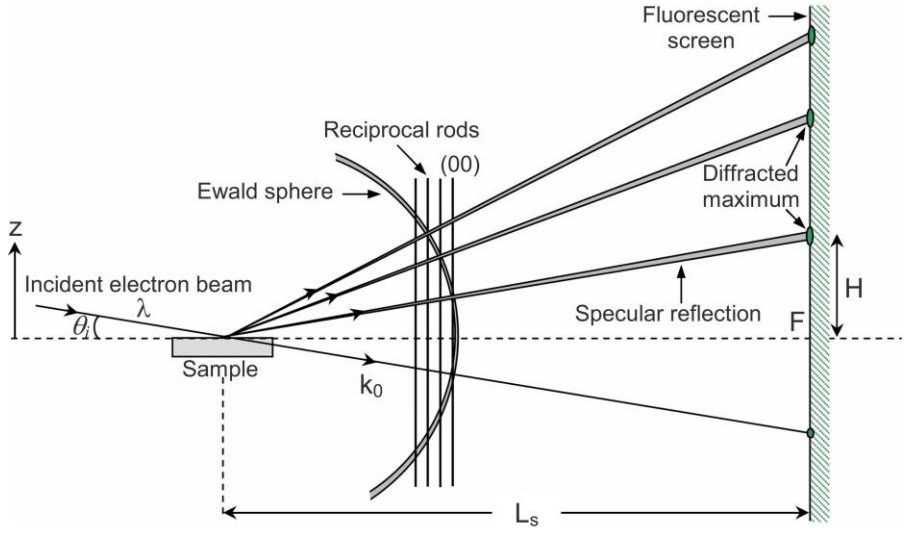

Figure 2.5 *geometry of incident and diffracted electron beams in RHEED[138]*

Since the incidence angle is very small, the electron diffraction is coming only from the surface atomic layers and the crystalline structure can be assimilated to a bidimensional lattice, for which the reciprocal space is composed of periodic infinite rods perpendicular to the sample plane. The sample can be azimuthally rotated around the surface normal to adjust the high symmetry orientation parallel to the beam. In an elastic scattering approximation $|K_0|=|K_f|$, all the scattered vectors lie on Ewald sphere with radius $|K_0|$. The diffraction occurs when the Laue condition is fulfilled, i.e, the difference between the incident and scattered wave vector $\vec{K}_0 - \vec{K}_f$ must correspond to a reciprocal lattice vector $\vec{G}$. Within this condition, the diffraction can be represented by the intersection the reciprocal space rods with the Ewald sphere, resulting in diffraction spots projected on the fluorescent screen (see **Figure 2.5**). The diffraction spots are orderly distributed on the screen over concentric circles, or the so-called Laue circles. Measuring the distance $e_{(hkl)}$ between two spots of the same circle, and knowing the distance screen-sample L_s, allows to deduce the in-plane lattice spacing $d_{(hkl)}$ of the real crystal using the equation (2.1) [139]:

$$\frac{e_{(hkl)}}{L_s} \cong \frac{\lambda}{d_{(hkl)}} \tag{2.1}$$

where λ represents the wavelength of the incident beam given by (2.2):

$$\lambda = \frac{h}{\sqrt{2meV}} \tag{2.2}$$

In order to determine the real space structure, it is necessary to rotate the sample and visualize the diffraction patterns along different azimuthal angles, then by measuring the angle between constructive diffraction angles, and the lattice spacing for each angle, we can simply reconstruct the reciprocal space lattice, from which we can reconstruct the real space lattice.

Ideally, for a flat surface of a single crystal, the RHEED pattern is composed of point spots. However, in practice spots are broadened by the finite coherence length of the electron beam. Furthermore, roughness of the surface, crystalline defects, and miscut angle contribute in the broadening of the diffraction spots and make the pattern streaky. When the roughness is very high, due to 3D islands growth for example, the diffraction happens in transmission and the reciprocal rods become dots in reciprocal space, the pattern present dots similar to TEM diffraction patterns. **Figure 2.6** summarizes different possible RHEED patterns depending on the crystallinity and the surface morphology of the sample.

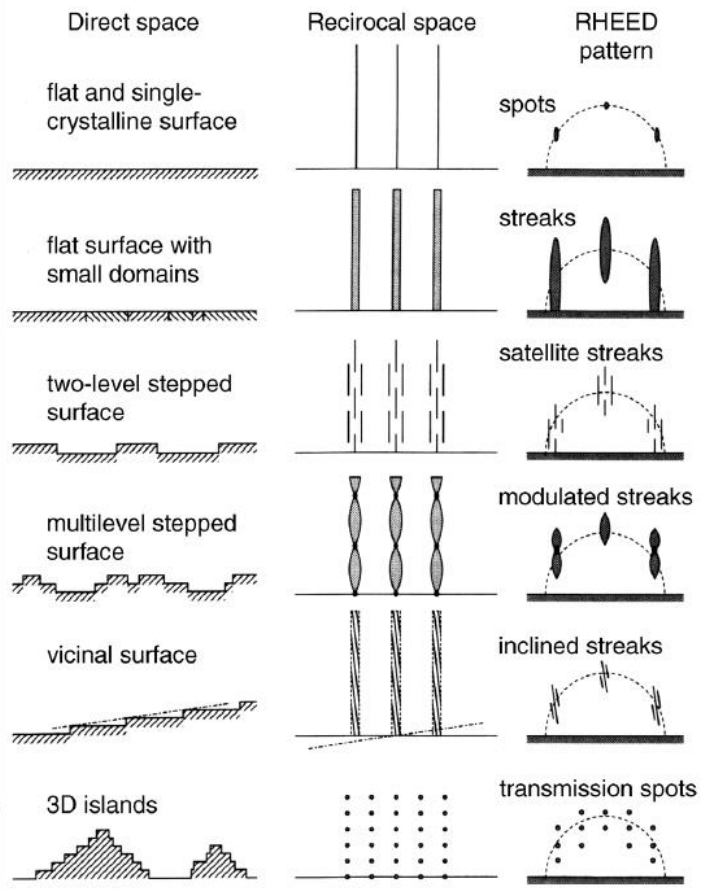

Figure 2.6 *schematic representation of real surfaces, their reciprocal space lattices and the corresponding RHEED patterns [140]*

Using RHEED to monitor the growth allows in certain cases to measure the growth rate, notably when the growth follows Frank-van der Merwe 2D layer-by-layer mode. The intensity of

diffraction rods varies with the coverage ratio of the surface. When the sample surface is fully covered with 2D layer, the RHEED intensity takes a maximum value. During the growth of the following layer, step edges and terraces are formed, what leads to a decrease of RHEED intensity to a lowest value with a half monolayer. The intensity increases again to reach a maximum with the growth of the full monolayer. These variations happen periodically and described as RHEED oscillations. We can calculate the growth speed by measuring the time separating two maximal intensities of the specular spot.

The RHEED instrument associated with our PLD chamber is a STAIB Instruments electron gun that is differentially pumped, allowing us to perform characterization with a pressure of 10^{-5} Torr in the chamber. All characterizations were performed with an electron energy of 10 kV (corresponding to a wavelength of $\lambda = 0.123$ Å) and an acceleration current of 1.5 A. Reflected electrons are collected on a fluorescent screen located 216.5 mm away from the sample, and patterns are recorded as single frames or in video mode during growth using a kSA CCD camera mounted behind the screen. The analysis is done with kSA 400 software.

2.3. X-ray diffraction

X-ray diffraction (XRD) is a non-destructive technique based on light-matter interaction, used mainly for structural characterization in order to evaluate the crystalline quality of thin films. It is the most exploited technique in this thesis and was used mainly to identify the present phases, their out-of-plane lattice parameters, and the in-plane epitaxial relationships film-substrate. Depending on the orientation of the sample to the X-ray source and the detector, different types of measurements are possible. In this section, we present the principal and the used XRD methods.

2.3.1. Bragg's law

Incident X-ray radiation interacts with the electronic cloud of atoms. Among the possible interactions there is elastic diffusion or "Rayleigh diffusion" through which the rays simply bounce off the electronic cloud, they are diffused in all directions of space, keeping the same energy, the same wavelength, but not the same direction. At a given point of the space P, the diffused amplitude depends on the contributions of waves diffracted by the atoms constituting the volume *v* of the irradiated crystal. Between waves diffracted by two atoms of the crystal to a point P, there is a path difference which may imply a phase difference. The path difference shows that the total amplitude in P is not an algebraic sum, as the two waves interfere;

the interference can be either constructive (maximal intensity) or destructive (null intensity) depending on the phase difference.

Consider a single crystal illuminated by a monochromatic X-ray beam. The incident beam makes an angle θ with the family of plans (hkl) as schematized in **Figure 2.7**. Each atomic plane reflects the X-rays with angle θ. If the path difference σ between two rays diffracted by two reticular planes equals a multiple of the wavelength λ, the diffraction occurs as the interference is constructive. The diffraction condition is formulated in Bragg's law (2.3) [141] that relates the diffraction angle θ, the inter-reticular distance d_{hkl}, and the X-rays wavelength as follows:

$$\sigma = 2 \cdot d_{hkl} \cdot \sin(\theta) = n \cdot \lambda \qquad (2.3)$$

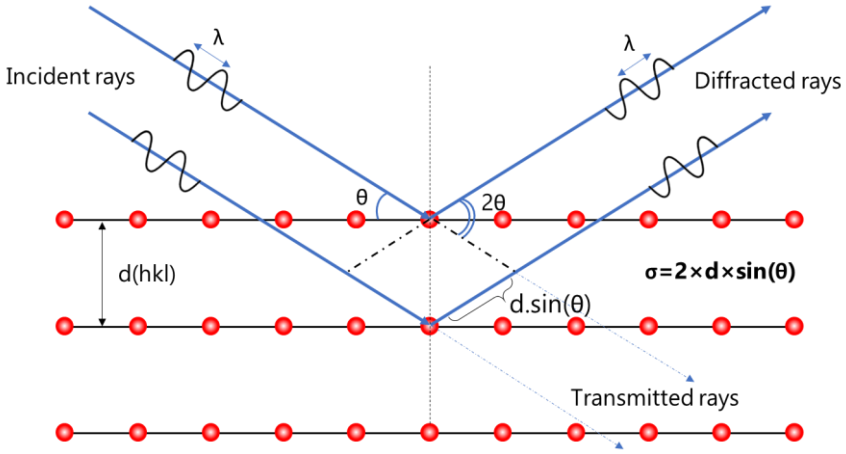

***Figure 2.7** schematic representation of the principal of X-ray diffraction*

Angles convention

Most X-ray diffractometers used for analyzing thin films are typically equipped with a four-circles goniometer, which enables precise positioning of the sample in relation to the X-ray incident beam and the detector.

Figure 2.8 schematizes the angles generally used in XRD which are described as:

θ the angle between the analyzed {hkl} plan family and the incident beam;

ω the angle between the sample surface and the incident beam;

ϕ the azimuthal angle around the normal of the sample; and

χ the angle perpendicular to the diffraction plane.

The adjustment and the movement along the four angles depend on the desired measurement configuration. For example, to perform coupled ω-2θ it is necessary to vary the incidence angle θ in the scan range, and with each step Δθ, we move the sample with Δω=Δθ/2.

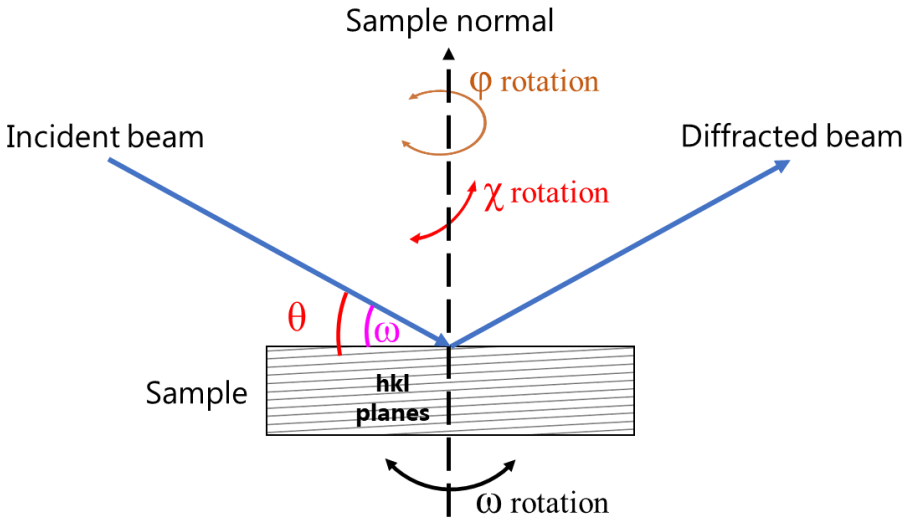

Figure 2.8 *X-ray Diffraction Angle Nomenclature*

2.3.2. Coupled θ-2θ scan (out-of-plane lattice parameter measurement)

In this configuration, a set of atomic planes parallel to the surface of the analyzed sample can be oriented to satisfy the diffraction conditions by varying the incident angle θ, and moving the X-ray detector to collect the diffracted rays making the angle 2θ with the incident beam. The collected data is represented as a curve presenting the diffraction intensity as a function of the angle 2θ, in which each peak corresponds to a measured inter-reticular d_{hkl} spacing.

Ewald sphere construction (**Figure 2.9**) can be used to visualize this type of scan. The radius of Ewald sphere is the wavevector of the incident wave $|K_i| = 2\pi/\lambda = |K_e|$, where λ is the X-ray wavelength and its center coincides with the origin of the reciprocal lattice of the analyzed sample. A node hkl* is in Bragg position when it is positioned on Ewald sphere. The nodes likely to be placed on the sphere of Ewald are inside a sphere of radius $2K_0$ that we call "limiting sphere".

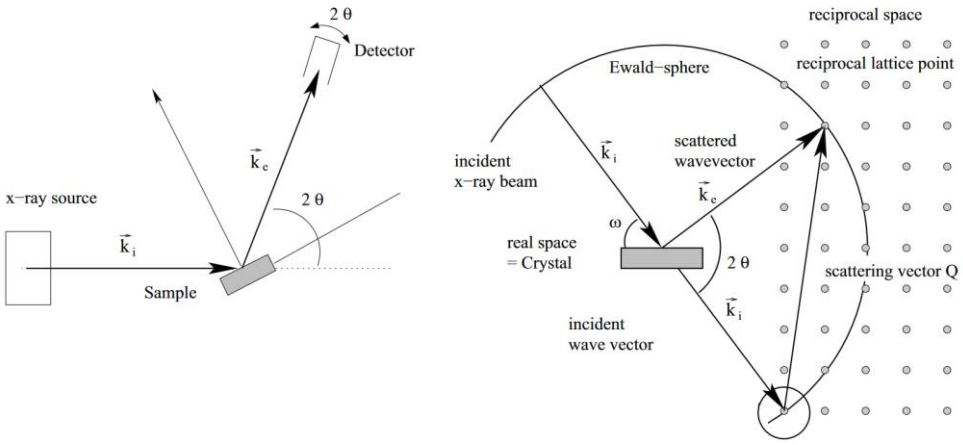

Figure 2.9 *Ewald sphere construction [142]*

2.3.3. Reciprocal space mapping

Reciprocal space mapping is a method that involves varying the incidence angle and the detector position in order to measure the intensity of diffracted X-rays as a function of both the incidence angle and the diffraction angle. The resulting data is then plotted in reciprocal space, which is a mathematical space that corresponds to the Fourier transform of real space. It is mainly used to analyze epitaxial thin films, allowing access to a wide range of information, notably the in-plane and the out-of-plane lattice parameter, from which we can evaluate the stress of the deposited films. In this technique we perform coupled ω-2θ scan of specific reciprocal point at several values of ω.

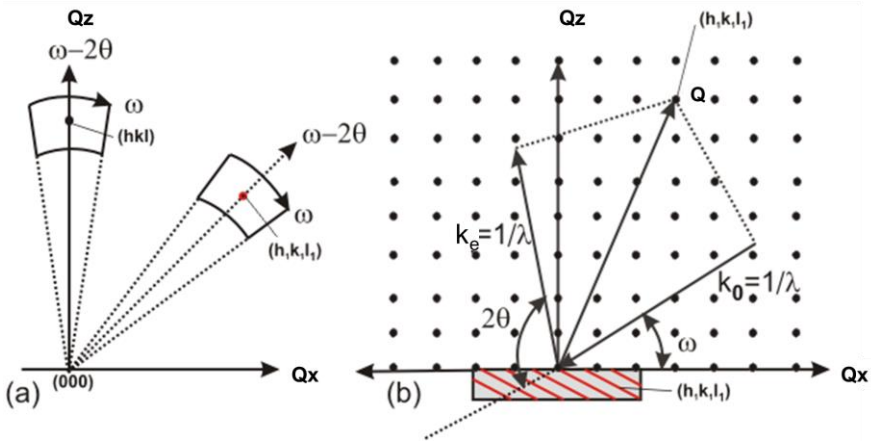

Figure 2.10 *(a) scan of symmetric (hkl) and asymmetric ($h_1k_1l_1$) reciprocal space points, (b) construction in the reciprocal space of the asymmetric reflection ($h_1k_1l_1$) , $Q=(k_e-k_i)$ represents the scattering vector [143]*

As illustrated in **Figure 2.10**, ω-2θ corresponds to a circular arc in the reciprocal space, while the ω-scan corresponds to a scan perpendicular to the scattering vector Q (Q is defined as the difference between the wavevector of the incident X-rays and the wavevector of the scattered X-rays $Q = (k_e - k_i)$). Combination of both scans allows a scan of vicinity of a selected Bragg reflection.

If we consider the case of a thin layer deposited on a substrate, such that Q_x and Q_z correspond respectively to the diffraction vectors in the directions perpendicular and parallel to the axis of growth, we can pass from the coordinates (θ,ω) to those of the reciprocal space (Q_x,Q_y) using to the relations (2.4) and (2.5):

$$Q_x = \frac{2}{\lambda} \cdot \sin(\theta) \cdot \sin(\theta - \omega) \tag{2.4}$$

$$Q_z = \frac{2}{\lambda} \cdot \sin(\theta) \cdot \cos(\theta - \omega) \tag{2.5}$$

where $Q_x = \frac{h}{a}$ and $Q_z = \frac{l}{c}$, with a and c the lattice parameters along x and z respectively.

2.3.4. Pole figure

Pole figures are a type of X-ray diffraction (XRD) analysis that is used to study the orientation and texture of a material. They provide information about the preferred crystallographic orientation of a set of crystallographic planes within a material.

To create a pole figure, the sample is first mounted on the diffractometer and aligned in a specific orientation, which depends on the atomic planes that we want to investigate. The goal is to determine whether these specific crystallographic planes are present and how they are oriented relative to the sample's surface. The X-ray beam is then directed at the sample and the diffracted X-rays are collected. The recorded diffraction patterns are then analyzed to determine the orientation of the crystallographic planes within the sample. The data is plotted on a pole figure, which is a graphical representation of the distribution of the crystallographic planes within the sample.

In a pole figure, the sample is represented as a stereographic projection onto a two-dimensional plane. The projection is centered on a specific crystallographic axis (generally growth axis in thin films), and each point on the projection represents a specific crystallographic orientation. By analyzing the pole figure, it is possible to determine the texture of the material, which can provide important information about its mechanical and physical properties.

Throughout this thesis, we utilized three diffractometers to analyze various samples:

(i) Siemens D5000 powder diffractometer with a two circles goniometer which was used only for analyzing films grown on flat substrates in θ-2θ configuration, available in GEMaC and ILV-Versailles.

(ii) Siefert XRD3000 with a four circles goniometer dedicated to thin film analysis, it was employed to analyze films grown on flat and miscut substrates in ω-2θ configuration, available in GEMaC.

(iii) Panalytical X'Pert Pro MRD diffractometer having also four circles goniometer and which is a more advanced instrument that enables faster alignment. It was used for ω-2θ measurements, pole figures, and reciprocal space mapping, available in CRHEA.

2.4. Secondary ion mass spectrometry

Secondary ion mass spectroscopy (SIMS) is a destructive experimental technique used to characterize the surface or near-to-surface composition of a material in the solid state. The method involves bombarding a solid sample placed in a vacuum with a primary ion beam, which has an energy greater than the energy of atoms bonding to the material's surface. SIMS apparatus consists mainly of an ion source, a mass spectrometer with associated optics and a detector, and an electron gun to adjust the surface potential of insulating samples at a fixed value [144].

Among the interactions possible when an energetic ion (primary ion) hits a solid surface is the implantation of this ion in the target lattice undergoing several collisions with the sample atoms. The implanted ion is decelerated, losing energy to the atoms constituting the sample. At some distance to the impact point, cascade collisions start near the surface leading to the emission of ions from the sample's surface (secondary ions) in a phenomenon known as erosion or sputtering. The resulting secondary ions are then extracted from the surface and separated by their mass-to-charge ratio using a mass spectrometer. By measuring the mass-to-charge ratio of the ions, the chemical composition of the sample surface can be determined.

Dynamic SIMS allows acquisition as function of time during continuous erosion to establish depth profiles of the collected elements. The output is expressed as intensity (count/s) as function of erosion time (s).

The ionic intensity of a secondary ion *X* is a function of three independent factors, given by the equation (2.6):

$$I_X = \eta(X) \cdot P_{sample}(X) \cdot F_p(X) \qquad (2.6)$$

Where η is the collect factor, depends on the collected spices, the sample texture, and the experimental conditions. P_{sample} represents the average ionization probability of the ion *X* in a given energy range, which depends of the eroded material. F_p is the pulverization coefficient.

For a low concentration of element *X* inside a target, it is generally considered that the sputtering yield (and, therefore, the erosion rate) will remain constant regardless of the material erosion depth [144].

To calculate the density [*X*] of the ion *X* in a matrix, we make use of Relative Sensitivity Factors *RSF* to convert the intensity I_X to volume concentration C_X (atom/cm^3). The *RSF* is defined as:

$$\frac{I_R}{C_R} = RSF_X \cdot \frac{I_X}{C_X} \qquad (2.7)$$

where I_R and C_R are the secondary ion intensity and the concertation of the reference material *R*. Generally, the R is taken as element of matrix containing the ions *X*, hence:

$$C_X = RSF_X \cdot \frac{I_X C_R}{I_R} \tag{2.8}$$

Assuming that the concentration of X element is at traces level, the concentration of the reference material remains constant. The values $RSF = RSF_X \cdot C_R$ are generally measured using standard samples for a given element in a specific matrix. Then concentration C_X can be calculated as:

$$C_X = RSF \cdot \frac{I_X}{I_R} \tag{2.9}$$

It is worth mentioning that sputtering across an interface where the sputtering rate may change, can give rise to a significant deviation from the actual concentration C_X.

The equipment used in the thesis is an **IMS7f CAMECA** available in GEMaC laboratory. It allows dynamic depth profiling with high sensitivity and resolution of few nanometers. The detection limit is 1.10^{14} atom/cm^3 with excellent mass resolution (M/ΔM= 10000). SIMS imaging allows the recording of in-plane special distribution of the sputtered elements in what we call checkerboard analysis mode. **Figure 2.11** represents a detailed scheme of the used **IMS7f CAMECA** apparatus.

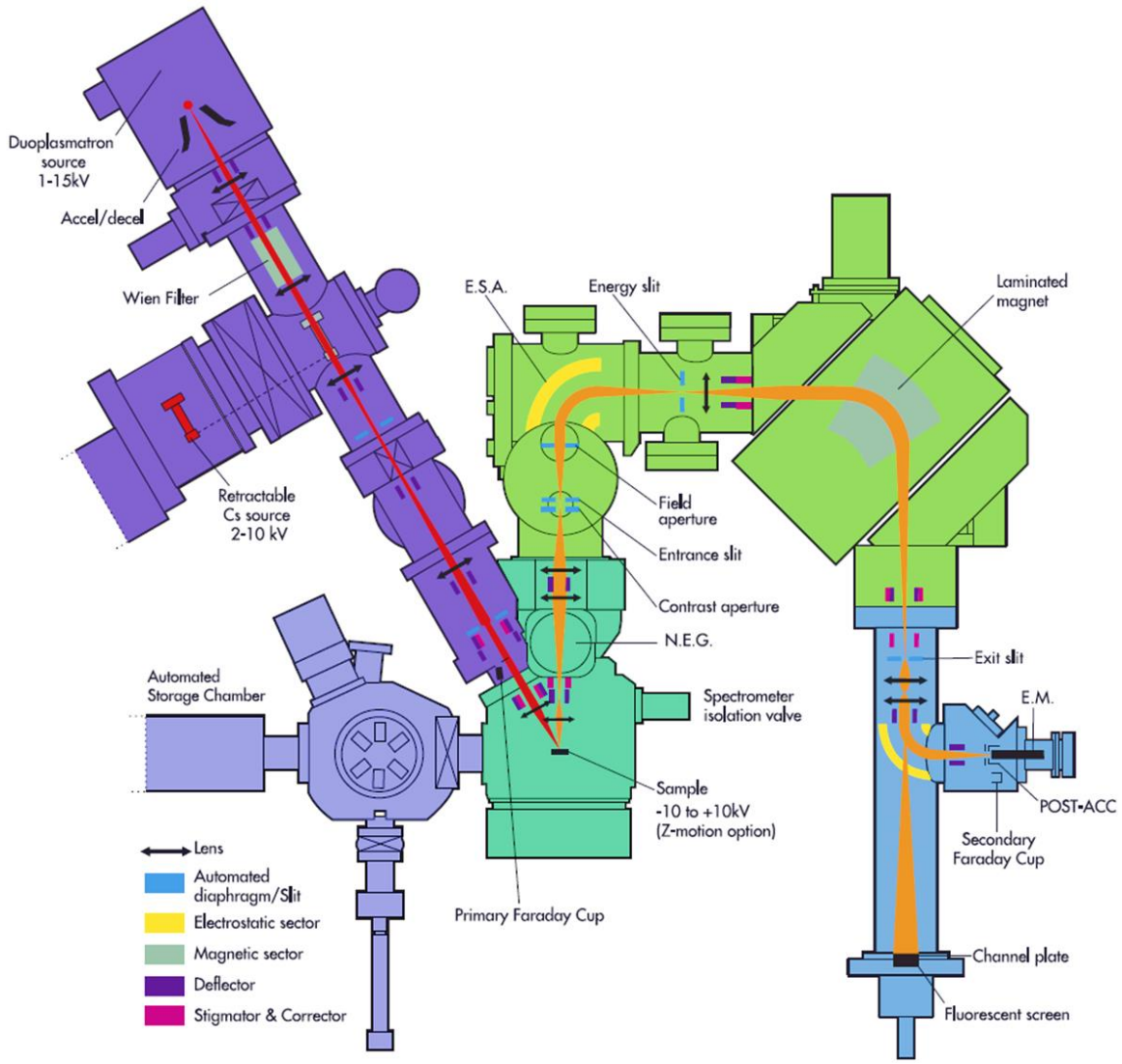

Figure 2.11 *Diagram of GEMaC SIMS IMS7f CAMECA equipment (from the IMS7f brochure)*

2.5. Vibrating sample magnetometry

Vibrating sample magnetometer (VSM) is a flux-based technique used to measure the magnetic moment of a magnetic sample. It was first introduced in 1956 by Simon Foner as an inexpensive and versatile technique that allows the measurement of variations in magnetic moment in the order of 10^{-5} emu to 10^{-6} emu as a function of temperature, magnetizing field, and/or crystallographic orientation [145]. The sample is placed inside a set of detection coils (pickup coils) and the ensemble is under a constant magnetic field gradient which doesn't induce any current in the pickup coils. It is important to mention that there are several detection coils arrangements that were developed to optimize the technique. **Figure 2.12** schematizes the VSM experimental setup. The sample is mechanically moved with a sinusoidal motion along the Z axis using an electromechanical motor. As a result of the sample oscillating around the central position Z_0; according to Faraday's law, an induced voltage is created in the pickup coils

due to the variation of the magnetic flux inside them [146]. The induced voltage is detected using lock-in amplifier and its proportional to the magnetic moment of the sample, and the oscillation (frequency and amplitude), it is given in the equation (2.10) [147]:

$$V(t) = G\, m\, \omega\, A \cos(\omega t) \qquad (2.10)$$

Where G is a geometrical factor of the pickup coils (known also as a sensitivity factor), m the sample magnetic moment, A is the oscillation amplitude, and ω is the motion frequency. Knowing that the factor G, the amplitude A, and the frequency ω are known values, and that the voltage V is a measured, one can calculate the moment m using Equation (2.10).

In the context of this thesis, VSM measurement were performed using Physical Properties Measurement System from Quantum Design "PPMS – 9T" with standard VSM accessory. It allows measurement of the magnetic moment of a sample: m(H) as function of applied magnetic field, m(T) as function of temperature in the range of [2K- 400K] or in the range [300K-1050K] with the option VSM oven, and we can measure m(H) at variable temperature with a sensitivity of 10^{-5}emu.

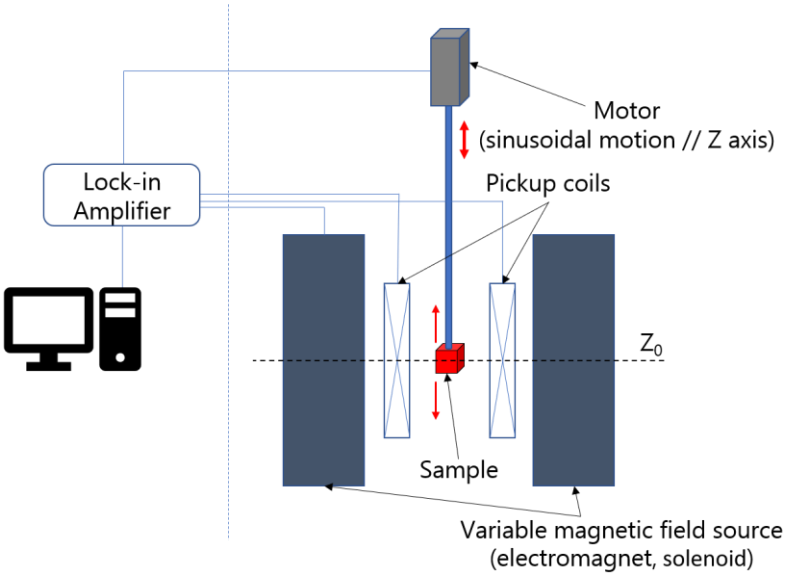

Figure 2.12 *measurement scheme of Vibrating Sample Magnetometer*

The magnetic field in PPMS – 9T VSM is generated parallel to the vibration axis using superconducting solenoid and it can be varied from -9T to 9T, and the flux variation detection is ensured by first order gradiometer assembly that we call "Coilset Puck" which are in axial arrangement, (coaxial configuration with the superconducting solenoid and //H). Two types of coilset puck with different bore dimensions are available and are used depending on the size of the measured samples: (i) "small bore" coilset puck, can be used to measure samples smaller

than 5 × 5 mm², and (ii) "large bore" coilset, which is used for larger samples up to 10 × 10mm². **Figure 2.13** shows a coilset puck and its schematic representation.

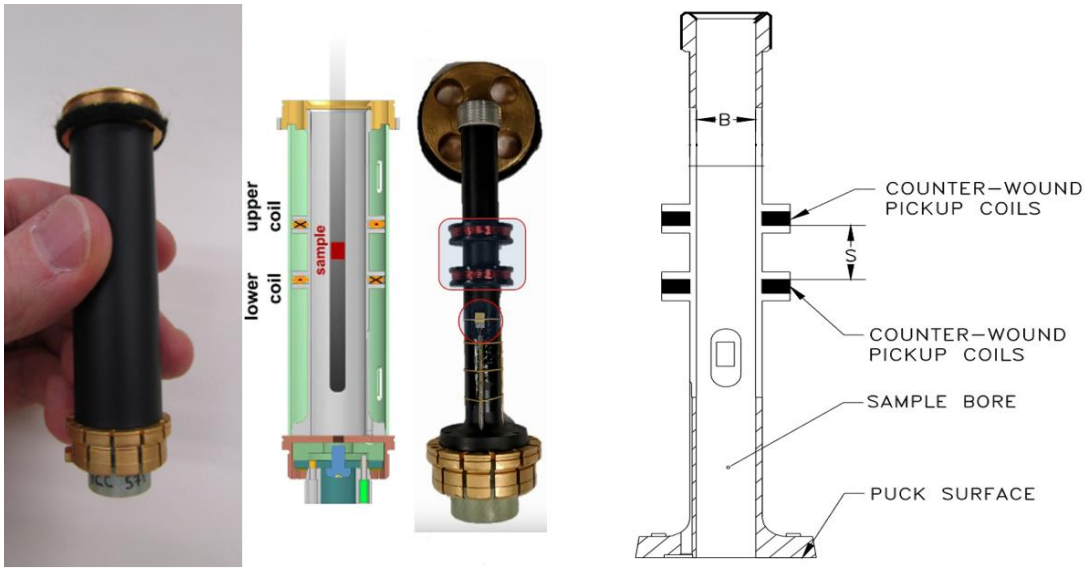

Figure 2.13 *coilset puck and the corresponding schematic representation, for the "small bore" coilset puck: B= 6 mm, S= 7 mm, and for the "large bore" coilset puck: B=10 mm, S=12 mm*

2.5.1. Subtraction of the diamagnetic contribution of the substrate

Generally, when we measure the hysteresis magnetic loop of a ferromagnetic thin layer, the recorded signal includes contributions from not only the film but also the substrate and sample holder. Therefore, we need to subtract these additional contributions to evaluate the net magnetization of the film. The commercial PPMS – 9T VSM comes with an ultrapure aluminum alloy sample-holder that produces a tinny diamagnetic signal. As a result, the signal to be subtracted from the raw measurement is mostly the contribution of the substrate, which in our case is ZnO (+ Teflon used to fix the sample on the holder) exhibiting a diamagnetic response.

Two ways are possible to do this subtraction, either by measuring the magnetization of a naked substrate before the growth of the Fe_3O_4 film then subtracting it of the measured magnetization after the growth of the film, or the estimation of the diamagnetic contribution from the linear part in the saturation region of the measured hysteresis magnetic loop of the sample (film + substrate). All the presented results in this thesis are corrected manually following the latter procedure by taking the linear slope as the average of slopes of the linear part measured under positive, and negative field (linear fitting from H_{sat+} to H_{sat+} + 1T, and from H_{sat-} to H_{sat-} - 1T respectively).

The net magnetization of the film is then calculated using the equation (2.11):

$$m_{film}(H) = m_{raw}(H) - H \times slope \quad (2.11)$$

Where m_{film} is the net magnetization of the film and m_{raw} is measured magnetization before the diamagnetic subtraction.

Figure 2.14(a) shows an example of the raw measured moment versus the applied magnetic field of an Fe_3O_4 thin film deposited on ZnO(0001) substrate. After the diamagnetic contribution subtraction using equation (2.11), the net magnetic moment representing only the magnetic response of the film is displayed **Figure 2.14(b)**.

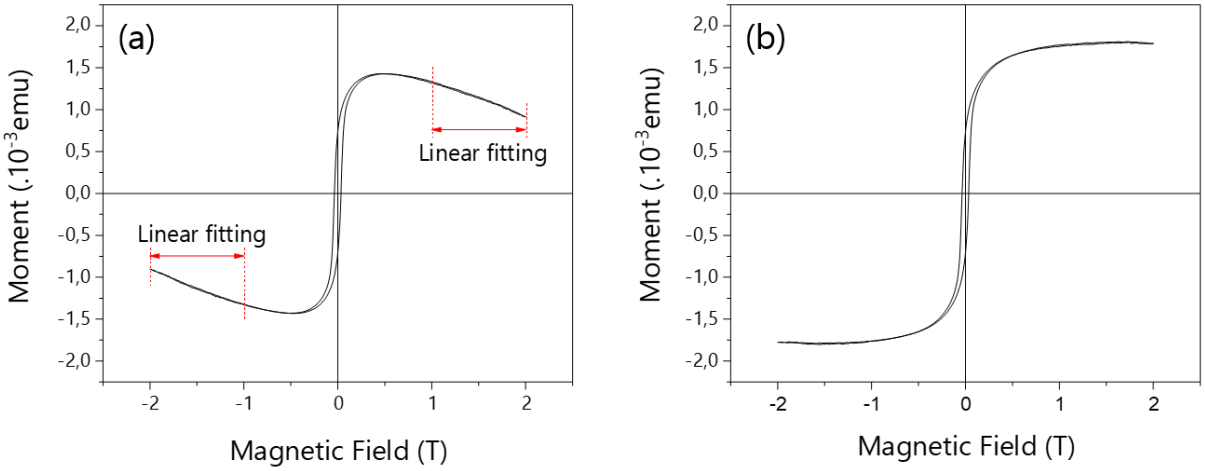

Figure 2.14 *(a) raw measured moment versus the applied magnetic field $m_{raw}(H)$, the diamagnetic slope is calculated as the average of the slopes of the linear regions estimated with linear fitting, (b) net ferromagnetic moment of the film versus the applied magnetic field $m_{film}(H)$ obtained after the diamagnetic subtraction using equation (2)*

2.5.2. Sample size effect on magnetization measurements

The VSM technique is well-suited for measuring a point dipole moment placed at the saddle point of the detection coilset (which we call the center), where the detection sensitivity is maximal [148]. However, real-life samples are not point-like and require some corrections. Most of the thin Fe_3O_4 films studied in this thesis were grown on ZnO substrates with dimensions of 10 × 10 mm² or 7 × 10 mm². The PPMS-9T VSM used in this study is calibrated using a standard palladium sample with a cylindrical shape and a diameter of D = 2.8 mm and length L = 3.8 mm and samples with similar dimensions are measurable with very high accuracy. Yet, samples with a length of up to 5 mm also can be measured with 98% accuracy when the length is parallel to the measurement axis (a table of sample sizes is provided in the VSM brochure). It should be mentioned that the lateral dimension (⊥ Z axis) of the sample does not strongly affect the measurement, but it is the longitudinal dimension (// Z axis) which causes the measurement error. Hence, a drastic deviation of around -30% in the measured moment,

compared to the true moment of the sample, is observed when a cylindrical sample of 10 × 3 mm² is measured parallel to the Z axis with the "small bore" coilset. To measure the magnetization of our samples, we rather use the large bore coilset puck as the samples do not fit the small bore one.

To establish the correction factor for determining the true magnetic moment of our samples, we measured Fe_3O_4/ZnO samples of W = 7 mm × L = 10 mm size in two configurations: L ⊥ Z and L // Z. **Figure 2.15** shows the measurement configurations and the corresponding hysteresis magnetization loops (after the diamagnetic contribution subtraction). The saturation magnetization measured in configuration (a) L ⊥ Z is Ms = 470 emu/cm^3, which is very close to the bulk saturation value (480 emu/cm^3). This indicates that for sample lengths up to 7 mm, the measurement is sufficiently accurate and represents the true moment of the sample. However, in the second measurement (b) where L // Z, a reduction of 10.5% was observed, with measured Ms = 420 emu/cm^3 (for the same sample). Therefore, a correction of + 10% is applied to all the 10 × 10 mm² samples in the following presented results.

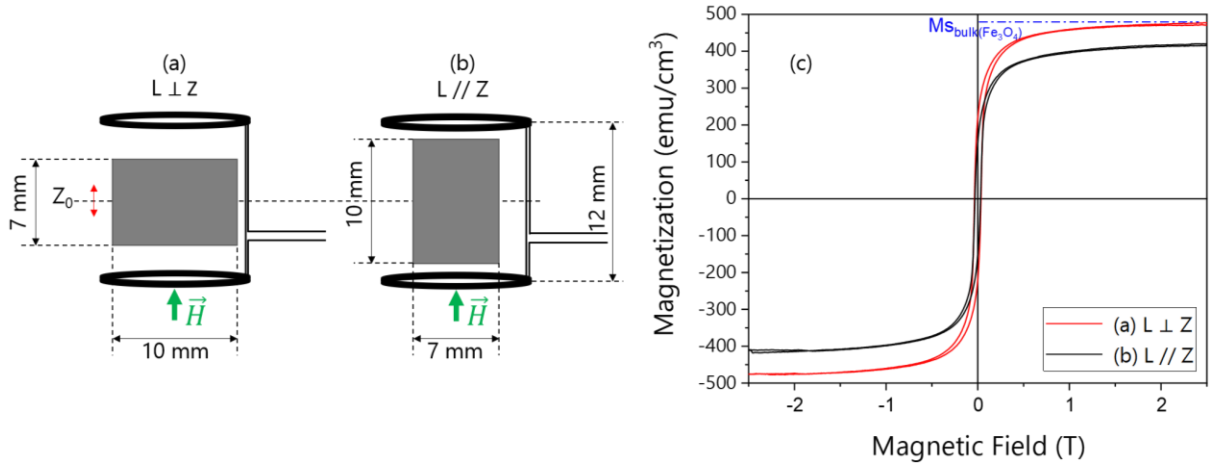

Figure 2.15 *(a) and (b): schematic representation of the sample possible orientations inside the detection coils of the coilset puck, (c) the corresponding measured magnetization curves M(H) after the diamagnetic contribution subtraction*

2.6. Transmission electron microscopy

2.6.1. Brief history

The first demonstration of transmission electron microscopy (TEM) dates back to the 30s of the 20th century, by Max Knoll and Ernst Ruska at the Technical University of Berlin. The instrument used an electron beam to produce images of a thin metal film placed in the path of the beam. The first TEM images were low-resolution and showed only the outlines of the metal particles. Over the following years, the resolution and clarity of TEM images were

improved by refining the design of the instrument and introducing magnetic lenses that have been used to focus the electron beam. Later, researchers continued to refine the design and introduce new technologies, such as aberration corrections and cryogenic electron microscopy to further improve the resolution and capabilities of TEM.

2.6.2. Principe of measurement

Transmission electron microscopy (TEM) operates on the principle of wave-particle duality, in which a beam of high-energy electrons (100 – 300 keV) is accelerated by an electron gun, forming a coherent wave. The electron beam is focused onto a thin sample, typically less than 200 nanometers thick, by a series of electromagnetic lenses that manipulate the trajectory of the electrons. The sample interacts with the incident electrons, causing them to scatter in various directions due to elastic and inelastic scattering processes and diffraction phenomena caused by the structure periodicity of the sample.

The scattered electrons are then detected by a detector positioned behind the sample. The detector collects the electrons and amplifies the signal that have passed through the sample or have been scattered by it, then converts the electron signal into an image. In some cases, detectors can also collect analytical data, such as electron energy loss spectroscopy (EELS) or X-ray energy dispersive spectroscopy (EDS), which are used to determine the crystalline structure and the chemical composition of the sample.

One of the key advantages of TEM is its ability to achieve high spatial resolution, typically ranging from a few nanometers. In fact, the resolution of a microscope is limited by the aberrations in its lenses. However, the utilization of an aberration corrector enables us to surpass this limitation and achieve a resolution below the Angstrom. This exceptional resolution achieved by TEM makes it a unique instrument for extremely detailed observations and allows the observation of the fine details in the structure of the sample, such as the arrangement of atoms in a crystal lattice.

2.6.3. Imaging modes

Transmission electron microscopy offers a versatile array of imaging modes, each tailored to reveal distinct details at the nanoscale. In the context of this thesis work, several of these modes were employed to investigate the chemical and crystalline properties of Fe_3O_4 thin films.

2.6.3.1. TEM and diffraction

The operation of a Transmission Electron Microscope (TEM) involves the interaction of an electron beam with the sample, resulting in the generation of various electron signals. These signals include electrons that pass through the sample without deflection, electrons that scatter in various directions due to interactions with the sample, and electrons that are absorbed by the sample.

An advantage of a transmission electron microscope lies in its ability to simultaneously provide information in both real space (imaging mode) and reciprocal space (diffraction mode).

Figure 2.16 provides a ray diagram illustrating the two primary analytical modes in transmission electron microscopy (TEM) along with the essential components of the microscope [149].

The electron beam is created in an electron gun and undergoes acceleration to attain the required high energy level. Subsequently, this electron beam passes through the condenser system, comprising specific magnetic lenses and apertures. This configuration facilitates the generation of two distinct beam types: a parallel beam suitable for micro-probing in TEM and a convergent beam with adjustable convergence angles, commonly employed in scanning transmission electron microscopy (STEM) and convergent beam electron diffraction (CBED) for nano-probing applications.

Following the condenser system, the electron beam continues through the sample, reaching the objective lens, one of the most important components, responsible for producing the initial intermediate image. The quality of this intermediate image critically influences the ultimate resolution of the final image viewed on the projection screen within the chamber or through a camera mounted below the microscope column.

The objective lens plays a dual role by forming a diffraction pattern in the back focal plane through the combination of electrons scattered and diffracted by the sample. In TEM, both the diffraction pattern and the image coexist, and their visibility can be selectively controlled by adjusting the focus strength of the intermediate lens.

In the diffraction mode, as the electron beam interacts with the sample, electrons scatter at varying angles, resulting in the creation of a diffraction pattern. The placement of a selected-area diffraction aperture (SAD) behind the sample enables the isolation and analysis of specific regions within the diffraction pattern.

In TEM imaging mode, the introduction of an objective aperture in the back focal plane permits the selection of one or more beams contributing to the final image, such as bright field (BF) or dark field (DF).

In BF TEM mode, the aperture is positioned in the back focal plane of the objective lens, allowing only the direct beam to pass through. Consequently, the image produced stems from the interaction of the direct beam with the sample, creating a two-dimensional projection of the sample's three-dimensional structure. Image formation in BF mode is influenced by mass-thickness and diffraction contrast, leading to dark contrast in thick areas, regions enriched with heavy atoms, and crystalline regions.

In contrast, DF TEM images are created by blocking the direct beam with the aperture while permitting one or more diffracted beams to pass through the objective aperture. DF images reveal information about planar defects, stacking faults, particle size, and other specimen characteristics due to the substantial interaction of diffracted beams with the sample.

This image formation process relies on both absorption and scattering contrast, with characteristics such as the atomic number and sample thickness influencing the observed contrast.

It is important to underline that maintaining a parallel electron beam is a fundamental requirement in TEM imaging mode, as it ensures the acquisition of high-quality images characterized by excellent contrast and resolution. The precise control of the objective lenses positions and focus enables the capture of clear and detailed images, revealing the structural features of the specimen.

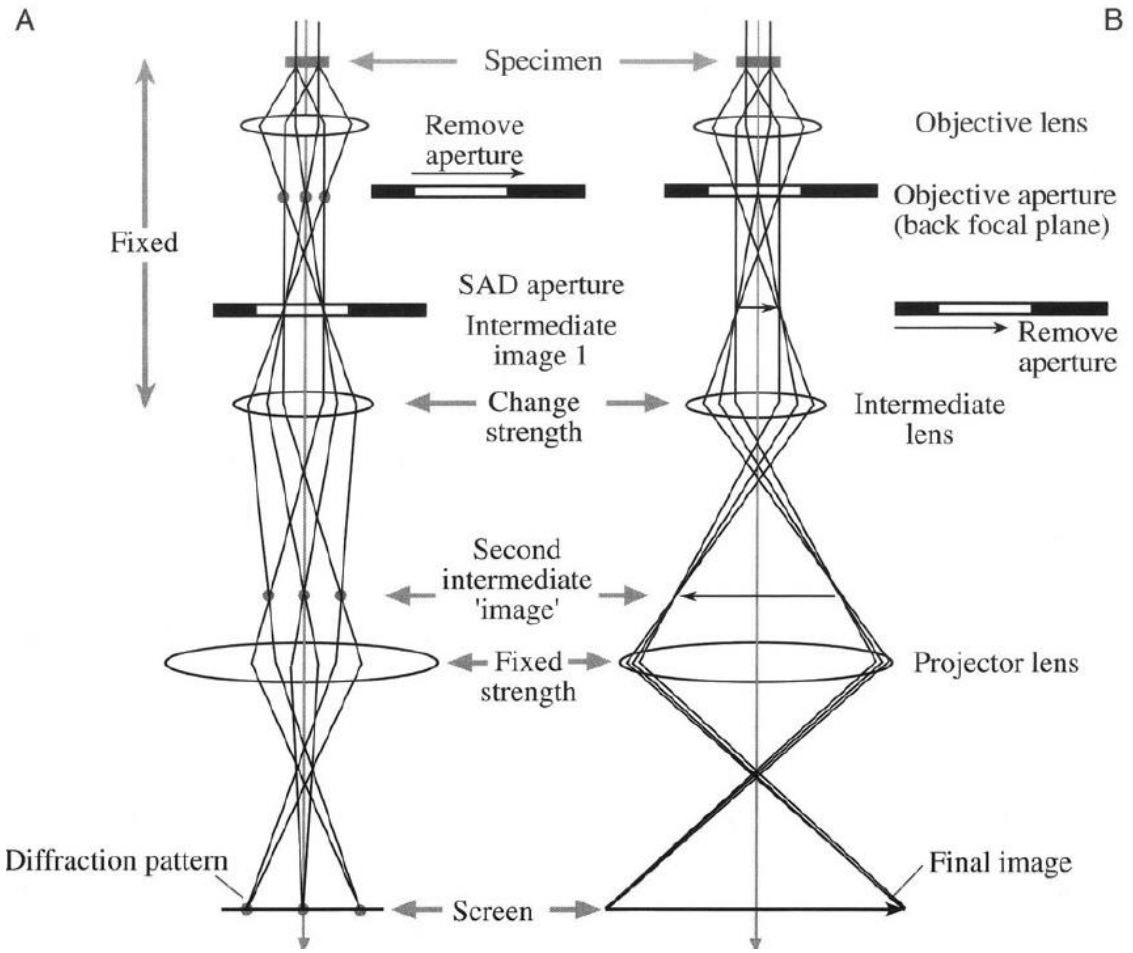

Figure 2.16 *Transmission electron microscopy ray diagram for: (A) diffraction mode, (B) bright field imaging [149]*

2.6.3.2. STEM

While TEM employs a parallel beam, scanning transmission electron microscopy (STEM) is distinguished by the use of a convergent electron beam. In STEM, this focused electron beam scans across a defined region of the specimen surface. The signals generated from the electron-sample interaction are collected by detectors, spot by spot, allowing for the creation of an image on a screen, pixel by pixel. This resulting image is reconstructed from the variations in signal intensity, which are influenced by factors such as the sample's crystalline structure, orientation, and chemical composition. Three imaging modes are possible for STEM imaging, as it is illustrated in **Figure 2.17**:

1. Bright Field (BF)-STEM: the detector is positioned along the microscope's optical axis to capture the intensity of the direct beam after its interaction with a point on the specimen. It provides information similar to BF-TEM.

2. Annular Dark Field (ADF)-STEM: a ring-shaped detector is employed to collects electrons scattered or diffracted at small angles (approximately 10-50 mrad), the ADF detector operates similarly to the DF-TEM mode. It predominantly provides crystallographic contrast by capturing electrons diffracted within crystalline regions, although it may also incorporate contributions from incoherent scattering.

3. High-Angle Annular Dark Field (HAADF)-STEM: in this mode, the detector consists of a disk with a larger inner diameter (> 50 mrad) than the ADF detector, which captures electrons scattered into high angles, primarily resulting from incoherent scattering events. Consequently, the HAADF mode generates chemical contrast, particularly achieving atomic number (Z) contrast, which allows for the visualization of variations in sample composition.

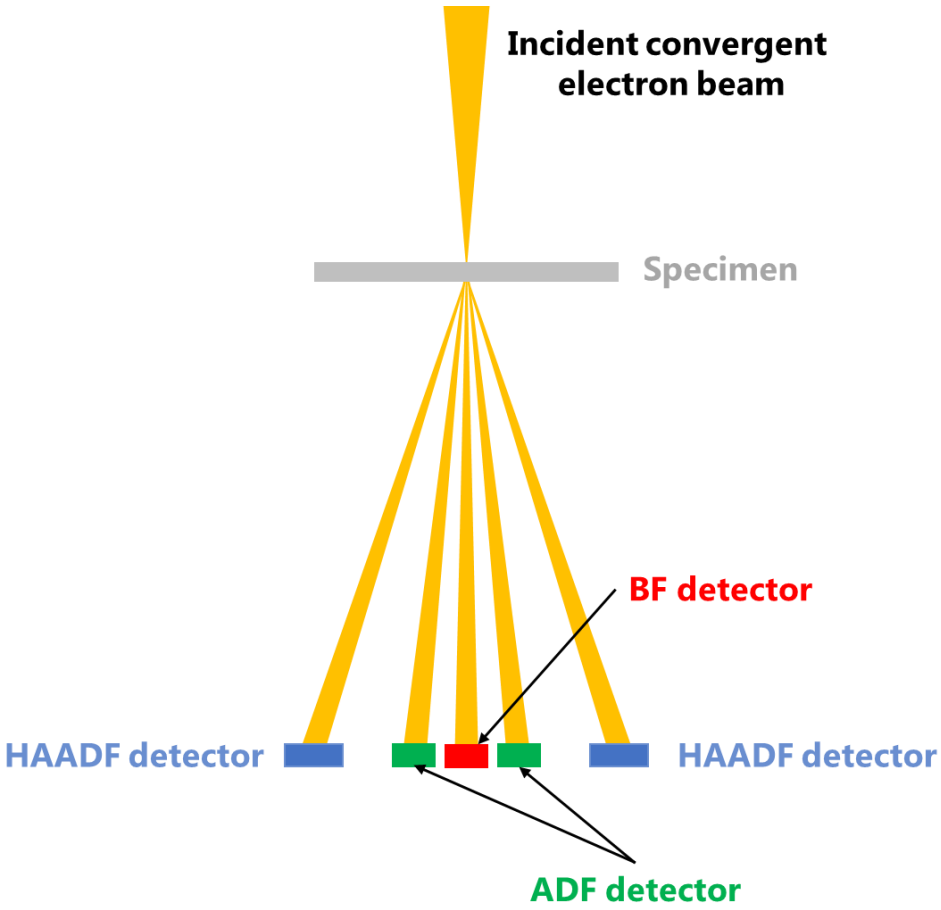

Figure 2.17 *schematic representation of the ray path and detectors configuration the scanning transmission microscopy*

2.6.4. Sample preparation

The objective is to obtain sample thin enough to achieve the electron transparency from ~ 80nm-thick films grown on 10×10 mm² substrates. Two types of manual sample preparation were carried out in the context of this thesis.

2.6.4.1. Cross-section lamellae preparation (sandwich technique)

To prepare a sample for a cross-section observation, we cut two slices from the sample along the desired observation zone axes and attach them face-to-face with a specific glue to create a sandwich. For the heterostructure $Fe_3O_4(111)/ZnO(0001)$, we are interested to carry out observations along $ZnO[11\bar{2}0]$ and $ZnO[1\bar{1}00]$ zone axes, so we make two cuts perpendicular to the edges of the substrate, knowing that the substrates have defined orientation. The typical dimensions of these slices are 2.3 x 7 mm² (the length can be smaller, depending of the size of the sample). From the prepared sandwich, we cut a lamella with a width of 500 µm and we mechanically polish one face until it reaches a thickness of 250 µm. Next, we glue the polished face of the lamella onto a metallic ring compatible with the TEM sample holder and we polish the second face of the lamella. Once we reach a thickness of 20 µm, we use Ar^+ ions for further thinning of the sample and achieving the electron transparency using ion milling in the PIPS (Precision Ion Polishing System). Practically we stop the ion thinning once the center of the sample is pierced. **Figure 2.18** illustrates the steps followed in preparing a cross-section sample. The observation area is the outline of the created hole.

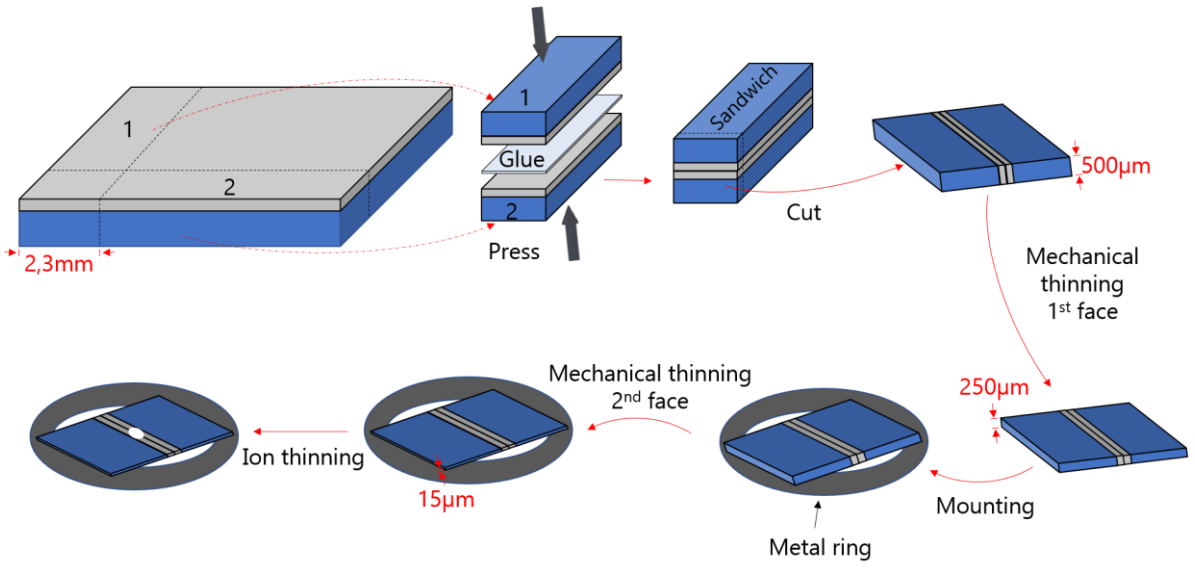

Figure 2.18 Schematic representation of cross-section lamella preparation

2.6.4.2. Plane-view sample preparation

Preparing a sample for a plane view TEM observation is much more delicate than the cross-section technique. We mechanically polish the substrate side of the sample at an angle of around 4° (see **Figure 2.19**) until the wedge of the sample reaches the electron transparency. Diamond grains with sizes up to ¼ µm were used during the polishing process, followed by the use of colloidal silica in the final polishing step.

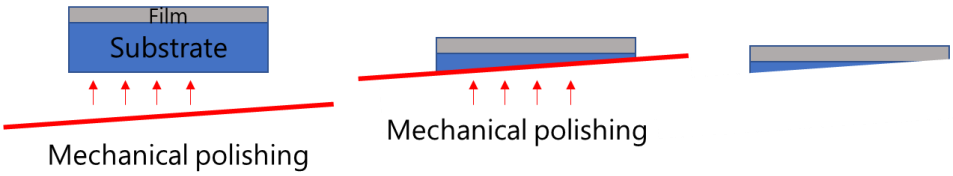

Figure 2.19. *Steps of preparation of plane-view lamella from left to right*

All TEM characterizations in this thesis were carried out in CRHEA laboratory using a Thermo Ficher Spectra 200 microscope. This microscope is equipped with a cold cathode electron source, which generates intense electron beams with low energy dispersion (0.4 eV). This feature accelerates chemical mapping through EDX and enhances spatial resolution in imaging. It offers selectable acceleration voltages of 200 kV, 120 kV, and 60 kV, with the lower voltage option preserving delicate samples. The microscope features a probe corrector, enabling STEM resolution as fine as 0.7 Å at 200 kV (1,1Å at 120kV and 60kV), and sectorial STEM detectors for visualizing light elements. Additionally, it has two large EDX detectors for high sensitivity (solid angle: 1.8 sr). The specimen holder allows for tilting up to +/-40° and +/-30°.

It is possible to capture up to 40 images per second at 4K×4K px resolution and up to 300 images per second at 512×512 px resolution, thanks to its rapid CETA CMOS camera.

2.6.5. Image analysis

2.6.5.1. Observation of defects in DF-TEM imaging

In DF-TEM, particularly under the two-beam condition, only the transmitted beam and a chosen diffraction vector 'g' actively participate in the image formation. We give the example illustrated in **Figure 2.20**, where the upper crystal (A) is fixed while the lower one (B) undergoes displacement by a vector 'R(r)' (in certain cases, rotation by an angle 'θ' about an axis). The two scenarios depicted in the figure reveal the fundamental distinction in crystallography. In (a), the stacking fault or displacement introduced does not disrupt the periodicity of the atomic planes diffracting g_1. This scenario typically results in a crystal region that adheres to the expected periodic lattice arrangement, and it appears consistent in DF-TEM

images. In contrast, in (b), the stacking fault significantly disrupts the periodicity of the atomic planes diffracting g_2. In this case, the lattice structure deviates from the regular crystalline order, and the crystal region exhibits distinct contrast characteristics in the DF-TEM image, making it possible to observe and analyze defect. It is important to note that defects become invisible in DF-TEM when the condition g.R = 0 or an integer. On the other hand, defects become visible when 'g.R ≠ 0,' indicating a deviation from the perfect periodic lattice structure. In both scenarios, a phase shift proportional to 'g.R' is introduced in the coupled beams, further contributing to the observed contrast in the image.

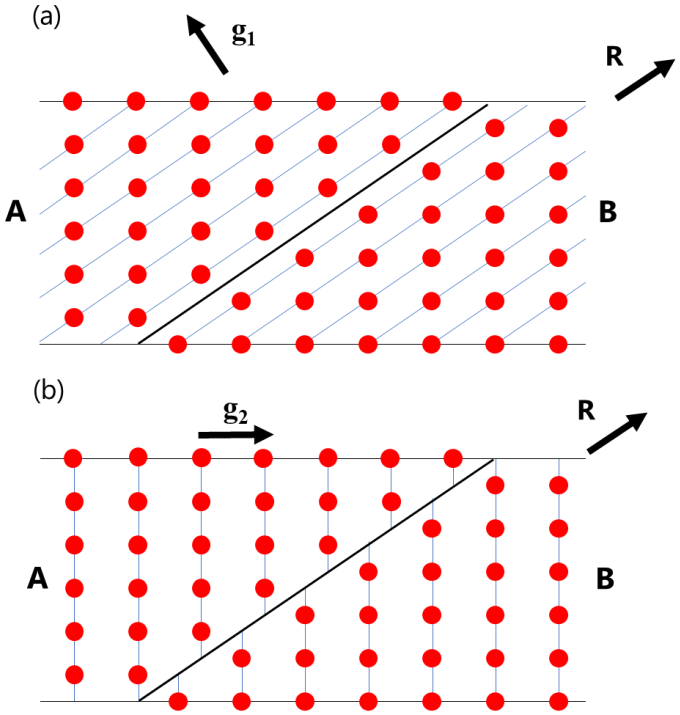

Figure 2.20 *schematic representation of two parts of crystal A and B, where B is shifted by a vector R with respect to A. The black line in both cases represents the same defect plane, in (a) the defect does not affect the periodicity of atomic planes diffracting the vector g_1, and in (b) the periodicity of atomic planes diffracting the vector g_2 is perturbed*

2.6.5.2. Geometric phase analysis

Geometric Phase Analysis (GPA) is a technique developed to extract quantitative data from high-resolution TEM images. GPA is particularly valuable for the analysis of phase variations within these images. It operates on the fundamental principle of examining phase gradients present in an image, with its primary objective being the quantification of local phase alterations. The method, introduced by Hÿtch et al. in 1998. [150], has garnered widespread usage in high-resolution TEM (HRTEM) for crystallographic analysis.

The process begins with a high-resolution image (TEM or STEM) that contains a series of atomic rows. The presence of atomic sequences in the image results in diffraction spots appearing in the Fourier transform of the image. Each of these diffraction spots is linked to both an amplitude and a phase, which provide essential information about positioning of atomic planes in real space. An ideal crystal typically results in a sharp peak in the Fourier transform, and any perturbation in the lattice spacing appears as diffuse intensities in the transform. By reconstructing a phase image from the sharp peaks and the diffuse intensities, it is possible to measure and map strain, displacement, rotation in the analyzed micrograph. The measurement of these quantities is performed in relation to a reference region within the same image which possess a known uniform lattice parameter (reference lattice).

The GPA methodology involves a sequence of steps, starting with the initial selection of a specific diffraction spot in Fourier space "g". This selection is carried out typically using a Gaussian mask, effectively isolating a frequency associated with the family of planes (Bragg filtering). By performing an inverse transform, the process yields a fringe image of both amplitude and geometric phase. For a particular set of lattice fringes[151], the Bragg fringes equation B(r) is:

$$B(r) = 2A_g(r)cos\{(2\pi g \cdot r + P_g(r)\} \quad (2.12)$$

Here, r represents the position within the image, A_g is the amplitude of the sinusoidal lattice fringes associated with the wavevector g, and P_g denotes the phase responsible for lateral shifts of the fringes in original image. It's important to note that deformation is directly proportional to the derivative of the measured phase $P_g(r)$. The illustration of a two-dimensional case is presented in **Figure 2.21.**

When describing an ideal set of lattice fringes (reference lattice), the phase and the amplitude in equation (2.12) become independent of r [152], resulting in (2.13):

$$B(r) = 2A_g cos(2\pi g \cdot r + P_g) \quad (2.13)$$

In the case of a displacement where "r" is transformed to "$r - u$", equation (2.13) becomes:

$$B(r) = 2A_g\, cos(2\pi g \cdot r - 2\pi g \cdot u) \quad (2.14)$$

Comparing equation (2.14) with (2.12) gives us:

$$P_g(r) = -2\pi g \cdot u \quad (2.15)$$

In this equation, the phase is directly related to u. Now, by considering only u_g, the component of displacement field perpendicular to the set of fringes defined by g (only the displacement in the direction perpendicular to the fringes); and taking $g = 1/d$ where d is the fringe spacing, we obtain:

$$P_g = -2\pi u_g / d \tag{2.16}$$

That gives us the displacement u_g as function of phase:

$$u_g = -\frac{P_g}{2\pi} d \tag{2.17}$$

In equation (2.17), the displacement is expressed as a fraction of the fringe spacing d, and the phase P_g in units of 2π. For example, for an antiphase boundary characterized by a half d-spacing displacement, a phase shift of 1 radian will give $u_g = \frac{1}{2\pi} d = 0{,}5d$.

Likewise, if we consider that the reciprocal lattice vector differs by Δg from the reference lattice vector g, it becomes "$g \rightarrow g + \Delta g$". Introducing this difference results in a new fringe image:

$$B(r) = 2A_g \cos(2\pi g \cdot r + 2\pi \Delta g \cdot r) \tag{2.18}$$

The introduced Δg correspond to a variation in the lattice spacing, or a rotation for example. Comparing (2.18) and (2.12) gives:

$$P_g(r) = 2\pi \Delta g \cdot r \tag{2.19}$$

The variation Δg generates an incline in the phase. Computing the gradient of (2.19) gives:

$$\vec{\nabla} P_g(r) = 2\pi \Delta g \tag{2.20}$$

This equation enables us to directly measure local deviations from the average reciprocal lattice vector using the phase, which allow the quantification of deformation and rotation of the fringes.

In this thesis, we used the "GPA plugin" of Gatan DigitalMicrograph software commercialized by HREM Research to conduct GPA analysis. The calculations in this plugin are automated, with displacement given in nanometers, rotation in degrees, and deformation expressed as a percentage relative to the reference lattice. It's important to mention that the resolution of this technique is intrinsically tied to the size of the mask in reciprocal space, typically around 0.5 nm^{-1}, equivalent to 2 nm. As such, this method offers the capacity to measure deformations with a sensitivity on the order of 10^{-3} [150], [153]. This, however, mandates relatively small dimensions, ideally on the order of a few hundred nm^2, for deformation mapping.

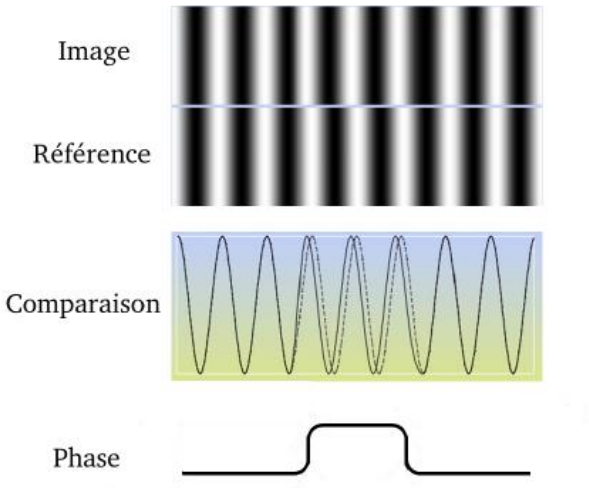

Figure 2.21 *GPA processing by phase difference between image and reference to estimate deformations [154]*

3. Fe_3O_4/ZnO heterostructure, growth and characterizations

3.1. Introduction

This chapter aims to present the scientific approach followed to achieve successful growth of Fe_3O_4 with high epitaxial quality onto ZnO (0001) substrates with either Zn or O polarities. We study the effect of the PLD growth parameters and the influence of the oxygen partial pressure that allows a precise control of the iron oxide stoichiometry. We show that it is possible to decrease the growth temperature of Fe_3O_4 down to 260°C while maintaining a high crystalline quality, comparable to higher temperature growth. This low growth temperature may limit the interdiffusion between the film and the substrate. At the end of this study, we establish a phase diagram of iron oxide stability at 260°C as a function of the oxygen partial pressure.

3.2. Substrate preparation

All ZnO substrates used in this work were prepared at the CRHEA laboratory using Rapid Thermal Annealing (RTA). The prepared substrates were then sent to the GEMaC laboratory for the deposition of Fe_3O_4 thin films using Pulsed Laser Deposition (PLD).
During the RTA process, the ZnO substrates underwent annealing at a temperature of 1080 °C for a duration of 2 minutes. This high-temperature treatment yielded significant improvements in the substrate surface cleanliness. The transformation achieved through RTA was confirmed by AFM images (see **Figure 3.1**). Prior to annealing, the as-received substrate surfaces exhibited an absence of discernible atomic steps, with the surface presenting a particle-contaminated appearance. Following annealing, distinct atomic steps became prominent, accompanied by a reduction in residual particle on the substrate surface. While the full AFM images revealing this reduction are not presented in this context, the marked effect of the annealing process on the substrate surface can be inferred. It is worth noting that while the terraces on the substrate surface exhibited slight deviations from perfect parallelism and straightness, certain V-shaped features were also observed as indicated on **Figure 3.1** with yellow circles. These V-shaped features might be caused by a pinning effect due to the residual particles that were present on the surface prior to the RTA.

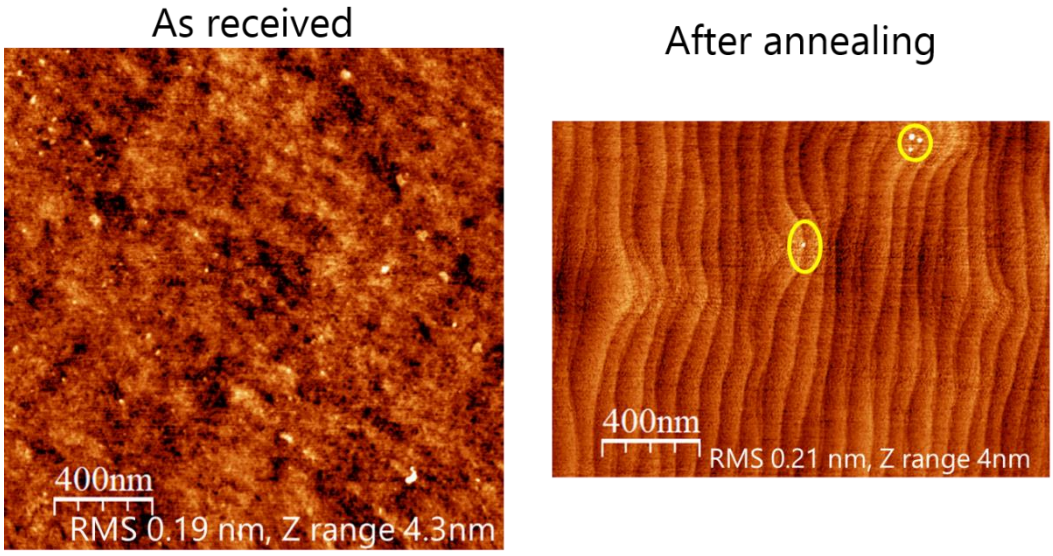

Figure 3.1 *AFM images of ZnO substrate: on the left as received, and on the right measured after annealing*

3.3.Fe_3O_4 phase stabilization (effect of growth conditions)

As discussed before, the difficulty of growing epitaxial Fe_3O_4 thin films derives from the possibility of forming other iron oxides, such as FeO and Fe_2O_3, depending of the growth environment. Contamination with other elements is not expected in the PLD technique if the target is pure iron oxide. To stabilize pure Fe_3O_4, four series of samples were grown, with each series corresponding to the variation of a single growth parameter in the following order: *(1)* the growth temperature, *(2)* laser fluence, *(3)* the growth temperatures once more, and finally *(4)* oxygen partial pressure. The best parameter from each series was used in the following one. The permutation between the optimization of growth temperature and laser fluence is justified by the fact that these two parameters are related in terms of the energy they can provide to the adatoms during the growth.

In this part, all the iron oxide samples have been grown on ZnO (000±1) substrates using pure ***Fe_2O_3 target*** and pulsed ***Nd:YAG laser*** at 10Hz with a wavelength of ***355nm***. The growth duration of each sample is 15 min, giving a thickness of around 80nm.

3.3.1. Growth temperature effect

The first set of samples was made to establish the appropriate growth temperature of Fe_3O_4. We choose the range between 500°C and 600°C based on previous reports and the conditions established in the GEMaC laboratory for other substrates [72], [73], [78], [155]. The depositions were performed under vacuum (without additional oxygen) where the pressure of the chamber before ablation was around 2×10^{-8} Torr, then it increases during ablation to ~ 2×10^{-7} Torr under the plasma plume expansion. The laser fluence is fixed at a value we denote

as ***Fluence$_{Max}$*** = 6.7 J/cm^2 (This value is an approximate estimation of the fluence resulting from the maximum power of the laser, see Appendix). **Figure 3.2** shows θ-2θ X-ray diffraction patterns of three samples grown at 580°C, 540°C, and 500°C. The presence of peaks indicates a crystalline growth of the thin films.

In addition to the peaks of the substrate ZnO (0001) and ZnO (0002) at 34.42° and 72.56°, the three samples present three families of peaks:

Fe(ll0): two peaks at 44.68° and 98.98°, identified as Fe(110) and Fe(220).

FeO(lll): two peaks at 35.87° and 76.02° identified as FeO (111) and FeO (222).

Fe$_3$O$_4$(lll): four peaks at 18.34°, 37.23°, 57.27°, and 79.05° identified as Fe$_3$O$_4$ (111), Fe$_3$O$_4$ (222), Fe$_3$O$_4$(333), and Fe$_3$O$_4$ (444) respectively.

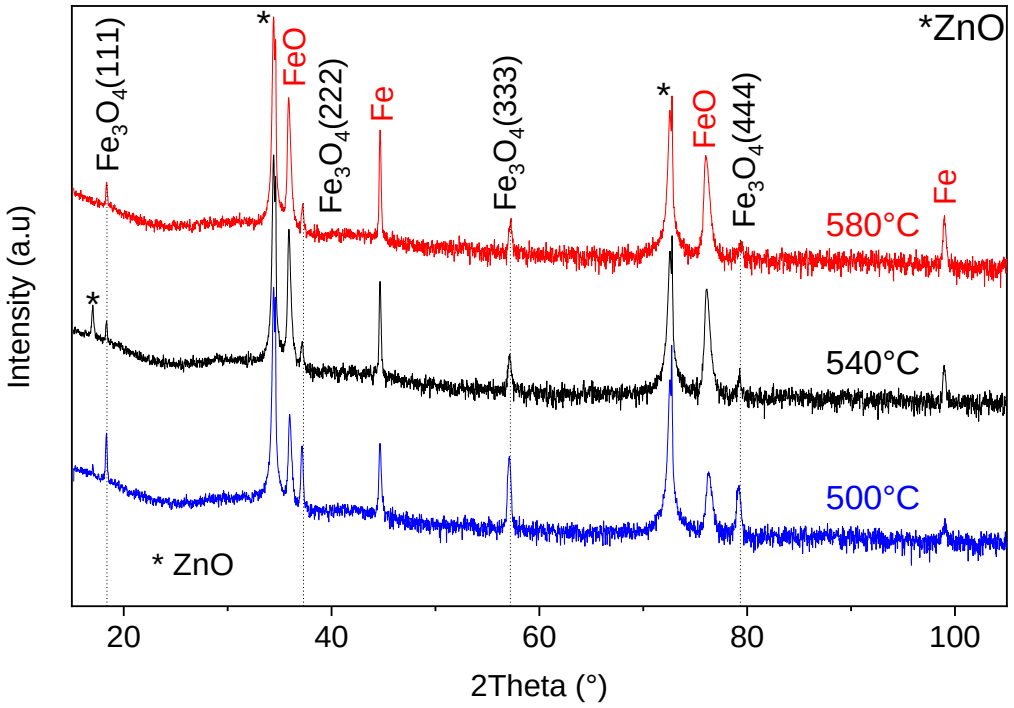

Figure 3.2 *Cu-Kα XRD patterns of thin films grown at Ts= 500°C, 540°C, and 580°C*

The effect of the growth temperature is observed in the intensities of peaks. Since the integrated diffracted intensity is proportional to the amount of the crystallized material, and its degree of crystallinity, we can apply the Direct Comparison Method to compare the proportion of Fe$_3$O$_4$ to the two other phases.

The intensities diffracted by a mixture of phases are related with the equation (3.1):

$$\frac{I_\alpha}{I_\beta} = \frac{R_\alpha c_\alpha}{R_\beta c_\beta} \qquad (3.1)$$

Where I_α and I_β are the diffracted intensities of the phases α and β, R_α and R_β are constants

depending on the crystal structure and lattice parameter of each phase, c_α and c_β are the volume fractions of α and β phases, respectively [156]. By assuming that the sum of volume fractions equals 1, and taking into consideration that all the XRD measurements are performed in the same conditions, we can compare the ratio $I_{Fe_3O_4}/(I_{Fe}+I_{FeO})$ for the different temperatures to choose the temperature that favors the growth of Fe_3O_4. **Table 3.1** resumes the θ-2θ integrated intensities and the comparison ratio of the peaks Fe(110), FeO(111), and Fe_3O_4(222), at different temperatures.

Table 3.1 *values of integrated intensities of the peaks FeO(111), Fe_3O_4(222), Fe(110) and the ratio $I_{Fe_3O_4}/(I_{Fe}+I_{FeO})$ at different growth temperatures*

Growth Ts (°C)	**Integrated intensity**			**Ratio $I_{Fe_3O_4}/(I_{Fe}+I_{FeO})$**
	I_{Fe}	I_{FeO}	$I_{Fe_3O_4}$	
580	22.03	107.87	3.09	0.02
540	15.33	123.08	4.18	0.03
500	9.64	33.02	9.24	0.22

At Ts=580°C, the film is mainly crystallized as a mixture of Fe and FeO. By lowering the growth temperature to 540°C, a small amount of Fe undergoes oxidation, resulting in the increased amount of FeO, while the fraction of Fe_3O_4 remains unchanged. Further decrease of the growth temperature to 500°C yields a significant increase in the ratio $I_{Fe_3O_4}/(I_{Fe}+I_{FeO})$ from 3% to 22%, indicating that lower temperatures promote the formation of Fe_3O_4 (while maintaining the other conditions fixed). This observation can be a direct result of a limitation of oxygen re-evaporation which transforms Fe and FeO into Fe_3O_4 after decreasing the substrate temperature. It is worth mentioning that the three samples grown at 580, 540 and 500°C present particles on the surface. Such particles are shown in **Figure 3.3**, an image of the sample surface taken using optical microscopy.

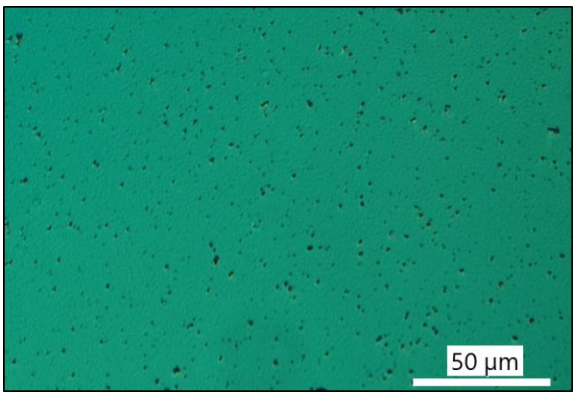

Figure 3.3 *image of the surface of the sample grown at 500°C using 6.7 J/cm^2, taken using Nomarski Microscopy*

In the PLD technique, splashing and aggregates are well-known disadvantages allowing the presence of particles on the surface of the deposited layer. Several reasons can be evocated, such as subsurface boiling of the ablated material, exfoliation, and liquid layer expulsion. In order to reduce the density of these particles, we proceed to reduce the laser fluence to near the ablation threshold.

3.3.2. Laser fluence effect

From the previous series of samples, we established the value of 500°C as the temperature that gives the maximum volume fraction of Fe_3O_4. Hence, we set the substrate temperature at **500°C** and deposit four samples at different laser fluences: 6.7 J/cm², 3.6 J/cm², 2.7 J/cm², and 1.7J/cm². **Figure 3.4** shows the surface images of the samples grown using 3.6J/cm² and 1.7J/cm².

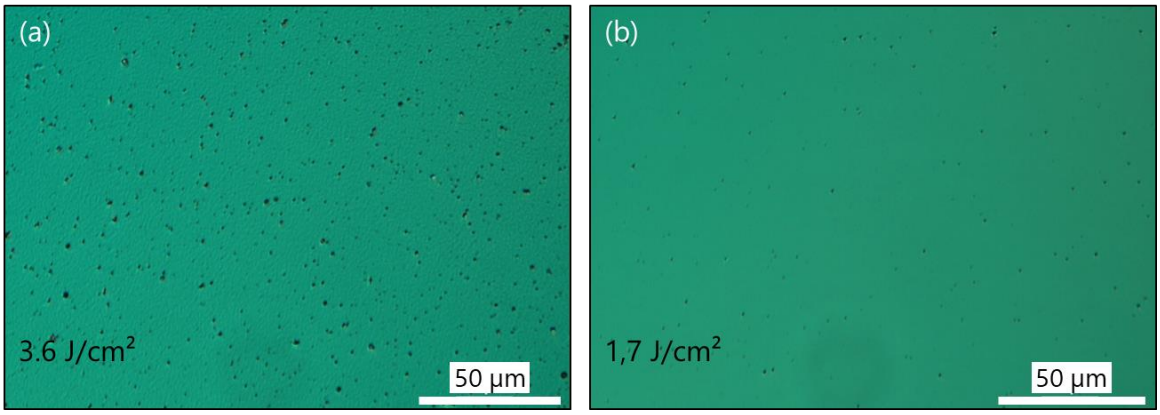

Figure 3.4 *surface photomicrograph of samples grown at Ts=500°C using: (a) 3.6J/cm², (b) 1.7J/cm²*

The density of particles present on the sample's surface is reduced from 2.9×10^{-2} to 4.6×10^{-3} particle/µm². Decreasing the laser fluence below 1.7 J/cm² does not entirely eliminate the particles but leads to poor target ablation. In fact, when the laser fluence was decreased to 1.7 J/cm², there was no peak related to iron cations on the optical emission spectrum of the plasma plume. We deduce that this value is just above the ablation threshold.

The amount of provided laser energy affects not only the number and size of the elements ejected from the target but also the nature (ions, radicals, atoms) and kinetic energy of these elements. Such an effect can be observed directly on the crystalline properties and the crystallized phases in our samples. **Figure 3.5** presents the XRD diffractograms of the samples grown using different laser fluences. As discussed in the previous paragraphs, the sample grown at 500°C with 6.7 J/cm² is a mixture of Fe, FeO and Fe_3O_4. By decreasing the fluence to 3.6J/cm², only the FeO*(lll)* and Fe_3O_4*(lll)* peaks are present in the XRD pattern. The disappearance of Fe phase is accompanied by an increase in the FeO peaks intensity.

Furthermore, decreasing the laser power to 1.7J/cm² increases the ratio of the integrated intensity of Bragg peaks related to Fe_3O_4 with respect to FeO ones.

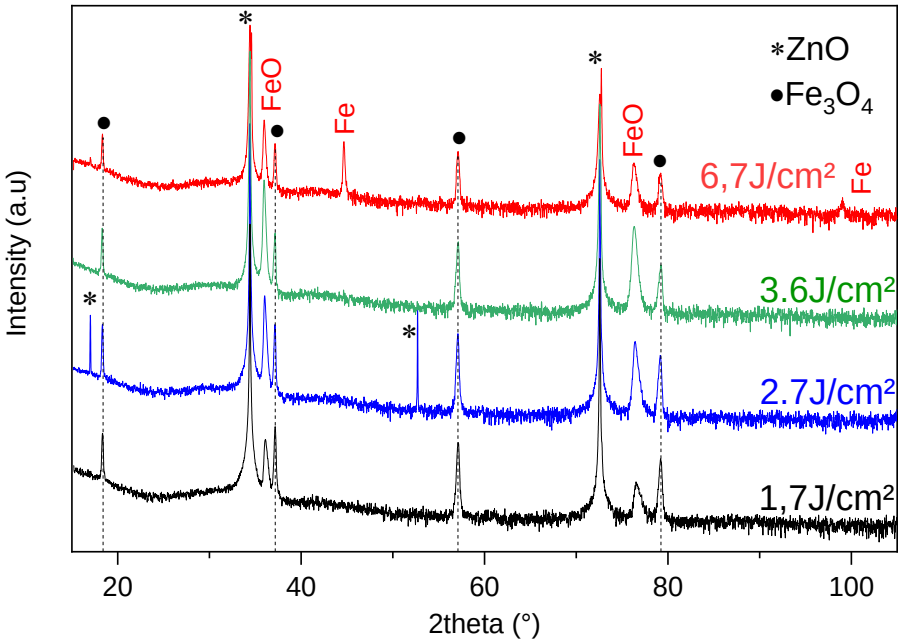

Figure 3.5 *Cu-Kα XRD patterns of iron oxide thin films grown at Ts=500°C using different fluences*

We can conclude that smaller laser fluences favor the formation of Fe_3O_4; consequently, the value **1.7J/cm²** will be used for the following growths as an optimal fluence to deposit the Fe_3O_4.

3.3.3. Suppression of FeO phase

After the establishment of 1.7J/cm² as an optimal fluence for our growth, we still have two parasite peaks at 36,0° and 76.3° in addition to the peaks of Fe_3O_4(*lll*) (**Figure 3.5**, black curve). Regarding the cubic symmetry and the close values of lattice parameters of the three iron oxides: Fe_3O_4, FeO, and γ-Fe_3O_4, it is difficult to assign the peak at ~36° (and 76°) from θ-2θ XRD scan to a given iron oxide phase. Hence, we perform pole figure measurement, through which we can access all the orientations of a selected family of planes in a specific sample.

We have chosen the sample grown at 500°C using 2.7J/cm², which presents parasite XRD peaks with comparable intensity to that of the peaks Fe_3O_4(*lll*) (**Figure 3.5**, blue curve). In order to confirm that the parasite peaks belong to the FeO(*lll*) phase, we investigate the reflection FeO(200), which is separated by 1° from the reflections of the other phases. We made pole figure measurement by fixing 2θ angle at 41.9° (FeO(200)), varying ϕ in the range 0°-360°, and varying χ in the range 0-90°. **Figure 3.6(a)** shows the obtained pole figure, where we detected six reflections with 60° periodicity, at a tilting value of χ=55°. While 2θ is fixed at 41.9°, the

present reflections correspond to {200} peaks of FeO. The measured tilt value matches the angle between (200) and (111) planes (54.74°), however in a cubic structure, only three reflections are expected: (200), (020), and (002) as represented in the simulation of pole figure of FeO(111) single crystal in **Figure 3.6(b)**, except that in thin films, the situation is different from the ideal single crystal. There is a possibility of forming rotational twins during the growth due to the difference in symmetry between the film and the substrate. In the case of (111)-oriented cubic structure growth onto a hexagonal substrate, a twinning of 180° can occur with equivalent proportions [107]. **Figure 3.6(c)** displays a simulation of the pole figure for FeO(200) reflection of FeO(111) film with both twins present. The simulated six reflections meet the exact positions of the reflections obtained experimentally, confirming that the parasite peaks are FeO(111) and FeO(222) diffractions.

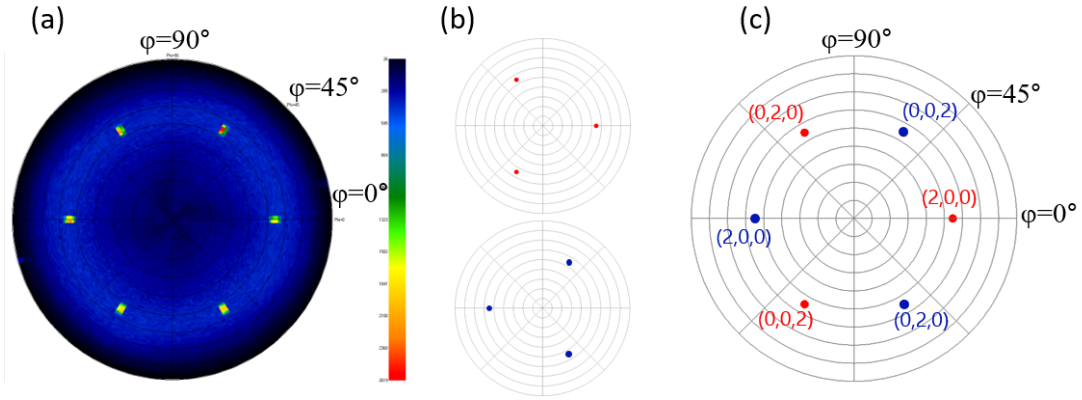

Figure 3.6 *(a) Pole figure measurement of sample grown at 500°C using 2.7J/cm² of the FeO(200) reflection within tilting range χ= 0-90°, (b) and (c) simulations of pole figure of FeO(200) reflection of separated, and overplayed diffractions by 0° and 180° twins*

Although the target is oxygen-rich, the presence of FeO peaks indicates oxygen deficiency. Two solutions are considered to compensate for this deficiency in order to achieve pure Fe_3O_4 growth, either by lowering the growth temperature to avoid the adsorbed oxygen reevaporating or by performing the growth in an oxygen-rich environment.

We first proceed by reducing the growth temperature as we aim to minimize the eventual interdiffusion across the interface Fe_3O_4/ZnO. The XRD pattern of a sample grown at 230°C is represented in **Figure 3.7**, where the peaks FeO(111) and FeO(222) are always present. The intensity of Fe_3O_4 considerably decreased at this substrate temperature. Thus, a further decrease in the temperature deteriorates the crystalline quality of the sample. The suppression of the FeO phase therefore requires additional oxygen to oxidize all the film as Fe_3O_4.

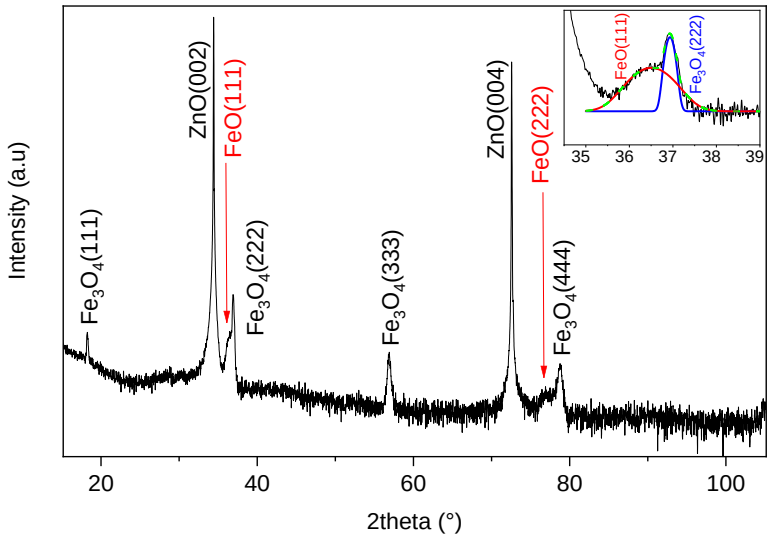

Figure 3.7 *Cu-Kα XRD pattern of sample deposited at Ts=230°C using 1.7J/cm², inset represents deconvolution of the peak near 37° using gaussian function*

Oxidizing the film in PLD is possible through introducing molecular oxygen during the growth using a flowmeter with controllable flux. At this aim, we have grown three samples under oxygen partial pressure P_{O_2}= 4.0×10^{-6}Torr and different temperatures (230°C, 260°C, and 350°C). The low temperatures were kept in order to introduce the minimum of oxygen and to avoid interdiffusion at the interface.

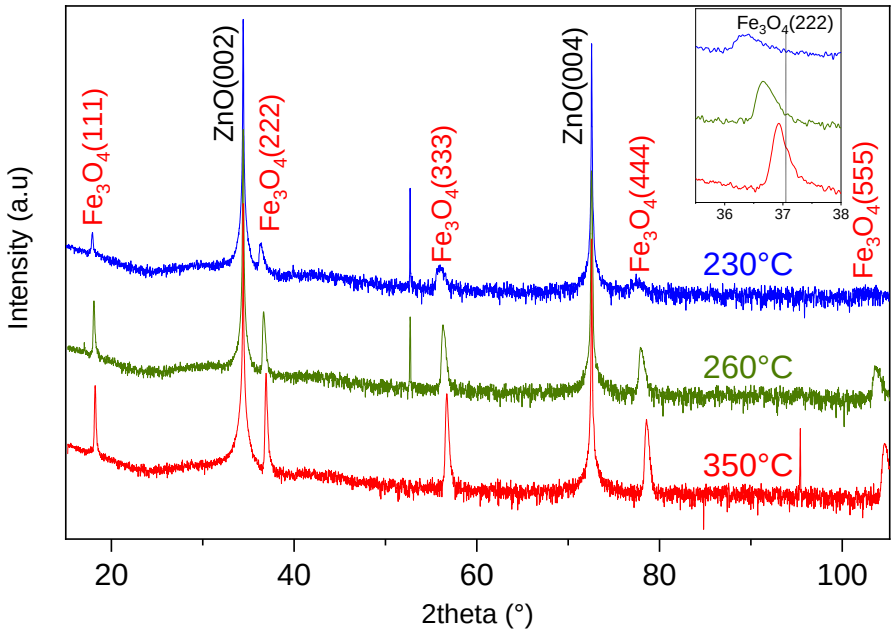

Figure 3.8 *Cu-Kα XRD pattern of samples grown under P_{O_2} = 4.0×10^{-6}Torr at Ts= 230°C, 260°C, and 350°C, inset: zoom around the peak Fe_3O_4(222)*

Apart from the peaks of the substrate ZnO(*000l*), only the peaks of Fe_3O_4(*lll*) are present, indicating successful suppression of FeO when the growth is performed with additional oxygen.

The sample grown at higher temperature exposes more intense peaks with smaller FWHM, a sign of better crystallinity. The measured out-of-plane lattice spacing (d_{111}) of the grown Fe_3O_4 decreases from 4.93Å at T_s=230°C to 4.86Å at T_s=350°C. This latter is closer to the bulk value $d_{111bulk}$=4.84Å. However, the interdiffusion of Fe^{3+} cations was evidenced in the case of Al_2O_3 and GaAs substrates at 400°C [74]. For this reason, we have chosen the temperature of 260°C as a compromise between good crystallinity and a sharp interface. The interdiffusion at the interface will be studied in detail in chapter 5.

The out-of-plane lattice parameter measured for the sample grown at 260°C equals 4.89Å. This value is tunable through fine control of the stoichiometry of the film by adjusting the appropriate oxygen partial pressure for this temperature.

3.3.4. Oxygen partial pressure effect at 260°C

To investigate the effect of the oxygen partial pressure on the crystalline and the physical properties of the Fe_3O_4 grown by PLD and to determine the very exact value necessary to obtain the best thin films, we deposited seven samples under different values of oxygen pressure ranging from 2.0×10^{-7} Torr (chamber residual pressure) to 1.0×10^{-4} Torr, using the previously established conditions. **Table 3.2** summarizes the list of samples.

__Table 3.2__. list of samples grown at 260°C under different oxygen partial pressures

Sample	FOZ1	FOZ2	FOZ3	FOZ4	FOZ5	FOZ6	FOZ7
P_{O_2}(Torr)	2.0×10^{-7}	6.5×10^{-7}	1.0×10^{-6}	4.0×10^{-6}	1.0×10^{-5}	4.0×10^{-5}	1.0×10^{-4}
Ts(°C)	260	260	260	260	260	260	260
Fluence (J/cm^2)	1.7	1.7	1.7	1.7	1.7	1.7	1.7

3.3.4.1. Structural characterizations

Figure 3.9 shows the RHEED patterns of the bare substrate surface and the seven films after cooling to room temperature, taken along the axis ZnO[$11\bar{2}0$]. The dotted diffraction spots and the presence of Kikuchi lines confirm the flat surface with a single crystal domain of the ZnO substrate (**Figure 3.9(a)**).

Sample FOZ1 deposited under P = 2.0×10^{-7} Torr exhibits a typical RHEED pattern of FeO (111) with an in-plane epitaxial relationship of FeO [$10\bar{1}$] || ZnO[$11\bar{2}0$] [157]. The elongated shape of the diffraction spots implies a flat surface with small crystallographic domains [140]. We estimate an in-plane lattice spacing from the RHEED streaks spacing as 3.08 ± 0.03Å, which is close to the calculated value of the bulk FeO. For samples FOZ2-FOZ5, increasing the

growth pressure by introducing oxygen between P_{O_2}= 6.5×10^{-7} Torr and P_{O_2}= 1×10^{-5} Torr, leads to the appearance of new less intense diffraction spots between the diffraction streaks of FeO as seen in **Figure 3.9(c-f)**. The present patterns characterize the Fe_3O_4 (111)-oriented [157], which has a lattice parameter nearly twice larger than the one of the FeO in the same configuration.

The stacking of (111) atomic planes of Fe_3O_4 on ZnO is schematized in **Figure 3.10**. Red arrows represent the unit vectors $\vec{a}$ and $\vec{b}$ of the ZnO, and the blue arrows represent the projection of the unit vectors $\vec{a}$, $\vec{b}$ and $\vec{c}$ of the Fe_3O_4 on the growth plane (111).

The in-plane orientation follows the relationship $Fe_3O_4\ [10\bar{1}] \parallel$ ZnO $[11\bar{2}0]$, and the lattice spacing varies from 6.03 ± 0.03Å to 5.88 ± 0.03 Å by increasing the oxygen pressure 6.5×10^{-7} to 1.0×10^{-5} Torr. It has to be noted that the precision of lattice parameters measurement by RHEED is low primarily due to a variety of instrumental error sources such as on the estimation of the precise 'sample-screen' distance after the sample movement and the electron beam divergence. The measured values are only evoked to point out the variation trend.

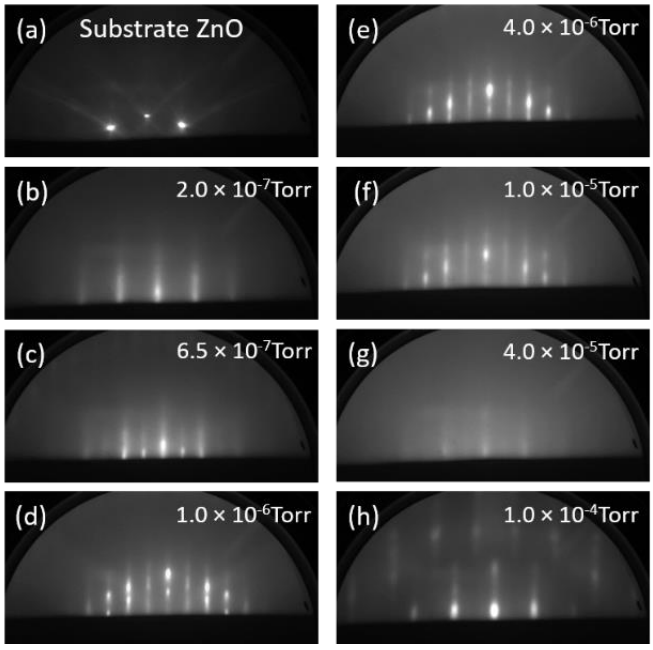

Figure 3.9 *In-situ 300K RHEED (10kV) patterns taken along ZnO $[11\bar{2}0]$ of: (a) pristine ZnO substrate, (b-h) iron oxide films after growth at different oxygen partial pressures*

Growth of the sample FOZ6 under P_{O_2}= 4.0×10^{-5} Torr results in a blurry RHEED pattern (**Figure 3.9(g)**), which is a sign of an amorphous or poorly crystallized structure. The layer may have an intermediate stoichiometry between Fe_3O_4 and Fe_2O_3.

The sample FOZ7 grown under the highest oxygen pressure P_{O_2} = 1.0×10^{-4} Torr presents clear diffraction spots, as seen in **Figure 3.9(h)**. This pattern corresponds to the α-Fe_2O_3(0001) surface with an in-plane relationship of α-Fe_2O_3 $[10\bar{1}0]$ || ZnO $[11\bar{2}0]$ which gives a mismatch of 10.5% with the ZnO substrate. The in-plane lattice spacing is measured as 5.06 Å, quite close to the bulk lattice parameter of the α-Fe_2O_3 (5.03 Å), indicating a near full relaxation of Fe_2O_3.

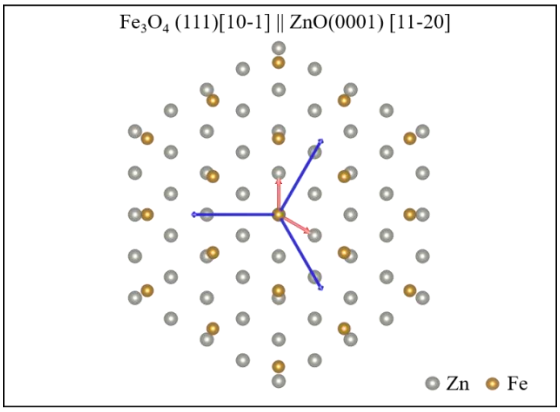

Figure 3.10 *Schematic representation of superposition of (111) atomic plane of Fe_3O_4 on ZnO (0001) atomic plane, red arrows represent $\vec{a}$ and $\vec{b}$ unit vectors of ZnO and blue arrows represent the projection on the growth plane of $\vec{a}$, $\vec{b}$ and $\vec{c}$ unit vectors of Fe_3O_4*

RHEED characterizations indicate that the crystallization of iron oxides at 260°C is possible under a broad range of oxygen pressure.

The value of the out-of-plane lattice spacing is evaluated by XRD. **Figure 3.11** shows the XRD diffraction patterns near the peak Fe_3O_4(222) of the samples FOZ1-FOZ7. The sample FOZ1 grown in the absence of oxygen presents two peaks at 36.21° and 37.15° attributed to FeO (111) and Fe_3O_4 (222), respectively [JCPDS powder diffraction file: 00-006-0615 and 00-019-0629]. A shift toward higher 2θ values of the peaks of both phases is observed compared to their nominal positions, 36.04° and 37.05°, which reflects a smaller lattice parameter, most probably due to oxygen deficiency in each phase ($Fe_{1-\delta}O$ and $Fe_{3-\gamma}O_4$) as was observed in previous reports on FeO [158]. The addition of oxygen up to P_{O_2} = 6.5×10^{-7} Torr in the case of the sample FOZ2 induces a considerable decrease in the FeO(111) peak intensity and an increase in the Fe_3O_4(222) intensity.

Higher oxygen pressures (between P_{O_2} = 1.0×10^{-6} Torr and P_{O_2} = 1.0×10^{-5} Torr) give raise only to Fe_3O_4(222) at 36.96°, 36.75°, and 36.63° for the samples FOZ3, FOZ4, and FOZ5 respectively. The result matches the observations by RHEED technique and confirms the epitaxial growth of Fe_3O_4.

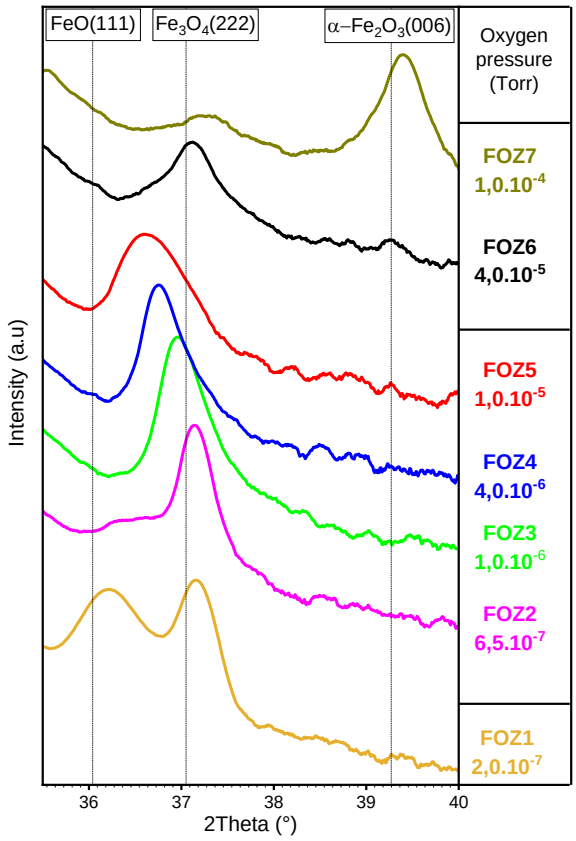

Figure 3.11 *Cu-Kα X-ray diffractograms around the Fe_3O_4 (222) peak of samples grown under different oxygen partial pressure at 260°C*

Among this set of samples, the sample FOZ3 has an out-of-plane lattice parameter of 4.86Å which is the closest to the bulk value (4.84Å). When we increase the oxygen pressure above 1.0×10^{-6} Torr up to 1.0×10^{-5} Torr, we record an expansion of d_{111} from 4.86Å to 4.90Å and a broadening of the θ-2θ peaks, with intensity diminution, what reflects a degradation of the crystalline quality of the Fe_3O_4 when $P_{O_2} > 1.0\times10^{-6}$ Torr. Such degradation might be attributed to the formation of iron vacancies in an oxygen-rich growth atmosphere. The sample FOZ6 grown under $P_{O_2}=4.0\times10^{-5}$Torr present onset of an α-Fe_2O_3(006) peak at 39.25° beside the peak (222) shifted from 36.63 (when $P_{O_2}=1.0\times10^{-5}$ Torr) to 37.10°. In this case, we can attribute this peak to an oxygen-deficient maghemite γ-$Fe_2O_{3-\delta}$(222), which is poorly crystallized regarding the weak intensity and broadening of the peak. Finally, the sample FOZ7 grown under $P_{O_2}=1.0\times10^{-4}$Torr is mainly crystallized as α-Fe_2O_3 considering the intensity of the corresponding peak.

In order to verify that the increase of the lattice parameter can be used to ascertain the film stoichiometry and is not related to an in-plane residual deformation due to epitaxial growth, XRD reciprocal space mapping have has been performed on the samples FOZ3 and FOZ4. We analyzed the asymmetric peak Fe_3O_4(533) as presented in **Figure 3.12**. The reflection (533) of

sample FOZ4 is shifted toward a lower value of Q_z, expressing a larger out-of-plane lattice spacing in real space as was found by θ-2θ scan. Despite the out-of-plane lattice expansion of sample FOZ4, the value of Q_x remains identical to the FOZ3, indicating the same in-plane lattice spacing, which is also found to correspond to the *fully relaxed* value according to TEM measurements which will be discussed in Section 5.2. Hence, the out-of-plane lattice spacing occurring for sample FOZ4 under the effect of higher oxygen partial pressure corresponds to a rhombohedral distortion along [111].

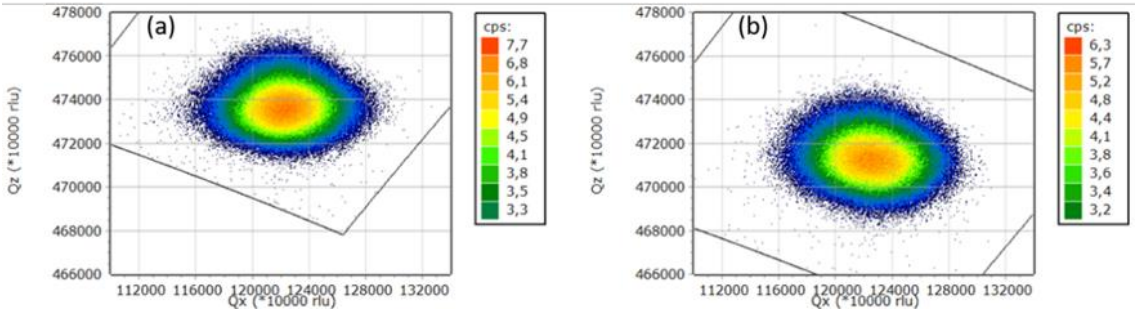

Figure 3.12 *XRD Reciprocal space map around Fe_3O_4(533) asymmetric peak of (a): sample FOZ3, (b): sample FOZ4. Q_x and Q_z are represented in reciprocal lattice unit (rlu)*

Depending on the oxygen partial pressure, we can distinguish three regions of formation of different iron oxide phases, summarized in **Figure 3.13**. ***Region (1)***: $P_{O_2} \leq 6.5\times10^{-7}$ Torr, coexistence of FeO and Fe_3O_4 (lll)-epitaxially grown onto the substrate ZnO(0001); ***Region (2)***: 1.0×10^{-6} Torr $\leq P_{O_2} < 4.0\times10^{-5}$ Torr, pure epitaxial Fe_3O_4(111)//ZnO(0001); and ***Region (3)***: $P_{O_2} \geq 4.0\times10^{-5}$Torr, coexistence of γ-$Fe_2O_3$(111) and α-$Fe_2O_3$(001) // ZnO(0001).

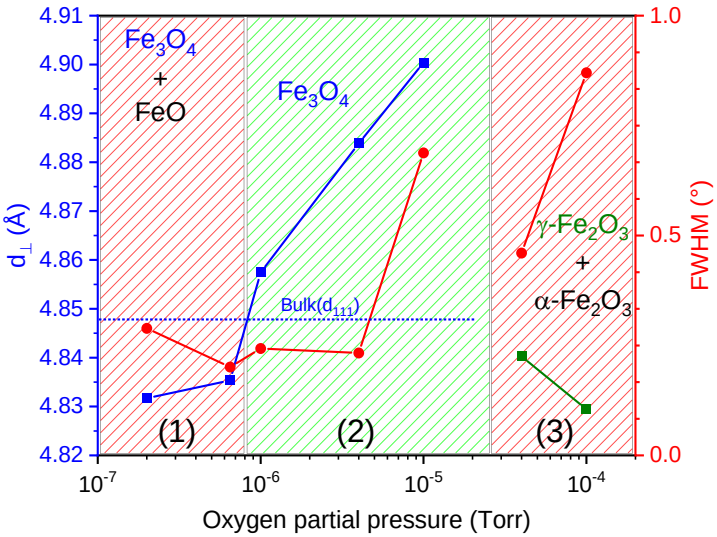

Figure 3.13 *variations of the out-of-plane lattice parameter of: Fe_3O_4(blue), γ-Fe_2O_3 (green); and the FWHM of the peaks: Fe_3O_4(222), γ-Fe_2O_3(222), and α-Fe_2O_3(006), versus the growth oxygen pressure*

In the first region, the formation of FeO beside the Fe_3O_4 is a direct consequence of the non-stoichiometric transfer of light elements in the PLD. The increase of oxygen partial pressure compensates for the lost amount of oxygen and leads to the oxidation of FeO which can be formed at lower pressures. The lattice parameter of Fe_3O_4 increases slightly with a narrowing of the corresponding peak. An optimal value of P_{O_2} to obtain stoichiometric Fe_3O_4 with exact nominal lattice parameter is between 6.5×10^{-7} Torr and 1.0×10^{-6} Torr. In the second region, the interplanar distance d_{111} expands proportionally with increasing P_{O_2}. A similar evolution of the lattice parameter was previously reported on complex metal oxides [159]–[164], where the effect was attributed to oxygen vacancies, except that in this range of oxygen pressure, one would exclude the presence of oxygen vacancies and expect more iron vacancies. Prieto *et al.* [75] observed that increasing the iron vacancies leads to a lattice expansion up to a certain amount before forming a small fraction with maghemite stoichiometry. The third region starts from $P_{O_2} \geq 4.0\times10^{-4}$ Torr, where the iron oxide with the highest degree of oxidation - Fe_2O_3 - appears. The peak (222) shifts to a higher 2θ value exposing a lattice parameter shrinking from 4.90 Å to 4.83 Å. However, the attribution of this peak to the magnetite or the maghemite is not evident by simple XRD analysis. We suppose that the present peak belongs to oxygen-deficient maghemite, which has the same symmetry as the magnetite.

3.3.4.2. Magnetic properties of Fe_3O_4 thin films

In this section, we will be interested only in the samples composed mainly of Fe_3O_4 as long as FeO and α-Fe_2O_3 are antiferromagnetic compounds with no detectable macroscopic magnetic response up to a field of about 10T. Using PPMS9 vibrating sample magnetometer, we measured at room temperature the magnetization of the samples FOZ2, FOZ3, FOZ4, and FOZ5 that were deposited under oxygen pressures ranging from 6.5×10^{-7} Torr to 1.0×10^{-5} Torr. We applied a magnetic field varied between -2T and 2T parallel to the plane (111) of the films. The obtained magnetic hysteresis loops are displayed in **Figure 3.14** after subtraction of the diamagnetic contribution of the substrate and the sample holder. The open loops confirm the expected ferromagnetic nature of the deposited layers, which is more pronounced in the case of low O_2 pressure samples.

Samples FOZ2 and FOZ3 show faster saturation due to the better crystalline quality as observed by XRD and to the stoichiometry closer to Fe_3O_4.

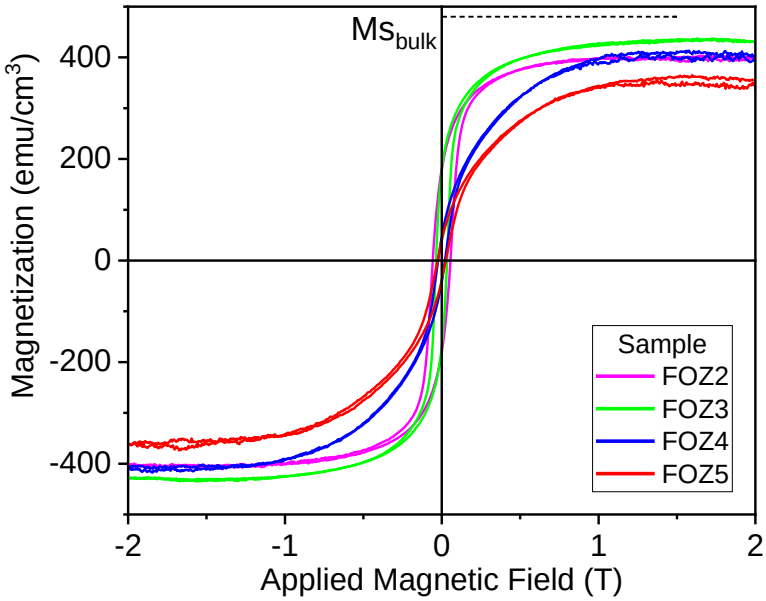

Figure 3.14 *Magnetic hysteresis loops of Fe_3O_4 samples (FOZ2, FOZ3, FOZ4, and FOZ5) as a function of applied magnetic field between-2T and 2T, measured at room temperature. Dotted line corresponds to the bulk Fe_3O_4 saturation magnetization Ms_{bulk}=480 emu/cm^3 at 300K*

Table 3.3 resumes the values of saturation and remanent magnetization, the ratio M_r/M_s, and the coercive field of the measured samples. The highest saturation magnetization is measured for the sample FOZ3 as 435 emu/cm^3, which is 9% smaller than the M_s value of bulk Fe_3O_4 (480 emu/cm^3) at room temperature. Such reduction of M_s is often attributed in literature to the formation of anti-phase boundaries during the growth of Fe_3O_4 on most substrates [62], [94].

The sample FOZ2 demonstrates a slightly diminished magnetization compared to FOZ3. This reduction can be attributed to the presence of FeO in FOZ2, as confirmed by XRD analysis. Being antiferromagnetic compound at room temperature, FeO does not contribute in the ferromagnetic response on the sample. Consequently, the ferromagnetic volume within the FOZ2 sample is smaller in comparison to FOZ3, which results in saturation magnetization of FOZ2 measures 400 emu/cm^3.

As for the samples FOZ4 and FOZ5, we observe a drastic decrease in the remanent magnetization and a slower approach to the saturation compared to the other two samples. Such a decrease of M_r might also arise from higher APBs density. The slow approach to saturation reveals a magnetic anisotropy distinct from that observed in samples FOZ2 and FOZ3. This difference originates from the departure of FOZ4 and FOZ5 from the ideal Fe_3O_4 stoichiometry, which triggers an expansion of the lattice in the out-of-plane direction. Consequently, this lattice distortion impacts the angle between the iron cations. This deformation of the lattice potentially weakens the exchange interactions, leading to a diminished ferromagnetic coupling among the iron cations.

In addition to the slow approach to saturation, sample FOZ5 shows a more reduced saturation (360 emu/cm^3). Our interpretations and hypotheses suggest that sample FOZ5 contains a relatively higher density of iron vacancies when compared to the other samples. This interpretation finds support from the observed decrease in saturation magnetization to 360 emu/cm^3 within FOZ5. According to our hypotheses, these increased vacancies are anticipated to predominantly occupy the octahedral sites of Fe_3O_4. This particular pattern of occupancy aligns seamlessly with the characteristic behavior of the ferrimagnetic nature of Fe_3O_4. Notably, the net magnetization of Fe_3O_4 arises primarily from these octahedral sites. As a result, the favored occupation of vacancies within these octahedral sites is postulated to contribute to a noticeable reduction in its overall net magnetization. This interpretation aligns well with the inherent ferrimagnetic properties of Fe_3O_4 and is additionally backed by earlier research suggesting that growth under high oxygen pressure can lead to the formation of iron vacancies dispersed randomly across the octahedral sites [75]. This latter reference confirms that increasing the oxygen content during the growth of Fe_3O_4 thin can introduce Fe vacancies.

Table 3.3 *magnetic properties extracted from the measured magnetic hysteresis loops. Ms: saturation magnetization, Mr: remanent magnetization, the ratio Mr/Ms expressed in (%), Hc the coercive field*

Sample	P_{O_2} (torr)	Ms (emu/cm^3)	Mr (emu/cm^3)	Mr/Ms(%)	Hc(T)
FOZ2	6.5×10^{-7}	400 ± 10,0	180 ± 4,5	45±2	0,057
FOZ3	1.0×10^{-6}	435 ± 10,2	178 ± 4,1	41±2	0,036
FOZ4	4.0×10^{-6}	400 ± 9,7	46 ± 1,1	12±1	0,023
FOZ5	1.0×10^{-5}	360 ± 9,3	39 ± 1,0	11±1	0,026

Stoichiometric magnetite is characterized by a structural transition called Verwey transition, occurring at around T_v =125K and accompanied by a change of physical properties, in particular, magnetization and conductivity [165]–[167]. During this transition, the inverse spinel structure with easy magnetization axis [111] above T_v transforms into a monoclinic structure having an easy magnetization axis [001]. In order to confirm the exact stoichiometry of Fe_3O_4, Zero Field Cooled (ZFC) and Field Cooled (FC) measurements were performed under 100Oe on the sample FOZ3 between 5K and 300K, **Figure 3.15**. The jump in magnetization occurring at 127K in the ZFC and the maximum of the FC curve match precisely the expected value of Verwey transition, giving another evidence on the Fe_3O_4 stoichiometry of this sample.

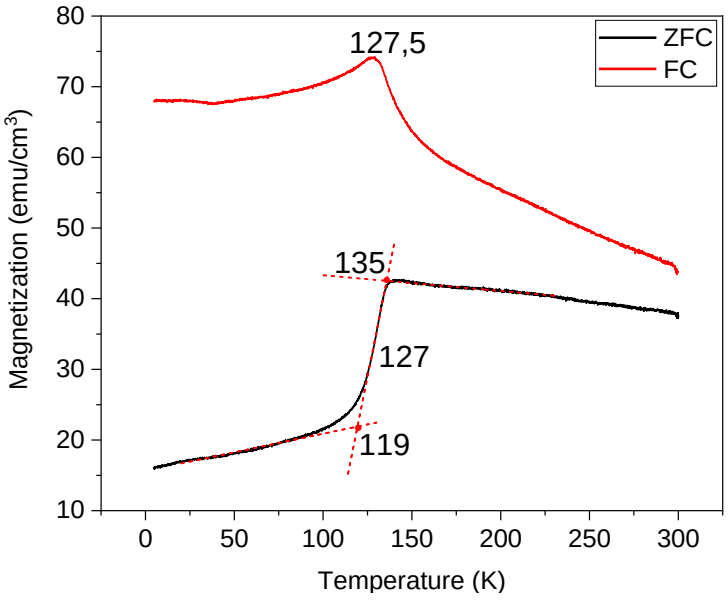

Figure 3.15 *ZFC and FC curves of sample FOZ3, Verwey transition occurs at 127K*

Crossing RHEED, XRD, and VSM results after exploring different growth pressures leads us to define the $\boldsymbol{P_{O_2}=1.0\times10^{-6}\ Torr}$ as a compromise between the stoichiometry, the highest saturation magnetization and the high remanence of pure epitaxial Fe_3O_4 growing (111)-oriented onto ZnO(000±1) substrates at ***260°C***.

3.3.4.3. Iron oxide phase diagram at 260°C

At the end of the optimization of the growth conditions, we were able to establish a PLD phase diagram of iron oxides formation on c-oriented ZnO substrate (**Figure 3.16**), including the variation of their lattice parameter and the corresponding RHEED patterns at 260°C, as a function of the oxygen pressure and fixed growth parameters (target Fe_2O_3, Nd:YAG, 355 nm,1.7 mJ/cm²). It can be summarized as follows: the optimal value of oxygen pressure to grow stoichiometric Fe_3O_4 is between 1.0×10^{-6} Torr and 6.5×10^{-7} Torr. Any increase of P_{O_2} leads to a larger lattice parameter (and smaller magnetization). Beyond 1.0×10^{-4} Torr, the film becomes mostly α-Fe_2O_3. When the growth is under background pressure (2.10^{-7} Torr), the film becomes a mixture of FeO and Fe_3O_4. Furthermore, it's important to note that the growth and characterizations were carried out on two different ZnO polarities: Zn-terminated and O-terminated ZnO substrates. Remarkably, no discernible distinctions were observed between the two series of samples in terms of their structural and magnetic properties (in XRD, RHEED, and VSM measurements).

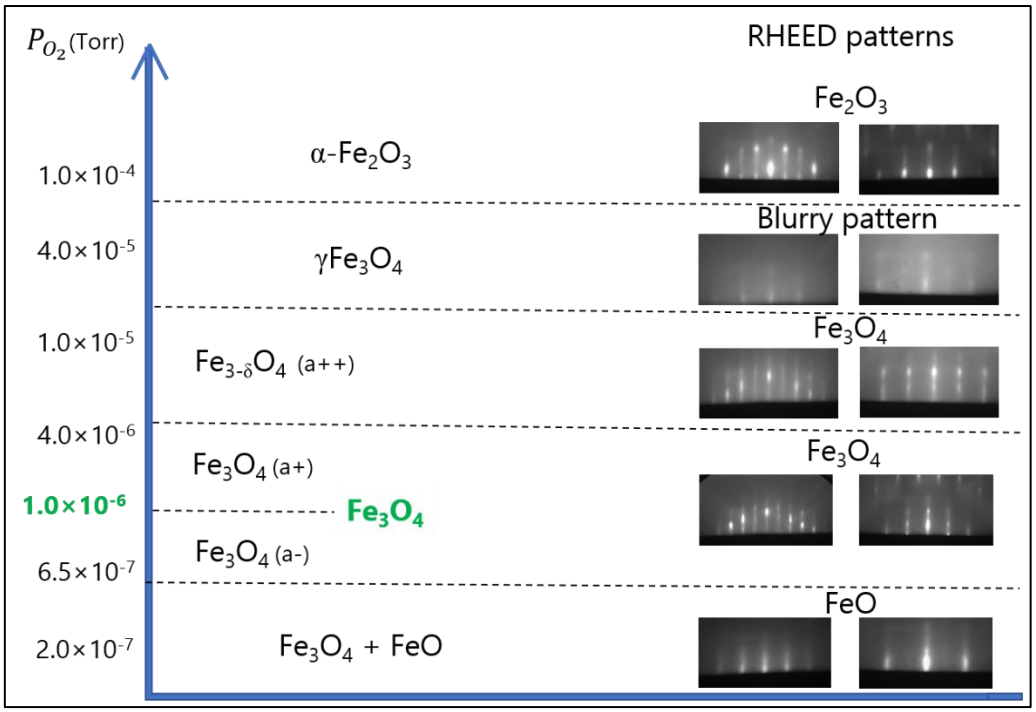

Figure 3.16 *phase diagram of iron oxide formation onto ZnO(000±1) substrates as function of oxygen partial pressure; a, a+, and a++ refer to the nominal lattice parameter of Fe_3O_4 and its expansion; RHEED patterns are taken: on the left parallel to ZnO [11$\bar{2}$0], on the right parallel to ZnO [10$\bar{1}$0]*

3.3.4.4. Higher temperature growth of Fe_3O_4/c-ZnO - 400°C

The previous series of samples has a reduced magnetization compared to the bulk Fe_3O_4 and a remanent magnetization lower by 50% than the saturation value. Since the remanence value is an essential criterion for the project SPINOXIDE as we target the fabrication of devices functioning at room temperature in the absence of an external magnetic field, we figured out some solutions to increase the saturation magnetization and to maximize the ratio M_r/M_s. In this section, we investigate higher growth temperatures in order to improve the crystallinity of the samples.

Considering the thermal expansion coefficients of ZnO and Fe_3O_4 [168], [169], the nominal mismatch decreases from 8.6% at room temperature to 7.9% at 500°C, which may decrease the density of misfit dislocations at the interface film/substrate and, furthermore, improve the crystalline quality.

The growth at higher temperatures requires increasing the oxygen pressure to compensate for the re-evaporation of oxygen during the growth. **Figure 3.17** displays the XRD pattern of samples grown at 400°C under P_{O_2}=1.0×10^{-6} Torr (optimal P_{O_2}established at 260°C) and P_{O_2}=4.0×10^{-6} Torr. On the XRD pattern of the sample grown at the lowest oxygen pressure, we observe the presence of FeO(111) peak at 36.30°, indicating oxygen deficiency. The increase

of P_{O_2} up to 4.0×10^{-6} Torr is sufficient to suppress the FeO and stabilize single epitaxial Fe_3O_4 phase.

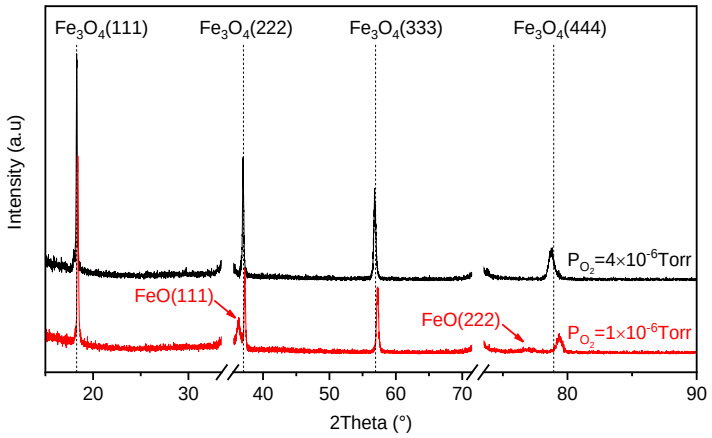

Figure 3.17 *Cu-Kα XRD patterns of samples grown at 400°C under $P_{O_2} = 1.0\times10^{-6}$Torr and $P_{O_2} = 4.0\times10^{-6}$Torr*

Comparing samples grown at 260°C and 400°C, the XRD reveals only slight increase in the Fe_3O_4 peak intensities when the films are grown at 400°C under the adequate oxygen pressure. However, the saturation magnetization is remarkably increased from 425 emu/cm^3 to 460 emu/cm^3 after increasing the substrate temperature to 400°C as seen in **Figure 3.18**. As for the ratio M_r/M_s, it is around 48% for both samples. These results are in good agreement, confirming a better crystallinity under the effect of higher temperature.

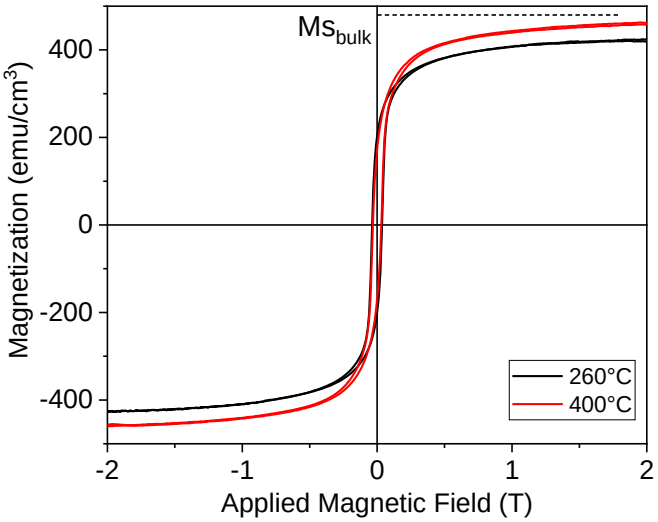

Figure 3.18 *Magnetic hysteresis loops as a function of applied magnetic field between-2T and 2T of samples grown at 260°C and 400°C, measured at room temperature. Dotted line corresponds to the bulk Fe_3O_4 saturation magnetization Ms_{bulk}=480 emu/cm^3 at 300*

Following the same trend, a further increase of the substrate temperature up to 500°C also allows the growth of pure epitaxial Fe_3O_4 under $P_{O_2}=8.0\times10^{-6}$ Torr, except that high growth

temperature can intensify the interdiffusion across the interface. Since our work aims to obtain a high crystalline quality of Fe_3O_4 with a *sharp interface,* we performed TEM observations on the interface Fe_3O_4/ZnO of samples grown at different temperatures. We illustrate HAADF cross-section micrographs obtained along the $[10\bar{1}0]$ ZnO zone axis in **Figure 3.19**. We see a flat interface when the samples are grown at 260°C and 400°C, while the sample at 500°C presents a wavy shape indicating a deterioration of the interface. Therefore, we focus the rest of the work on 260°C and 400°C growths.

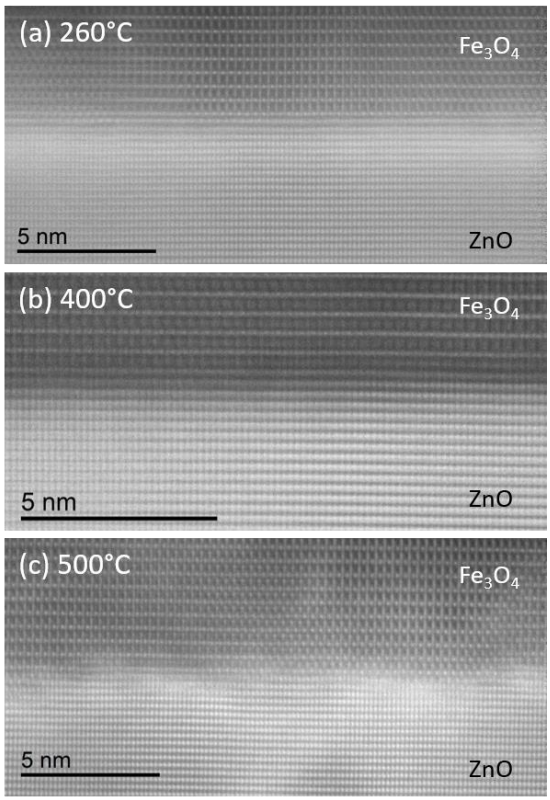

Figure 3.19 *HAADF interface Fe_3O_4/ZnO cross section micrographs (taken along the Fe_3O_4 $[11\bar{2}]$ zone axis) of samples grown at: (a) 260°C, (b) 400°C, and (c) 500°C*

3.4. Growth of pure FeO using Fe_3O_4 target

The previously presented results concern samples prepared using a Fe_2O_3 target. The growth can also be done using a Fe_3O_4 target which is oxygen-deficient compared to Fe_2O_3. Before each growth, the Fe_3O_4 target is systematically pre-ablated using 1.7J/cm² fluence to clean the surface from any eventual oxidation. Pure FeO film could be obtained at 260°C using the latter target without additional oxygen during the growth. RHEED patterns of 100nm-thick FeO film taken respectively parallel to $[11\bar{2}0]$ and $[10\bar{1}0]$ directions of ZnO are shown in **Figure 3.20(a)** and **Figure 3.20(b)**, from which an epitaxial growth with a flat surface is asserted. **Figure 3.20(c)** presents the XRD θ-2θ diffractogram of the corresponding film, where

only two peaks of FeO(*lll*) are detected at 36.03 and 76.45° beside the peaks of the substrate, indicating the absence of other iron oxide phases.

The in-plane and the out-of-plane lattice parameters are estimated from RHEED and XRD patterns to be 3.06 Å and 2.48 Å, respectively, matching the nominal values of bulk FeO perfectly. The epitaxial relationship follows FeO (111)[$10\bar{1}$] || ZnO (0001)[$11\bar{2}0$].

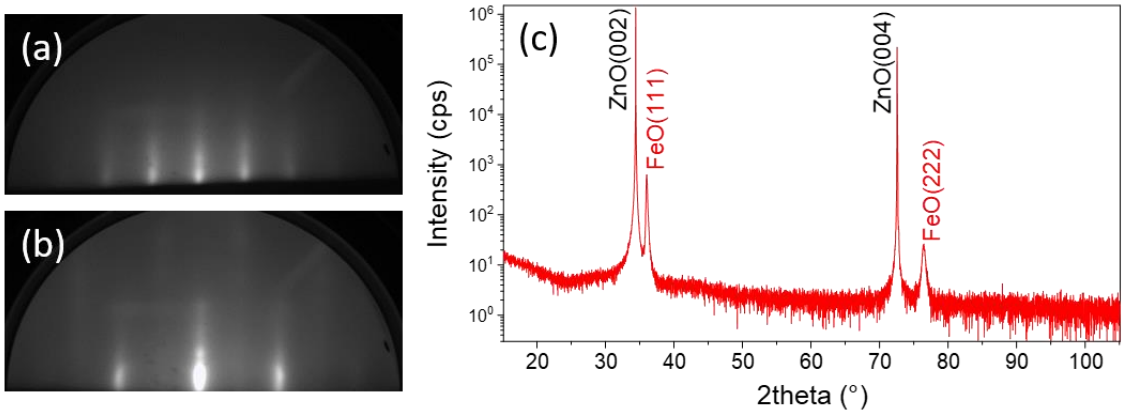

Figure 3.20 *(a) and (b): RHEED patterns, and (c) Cu-Kα XRD diffractogram of 100nm FeO film grown using Fe_3O_4 target at 260°C*

3.5. Conclusion

In summary, we have successfully grown high-quality thin films of Fe_3O_4 on ZnO(000±1) substrates at various temperatures (260°C, 400°C, and 500°C), leading to the following conclusions:

Epitaxial Relationship: the epitaxial relationship established, specifically Fe_3O_4 (111)[$10\bar{1}$] || ZnO(0001)[$11\bar{2}0$], is a key observation. This relationship is significant as it underpins the achievement of desired epitaxial quality.

Substrate Polarity Neutrality: importantly, our investigations reveal that the polarity of the substrate has no discernible impact on the volume properties of the thin film. This promising finding suggests that Fe_3O_4 thin films can be successfully grown on diverse ZnO substrates without compromising their structural integrity.

Precise Control of Stoichiometry: The stoichiometry of Fe_3O_4 can be finely tuned by precisely adjusting the oxygen partial pressure during growth using the Fe_2O_3 target at different temperatures. This balance is crucial for achieving the desired chemical composition. For instance, growth at 260°C requires an oxygen partial pressure of 1.0×10^{-6} Torr for pure and

stoichiometric Fe_3O_4 thin films, while a 400°C growth necessitates an increased P_{O_2} to 4.0×10^{-6} Torr.

Magnetization Properties: Examination of magnetization properties indicates that films grown at 400°C closely approximate bulk magnetization (480 emu/cm^3),and even at a lower substrate temperature of 260°C, magnetization remains relatively high (435 emu/cm^3). This difference in saturation potentially due to improved crystalline quality in high-temperature growth. Importantly, the critical ratio Mr/Ms remains consistent in both cases, attesting to the reliability of our thin film quality.

Interface Characteristics: TEM imaging reveals that the interface Fe_3O_4 | ZnO is geometrically flat when growth is performed at substrate temperatures under 400°C. However, it becomes curvy when the growth is executed at 500°C, implying thermally activated interdiffusion between the film and the substrate at higher temperature growth.

Epitaxial Wurtzite FeO(111) Growth: In addition to growing pure Fe_3O_4, we have also demonstrated the ability to grow pure epitaxial wurtzite FeO (111) on ZnO(0001) at different temperatures using an Fe_3O_4 target. This paves the way for employing FeO as an ultra-thin interfacial layer between Fe_3O_4 and ZnO, with potential implications for the structural and magnetic properties of the Fe_3O_4 grown atop it.

These conclusions significantly advance our understanding of the growth of Fe_3O_4 thin films and their properties on ZnO substrates, directly contributing to the "SPINOXIDE" project's goals in the realm of spintronics.

4. Influence of interface engineering (buffer FeO, miscut) on the structural and magnetic properties of Fe_3O_4 thin films deposited onto ZnO(0001)

4.1. Introduction

In the previous chapter, we discussed the growth conditions and characterizations of epitaxial Fe_3O_4 thin films at different temperatures. In this chapter we focus on the interface and the early stage of the growth. Previous reports of researches conducted at small scale near the 'Fe_3O_4/substrate' interface has suggested that a natural formation of other iron oxide phase, specifically wüstite (FeO), occurs during the early stages of growth. This phenomenon was observed regardless of the substrate material and has been observed in films grown on various metal and oxide substrates, including ZnO [16], [73], [170]–[173].

The objective of the SPINOXIDE project is to achieve efficient spin injection and detection in opto-spintronic devices. To ensure optimal device functionality, it is crucial to establish a well-defined sharp contact "ferromagnet|semiconductor", thereby avoiding spin depolarization at the interface. However, as mentioned earlier, the thickness of the naturally formed FeO is uncontrollable and strongly dependent on the growth conditions. The presence of FeO at the interface can alter the contact nature to "antiferromagnet|semiconductor" due to its antiferromagnetic properties. This can pose a challenge to the efficient operation of the targeted devices. Nevertheless, Spiridis *et al.* demonstrated that ultra-thin FeO(111) films, grown on a Pt(111) substrate, can exhibit ferromagnetic properties up to a critical thickness of 16 monolayers (ML), beyond which the FeO film reverts to its bulk antiferromagnetic nature [174], [175].

Based on the above-mentioned finding, we have chosen to investigate the ***intentional and controllable growth*** of 1 nm (~5 ML) of FeO and to study its effects on the subsequent growth of Fe_3O_4 on ZnO. The first section of this chapter will be devoted to the growth of Fe_3O_4 with FeO buffer layer at 260°C and 400°C.

The ultra-thin FeO layer grown in this study may act as a buffer layer, reducing the density of defects such as misfit dislocations at the Fe_3O_4|ZnO interface. This is because the in-plane lattice mismatch between FeO(111) and ZnO(0001) is smaller compared to that between Fe_3O_4(111) and ZnO(0001) (6.3% vs. 8.6%, respectively). Additionally, we aim to investigate the potential blocking effect of FeO on the cationic interdiffusion at the Fe_3O_4|ZnO interface. Wangoh *et al*. reported that the formation of an ultra-thin layer of $Mg_xFe_{1-x}O$ with a rock salt structure (similar to FeO crystalline structure) can inhibit cationic interdiffusion between Fe_3O_4 thin films and an MgO substrate [176].
By studying these aspects, we aim to gain insights into the role of the intentional FeO layer in improving the interface quality, reducing defects, and preventing cationic interdiffusion.

As a complementary way of interface engineering, the second section of the current chapter will focus on the growth of Fe_3O_4 on ZnO(0001) vicinal substrates. We will examine the effect of a 1° miscut toward two different orientations of the substrate: $[11\bar{2}0]$ and $[10\bar{1}0]$.

4.2. Operando RHEED analysis

In order to investigate the initial stage of Fe_3O_4 growth on a ZnO(0001) substrate, we performed real-time RHEED monitoring. This involved growing Fe_3O_4 while simultaneously acquiring RHEED patterns. In this particular section, our focus is solely on the pattern type rather than the in-plane lattice spacing.

Consistent with the observations of Paul et al. [73], the RHEED pattern we obtained during the growth of the first layers of Fe_3O_4 exhibits a typical FeO pattern. Our strategy was introducing additional oxygen during the period corresponding to the growth of the first 2 nm, and subsequently continuing the growth under the optimal conditions established in the previous chapter for T_s = 260°C. This approach was pursued with the goal of initiating the growth directly as Fe_3O_4, bypassing the initial formation of FeO as previously discussed.

A first sample of Fe_3O_4 film was grown on ZnO(0001) substrate at 260°C under oxygen partial pressure $P_{O_2} = 4\times10^{-6}$ Torr during the first 20 seconds, then it was decreased to the optimal value $P_{O_2} = 1\times10^{-6}$ Torr for the remaining duration of the growth time, which was 6 minutes.

Figure 4.1(a) and **Figure 4.1(b)** display the RHEED patterns obtained with an electron beam parallel to the azimuth ZnO$[11\bar{2}0]$ at 15 seconds and 160 seconds of the growth, respectively. The pattern displayed in **Figure 4.1(a)** corresponds to a typical FeO(111) RHEED pattern,

despite the oxygen pressure being higher than the value necessary to achieve Fe_3O_4 stoichiometry. In contrast, the pattern displayed in **Figure 4.1(b)** matches a typical RHEED pattern of Fe_3O_4, indicating a transition from FeO to Fe_3O_4 during the growth.

To visualize RHEED pattern transition from FeO to Fe_3O_4, we plot an integrated image of the line intensity profile, which horizontally intersects the RHEED reflections of the film (see **Figure 4.1(c)**). It corresponds to a growth duration of 42 seconds. Here we precise that the intensity fluctuations do not represent RHEED oscillations but are caused by electromagnetic interaction of the electron beam with the rotating targets.

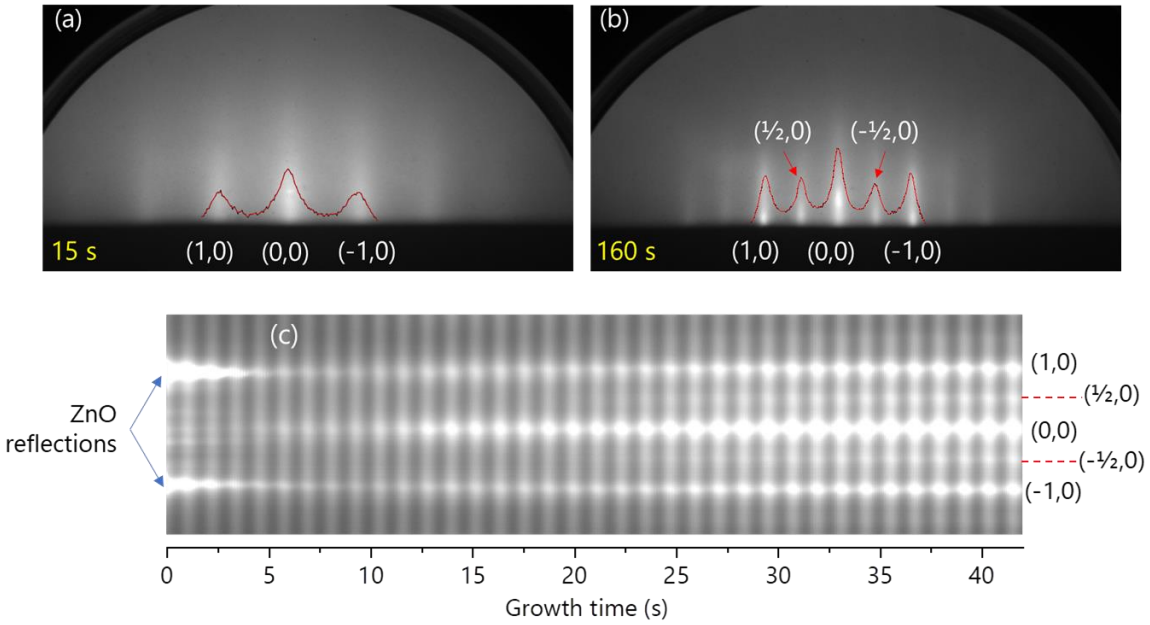

Figure 4.1 *(a) RHEED pattern of the film taken after 15s of growth, (b) RHEED pattern of the film taken after 160s of growth, (c) time integrated RHEED image of the line intensity profile of* $Fe_3O_4(111)/ZnO(0001)$ *recorded along the azimuth* $[11\bar{2}0]$ *of ZnO*

At t = 0 seconds, we observe two reflections of the substrate (point spots) with high intensity, which tend to disappear with the start of the growth. This decrease in intensity to a minimum (at around 5s) is due to a partial coverage of the substrate surface.

The two reflections appear again as streaks (1,0) and (-1,0), similar to the pattern presented in **Figure 4.1(a)**, indicating the crystallization of the film in a FeO or FeO-like structure. After around 21 seconds of growth, the crystallization of Fe_3O_4 starts with the appearance of the intermediate reflections (½,0) and (-½,0) (**Figure 4.1(b)**).

A second sample was grown with higher oxygen partial pressure during the first 20s of the growth, this time initial P_{O_2} = 8×10^{-6} Torr then it was decreased to P_{O_2} = 1×10^{-6} Torr for the rest of the growth. Same RHEED pattern evolution was recorded.

In order to determine the thickness at which the transition occurs, we must determine the instant when (½,0) and (-½,0) reflections appear. For this, we plot in **Figure 4.2** the variation of the FWHM of (½,0) reflection as a function of deposition time for the two samples grown with oxygen excess during the initial 20s.

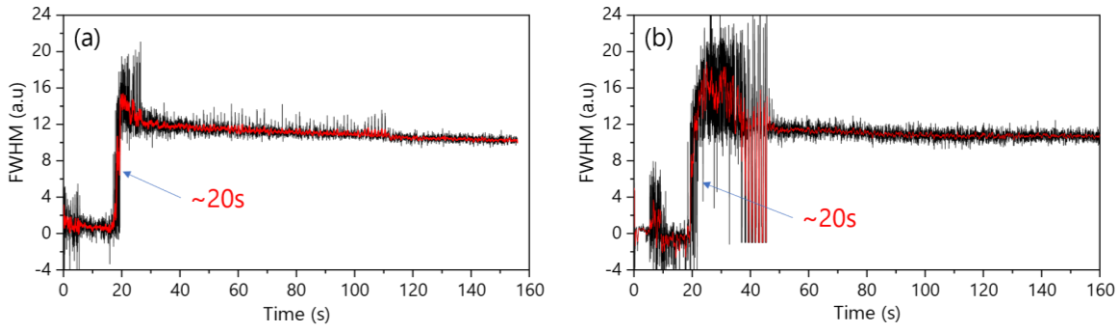

***Figure 4.2** FWHM of RHEED (½ ,0) reflection as function of growth time of: (a) sample grown with P_{O_2} = 4×10^{-6} Torr, (b) sample grown with P_{O_2} = 8×10^{-6} Torr. Red curves are the smoothing of the experimental data (black)*

For both samples grown with oxygen excess at the beginning, after initiating the growth, we observed a negligible (≈ 0) FWHM for the (½,0) reflection, which indicates its nonexistence at the beginning. However, after approximately 20 seconds, a sudden increase in FWHM was observed. This jump signifies the appearance of the (½,0) reflection on the RHEED fluorescent screen, indicating the crystallization of Fe_3O_4. The duration of 20 seconds corresponds to a growth thickness of approximately 1.8 nm.

Regardless of the oxygen partial pressure at the beginning of the growth, up to a thickness exceeding 1.5 nm, the observed RHEED pattern corresponds to the FeO iron oxide phase.

4.3. Intentional growth of a FeO template layer

Based on the previous RHEED analysis, it appears that the growth of the Fe_3O_4 structure is not possible since the first monolayer on the ZnO(0001) substrate, even with an excess of oxygen. The naturally formed FeO layer reaches almost 2 nm, which makes it disadvantageous for spintronic applications as it might act as a spin depolarizing barrier, due to the antiferromagnetic nature of FeO. In this section we will investigate the intentional growth of 1 nm FeO buffer layer as a template for a subsequent Fe_3O_4 growth.

As discussed in Section 3.4, it is possible to grow pure FeO at 260°C using an Fe_3O_4 target without additional oxygen. The required duration to obtain 1 nm of FeO is 12 seconds. **Figure 4.3** illustrates the evolution of the RHEED pattern over time during and after the growth of 1 nm of FeO. The pattern on the left corresponds to the bare substrate pattern, while the pattern on the right corresponds to the 1 nm of grown FeO. In the recorded RHEED pattern, the reflection spots corresponding to FeO start appearing immediately after interrupting the ablation at 12 seconds, as marked by the blue dotted line in **Figure 4.3**.This pattern remains stable over time (up to 40 min monitored), and it shows no reconstruction or evidence of Fe_3O_4 formation, under this low-pressure condition (base pressure of 1×10^{-8} Torr).

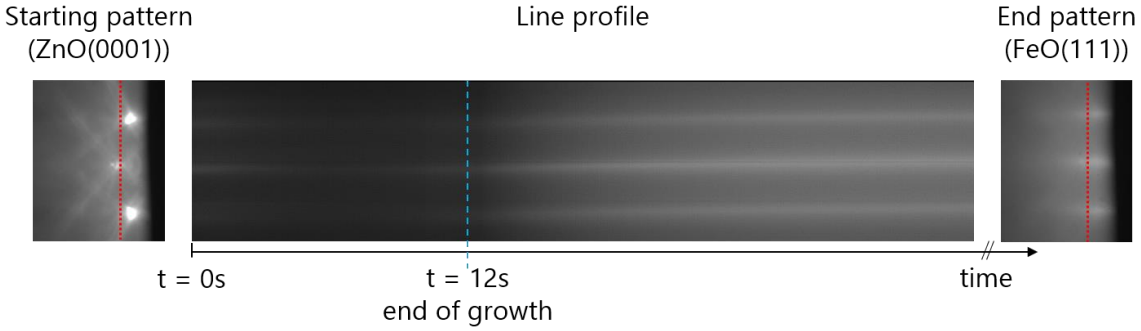

***Figure 4.3** RHEED pattern evolution as function of time during and after the growth of 1 nm of FeO (12s) at 260°C, electron beam is parallel to ZnO[11$\bar{2}$0]. "Starting pattern" corresponds to the substrate pattern at t = 0s, and "End pattern" is the pattern of the 1nm of FeO after deposition*

The growth of 1 nm of FeO is then followed by 6 min growth of Fe_3O_4 using an Fe_2O_3 target under P_{O_2} = 1×10^{-6} Torr. Just before initiating the target ablation, we inject oxygen using the flowmeter to establish the desired pressure in the PLD chamber, which takes up to two to three minutes to stabilize. Switching between targets inside the PLD chamber is instant thanks to the computer-controlled multi-target carousel. The FeO RHEED pattern remains unchanged during the elapsed time until pressure stabilization.

Figure 4.4 shows the RHEED pattern evolution during the growth of Fe_3O_4 (on the previously deposited FeO) as a function of deposition time. Even though FeO is separately deposited, it still takes some time to observe the characteristic RHEED pattern associated with the presence of Fe_3O_4.

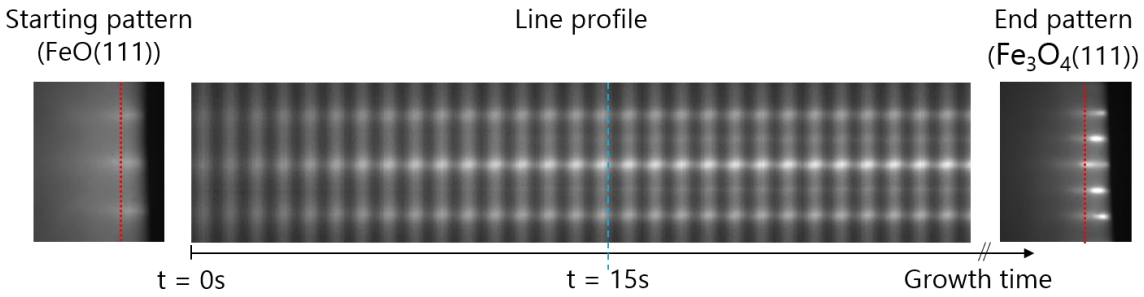

Figure 4.4 *RHEED pattern evolution during the growth of Fe_3O_4 on the 1nm of FeO deposited on ZnO(0001) substrate, electron beam is parallel to ZnO[11$\bar{2}$0]. "Starting pattern" correspond to t = 0s the instant of starting the ablation, "End pattern" corresponds to t = 6min of Fe_3O_4 growth*

According to the variation of FWHM of (½,0) reflection plotted as a function of time in **Figure 4.5**, the appearance of the (½,0) reflection, which indicates the formation of Fe_3O_4, occurs after around 11 seconds of deposition. The duration is equivalent to a thickness of ~ 1 nm.

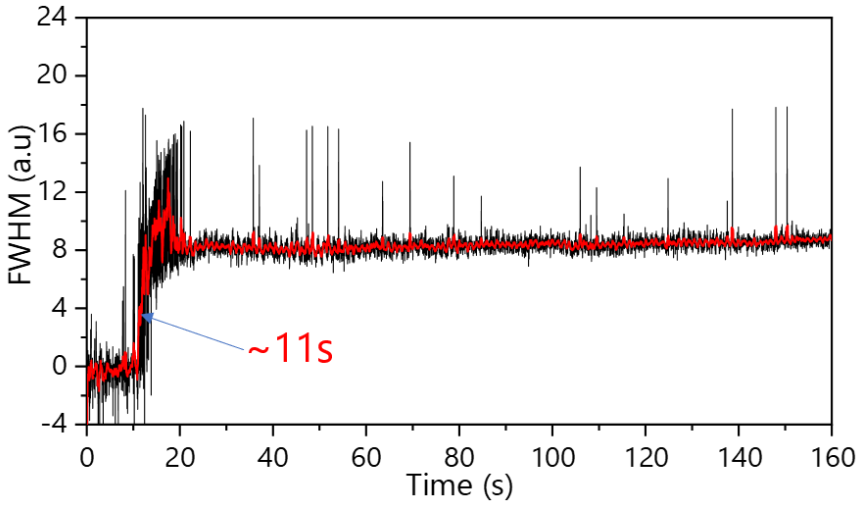

Figure 4.5 *FWHM of (½,0) reflection as a function time of Fe_3O_4 deposition on 1nm FeO deposited on ZnO substrate. Black curve is raw data, and red curve after a "5-point adjacent averaging)" smoothing.*

Conclusion: According to operando RHEED characterizations, the crystallization process of Fe_3O_4 is consistently initiated by the formation of the FeO phase or a FeO-like structure exhibiting an atomic arrangement that closely resembles that of FeO.

From the analysis of the exact position of (1,0) and (½,0) RHEED diffraction, Paul *et al.* [73] suggested that the formation of the FeO-like structure plays a role of intermediate layer for the progressive in-plane lattice spacing relaxation from ZnO to Fe_3O_4 and full relaxation can be achieved at the thickness of 2.1 nm.

These observations, however, are limited to the dynamic behavior during the growth, and characteristics of the very topmost monolayers of the film. It is crucial to underline that RHEED characterizations primarily provide information on the surface properties of thin films. As the thickness of the film increases, our understanding of the early stage of the growth remains incomplete. It is therefore challenging to study the stability of the assumed FeO-like structure or FeO phase with depth when the film thickness increases.

Structural and magnetic characterization

To examine the influence of intentionally grown 1 nm FeO template on the volume properties of Fe_3O_4, we conducted an experiment by depositing two samples of 85 nm film of Fe_3O_4 on the ZnO(0001) substrate at a temperature of 260°C. One sample was directly deposited on the substrate, while the other sample involved the initial growth of a FeO template layer before the deposition of Fe_3O_4. **Figure 4.6** depicts the ω-2θ X-ray diffraction patterns of the investigated samples. Remarkably, both samples exhibit Fe_3O_4 crystalline structure with a (111) orientation, as evidenced by the (*lll*) peaks positions. The intensity and broadening of the Fe_3O_4 Bragg peaks appear identical between the two samples. This observation suggests that the structural properties and the crystalline quality of Fe_3O_4 remain unchanged in both cases.

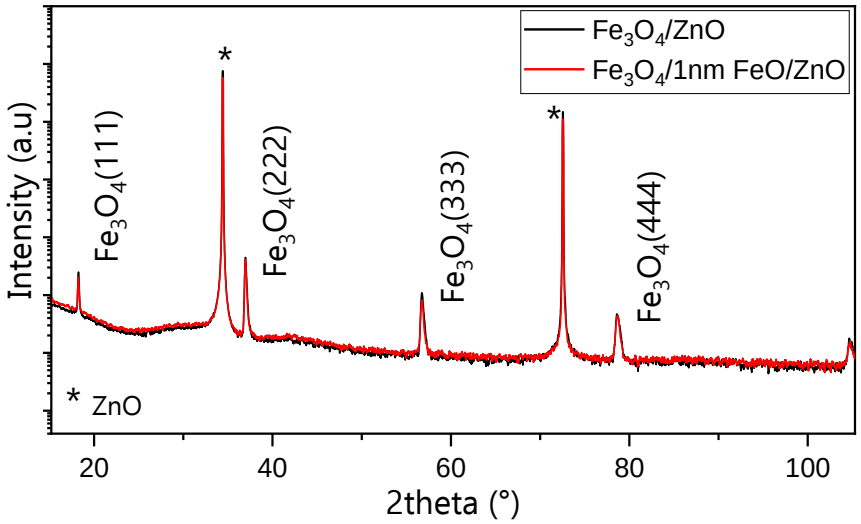

Figure 4.6 *ω-2θ X-ray diffraction patterns of the two samples: (black) 85nm Fe_3O_4 on ZnO(0001) substrate, and (red) 85nm Fe_3O_4 on 1nm FeO on ZnO(0001) substrate*

Consistently with the XRD results, VSM measurements reveal that the deposition of 1nm of FeO has no significant effect on the magnetic properties of the film. The measured magnetic hysteresis loops of the two samples presented in **Figure 4.7** are nearly identical, indicating similar saturation and remanent magnetization, which confirms the preservation of the Fe_3O_4

film quality when grown on the FeO template. It is worth mentioning that the samples do not present any in-plane magnetic anisotropy.

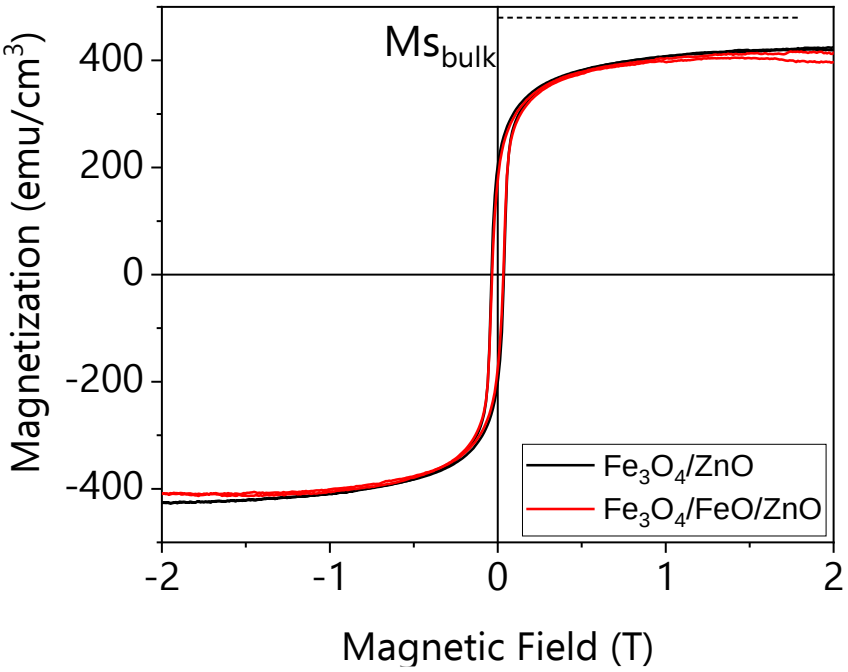

Figure 4.7 *Room temperature magnetic hysteresis loops as a function of applied magnetic field between -2T and 2T of the two samples: (black) 85nm Fe_3O_4 on ZnO(0001) substrate, and (red) 85nm Fe_3O_4 on 1nm FeO on ZnO(0001)*

To gain comprehensive information about the structure at the interface and behavior of the initial intentionally deposited FeO before the growth of Fe_3O_4, further investigations employing transmission electron microscopy were performed**. Figure 4.8(a)** depicts a cross section HAADF-STEM image showing the interface film/substrate of the Fe_3O_4 film grown on the FeO template, taken parallel to the zone axis [$11\bar{2}$] Fe_3O_4. This image reveals a high crystalline quality of the sample, additionally, no other phase was detected on lower magnification images, confirming that the integral volume of the film is composed only of Fe_3O_4. **Figure 4.9** represents the fast Fourier transform (FFT) of the present HAADF-STEM image where we observe only one orientation of the Fe_3O_4, which is in a good agreement with XRD and RHEED results and confirms the epitaxial relation: $Fe_3O_4(111)[11\bar{2}]||$ ZnO$(0001)[10\bar{1}0]$. The diffractions indexed in **Figure 4.9** belong either to the substrate ZnO(0001) (white) or to the Fe_3O_4 phase (yellow), which indicates the absence of the FeO.

The magnification around the interface displayed in **Figure 4.8(b)** shows a sharp and flat interface between the film and the substrate, with no observable presence of the deposited FeO. Starting from the interface, the atomic arrangement of the film corresponds to the projection of the spinel structure parallel to the observation axis (see the golden sketch on the image). From

this result, we understand that RHEED observations represent only a dynamic behavior at the beginning of the growth, and the formed FeO at the early stage of the growth is transformed into Fe_3O_4 even when the FeO was intentionally grown on the ZnO using well-established conditions to obtain pure and stable FeO. This finding agrees well with the observations that has been reported on MgO and $SrTiO_3$ in [177] suggesting the oxidation of the initially formed FeO on these substrates.

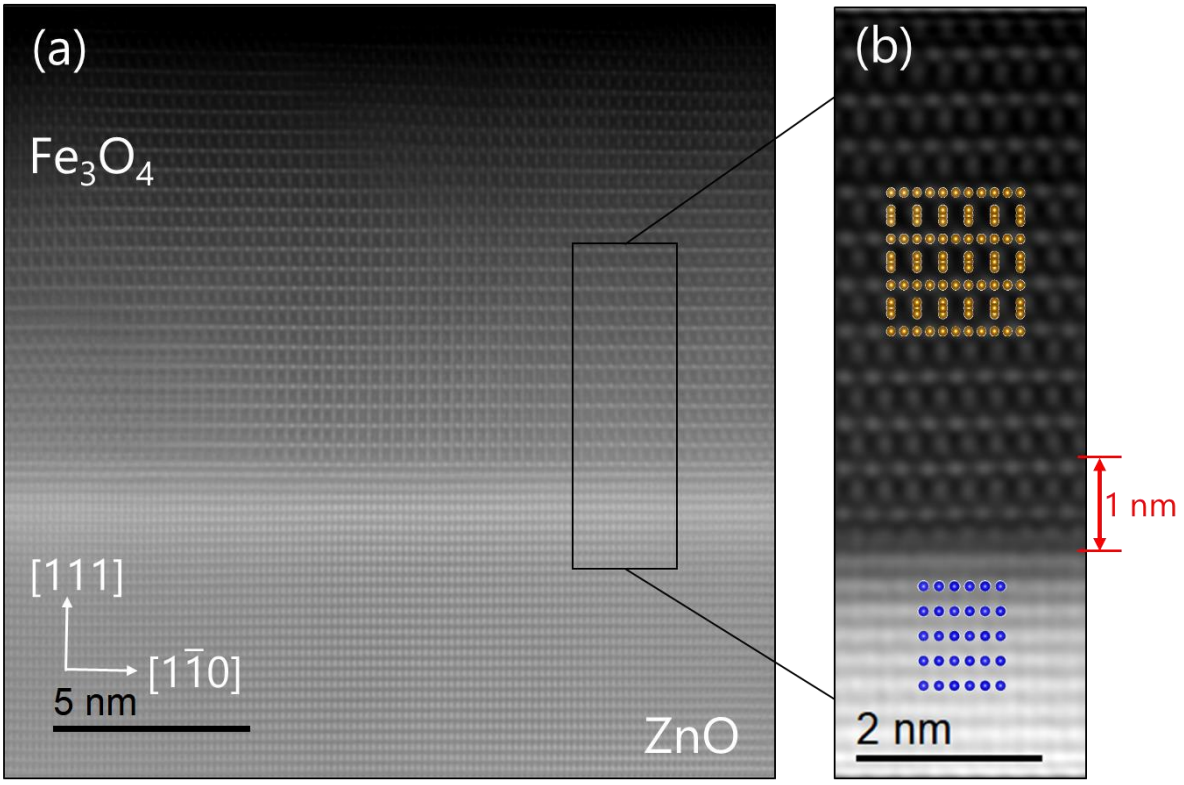

Figure 4.8 *(a) cross-section HAADF micrograph taken // [11$\bar{2}$] zone axis of a Fe_3O_4 film grown at 260°C with 1nm FeO at the interface, (b) magnification near the interface Fe_3O_4|ZnO, golden and blue sketches represent the Fe and Zn atomic arrangement in Fe_3O_4 and ZnO structures respectively, the up down red arrow shows the distance from the substrate surface equivalent to 1nm.*

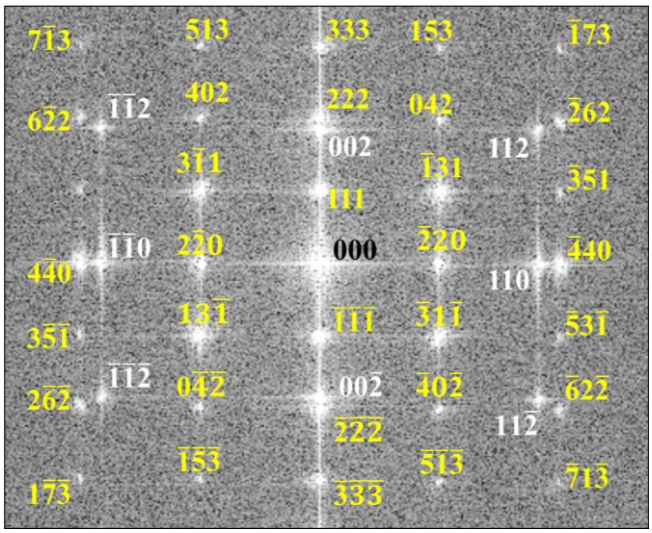

Figure 4.9 *Fast Fourier Transform (FFT) of the HAADF-STEM image in* ***Figure 4.8****, yellow index represent the Fe_3O_4 diffractions and white indexes represent the substrate ZnO diffractions, no diffraction could be attributed to FeO*

4.4. Growth of Fe_3O_4 on vicinal ZnO(0001) substrates

The nucleation dynamics of thin film growth is strongly influenced by the crystallographic orientation of the substrate (substrate face). The arrangement of atoms on the substrate surface, which is determined by its crystallographic orientation, directly impacts the growth orientation of the film and the resulting strain between the film and the substrate. These factors originating from the substrate face play a crucial role in determining the growth behavior and properties of the thin film. Furthermore, the presence of steps and terraces on a substrate face due to a miscut changes the surface energy of the substrate [178]. A flat substrate is characterized by homogeneous surface energy over the entire growth plane. However, in the case of a miscut substrate (where the surface is called vicinal), the presence of steps induces variations in the number of dangling bonds at the step edges, which can energetically favor or disfavor the incorporation of adatoms at the step edges during the growth. (see **Figure 4.10(b)**). The movement of an adatom on a flat substrate involves several atomic processes, including: deposition, where the adatom is added to the surface with a flux represented by F, diffusion on the surface with a constant diffusion coefficient represented by D, and desorption, where the adatom leaves the surface after a certain desorption time represented by τ.

On a vicinal surface, in addition to the processes mentioned above, there is an additional process called line diffusion. Line diffusion refers to the movement of adatoms along the steps present on the surface, which is represented by D_L. Furthermore, adatoms on the vicinal surface can

attach or detach from the steps at a rate represented by ± ν. These processes are illustrated in **Figure 4.10(a)**.

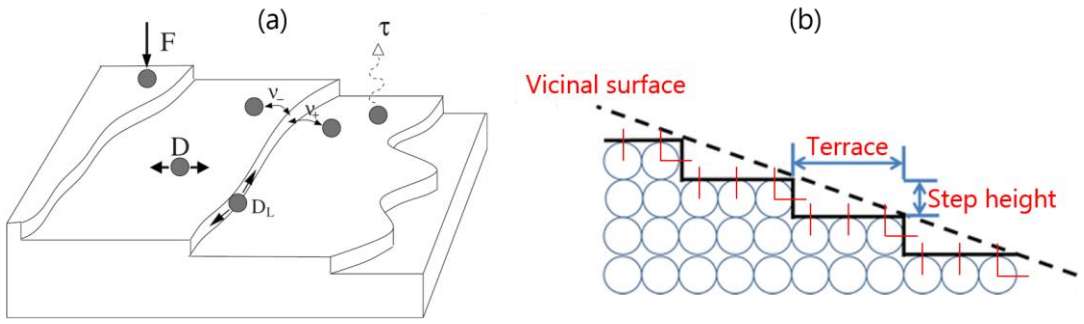

Figure 4.10 *(a) Schematic representation of a vicinal surface illustrating the possible atomistic processes (refer to the text for details) [179]. (b) Schematic representation of a cross-section of a crystal presenting a vicinal surface*

The growth of thin films on vicinal surfaces can be highly advantageous in enhancing the epitaxial quality of the grown film through enhancing the surface mobility of adatoms which have higher probability to attach or detach and diffuse along the step edges compared to the flat surface regions. In addition, the presence of steps on the substrate surface can reduce the density of threading dislocations and antiphase boundaries as was observed in several heteroepitaxial systems [180]–[182].

Specifically, in the case of magnetic thin films, vicinal substrates can induce a preferred magnetic orientation or anisotropy in the grown films. The steps present on surface can act as pinning sites for the magnetic domains, leading to an alignment of the magnetization along a specific direction. This controlled magnetic anisotropy is crucial for spintronic devices. Golub *et.al* have reported a strong magnetic anisotropy in thin Fe_3O_4 films grown on miscut MgO(001) substrates due to the dependence of APBs density which was correlated to orientation of the step edges and the miscut value [183], [184]. In fact, the steps and terraces on the vicinal surface can act as nucleation sites, leading to the formation of specific magnetic domain patterns.

Based on the aforementioned information, we devote this section to the examination of the growth of Fe_3O_4 on ZnO(0001) substrates with 1° miscut in the two different cases: with and without utilizing the FeO layer template. We investigated the growth on two different miscut orientations, namely $[11\bar{2}0]$ and $[10\bar{1}0]$. We choose the temperature of 400°C to perform this growth to maximize the atom mobility on the substrate surface and to mark any eventual effect of the miscut. Additionally, despite the FeO template layer has no effect on the structural and

magnetic properties of the deposited films at 260°C, it is beneficial to study its potential effect at higher temperatures. **Table 4.1** lists the ensemble of samples that we will discuss in this section. The sample **A1** is considered as the reference sample.

__Table 4.1__ list of Fe_3O_4 samples grown on substrate miscuts orientations

Sample	Substrate miscut	Growth T (°C)	P_{O_2}(Torr)	Structure
A1	0°	400	4×10^{-6}	Fe_3O_4/ZnO
A2	0°	400	4×10^{-6}	Fe_3O_4/FeO/ZnO
B1	1°→[11$\bar{2}$0]	400	4×10^{-6}	Fe_3O_4/ZnO
B2	1°→[11$\bar{2}$0]	400	4×10^{-6}	Fe_3O_4/FeO/ZnO
C1	1°→[10$\bar{1}$0]	400	4×10^{-6}	Fe_3O_4/ZnO
C2	1°→[10$\bar{1}$0]	400	4×10^{-6}	Fe_3O_4/FeO/ZnO

4.4.1. Structural characterization

Figure 4.11 displays the RHEED patterns of sample B1 and C1 after the growth of Fe_3O_4 taken along the directions [11$\bar{2}$0] and [10$\bar{1}$0] of ZnO. These patterns are similar to the patterns obtained for the films grown at 260°C and 400°C on flat substrates, affirming the epitaxial growth and the conservation of the same in-plane epitaxial relationship between the film and the substrate with a value of miscut of 1°.

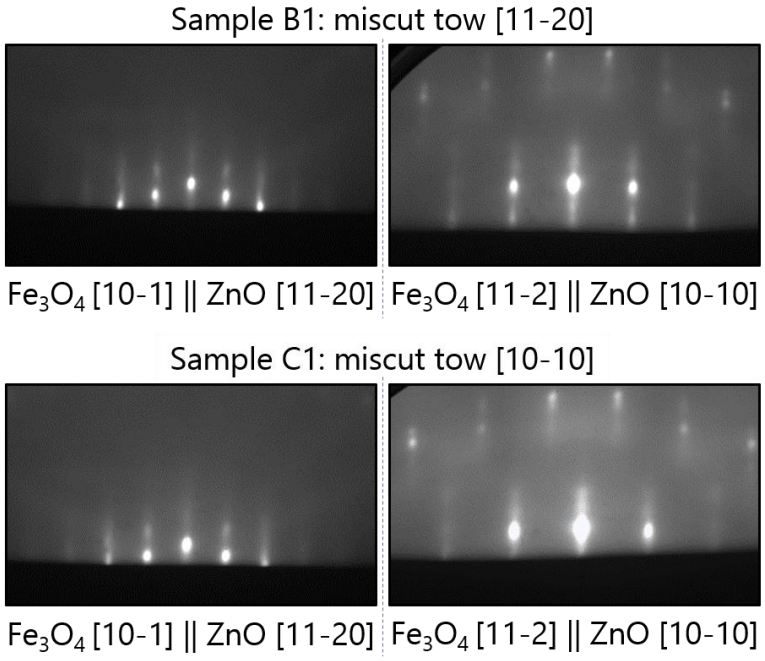

__Figure 4.11__ RHEED patterns of samples B1 and C1 taken along [10$\bar{1}$] Fe_3O_4 and [11$\bar{2}$] Fe_3O_4 after the growth

Figure 4.12 shows the X-ray diffraction θ-2θ patterns of samples A1-C2 measured in the Bragg-Brentano configuration. The alignment of the samples was performed using the

ZnO(0002) Bragg peaks. The peaks marked with (∗) correspond to the "forbidden" (for the $P6_3mc$ space group) reflections the ZnO substrates: 0001, 0003, and 0005. Their angular widths are comparable to the wurtzite ZnO allowed ones (0002 and 0004) in order of 0.03° for the 0003, in the instrumental measurement conditions. Such "forbidden" peaks are usually observed under experimental high-resolution conditions in cases of high-quality substrates i.e. with large single crystalline domains with very low orientational mosaicity: Si, Al_2O_3, etc. [185]. First report was by Renninger in 1937 [186] associated to case of 111 peaks in diamond symmetry. Origin is low intensity structural peak arriving by an azimuthal rotation of the substrate to Laue interference conditions associated to a "forbidden" inter-reticular *hkl* planes for Bragg conditions in θ-2θ experiment [187]. Names of such unexpected peaks are so-called "Renninger", "Umweganregung" or "X-ray multiple" reflections. Grundmann *et al.* [188] analyzed recently the situation for wurtzite ZnO substrates and epitaxial thin films. Observation of these peaks is a signature of large single crystals variants well oriented of ZnO(0001) used substrates.

For all the substrates, only the (*lll*) family of planes of Fe_3O_4 is present, indicating an epitaxial growth of Fe_3O_4 on the c-plane of ZnO flat and 1° miscut substrates. Hence, the substrate miscut does not affect the growth orientation of the film. However, this result does not exclude the possibility of a tilt of (*lll*) planes of Fe_3O_4 with respect to the ZnO(*000l*) planes. If there is a tilt, up to certain value the (*lll*) peaks can still be detected, though with lower intensity.

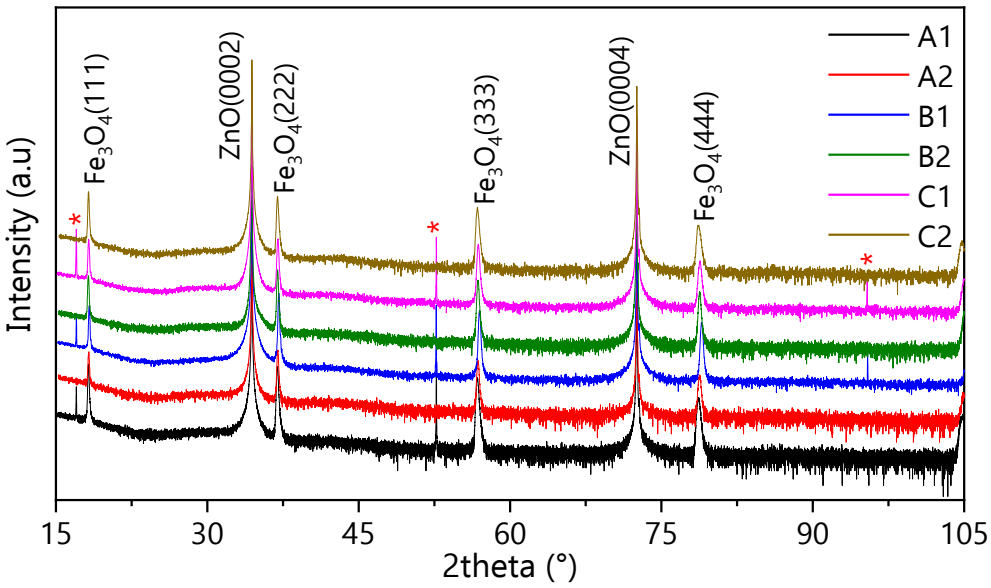

Figure 4.12 *Cu-Kα XRD patterns of samples A1-C2 (intensity in log scale)*

In order to accurately determine the precise orientation of (*lll*) planes of Fe_3O_4, a thorough analysis was conducted employing an ω-scan technique. This involved examining the

symmetric peaks of ZnO(0002) and Fe_3O_4(222) at various values of φ, followed by a comparison of the ω offset observed at each φ. By performing this comparison, valuable insight was obtained regarding the out-of-plane orientation of the film planes with respect to the substrate.

To calculate the tilt, the following equation was utilized:

$$tilt_{f/s} = (\omega_f - \bar{\omega}_f) - (\omega_s - \bar{\omega}_s) \quad (4.1)$$

In this equation, ω_f and ω_s refer to ω values of the film and the substrate at each φ, respectively, and $\bar{\omega}$ denotes the average value of the measured ω over all φ values for each peak.

The measured ω values of each peak for the two samples, B2 and C2, are depicted in **Figure 4.13(a)** and **Figure 4.13(b)**, respectively. In both miscut orientations, the curves representing the variation of ω as a function of the sample orientation for the ZnO(0002) and Fe_3O_4(222) peaks are observed to be parallel. This parallel behavior suggests the parallelism between the considered atomic planes.

The exact values of the tilt are presented in **Figure 4.13(c)** and **Figure 4.13(d)**. It is noteworthy that throughout the entire range of 0°-360°, the variations in the tilt remain approximately equal to 0°. This consistent value confirms the parallelism between the (*lll*) planes of Fe_3O_4 and the c-plane of ZnO.

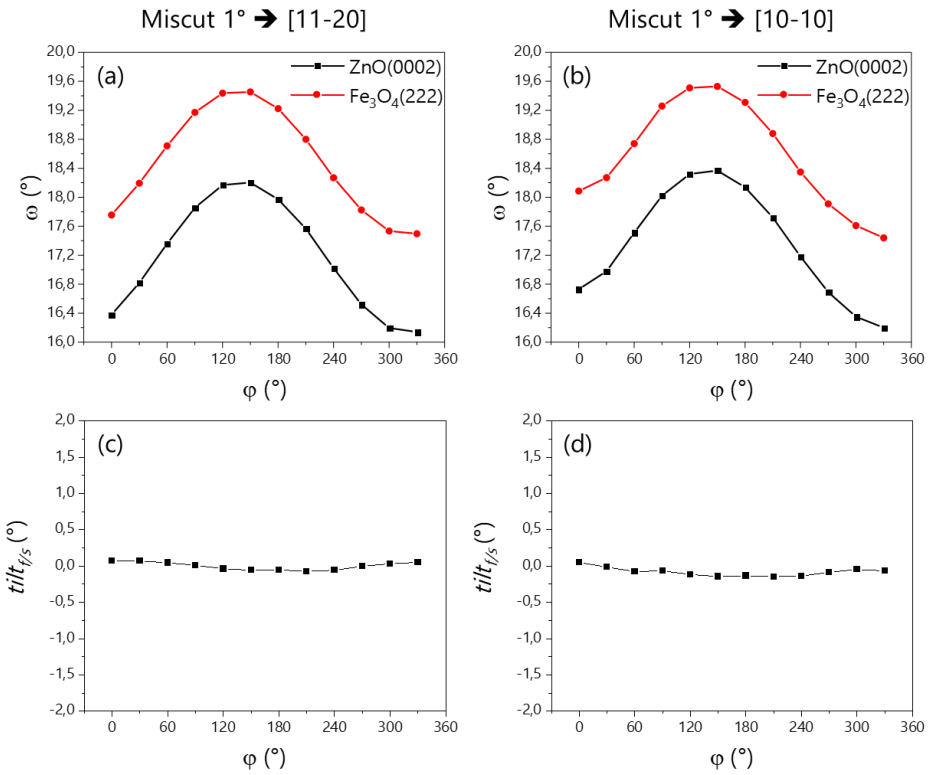

Figure 4.13 *(a) and (b): the measured ω of ZnO(0001) and Fe_3O_4(222) peaks as a function of the azimuthal angle φ of samples B2 and C2 respectively, (c) and (d) tilt value of atomic plane (lll) of the Fe_3O_4 with respect to the ZnO (000l) atomic planes of the corresponding samples*

The present results indicate that the examined miscuts of 1° does not affect the growth orientation and does not result in any measurable tilt between the (*lll*) planes of Fe_3O_4 and the c-plane of ZnO. Additionally, the growth onto the FeO template layer does not induce any remarkable effects on the structural properties at the temperature of 400°C either (same observation at 260°C).

One of the characteristics of Fe_3O_4 thin films that can be affected by a substrate miscut is crystallographic twinning. During the initial nucleation stage of film formation, rotational twinning can occur, which is closely associated with the deposition of Fe_3O_4 atoms in a triangular arrangement on the atoms of ZnO, which have a hexagonal arrangement. This arrangement results in the formation of two domains with a mirror relationship i.e. 180° in-plane rotation (as illustrated in **Figure 1.13** in Section 1.4).

In the case of a flat substrate, the ratio of domains must be equal because the probability of deposition for each domain is 50%. However, on a miscut substrate, step edges can serve as preferential nucleation sites for one of the twins, leading to an imbalanced twin density. This means that one of the twin domains may dominate over the other, resulting in an unequal

distribution of twins in the thin film. A successful growth of single crystallographic domain was reported for various oxides utilizing miscut substrates [189]–[191].

In order to investigate the effect of 1° miscut of the substrate on the twin domain density, φ-scans were performed to probe Fe_3O_4(311) and ZnO(10$\bar{1}$1) asymmetric peaks of the sample B1. To obtain these scans, the sample was tilted (χ angle) by 29.5° and 61.6° with respect to the standard θ-2θ scan, to reach the Fe_3O_4(311) and ZnO(10$\bar{1}$1) peaks, respectively. **Figure 4.14(a)** illustrates the atomic arrangement projection along the [10$\bar{1}$]Fe_3O_4 axis in the Fe_3O_4//ZnO heterostructure, as well as the disposition of considered atomic planes. The two particular peaks were selected due to their higher intensity compared to other X-ray diffraction peaks of Fe_3O_4 and ZnO. The φ-scan was then performed while keeping the sample in an oblique position. **Figure 4.14(b)** shows the obtained diffractograms. Six peaks of ZnO(10$\bar{1}$1) with a periodicity of 60° are present, which is expected for the six-fold symmetry of the wurtzite structure of ZnO. Nevertheless, for a cubic symmetry (111)-oriented, only three peaks with 120° periodicity are expected for a single domain. Detecting six peaks related to the (311) diffraction evidences the 180° rotational twinning occurring in the Fe_3O_4. Furthermore, the intensities of the six Fe_3O_4(311) peaks are equivalent, suggesting that the two domains are equivalently present in the Fe_3O_4 thin film and that the substrate miscut of 1° does not lead to a preferential crystallization of one twin over the other. Another important information about the high epitaxial quality is that the diffraction occurs at well-defined φ angle values with sharp peaks, confirming that there is no texture in the film plane and the film is only crystallized epitaxially in the two twinned domains.

The absence of a discernible effect of substrate miscut on Fe_3O_4 twinning may be attributed to the large size of the terraces (~30 nm for 1° miscut with double interplanar height steps) in comparison to the domain sizes. Conducting further studies with higher miscut values (> 1°) would be interesting to explore the reduction of terrace size and its potential impact on domain nucleation.

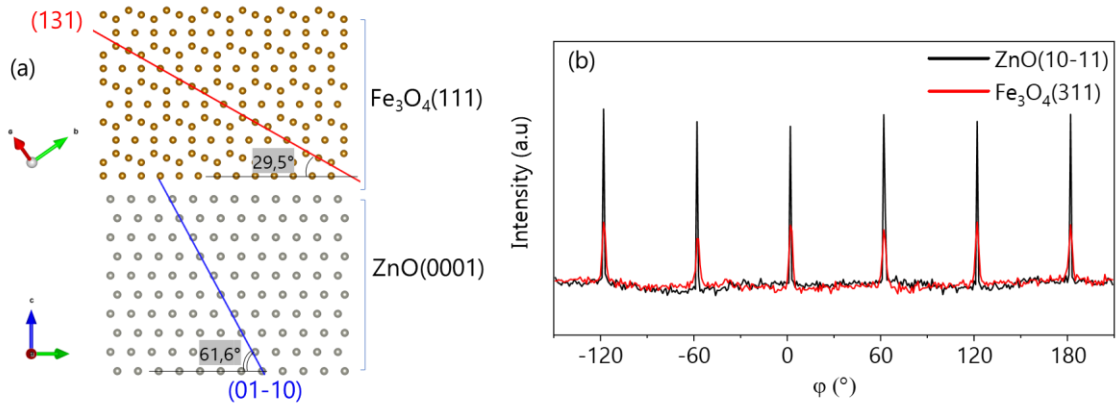

Figure 4.14 *(a) schematic representation of the atomic stacking in the heterostructure Fe_3O_4//ZnO (only cations are shown) projected along [10$\bar{1}$] Fe_3O_4 axis, red and blue lines represent atomic planes Fe_3O_4(131) and ZnO(01$\bar{1}$1), respectively, (b) X-ray φ-scan of Fe_3O_4(311) and ZnO(10$\bar{1}$1)*

4.4.2. Magnetic characterization

The magnetization of the samples A1-C2 was measured using VSM with magnetic field applied parallel to the film plane along [10$\bar{1}$0] and [11$\bar{2}$0] directions of ZnO. The magnetic hysteresis loops of these samples are shown in **Figure 4.15**.

The measured magnetization behavior confirms the ferrimagnetic nature of the deposited films on the flat and the miscut substrate with the two different miscut orientations, which is in good agreement with the XRD measurements that confirm the preservation of epitaxial growth of Fe_3O_4 on the ZnO substrate. Overall, the samples A1-C2 exhibit saturation magnetizations close to the bulk value, as they were measured within the range of 445 emu/cm³ to 480 emu/cm³.

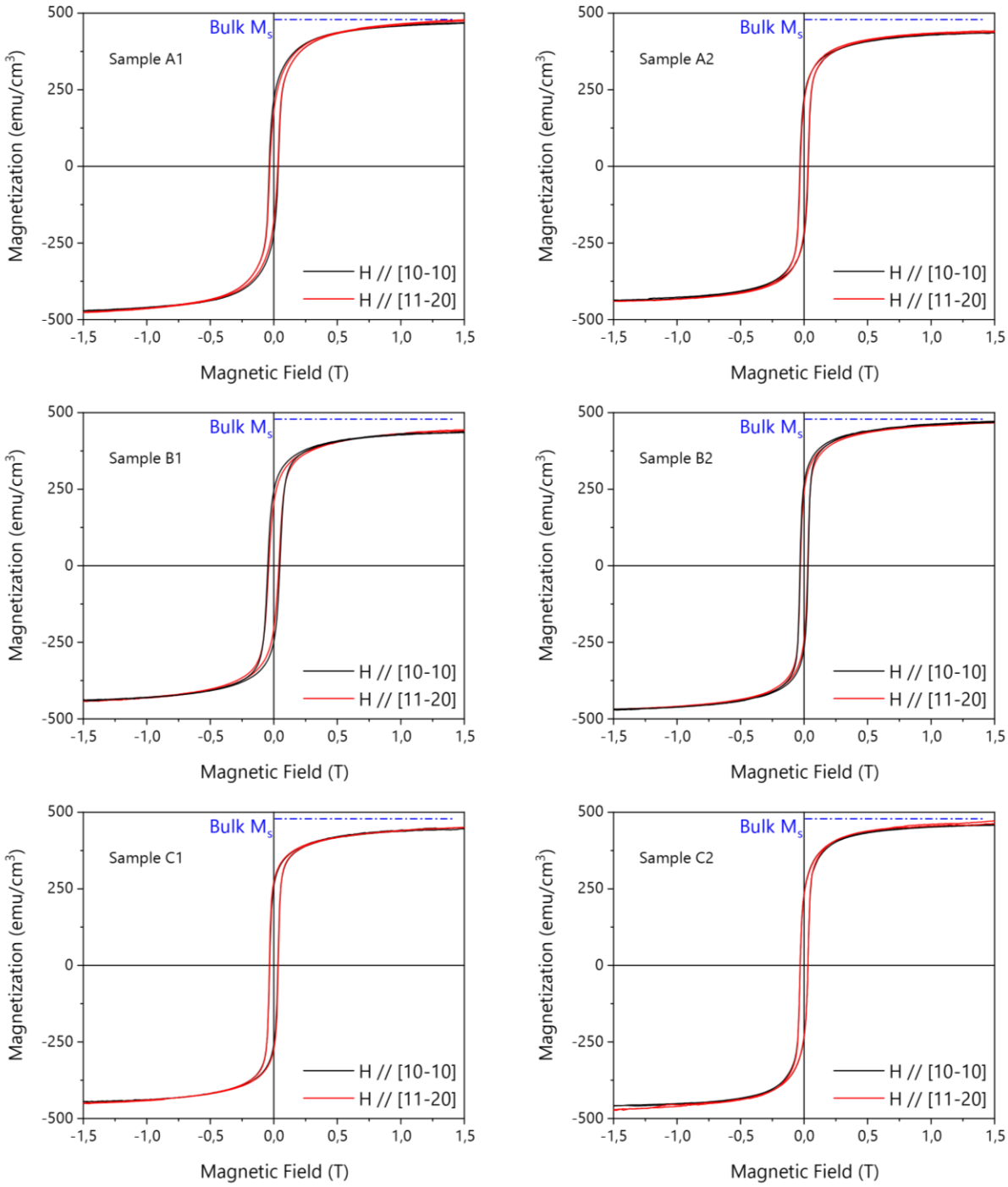

Figure 4.15 *Magnetic hysteresis loops of samples A1-C2 measured using VSM at room temperature*

Table 4.2 Magnetic properties of samples A1-C2, error in Ms of around ± 10 emu/cm^3 lists in details the magnetic properties of the samples discussed in this section, which were measured along the two different directions.

Table 4.2 *Magnetic properties of samples A1-C2, error in Ms of around ± 10 emu/cm^3*

Sample & miscut	**A1** 0°		**A2** 0°		**B1** 1° → $[11\bar{2}0]$		**B2** 1° → $[11\bar{2}0]$		**C1** 1° → $[10\bar{1}0]$		**C2** 1° → $[10\bar{1}0]$	
Measurement orientation	// $[10\bar{1}0]$	//$[11\bar{2}0]$	// $[10\bar{1}0]$	// $[11\bar{2}0]$	// $[10\bar{1}0]$	// $[11\bar{2}0]$	// $[10\bar{1}0]$	// $[11\bar{2}0]$	// $[10\bar{1}0]$	// $[11\bar{2}0]$	// $[10\bar{1}0]$	// $[11\bar{2}0]$
Ms (emu/cm^3)	478	478	445	445	445	445	470	470	455	455	465	465
Mr (emu/cm^3)	218	179	223	210	246	205	266	241	259	272	233	230
Mr/Ms (%)	46	37	50	47	55	46	57	51	57	60	50	50
Hc (Oe)	360	315	322	298	473	400	315	290	330	350	310	310

Observations

The saturation magnetization: The highest saturation magnetization is obtained with the flat substrate A1 as 478 emu/cm³, while it is slightly reduced to 445 emu/cm³ in the case of the sample A2 where the Fe_3O_4 is deposited on the FeO template. This observation appears to be specific to the flat substrate and may not be projectable or generalizable to the other results as we see the opposite observation in the case of samples B1 vs B2 and C1 vs C2 where the higher saturation magnetization is measured in the case of the growth on FeO template layer.

The remanent magnetization and the coercive field: Interestingly, the remanent magnetization is greater in the case of films deposited on miscut substrates, despite having lower saturation compared to the film on flat substrate (sample A1). This enhancement of remanence could be attributed to the role of the miscut, although the difference is not very significant.

For all samples, both the remanent magnetization and the coercive field tend to be higher along the $[10\bar{1}0]$ direction, except for sample C1, which shows the highest remanence among this set of samples when measured along the $[11\bar{2}0]$ direction (perpendicular to the miscut orientation), with a value of 272 emu/cm^3.

The in-plane anisotropy: in the analysis of in-plane anisotropy, we compare the remanent magnetization ratio (Mr/Ms) measured along the two different directions. Samples A2, C1, and C2 exhibit a relatively isotropic behavior within the plane, with a difference in the Mr/Ms ratio lower than 3%. However, sample B2 presents a higher degree of anisotropy, as indicated by an increasing difference in the Mr/Ms ratio from 51% to 57%. Moreover, samples

A1 and B1 have the highest anisotropy, with the Mr being 9% higher when measured along $[10\bar{1}0]$ compared to $[11\bar{2}0]$ direction.
Another important remark is that the difference in the ratio Mr/Ms between the measurement directions is reduced by introducing the FeO template layer for all substrates.

Discussion

The value of the saturation magnetization is determined through calculation that consider the thickness of the sample (magnetic moment/thickness). It is important to note that inaccurate estimation of the sample thickness can lead to erroneous evaluation of saturation magnetization. However, the estimated saturation magnetizations obtained from our measurements do not exhibit significant differences between the samples, falling within the range of 445 emu/cm^3 to 478 emu/cm^3. It is important to highlight that most thin films of Fe_3O_4, deposited by either PLD or MBE, have been reported to possess saturation magnetization values within this range [78], [192]–[197]. Consequently, relying solely on saturation magnetization as a criterion for evaluation may not be sufficient in distinguishing the best samples among this set. The key parameter that we will consider is the remanent magnetization, particularly because some samples exhibit higher remanence despite having lower saturation magnetization compared to other samples. It is also an important parameter in the context of our project SPINOXIDE as we aim to fabricate devices functioning at room temperature in absence of magnetic field. To effectively compare the samples, we introduce the ratio of remanent magnetization to saturation magnetization **Mr/Ms** as a suitable metric.

Films grown on a flat substrate and a substrate miscut toward $[11\bar{2}0]$ (A1 & B1) exhibit a higher ratio of Mr/Ms along the $[10\bar{1}0]$ axis. In contrast, the film grown on the substrate miscut towards $[10\bar{1}0]$ (C1) demonstrates a higher ratio of Mr/Ms along the $[11\bar{2}0]$ axis. This change in $(Mr/Ms)_{max}$ between axes indicates that the miscut plays a role in creating a step-induced uniaxial anisotropy. A similar effect was previously observed on MgO(001) miscut substrates [184], where a stronger in-plane anisotropy was observed for a miscut towards the [011] axis compared to the [010] axis. This difference in anisotropies was attributed to a higher number of antiferromagnetic exchange interactions across the step-induced antiphase boundaries in the case of miscut towards [011]. Since the magneto-crystalline anisotropy is expected to have a minor impact on magnetization in the (111) plane [198], the change in anisotropy observed in our films highlights the role of the miscut in giving a rise to a preferred orientation of the antiphase domains.

The measured ratio Mr/Ms is effectively enhanced along both measurement directions by introducing the 1° miscut. This enhancement can be explained by a reduction of defects, mainly the density of APBs, which are known to have a the major impact on magnetization [99], [199]–[202].

The difference in the Mr/Ms value between the two directions was reduced by the growth of the FeO template layer. Despite the fact that the FeO disappears after the growth of Fe_3O_4, its effect is observed in the magnetic properties of the samples grown at 400°C. The nucleation of defects, such as dislocations, and antiphase boundaries which directly affect the magnetization, occurs at the first monolayers. Here comes the role of the FeO template layer as a buffer layer to promote uniform growth and suppress the preferential nucleation of antiphase domains along a specific direction before its oxidation.

The next chapter will focus on the quantitative study of APBs in samples grown with and without the FeO template layer.

4.5. Interface properties of Fe_3O_4//ZnO

In order to investigate the effect of the growth temperature and the role of the FeO template on the interface between the Fe_3O_4 thin films and the ZnO substrate, we have carried out SIMS analysis.

SIMS depth profiling was conducted on two pairs of samples that were deposited at 260°C and 400°C. In each temperature set, one sample consisted of Fe_3O_4 directly grown on ZnO, while the other sample comprised Fe_3O_4 deposited on a 1 nm FeO template on ZnO. The SIMS primary beam consists of O^{2+} ions accelerated under 5 keV impact energy, to reach the sample with an incidence angle of 45° to the normal of the film plane. The elements ^{64}Zn, ^{54}Fe, and ^{16}O were collected in a positive polarity from a 150×150 µm² crater. The analyzed zone was restricted to 33 × 33 µm² area to avoid the border effects. **Figure 4.16** shows the SIMS depth profiles of the elements ^{64}Zn, ^{54}Fe, ^{16}O for the samples grown at 260°C and 400°C without FeO template layer. The same profiles were obtained for the samples grown with the FeO template. We define the interface position indicated by dashed vertical line at the crossover of iron ^{54}Fe and zinc ^{64}Zn intensity curves (equivalent to ~86nm measured with profilometer).

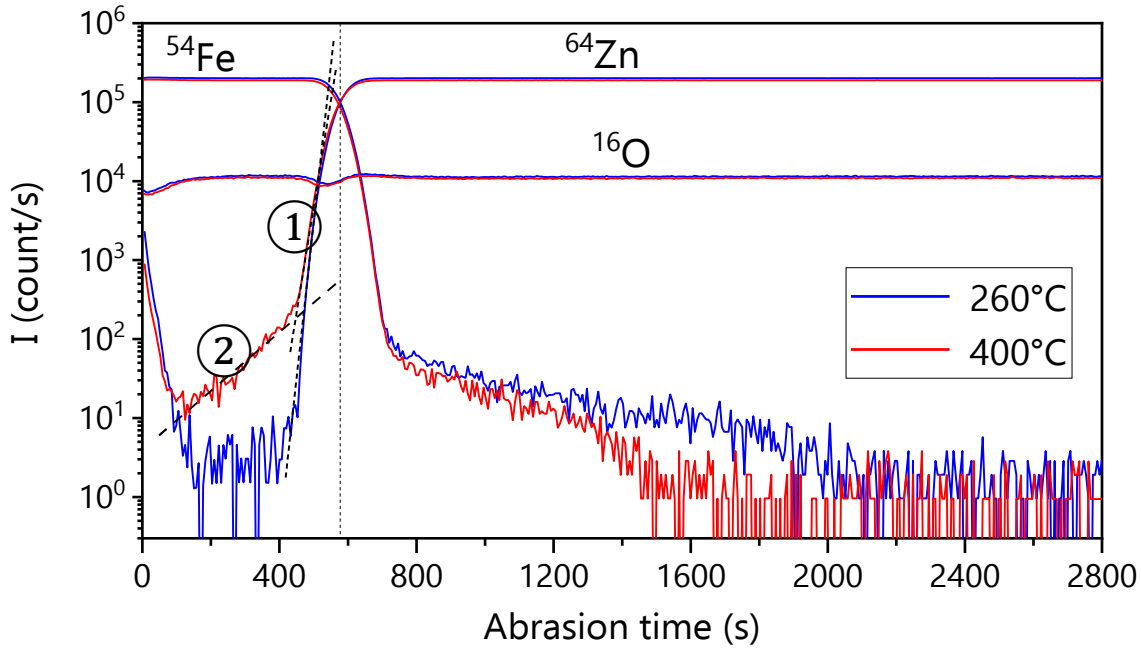

Figure 4.16 *normalized SIMS depth profiles of two Fe_3O_4 thin films deposited on ZnO at: 260°C (blue curves) and 400°C (red curves)*

In the absence of calibration standards to determine the precise atomic concentration of the collected elements, particularly Zn within the Fe_3O_4 and Fe within the ZnO substrate, it is practical to compare the intensities (cnt/s) and the variations of intensity (in decade.nm^{-1}) of these elements under different growth conditions. This approach is relevant when analyzing SIMS depth profiles. In **Figure 4.16** we indicate the dashed lines ① and ②, which are the linear fitting of Zn intensity profile near and far from the interface, respectively, in the Fe_3O_4 layer. The slope of ① characterizes the Zn concentration variation near the interface, which depends on the Zn content in the film, and also on the experimental broadening of the interface under the erosion dynamics. The slope of ②represents [Zn] variation far from the interface, which gives more precise information about the actual content of Zn in the film independently of the interface crossing effects related to the erosion, i.e. the slope ② is only Zn diffusion related.

First, we will discuss the Fe_3O_4 film side. Comparing the collected intensities which are proportional to the concentration of the analyzed elements (Fe, O, and Zn), reveals a perfectly identical concentration of Fe and O in both samples. However, the Zn concentration seems to be higher when the growth temperature was 400°C.

If we take the maximum intensity of ^{64}Zn collected from the substrate as reference, where the Zn concentration [Zn] = 4.2×10^{22} atom/cm^3, and by assuming that the ionization of Zn does not change considerably in the two oxide environments, the concentration [Zn] in the 400°C grown

Fe_3O_4 films can estimated in the order of 10^{19} atom/cm^3 at around 20 nm from the interface, while it's virtually absent in the 260°C films ($\leq 10^{17}$atom/cm^3). This result indicates a remarkable interdiffusion suppression by decreasing the growth temperature from 400°C to 260°C. In comparison, a thermally activated diffusion of Zn and Mg toward Fe_3O_4 films has been reported in [203], [204] at temperatures close to 400°C.

The diffusion of Zn toward Fe_3O_4 is also observed on the variation of Zn concentration near the interface given by the slope ①. This variation is correlated with the chemical sharpness of the interface in a following way: the higher the slope value, the sharper the interface. **Table 4.3** summarizes the values of slopes ① and ② of the samples deposited at 260°C and 400°C with and without 1 nm FeO template layer. In addition to the absence of Zn in the volume of the film grown at 260°C compared to the one grown at 400°C, the slope ① is increased from 0.26 to 0.42 decade.nm^{-1} by lowering the growth temperature, which confirms a significant reduction of Zn diffusion from the substrate toward the film.

Table 4.3 *slopes of the variation of ^{64}Zn intensity linearly fitted near the interface of films grown at 260°C and 400°C with and without FeO template layer*

Sample	**Slope ① (decade.nm^{-1})**	**Slope ② (decade.nm^{-1})**
260°C Fe_3O_4/ZnO	0,42	- - -
260°C Fe_3O_4/FeO/ZnO	0,47	- - -
400°C Fe_3O_4/ZnO	0,26	0,03
400°C Fe_3O_4/FeO/ZnO	0,29	0,03

The insertion of 1 nm-thick FeO template layer leads to the increase of the slopes ① from 0.26 to 0.29 and from 0.42 to 0.46 decade.nm^{-1} in the sample grown at 400°C and the one 260°C respectively. The latter variations of the slope ① indicate a minor change, suggesting that the insertion of a FeO template layer has a negligible effect on interdiffusion.

Now we will discuss the ZnO side of the interface in **Figure 4.16**, where SIMS intensities are collected only from the substrate. The concentration of Zn and O are constant in depth, which is expected for ZnO. Unexpectedly, the concentration of Fe does not drop instantly after crossing the interface (in the range 800 s – 1600 s) but decays gradually over more than 300 nm of substrate depth for both growth temperatures. One might hypothesize the possibility of iron diffusion to the substrate; nevertheless, considering a diffusion of such depth magnitude appears implausible, particularly in low temperature samples.

To gain a comprehension of the measured [Fe] in the substrate, we carried out an experiment known as Checkerboard SIMS depth profiling. This method involves mapping the spatial distribution of abraded elements from the crater surface instead of averaging the amounts over the entire surface. By performing this profiling at different depths, we can capture the spatial chemical composition of the abraded volume as schematized in **Figure 4.17**. Then we can extract composition profiles in specific regions within this volume. A lateral resolution of 2 µm can be attained with GEMaC's SIMS apparatus used in these analyses.

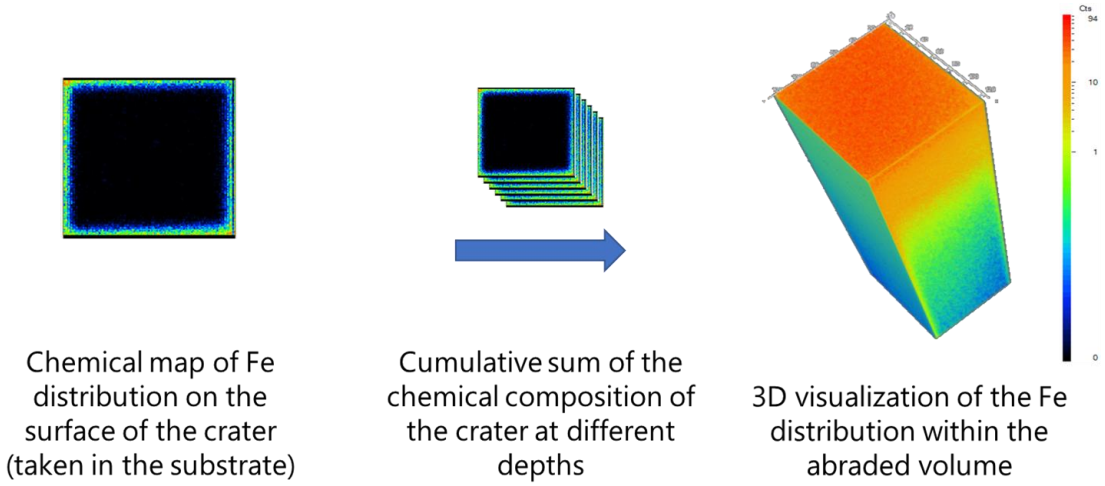

Figure 4.17 schematic representation of 3D SIMS depth profiling principle

Figure 4.18(a) presents a top view of a 130 × 130 µm² SIMS crater obtained using the checkerboard procedure. The three distinct white squares in the figure represent the ROIs (regions of interest) from which the depth profiles are derived and plotted in **Figure 4.18(b)**. For the three ROIs, the measured intensities of Zn, O, and Fe in the film are found to be equal, indicating the same concentration of these elements. This observation suggests a homogeneous chemical composition in the plane of the film. Nevertheless, the Fe content in the substrate varies depending on the selected ROI. Notably, in ROI 1, the Fe intensity is higher in the range of 800 s – 1600 s, while it is lower in ROI 2, and even lower in ROI 3, where it tends to approach to 0 at around 1200 s of abrasion time. The varying Fe intensities across different ROIs indicate non-uniform distribution of iron atoms within the substrate.

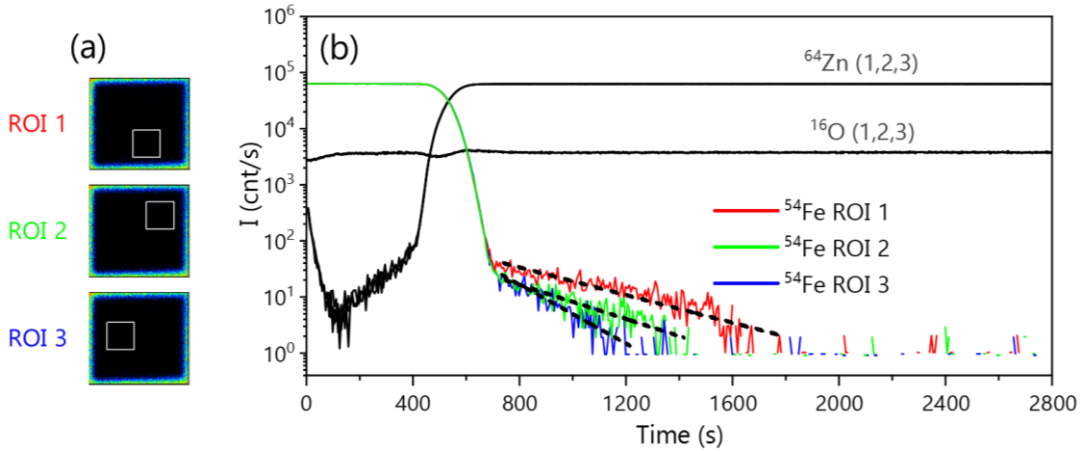

Figure 4.18 *(a) top view of SIMS crater with specification of three different ROI (Region Of Interest), (b) SIMS depth profiles of the elements ^{64}Zn, ^{16}O, and ^{54}Fe obtained from the three ROIs*

To allow a better visualization of the localized distribution of Fe in the substrate, we represent in **Figure 4.19(a)** the spatial distribution of Fe within the abraded volume. In this figure, the orange volume corresponds to the film where the Fe intensity takes its maximum, while the region with less intensity (blue dots) corresponds to the substrate which is containing "carrot-shaped" zones with higher Fe concentration. The projection of Fe distribution in the substrate (red cube in **Figure 4.19(a)**) on the horizontal plane is represented in **Figure 4.19(b)**, on which we can distinguish four regions with higher Fe concentration.

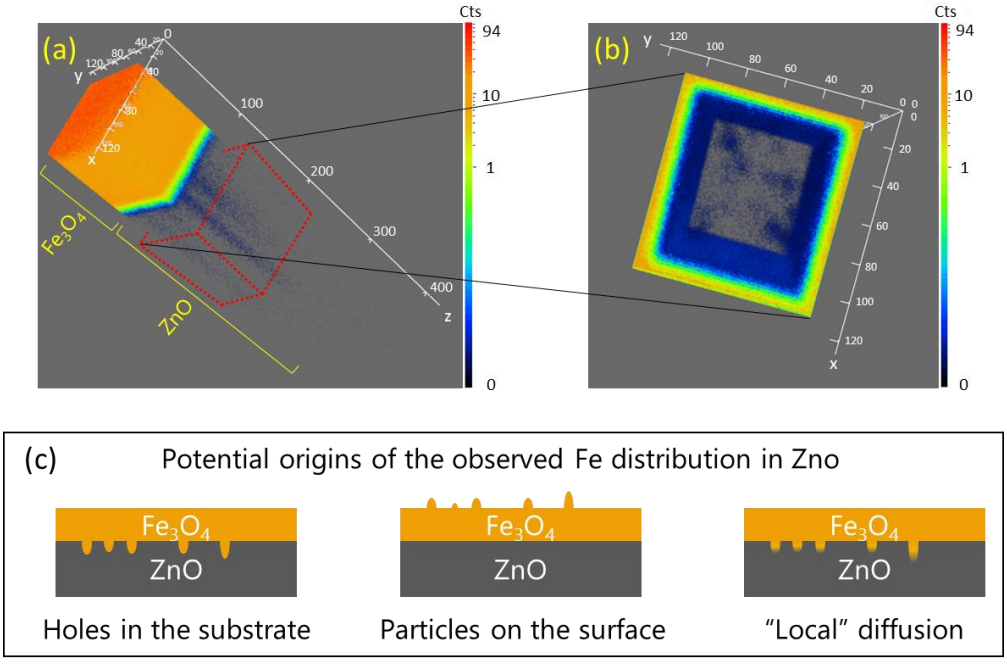

Figure 4.19 *(a) 3D distribution of Fe in Fe_3O_4/ZnO, (b) cumulative counts of Fe inside the substrate projected on the crater plane, (c) schematic representation of the possible origins of the detection and the localized distribution of Fe in the substrate*

The presence of iron at a significant depth (~300 nm) and the unexpected distribution of iron in the substrate that was highlighted by SIMS analysis may have three origins as illustrated in **Figure 4.19(c)**. The first possibility is that the substrate surface contains holes or voids where iron atoms are deposited. The second possibility is that the surface of the Fe_3O_4 film is covered by particles that can delay abrasion, and when the abrasion of the film is complete, residues of these particles remain on the substrate. The third possibility is the localized diffusion of iron within the substrate.

The first and third hypotheses can be excluded. AFM characterization of the substrate prior to deposition confirm the absence of any surface holes. Additionally, there is no apparent reason to support the localized diffusion of iron in specific regions of the substrate, especially considering that the substrate was uniformly heated during the growth process. However, the second hypothesis suggesting the presence of particles on the film surface seems to be suitable explanation of the observed Fe depth profiles. The presence of randomly distributed surface particles was confirmed and discussed in Section 3.3. **Figure 4.20** displays the height profiles of such particles which was measured with a profilometer in two different regions of the film surface. It was found to be ranging from tens of nanometers up to 300 nm.
Although the density of these particles was reduced by reducing the laser fluence, a complete elimination of these particles was not achieved.

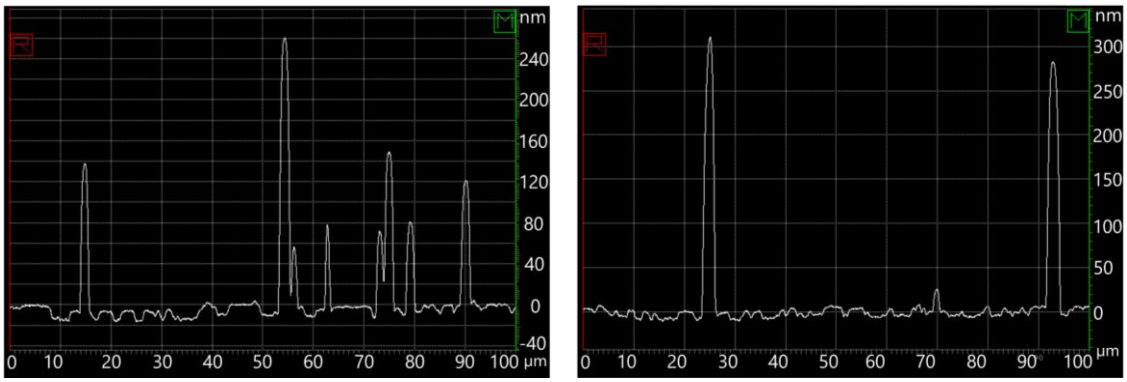

Figure 4.20 *height profiles measured in two different regions of the film surface, the peaks correspond to particles present on the surface (measured using profilometer)*

The detected Fe at a significant depth in the substrate is not due to diffusion but most likely is a result of delayed abrasion caused by particles on the film surface.

4.6. Conclusion

In summary, this chapter focused on three axes: (i) the initial stage of Fe_3O_4 growth on ZnO(0001) substrates, with an emphasis on the transformation of FeO to Fe_3O_4 during subsequent growth; (ii) the effect of substrate miscut orientation on magnetization, and (iii) the impact of growth temperature on the interfacial compositions.

Our *in-situ* RHEED measurements supported previous findings [73] by confirming that the growth process of Fe_3O_4 begins with the formation of a thin layer of FeO or FeO-like structure. However, it is important to note that these measurements only examine the very topmost atomic planes during growth. By HR-TEM imaging we demonstrated that the FeO formed initially undergoes oxidation, transforming into Fe_3O_4 as thicker Fe_3O_4 layers develop on top, even when intentionally growing a 1 nm FeO template. However, despite the oxidation of the deposited FeO, its impact was still observed in samples grown at high temperatures (400°C), as evidenced by the reduced magnetic anisotropy between the two measured directions, $[11\bar{2}0]$ and $[10\bar{1}0]$, of ZnO. This suggests that the presence of FeO during the early stages of growth influences the magnetic properties of the final Fe_3O_4 film.

We investigated the growth of Fe_3O_4 on 1° miscut substrates towards two different orientations, $[11\bar{2}0]$ and $[10\bar{1}0]$. Our results revealed that the miscut increased the remanent magnetizations, and the sample miscut towards $[10\bar{1}0]$ exhibited the highest remanence (272 emu/cm^3), highlighting the influence of substrate miscut orientation on the magnetic behavior of Fe_3O_4.

Finally, we explored the effect of growth temperature using SIMS depth profiling. When the substrate temperature was maintained at 400°C, the diffusion of Zn was detected in the Fe_3O_4 film. Conversely, reducing the growth temperature to 260°C resulted in the virtual absence of Zn in the Fe_3O_4 film.

5. Advanced structural characterizations using transmission electron microscopy

5.1. Introduction

In this chapter, we delve into the structural aspects of our Fe_3O_4 thin film samples to better understand their properties. We employ Transmission Electron Microscopy techniques to investigate the crystal structure and quantify the occurrence of Anti-Phase Boundaries (APB). The influence of growth conditions, miscut orientation, and the growth of a FeO template layer on the magnetic properties have been discussed in the previous chapters. Through high-resolution imaging and quantitative analysis, we aim to correlate these observed effects with the structural characteristics of the thin films. By examining the nanoscale features and trying to quantify the presence of APBs accurately, we aim to establish a direct relationship between structural defects and the observed magnetic characteristics.

5.2. Strain relaxation

To investigate the strain relaxation of Fe_3O_4 thin films grown at different temperatures, we used GPA to analyze fringe deformations obtained from HR STEM cross-section micrographs. **Figure 5.1** and **Figure 5.2** show HAADF-STEM images along the Fe_3O_4 [$11\bar{2}$] zone axis, along with the corresponding phase images, power spectra (FFT), deformation maps, and deformation profiles of samples grown with FeO template layer at 260°C and 400°C, respectively.

The HAADF-STEM images reveal the atomic arrangement of ZnO and Fe_3O_4 in the lower and upper parts of the image, respectively. In a HAADF image (Z-contrast) only the heavier elements are observed, O atoms are not visible. In addition, Zn atoms having a higher atomic number, appear brighter in the HAADF image than the Fe atoms. **Figure 5.1(b)** and **Figure 5.2(b)** display the FFT of the HAADF-STEM images. For the construction of the corresponding phase images presented in **Figure 5.1(c)** and **Figure 5.2(c),** we selected a mask in the power spectrum (the FFT image) that includes the ZnO($\bar{1}20$) and Fe_3O_4($4\bar{4}0$) reflections, corresponding to vertical planes in the image to quantify the *xx* deformation of these latter planes. As a reference for our analysis, we chose the substrate which have a well-defined lattice parameter.

The fringe deformation maps are presented in **Figure 5.1(d)** and **Figure 5.2(d)**, where we distinguish two homogeneous regions: green corresponds to the substrate (reference, no deformation) and blue corresponds to the film, which are separated by a sharp interface.

The measured deformation in this study is parallel to the $[1\bar{1}0]_{Fe3O4}$ axis (horizontal of the image); it corresponds to ε_{xx} strain. For both temperatures, the deformation value is around -8.6%, which perfectly corresponds to the nominal lattice mismatch between Fe_3O_4(111) and ZnO(0001), indicating that the film is fully relaxed on the substrate. The fact that we observe an abrupt jump in the deformation line profile from 0 to -8.6% immediately at the interface indicates that a full strain relaxation occurs within a distance of less than 5 Å. This result aligns well with the findings of Tian *et al.* [205] and Brück *et al.* [194], which have reported a full strain relaxation and bulk properties recovery of Fe_3O_4 within a distance between 2.5 Å and 5 Å from the interface Fe_3O_4//ZnO.

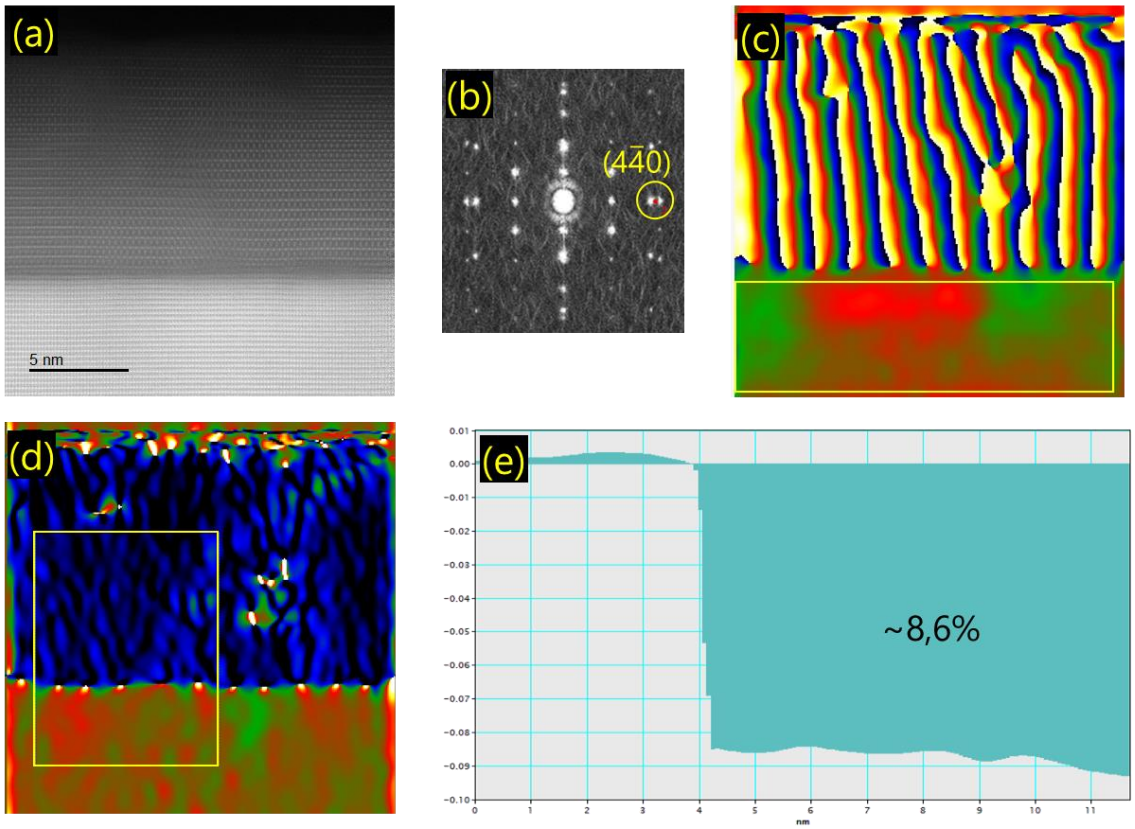

Figure 5.1 *(a) HAADF-STEM cross-section micrograph of Fe_3O_4 deposited on c-ZnO at 260°C taken along the Fe_3O_4 [11$\bar{2}$] zone axis, (b) Power spectrum, marked spot indicates the vector used to construct the phase image, (c) phase image obtained with GPA, yellow rectangle delimits the phase reference area, (d) deformation map, (e) deformation line profile integrated over the yellow rectangle in the deformation map*

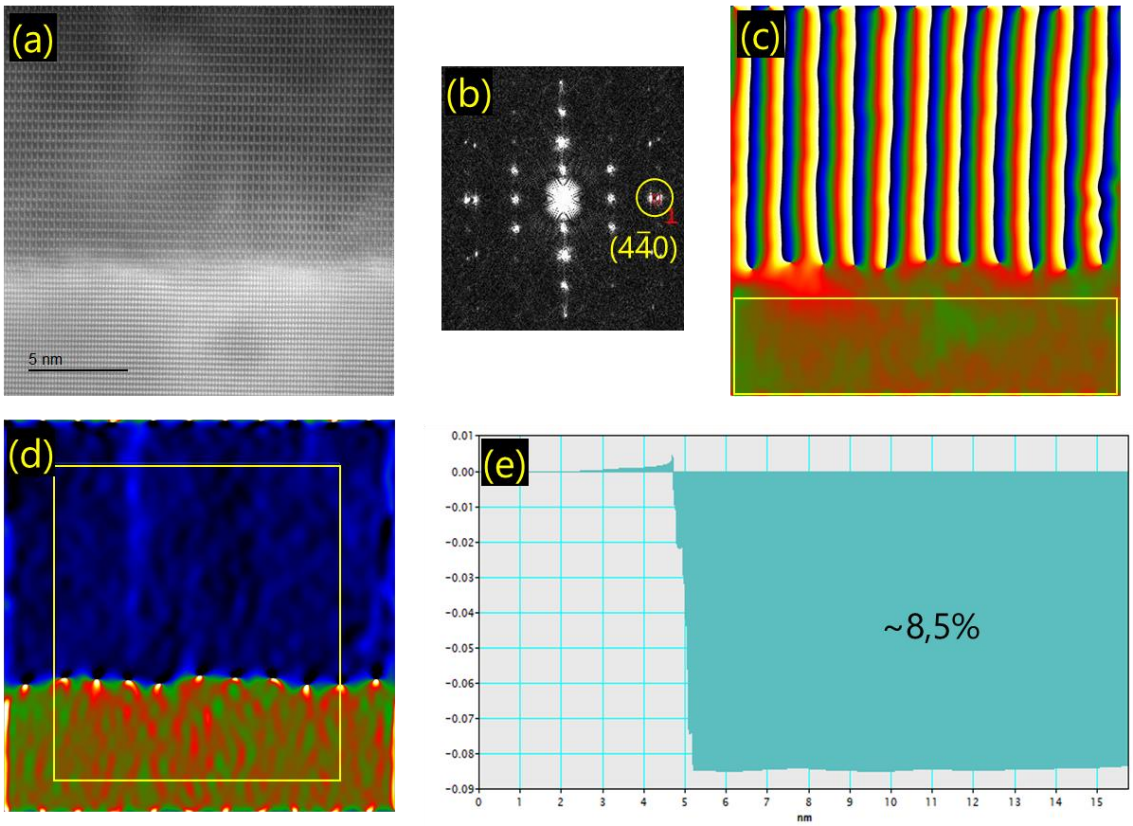

Figure 5.2 *(a) HAADF-STEM cross-section micrograph of Fe_3O_4 deposited on c-ZnO at* ***400°C*** *taken along the Fe_3O_4 [11$\bar{2}$] zone axis, (b) Fast Fourier Transform, marked spot indicates the vector used to construct the phase image, (c) phase image obtained with GPA, yellow rectangle delimits the reference area to measure the deformation, (d) deformation map, (e) deformation line profile integrated over the yellow rectangle in the deformation map*

On the deformation maps in **Figure 5.1** and **Figure 5.2**, we observe local points of intense deformation periodically distributed at the interface. To better visualize the phenomenon at these highly deformed regions, we construct the inverse fast Fourier transform (IFFT) of the HAADF-STEM image using the vector ***g*** (4$\bar{4}$0). **Figure 5.3** shows the IFFT obtained from the selected area in the HAADF-STEM image presented in **Figure 5.1(a)**, and the magnification around a high deformation region. Each point corresponds to a half atomic plane in the film, which lacks continuity in the substrate. It consists of misfit dislocations. relaxing the high mismatch of 8.6% between the film and the substrate

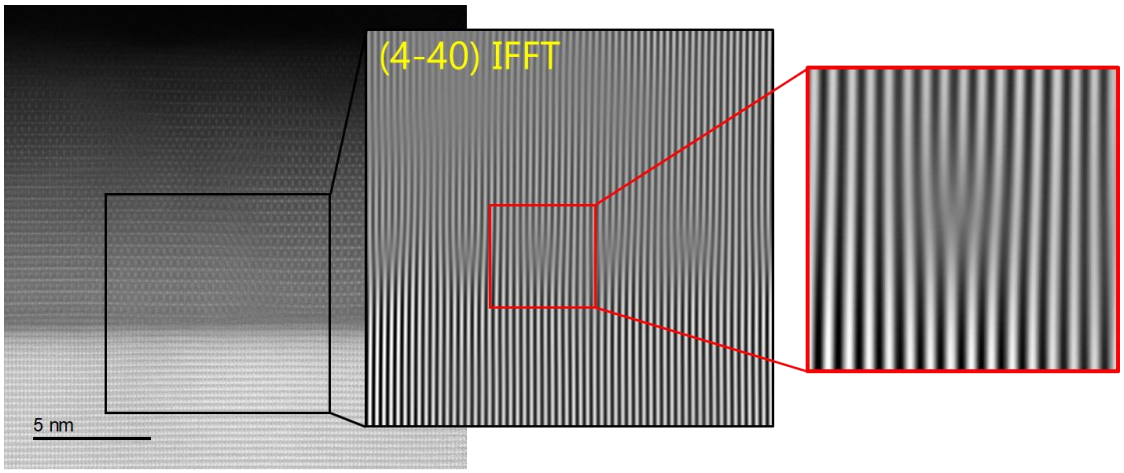

Figure 5.3 *from left to right: HAADF-STEM image taken along ZA [11$\bar{2}$] of Fe_3O_4, IFFT of the selected area on the HAADF-STEM image obtained using the vectors g $(4\bar{4}0)_{Fe_3O_4}$ and g$(\bar{1}20)_{ZnO}$, magnification of IFFT around region with high deformation in the deformation map presented previously*

To quantify the density of dislocations (the occurrence of dislocations per unit length along [10$\bar{1}$]), it is useful to construct the fringe rotation map using GPA, consistently utilizing the vectors g $(4\bar{4}0)_{Fe_3O_4}$ and g $(\bar{1}20)_{ZnO}$. The atomic planes of the film are parallel, except in the vicinity of a dislocation where the stress induces a minor rotation of the adjacent planes near its core. This effect is directly observable on the fringe rotation map calculated from the phase image, depicted in **Figure 5.4(a)**. Near each dislocation, positive and negative rotations (~5°) exist that correspond to the rotation of the adjacent atomic planes on either side of the dislocation.

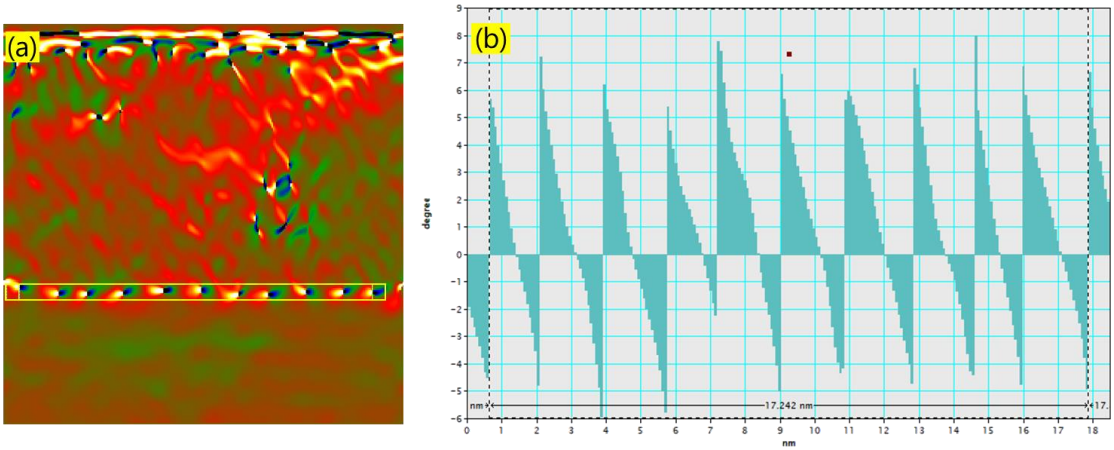

Figure 5.4 *(a) fringe rotation map calculated from HAADF-STEM image in Fig5.1(a), (b) rotation line profile integrated over the yellow rectangle in the rotation map*

Figure 5.4(b) shows the rotation line profile measured at the interface Fe_3O_4/ZnO. To determine the average inter-dislocation distance, we count the number of times the rotation

value changes sign from positive to negative, and we divide it by the distance over which these changes are measured. From this calculation we determine an average distance δ = 1.73 nm between the misfit dislocations at the interface. This value is achieved in the sample grown at 400°C on the miscut substrates.

The average distance between misfit dislocations can be theoretically estimated for a fully relaxed film using the following formula (5.1):

$$\delta = \frac{a_f \cdot a_s}{\Delta a} \qquad (5.1)$$

where a_f is the lattice parameter of the film, a_s is the lattice parameter of the substrate, and Δa is the difference in lattice parameters between the film and substrate [206]. This estimation is valid under the assumption that the film is fully relaxed, allowing for the use of bulk values for both materials. Hence, the lattice spacings that we consider for this calculation are the d-spacing of $Fe_3O_4(4\bar{4}0)$ and $ZnO(\bar{1}20)$. Considering bulk values for both materials $d_{Fe_3O_4\,(4\bar{4}0)}$ = 1.49 Å and $d_{ZnO\,(\bar{1}20)}$ = 1.63 Å, the resulting average distance between dislocations is 1.74 nm.

The experimental measured average inter-dislocation distance matches perfectly the theoretically estimated distance for a fully relaxed $Fe_3O_4(111)$ thin film on ZnO(0001) substrate, such agreement confirms the full strain relaxation of our samples.

5.3.Defects in Fe_3O_4 thin films: Twinning and APBs

Unlike an ideal single crystal with consistent crystalline orientations, an epitaxial thin film exhibits the same crystalline orientation within the film plane; however, it can contain domains with varying in-plane orientations. In our Fe_3O_4 thin films, the presence of two domains rotated by 180° is evidenced using TEM characterizations (was also demonstrated in chapter 4 using XRD φ-scan).

Figure 5.5 displays a HAADF-STEM cross-section image of Fe_3O_4 thin film taken along the $[1\bar{1}0]$ Fe_3O_4 zone axis. It shows two distinguishable domains separated with a boundary (twin boundary indicated with blue arrows) slightly tilted with respect to the growth axis (~15°).

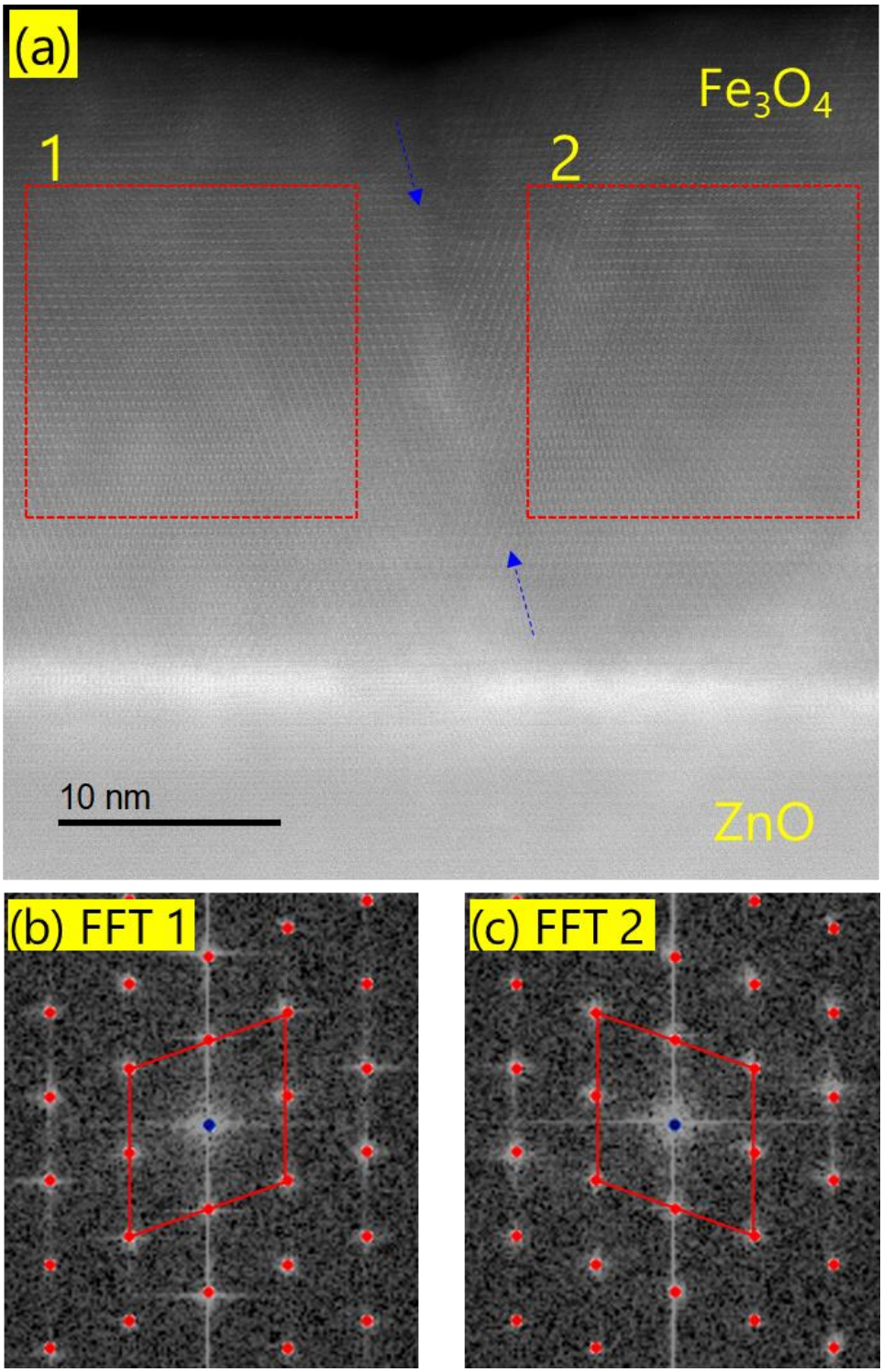

Figure 5.5 *(a)HAADF-STEM cross-section image of Fe_3O_4 thin film taken along [1$\bar{1}$0] showing two domains twinned with 180°, the twin boundary indicated with blue arrows makes 15° with the [111] axis, red squares defines the areas for which are presented the FFTs, (b) FFT of the selected area 1 situated in the left twin, (c) FFT of the selected area 2 situated in the right twin. Red dots in the FFT images represent the simulation of Fe_3O_4 diffraction for each twin*

The twin symmetry becomes evident when conducting a fast Fourier transform (FFT) on the HAADF-STEM image. **Figure 5.5(b)** and **Figure 5.5(c)** represent the FFTs of the area on each twin indicated with red squares 1 and 2 on the HAADF image. Red dots in the latter two figures represent the simulation of Fe_3O_4 electron diffraction along $[1\bar{1}0]$ zone axis. The presence of a twinning is characterized by a mirror image relationship between the diffraction patterns with a 180° rotation around the growth axis (vertical of the image).

Twinning in face centered cubic structures is a well-known phenomenon in particular in spinel structures [207]–[211]. In Fe_3O_4(111) thin films, it occurs as a result of a difference in atomic stacking sequence along the growth direction (ABCABC… and ACBACB…) during the initial growth of two different islands, which coalesce to form the twin boundary (TB) separating the two domains (see **Figure 5.6**). Across the twin boundary, there is a continuity of the 'A' layer every three stacks; however, the 'B' and 'C' layers are interchanged in one domain compared to the other. It is noteworthy that the TBs do not always lay in a high symmetry plane; as seen in **Figure 5.5**, the TB makes ~15° with the growth axis.

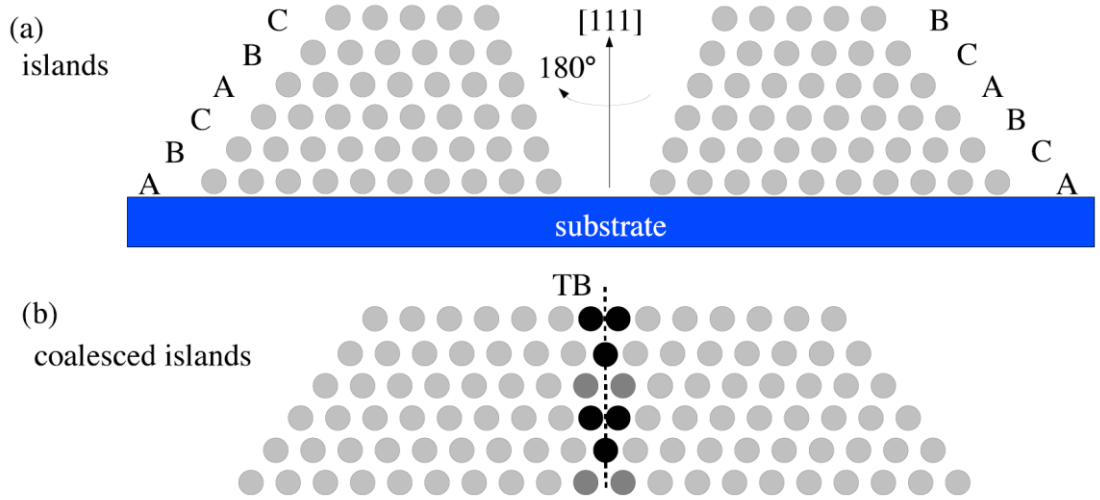

Figure 5.6 *schematic representation of (111) atomic planes sequence of 180° twinned domains, from [73]*

The magnetic coupling across the TB is insufficiently investigated in literature and there is no precise determination of the coupling nature. Only the TB with (111) twin planes are investigated. Chen *et al.* [108] suggested three types of (111) TBs, and the coupling can be either ferromagnetic or antiferromagnetic, depending on the TB type. In Fe_3O_4(111)/ZnO(0001) thin films, most of TB are oriented out of the growth plane due to the twinning origin (the initial nucleation of triangles on hexagons implies the rotation in the growth plane). Hence, thorough

quantitative and theoretical studies of atomic structure and magnetic coupling are necessary to identify the effect of twinning on the magnetic properties of Fe_3O_4 thin films.

The second type of defect is the anti-phase boundaries (APBs), which are confirmed to drastically affect the magnetic properties of Fe_3O_4 thin films. Due to the antiferromagnetic coupling across the APB, the reduction of magnetization and the slow approach to saturation was often attributed in literature to the presence of these defects in Fe_3O_4 thin films [21], [34], [77], [99], [212], [213]. In this section, we will illustrate the observed APBs in the analyzed cross-section samples, then in the next section, we will be interested in the quantitative study of the APBs density.

The identification of an APB requires the determination of its translation vector as well as of its plane. Seven translations for forming an APB are possible in the spinel structure which are listed in **Table 5.1** [94]. The translations vectors occurring within the (111) growth plane are referred to as "in-plane shifts", while the remaining shifts are denoted as "out-of-plane shifts".

Table 5.1 *possible APB translations in* Fe_3O_4

Out-of-plane shifts	In-plane shifts
R1 ¼[110] R2 ¼[101] R3 ¼[011] R4 ½[100]	R5 ¼[1$\bar{1}$0] R6 ¼[10$\bar{1}$] R7 ¼[01$\bar{1}$]

To investigate APBs in cross-section samples, we perform observations along the [11$\bar{2}$] zone axis of Fe_3O_4. **Figure 5.7(a)** shows a HAADF-STEM image illustrating one of the observed APBs in our films. We observe two domains, one on the left and one on the right of the plane boundary. **Figure 5.7(b)** schematizes the stacking sequence of Fe atoms on the left and the right of this APB, where the only difference between the two domains is a vertical shift of one domain with respect to the other. For this APB, it is clear that the boundary is perfectly perpendicular to the growth plane and parallel to the observation ZA (sharp boundary, no boundary enlargement is observed due to a potential tilt in the observation direction). One can deduce that the boundary plane is (1$\bar{1}$0). Nevertheless, this is not always the case; other APBs with different boundary planes were also observed. We present two cases; in **Figure 5.8**, an APB with ~50° tilt to the growth direction having a shift vector of ½[001] (or ¼[110]), and in **Figure 5.9**, a small domain on the right lower part of the film delimited with 'tilted' + 'horizontal' APBs, which correspond to a shift of ½[001] (or ¼[110]) + ¼[01$\bar{1}$].

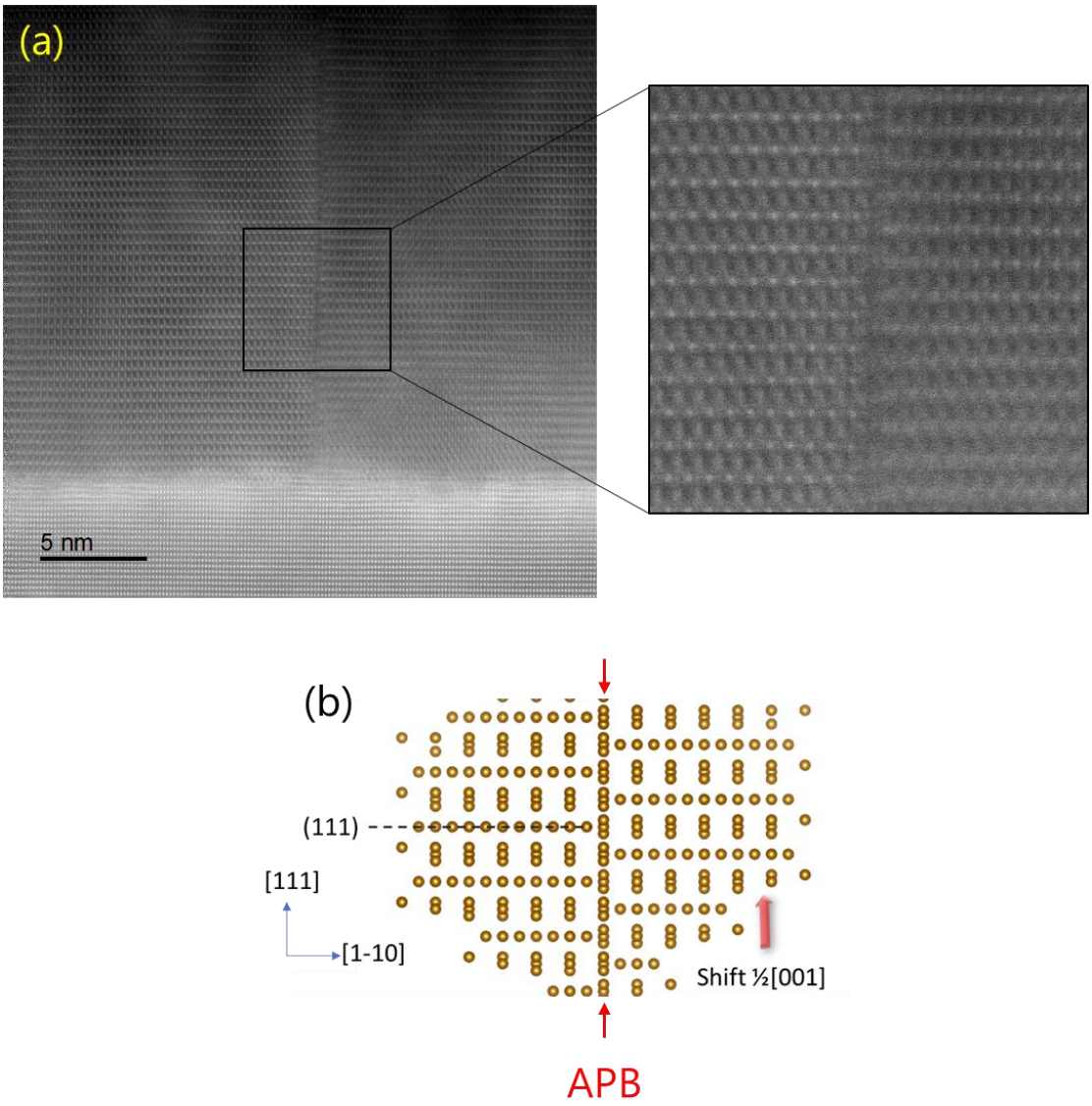

Figure 5.7 *(a) cross-section HAADF-STEM image illustrating an APB with ½[001] (or ¼[110]) shift and $(1\bar{1}0)$ boundary plane, (b) schematic representation of Fe atomic structure of the present APB.*

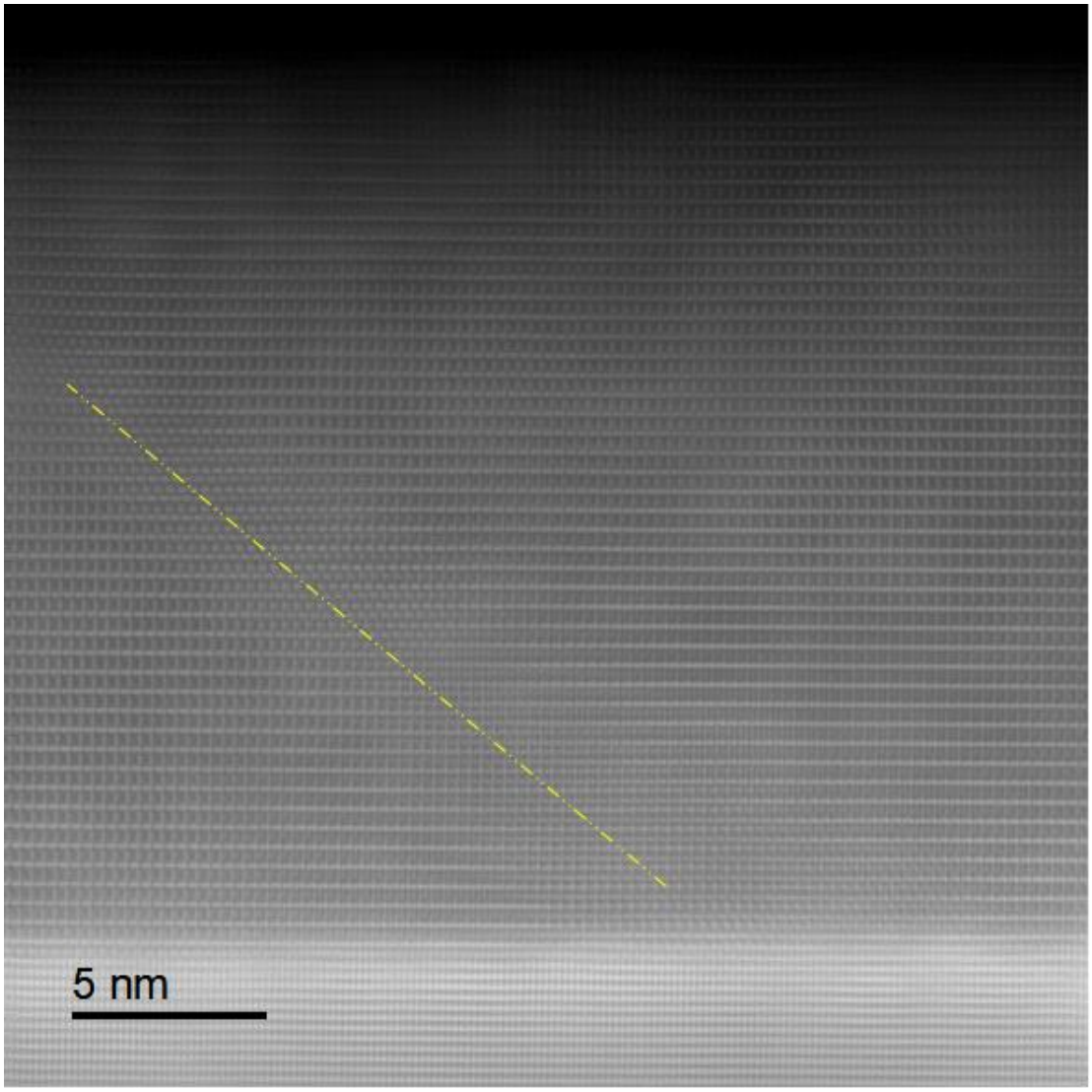

Figure 5.8 *illustration of APB tilted ~50° with respect to the growth direction*

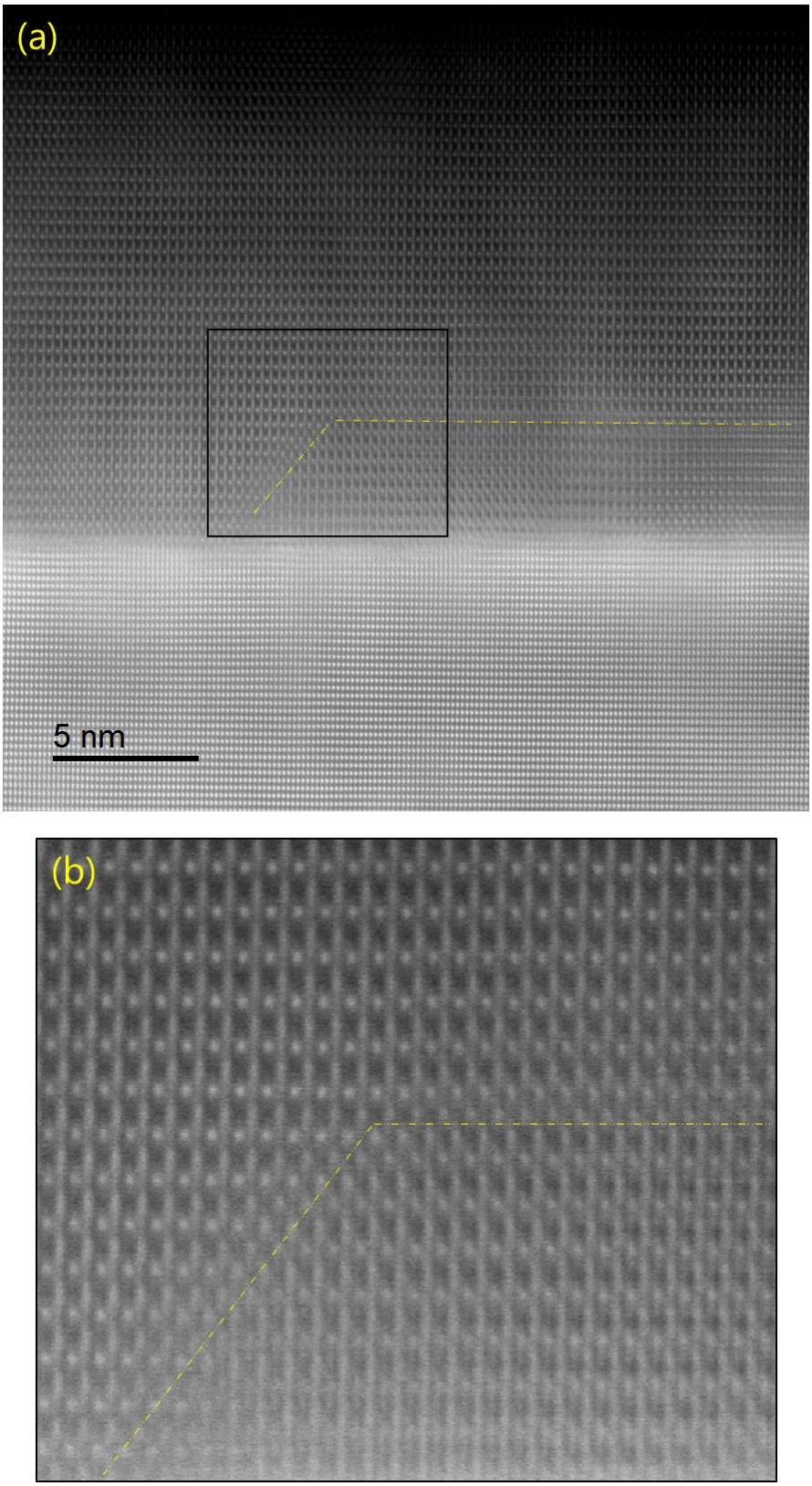

Figure 5.9 *(a) illustration of domain delimited with two APBs one horizontal (parallel to (111) plane) and one making ~50° with the [111] axis of the film, (b) zoom around the black rectangle*

The last APB example we illustrate is a curved APB (**Figure 5.10(a)**). The displacement of (111) planes is measured using GPA as 0.24 nm (**Figure 5.10(b)**), which corresponds to the projection of ½[001] (or ¼[110]) on the [111] axis.

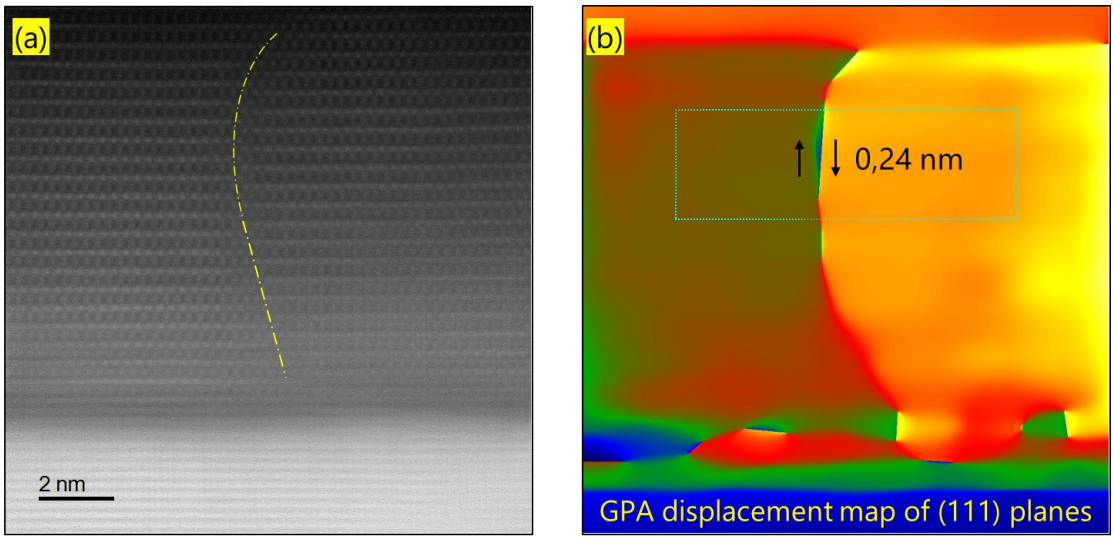

Figure 5.10 *(a) example of a curved APB, (b) GPA fringe displacement map reveals a 0,24 nm displacement of (111) atomic planes across the APB*

To observe APBs on a larger scale, we conducted dark-field TEM imaging using g(111) which allows the visualization of APBs with a shift parallel to the growth axis [111]. **Figure 5.11(a)** and **Figure 5.11(b)** shows the obtained DF images for two samples grown at 260°C and 400°C respectively. In both samples we observe vertical and curved APBs separated by several tens of nanometers.

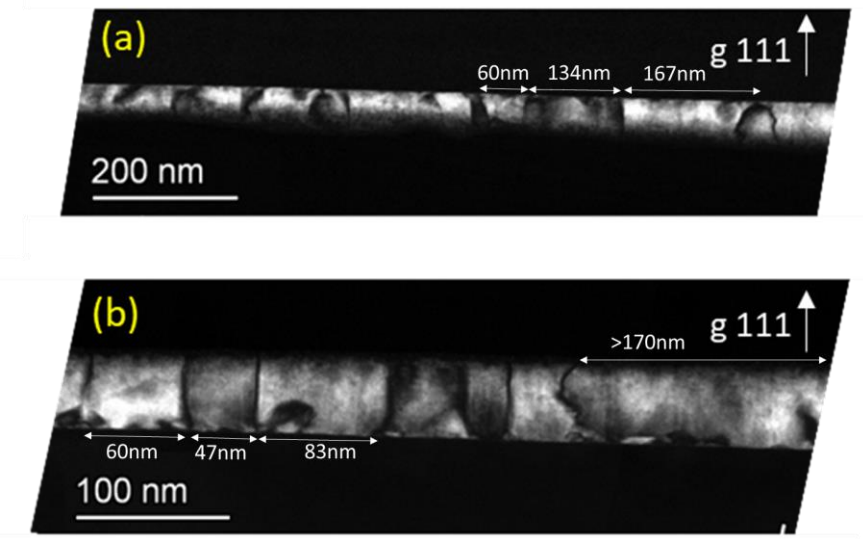

Figure 5.11 *Dark-Field TEM images obtained using g(111) for (a) 260°C and (b) 400°C grown samples, arrows indicate the lateral size of some antiphase domains*

In summary, we have spotlighted defects such as twin and antiphase boundaries in our Fe_3O_4 thin films. We demonstrated that these boundaries do not necessarily lay in high symmetry planes, and can even manifest as curved boundaries. Furthermore, our observations indicate that a shift of ½[001] and/or ¼[110] primarily characterizes the observed antiphase boundaries in the cross-section along the $[11\bar{2}]$ zone axis.

5.4. APBs density

We mentioned in the previous section that seven crystallographic shifts were identified to possibly form an APB. A study by McKenna *et al.* [101] has shown that the energetically favorable APBs in the Fe_3O_4, are the {110} APBs characterized by the translation ¼[110] (the most stable), then the ones characterized by ¼[110] + ¼$[1\bar{1}0]$ with higher formation energy, and confirmed that magnetic coupling is antiferromagnetic across both of these APBs.

An analysis of larger TEM images is required to investigate the density of APBs and establish a correlation with the magnetic properties of our samples. The cross-section observation revealed antiphase domains with different boundary planes; nevertheless, the number of observed APBs is restricted due to the necessity for high-resolution images. To overcome this limitation, we proceed with analyzing plane-view images captured along the Fe_3O_4 [111] zone axis.

Two methods can be followed to investigate the APBs in the plane view images:

(i) **Dark-Field TEM imaging**: Since the majority of the APBs are expected to be in {110} planes due to their energetic stability [101], by selecting one of *g* {220} reflections to capture a DF-TEM image, all the APBs having shift vector perpendicular to *g* will be out-of-contrast. Consequently, only two-thirds of the APBs will be observed on the DF image (if we assume that the APBs are equally present in {110} planes). This method was previously used in several works [62], [94], [95], [199], [201], [214]

(ii) **ADF-STEM imaging**: As we will demonstrate, the APBs are clearly observable on the ADF-STEM images which exhibit distinct crystallographic contrast. Our prepared samples for the plane-view observations were thinned enough to have observation regions containing only the Fe_3O_4 film. Unlike DF images, in ADF images, all the APBs {110} are detected. The disadvantage of this method is that other crystallographic defects might also appear.

The focus in this section is on the samples named in **Table 4.1** as 'B1' and 'B2', which were deposited on ZnO (0001) substrates with 1° miscut toward [11$\bar{2}$0]. Sample B1 consists of Fe_3O_4 directly deposited on the substrate, while sample B2 is Fe_3O_4 grown on 1 nm of FeO template layer deposited on the substrate. The objective is to investigate the role of the FeO template on the APB density.

5.4.1. Dark-Field TEM imaging

Figure 5.12(a) shows the diffraction patterns taken along [111] zone axis of the plane-view of the samples B1. We observe strong diffraction spots hexagonally distributed around the direct beam, showing the six-fold symmetry around the [111] zone axis. The absence of double diffraction phenomena frequently observed in plane-view observations confirms that the observed lamellas consist only of the film with no evidence of electron diffraction by the substrate. Electron diffraction patterns of Fe_3O_4 simulated using JEMS software suggest that all the diffraction spots belong only to the Fe_3O_4 phase, excluding other iron oxide phases, and confirm again the excellent quality of our samples (same result is obtained for the sample B2).

To capture DF images of the APBs, we set up in the two-beams conditions to have mainly two intense spots: the transmitted beam and one of the diffracted beams that are circled in red. The obtained micrographs are displayed in **Figure 5.12(b)**, **Figure 5.12(c),** and **Figure 5.12(d)**. The APBs are oriented at 60° angles to each other, aligning exclusively with $(1\bar{1}0)$, $(10\bar{1})$, and $(01\bar{1})$ atomic planes.
Considering the extinction condition for DF-TEM imaging: $g \cdot R = 0$ or n; where g is the active diffraction and R is the shift vector of the APB, we can establish the extinction criteria of these defects, which are summarized in **Table 5.2**.

From **Table 5.2**, it is evident that APBs with a ½[100]-type shifts (R4) consistently appear out of contrast in the (111) plane-view DF-TEM micrographs. This absence of contrast can be attributed to the fact that these APBs do not disrupt the atomic periodicity within the (111) atomic planes. As for the ¼ <110> APBs, only two-thirds are in contrast in each micrograph. It is important to note that distinguishing between APBs of R1 and R5, R2 and R6, and R3 and R7 is not possible because they have the same extinction criteria.

Table 5.2 *extinction criteria of APBs as function of the diffraction conditions "g", and "R" the shift vector of the APB*

	Visibility of APBs						
g \ R	R1 ¼ [110]	R2 ¼ [101]	R3 ¼ [011]	R4 ½ [100]	R5 ¼ [1$\bar{1}$0]	R6 ¼ [10$\bar{1}$]	R7 ¼ [01$\bar{1}$]
($\bar{2}$02)	visible	extinct	visible	extinct	visible	extinct	visible
(0$\bar{2}\bar{2}$)	visible	visible	extinct	extinct	visible	visible	extinct
(2$\bar{2}$0)	extinct	visible	visible	extinct	extinct	visible	visible

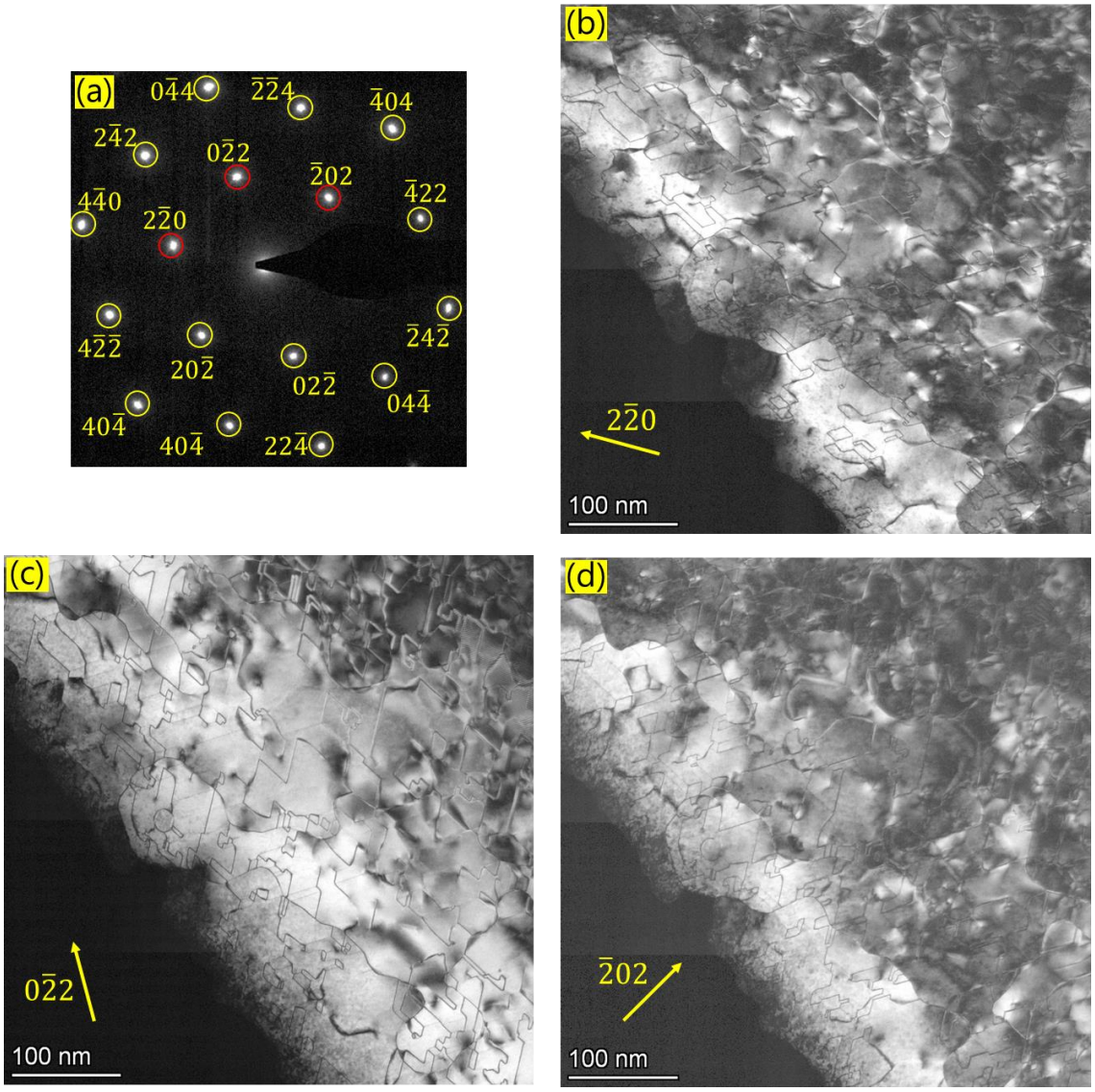

Figure 5.12 *(a): electron diffraction patterns of samples B1 taken in plane-view ([111] ZA of Fe_3O_4), (b), (c), and (d): dark-field TEM micrograph in plane-view on the samples B1, taken by selecting the (2$\bar{2}$0), (0$\bar{2}\bar{2}$), and ($\bar{2}$02) diffraction spots, respectively*

To compare the samples B1 and B2 we illustrate DF-TEM images obtained using $g(2\bar{2}0)$ in **Figure 5.13(a)** and **Figure 5.13(b)**. Qualitatively, the DF-TEM images appear to be very similar. For a quantitative estimation of the APB density, one must analyze at least two DF

images obtained from two different 220-reflections for the same micrograph and consider excluding the APBs observed multiple times.

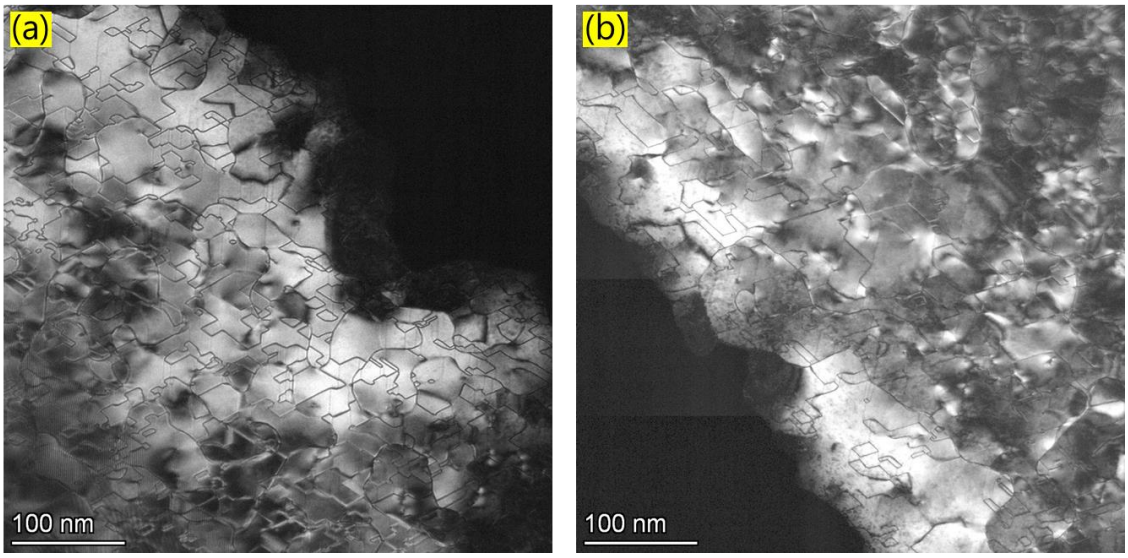

Figure 5.13 *DF-TEM micrograph in plane-view (ZA [111] of Fe_3O_4) of (a): sample B1and (b): sample B2, taken using $(2\bar{2}0)$ diffraction spot*

To simplify the work, we have chosen to proceed with analyzing ADF-STEM micrographs since the lamellas are perfectly prepared to observe only the film.

5.4.2. ADF-STEM imaging

Figure 5.14(a) and **Figure 5.14(b)** show the ADF-STEM micrographs of samples B1 and B2, respectively, taken along [111] Fe_3O_4 zone axis. It is important to underline that only the Fe_3O_4 film is observed in these images.

Both samples are marked by the presence of curved lines with higher contrast that we did not observe in the (220) DF-TEM images. Under our measurement conditions (camera length, detection angle), the presence of such lines indicates the presence of crystallographic defects such as domain boundaries. Notably, the absence of these defects in the DF-TEM micrographs indicates that they do not arise from translations within the (111) plane.

Higher magnification ADF-STEM micrographs of the two samples are presented in **Figure 5.15(a)** and **Figure 5.15(b)**. In addition to curved defect, straight ones are now detectable; they delimit smaller domains than the ones defined by curved defects. These straight lines are predominantly well-defined and structured in a specific pattern making precisely 60° between each other, corresponding to the angle between {110} planes. Compared to curved defects, straight defects are typically sharp. This sharpness can be attributed to the fact that these defects

are parallel to the observation axis, unlike curved defects that may be inclined with respect to the observation axis.

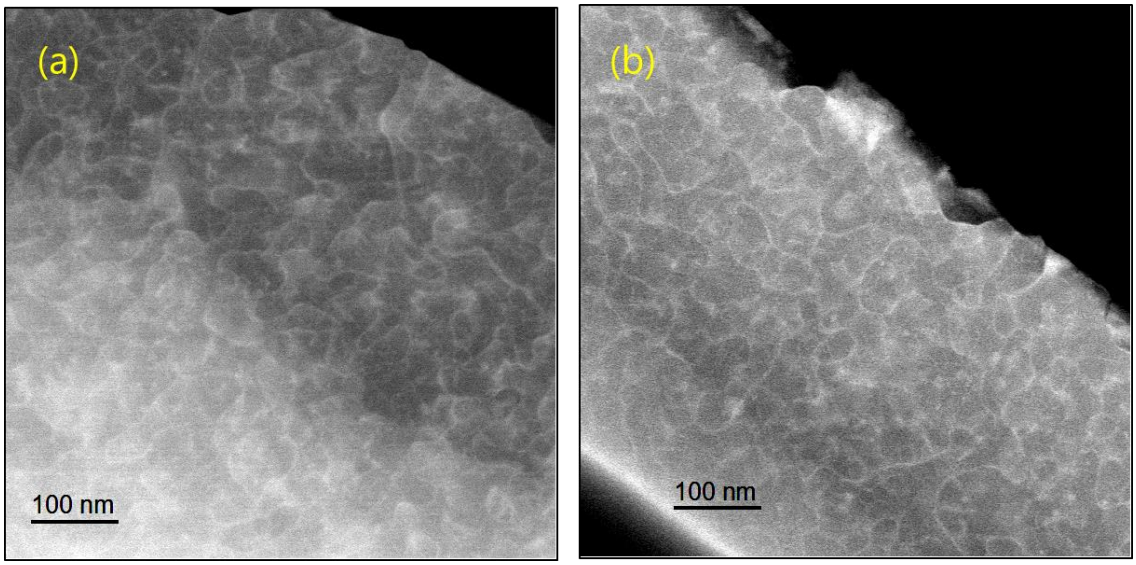

Figure 5.14 *ADF-STEM plane-view (// [111]) micrographs of (a): sample B1, and (b): sample B2.*

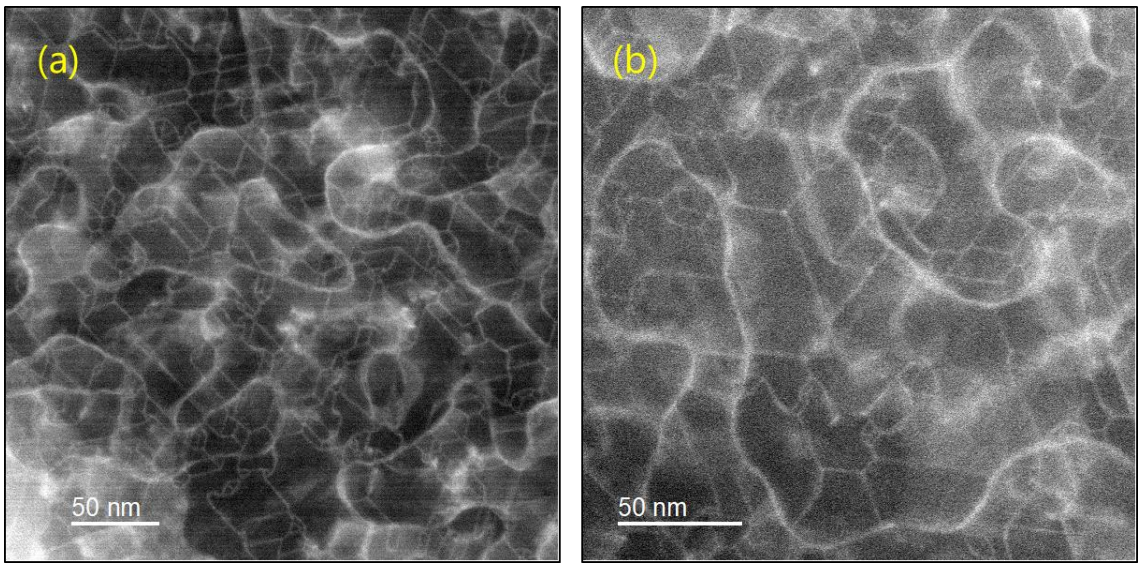

Figure 5.15 *ADF-STEM plane-view (// [111]) micrographs of (a): sample B1, and (b): sample B2*

In order to better understand the nature of the defects observed in the previous figures, we carried out high-resolution analysis to identify their displacement fields.

5.4.2.1. Straight defects: APBs

Figure 5.16(a) shows a high-resolution ADF-STEM micrograph focused on a straight defect. Using FFT, we index the atomic planes and reach out that this defect is in the $(1\bar{1}0)$ plane.

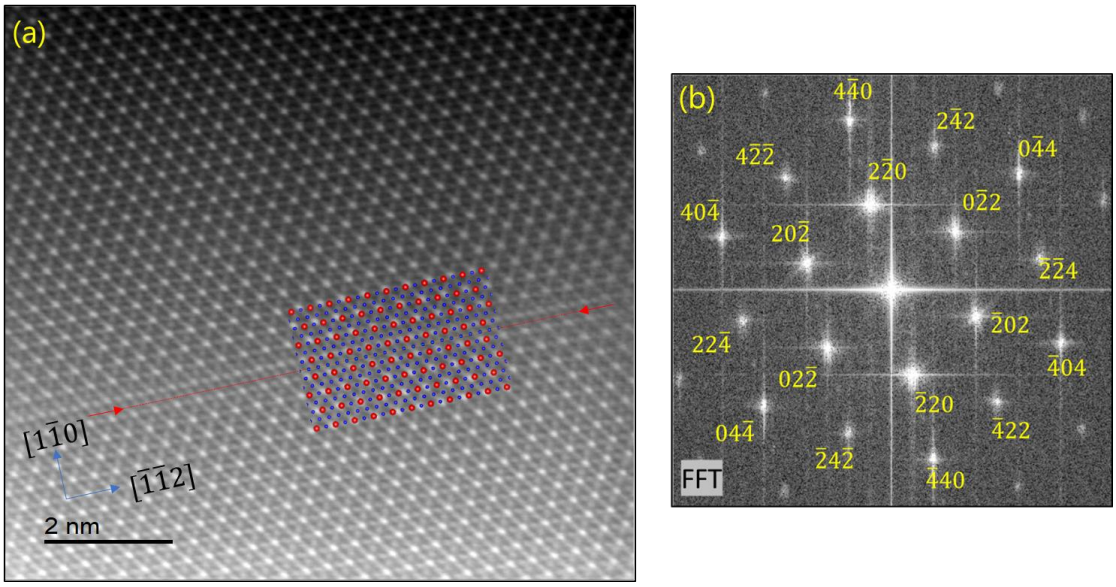

Figure 5.16 *(a) ADF-STEM Fe_3O_4 plane-view micrograph of straight defect (APB) in $(1\bar{1}0)$ plane, the sketch on the image is the projection of the atomic arrangement of Fe_3O_4 along [111] where the blue dots represent atomic columns composed of Fe_{oct} and red dots represent atomic columns comosed of Fe_{oct}+ Fe_{tetra} , (b) the correspponding FFT of the ADF image*

Figure 5.17(a) and **Figure 5.17(b)** show a lower magnification ADF-STEM micrograph of the above-presented defect and the corresponding FFT of the micrograph, respectively. We used GPA to determine the shift value related to this defect. We selected the frequencies circled in red on the FFT image (denoted as **1**, **2**, and **3**): $(2\bar{2}0)$, $(20\bar{2})$, and $(0\bar{2}2)$, respectively; to generate phase images from the ADF-STEM image. The analysis results are summarized in **Figure 5.18.** The extinction criteria of defects are similar to the DF images mentioned earlier.

The phase images obtained from the spots **1** and **3** show two domains separated with a sharp interface, and the one obtained from the spot **2** shows a more homogenous phase image. The displacement value is measured around 0.16 nm for spots **1** and **3**, while no displacement is measurable from spot **2**. These values represent the projection of the translation vector characterizing this APB on the normal of the investigated atomic planes. A value of 0.15 nm represents precisely the projections of the ¼$[1\bar{1}0]$ shift vector onto $[0\bar{1}1]$ and $[10\bar{1}]$, while the projection onto $[1\bar{1}0]$ is null because the vectors are parallel. In this case, the shift vector is perpendicular to the boundary plane.

Another shift that can be responsible for such APBs is the ¼[110], which is in the boundary plane $(1\bar{1}0)$. Both shifts exhibit the same atomic structure when viewed along the [111] zone axis. Hence, to distinguish between these two shifts, a cross-section observation is necessary. In the case of the shift ¼$[1\bar{1}0]$ (perpendicular to $(1\bar{1}0)$ APB), the (111) atomic planes are

undisturbed, while in the case of the shift ¼[110] (in the $(1\bar{1}0)$ APB), the (111) atomic planes are displaced with ½d_{111} across the APB.

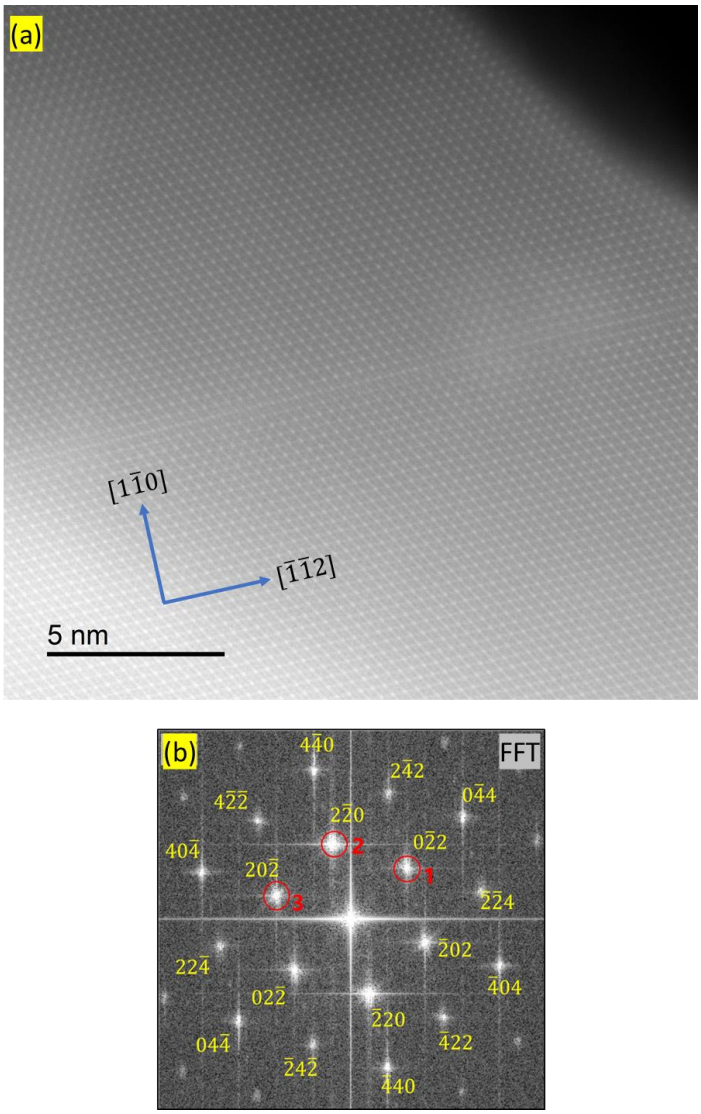

Figure 5.17 *(a) ADF-STEM plane-view micrograph of straight defect (APB) in the $(1\bar{1}0)$ Fe_3O_4 plane, (b) the corresspponding FFT*

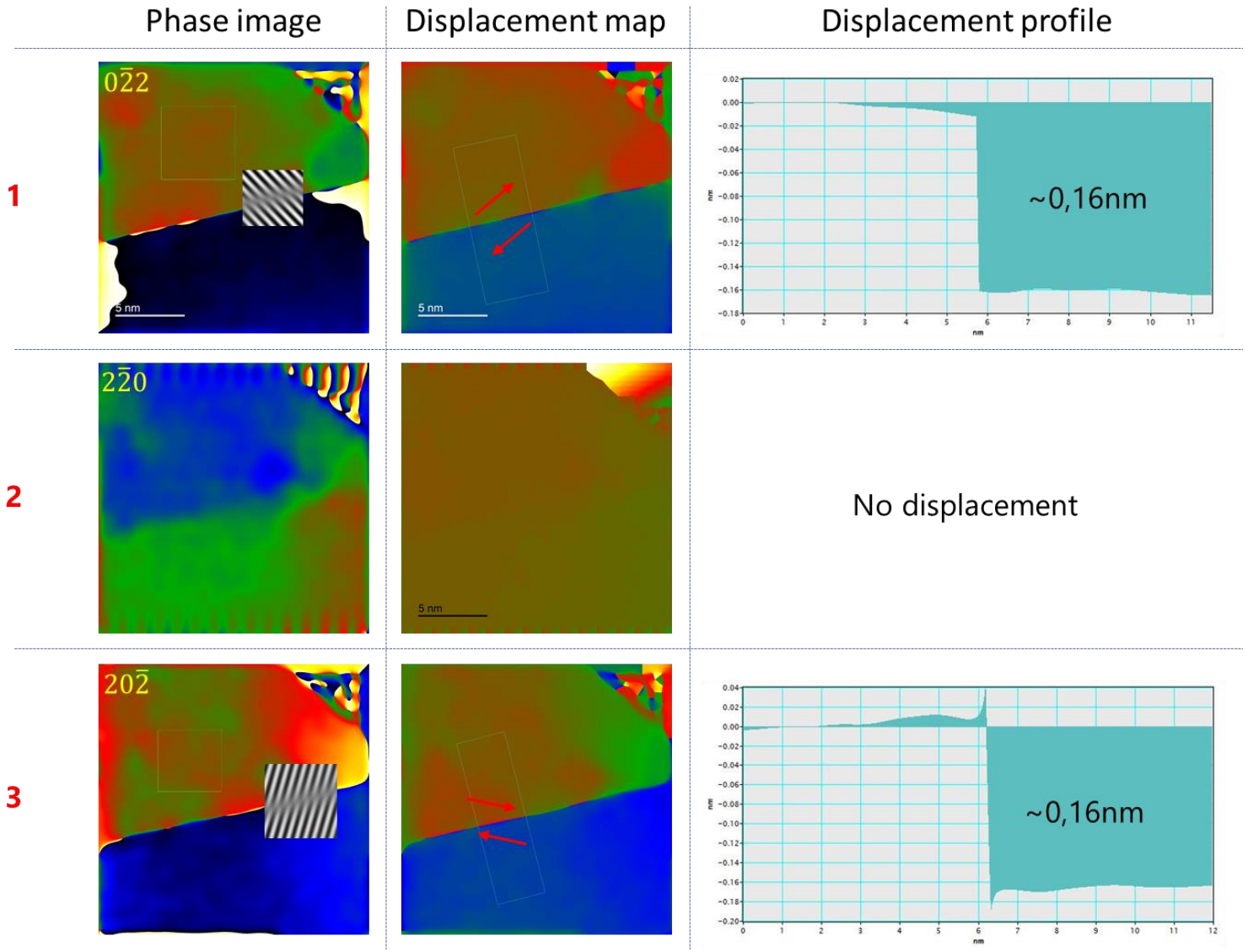

Figure 5.18 *GPA phase images (gray inset represents the corresponding IFFT magnified around the defect), displacement maps (red arrows indicate the displacement directions), and displacement profiles related to the APB presented in Figure 5.17(a). Numbers 1, 2, and 3 refer to the vector g used to obtain the phase image (mentioned in figure 17(b))*

The atomic structure of the APB we obtained experimentally using ADF-STEM matches the atomic structure of an APB simulated by McKenna *et al.* (**Figure 5.19(b)**) [101] which is characterized by a boundary plane (110) and shift vector of ¼[110].

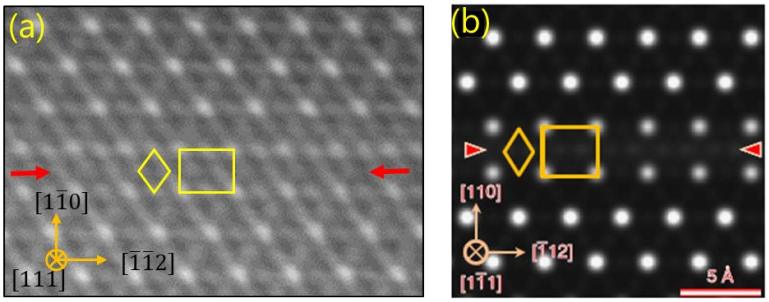

Figure 5.19 *(a) magnification around the APB presented in figure 16: (1$\bar{1}$0) boundary plane with a shift vector of ¼[110] (or ¼[1$\bar{1}$0]), (b) HAADF-STEM image simulation of the atomic structure of a similar APB from [101]*

All the APBs with straight feature are oriented making 60° between each other as we show in **Figure 5.20**. They lay mainly in (1$\bar{1}$0), (10$\bar{1}$), and (01$\bar{1}$) planes. Same GPA analyses have been carried out to characterize the (01$\bar{1}$) and (10$\bar{1}$) APBs. The displacements of domains always correspond to the projection of ¼{110} translation vectors.

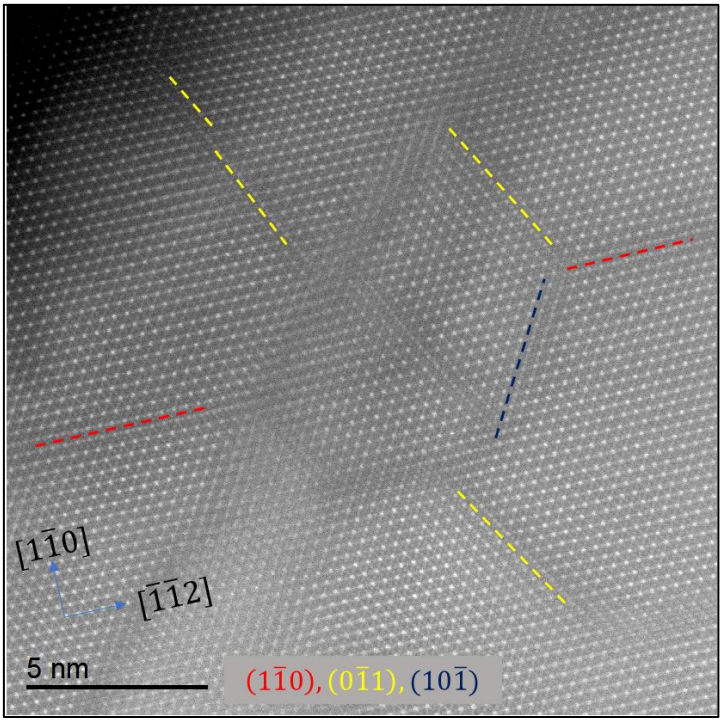

Figure 5.20 *{110} APBs network in plane-view ADF-STEM image taken along [111] zone axis of Fe_3O_4*

5.4.2.2. Curved defects & other straight defects

By analyzing around 10 micrographs, four types of defects were observed in both samples. In the previous section, we discussed the {110} APBs, which represent the majority of straight defects; however, some other defects do not lay within the {110} planes. Additionally, there are curved defects that define domains larger than ones defined straight defects.

We chose to present the HAADF-STEM micrograph in **Figure 5.21**, which illustrates a network of defects bringing together the four observable cases in our samples. In the figure, we name **A** and **B**, the straight defects, and **C** and **D**, the curved ones.

The HAADF-STEM image shows that A and C are sharp lines with almost the same contrast as the domains on either side, only with different atomic structures, while B and D appear to be darker and relatively larger than the defects A and C. This broadening can be explained by the fact that these defects are planar defects inclined with respect to the axis of the observation.

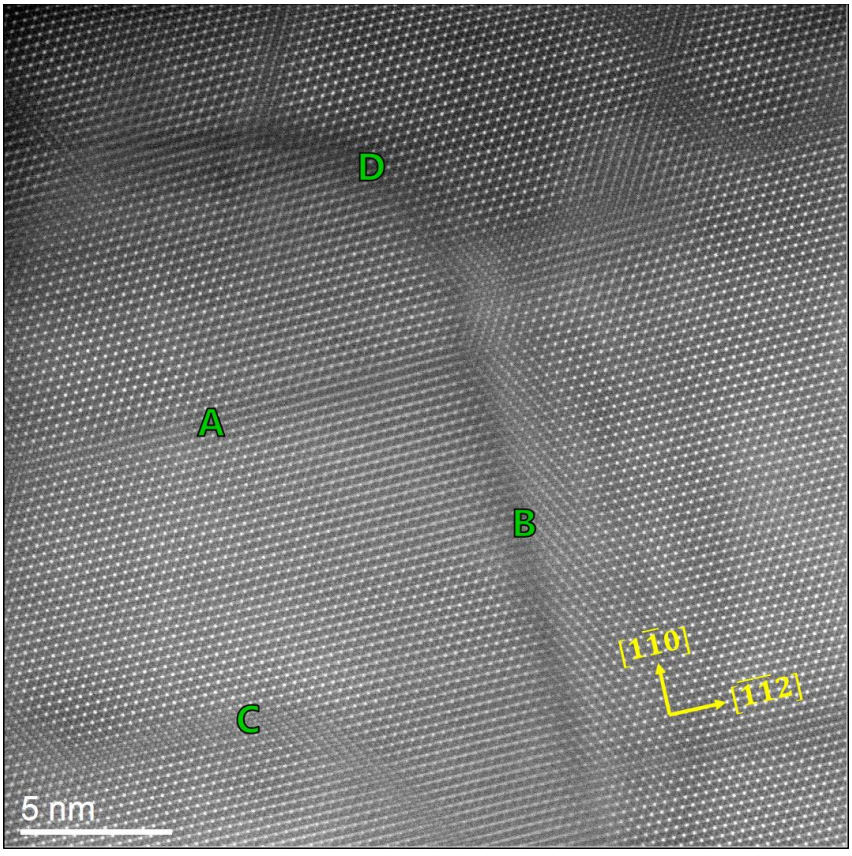

Figure 5.21 *HAADF-STEM image observed in plane-view (// [111]) illustrating the straight defects A and B, and curved defects C and D*

Similarly, we use the GPA technique to identify the translations between corresponding to defects **A**, **B**, **C**, and **D**. Details are presented in **Figure 5.22**.

By selecting the spot $(0\bar{2}2)$ on the FTT image, the phase image shows two domains that we denote as A1 and A2. They are separated with defect **A**. Displacement of 0,15 nm between A1 and A2 is estimated from the fringe displacement map. This defect (**A**) is observable again on the phase image obtained using the spot $(20\bar{2})$ with a displacement of 0,15 nm. It is a $(1\bar{1}0)$ APB with ¼$[1\bar{1}0]$ shift, similar to the one described in the previous section.

The phase image obtained from the FFT spot $(2\bar{2}0)$ highlights the defect **B**. The orientation of **B** does not align with any of the {110} planes, but is parallel to $(11\bar{2})$.
Even though defect **B** seems to continue to the bottom of the image, only the upper part of the domain B2 is shifted with 0,15 nm with respect to the domain B1. The same observation is achieved when we take the spot $(20\bar{2})$. We conclude that **B** is composed of two parts: the upper part corresponds to an APB with a shift of ¼$[01\bar{1}]$, which, based on the broadening observed on the HAADF-STEM image, appears to be an inclined APB; and the lower part which exhibit any shift or displacement between the domains. It has to be noted that in that case, unlike the APBs in the {110} planes, the shift vector of **B** does not lie within the APB nor is it perpendicular to the APB.

Now we discuss the curved defects. The defect **C** separates two domains with a displacement of ~ 0,15nm on the phase images obtained using $(2\bar{2}0)$ and $(20\bar{2})$, while it is not observable on the one obtained using $(0\bar{2}2)$ (only one domain A1). These displacements correspond to a shift of ¼$[01\bar{1}]$, similar to the one characterizing straight APBs. However, the atomic structure of the boundary might be different since the domain boundary does not follow one of the {110} planes. Further studies would be required to determine the nature of the magnetic coupling across such kinds of boundaries.

No in-plane translation is associated with defect **D**. This is consistent with DF images where most curved defects are out-of-contrast.

To summarize, our analysis of ADF and HAADF STEM plane-view images has revealed the presence of defects that can be categorized into two distinct types: those associated with translation vectors of ¼<110> (APBs) and others without such translations. Notably, all the observed APBs share a common type of translation vector, predominantly aligning with {110} planes, with some instances occurring within $\{11\bar{2}\}$ planes. Furthermore, in the analyzed micrographs, we have also identified defects that appear to exhibit curvature. Our investigation

suggests that these curved defects may possibly correspond to APBs with ¼<110> translation vectors. However, it's important to note that some of these curved defects do not exhibit the characteristics of APBs. Instead, they may represent interfaces resulting from the coalescence of islands, a phenomenon often associated with heteroepitaxy such as twin boundaries that were highlighted in the cross-section micrographs.

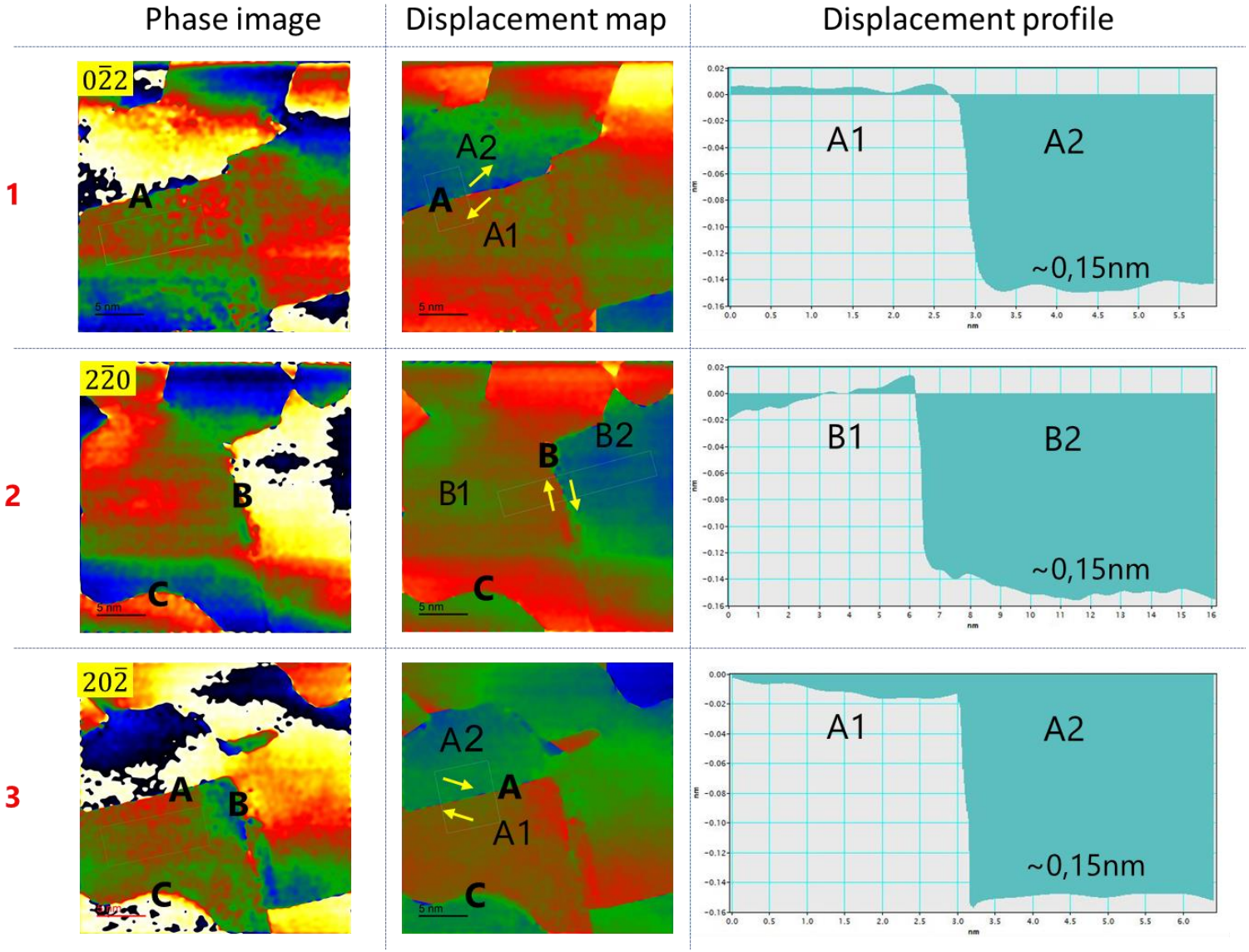

Figure 5.22 *GPA analysis of translations related to the defects named A, B, C, and D in the figure 5.21. Numbers 1, 2, and 3 in red on the left refer to the vectors g used construct the phase image (identical to figure 5.17(b)). A1, A2, B1, and B2 in fringe displacement maps refer to the domains separated by a defect A and B respectively, and the shift between direction between each two domains is indicated with yellow arrows on the displacement maps. Lined profiles show the displacement value between domains 1 and 2 in each case*

5.4.3. Quantification of defects density in HR-STEM plane-view images

The difference in the ratio Mr/Ms values when measured along $[10\bar{1}0]$ or $[11\bar{2}0]$ reveals a different anisotropy from one sample to the other when we compare the samples B1 and B2 (55% vs 46% for sample B1 against 57% vs 51% for sample B2). The density of APBs is reported to be sensitive to the thickness of the sample and the temperature [94], [199], and since these samples are deposited at the same temperature and have the same thickness (~85nm), the only parameter possibly affecting APB density is the growth of Fe_3O_4 on the FeO template layer in the sample B2. Although the FeO was not detected with HR-STEM cross-section imaging, it may have an effect on the APB density since the nucleation of these defects occurs at the very first deposited monolayers just before the oxidation of our FeO template (we confirmed with RHEED monitoring that the FeO exist till the beginning of Fe_3O_4 growth).

While most of the defects observed in ADF-STEM images are {110} APBs, which are known contributors to the reduction of magnetization, distinguishing between curved APBs and other curved defects proves challenging. Therefore, we have opted to focus on quantifying the total sum of all defects. Our chosen criterion for comparison is the length of the lines representing defects (both straight and curved) per unit area. This characteristic length serves as a measure similar to what was used to compare APB density in the thesis of A. Bataille, utilizing DF-TEM imaging [48]. It's important to note that while the impact of APBs in {110} planes on Mr/Ms is well-established, the effects of other defects remain not understood. Nevertheless, our approach allows us to quantify all defects by measuring their length per unit area

Implementing an automated procedure for detecting lines in ADF-STEM images presents significant challenges due to variations in image details and resolution and the presence of defects that vary in width, which can be measured twice in an automated algorithm. Despite requiring considerable time and effort, a practical approach involved manually reproducing the defect network on a transparent paper, followed by density measurement using image processing software. **Figure 5.23(a)** displays an example of the analyzed ADF-STEM images. When required, an FFT bandpass filter was applied using ImageJ software to accentuate the defects and distinguish the lines in the image (see **Figure 5.23(b)**). The defects are then manually redrawn on a transparent paper from the filtered image and skeletonized using Fiji software [215] to obtain the image used for the line length quantification displayed in **Figure 5.23(c)**.

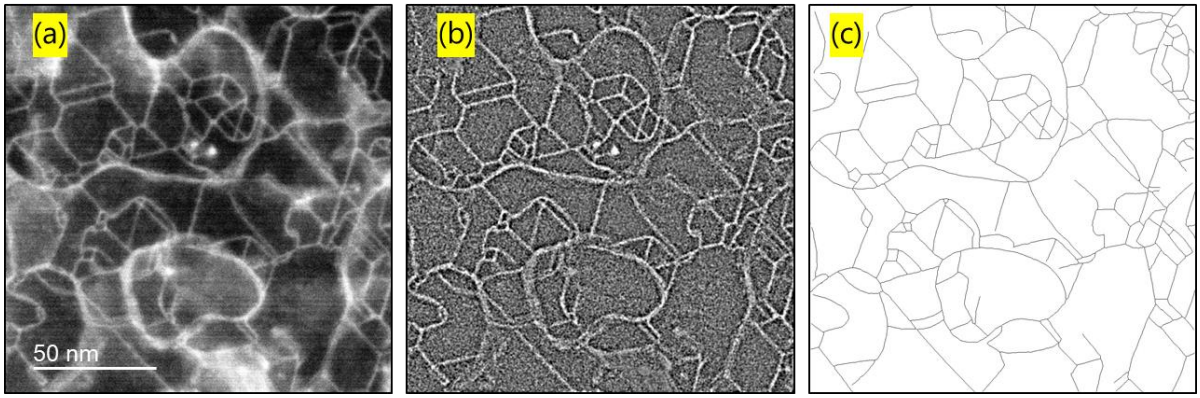

Figure 5.23 *steps of the quantitation of line defects density. (a) raw HAADF-STEM image, (b) same image filtered using FFT bandpass filter, (c) lines drawn from the filtered image and skeletonized using ImageJ software*

The function "Ridge Detection" available in the library of Fiji (version of ImageJ), allows a very accurate measurement of the line length from the skeletonized image. Results obtained from images of different sizes are listed in **Table 5.3**. (Images are available in the Appendix)

Table 5.3 *average length per unit area of the defects observed on the HAADF-STEM images of samples B1 and B2*

		Surface (nm^2)	Line length (nm)	Line density (nm^{-1})	Average density (nm^{-1})
Sample B1	Image 1	98665	11592	0,12	0,12
	Image 2	49233	5952	0,12	
	Image 3	24441	3248	0,13	
Sample B2	Image 1'	60723	5507	0,09	0,10
	Image 2'	48985	5135	0,10	
	Image 3'	30175	3289	0,10	

Characteristic lengths of defects per surface unit of 0.12 nm^{-1} and 0.10 nm^{-1} are measured for samples B1 and B2, respectively. Compared to what has been reported in the literature about "APBs density", smaller values of APB length per unit area were measured in Fe_3O_4(111) films grown on Al_2O_3(0001), as the value of 0.05 nm^{-1} was assigned to a film of a thickness of 50nm [199], relatively thinner than our films, for which one would expect more APBs. This difference may be attributed to disparities in growth conditions between our study and the reference study. Notably, variations in nucleation conditions, such as temperature or substrate miscut, may have led to differences in the formation of nucleation islands. It is conceivable that a higher number of nucleation islands, influenced by factors like temperature or substrate surface properties, could potentially result in a greater density of APBs. However, if we consider that APBs and the remaining curved defects that are not APBs, occur in approximately equal proportions, we

obtain a value of 0,05 nm^{-1} for our samples, which closely aligns with the value reported in [199].

From the results obtained from the total defect density quantification, both samples present a comparable characteristic length, although there is a difference in the anisotropy between the two samples. One of the probable explanations is that the fraction of APBs among the total measured length of defects is slightly different from sample B1 to sample B2, and the directionality of APBs may have a preferential orientation in sample B1 which has a higher anisotropy.

Based on the observations mentioned above, it's apparent that a comprehensive analysis involving both DF-TEM images and ADF-STEM images is necessary to achieve the most accurate quantification of APBs density. While the ADF-STEM images provide a global vision of defects, they do not exclude other defects than APBs. On the other hand, the DF-TEM images, while useful in detecting APBs, may not capture the complete population of APBs in the film. Therefore, a combined examination of both imaging techniques is essential for a more comprehensive understanding of the APBs and their density in the Fe_3O_4 thin films.

5.5. Conclusion

In our study, we employed advanced TEM measurements, particularly DF-TEM, high-resolution HAADF-STEM, and ADF-STEM imaging, to conduct an in-depth analysis of the epitaxial growth of Fe_3O_4(111) on ZnO(0001). Through GPA analysis, we have provided compelling evidence of relaxed epitaxial growth, with strain relaxation occurring within a remarkably thin layer of less than 5Å. This relaxation is facilitated by the formation of misfit dislocations at the Fe_3O_4/ZnO interface, showcasing a periodicity of 1.74 nm along the $[1\bar{1}0]$ direction, consistent with the lattice mismatch between Fe_3O_4 and ZnO.

Our investigation unveiled primarily two categories of defects: twin boundaries and antiphase boundaries. It is noteworthy that these boundaries may not always align with high-symmetry planes and can exhibit curvature or tilt relative to the growth axis. Additionally, apart from twin and antiphase boundaries, we observed other defects in the ADF-STEM plane-view observations that do not exhibit the crystallographic characteristics of antiphase boundaries.

Furthermore, we quantified a characteristic defect length per unit area from HAADF-STEM images, measuring 0.12 nm^{-1} for samples grown with the FeO template layer and 0.10 nm^{-1} for samples without it. The orientation and fraction of antiphase boundaries, relative to the estimated density of total defects, can differ between these two sample types.

Summary and perspectives

In the course of this thesis, we embarked on a journey to explore the epitaxial growth of Fe_3O_4 thin films on ZnO substrates. The goal was to uncover valuable insights and make significant contributions to the overarching objectives of the "SPINOXIDE" project, which is focused on advancing the field of spintronics. Our research has yielded an abundance of findings, and this global conclusion serves to distill the essence of our research.

In the realm of epitaxial growth, we have made noteworthy strides. Central to our achievements is the establishment epitaxial growth of Fe_3O_4 thin films on ZnO(000±1) substrates following the relationship Fe_3O_4 (111)[$10\bar{1}$] // ZnO(0001)[$11\bar{2}0$]. We have found that the polarity of the substrate plays no discernible role in influencing the volume properties of Fe_3O_4 thin films. This finding opens up exciting possibilities, as it suggests that Fe_3O_4 thin films can be grown on both polarities of ZnO substrates without any compromise to their structural integrity.

By precisely adjusting the oxygen partial pressure during the growth process, we've achieved stoichiometric Fe_3O_4 thin films. For instance, when grown at 260°C, the oxygen partial pressure needed for pure and stoichiometric Fe_3O_4 thin films was 1.0×10^{-6} Torr. This delicate balance of stoichiometry is a cornerstone for achieving the desired chemical composition, and it underscores the precision of our approach.

As we delve deeper into the properties of these thin films, we find that the magnetization properties closely resemble those of bulk Fe_3O_4. Films grown at 400°C come exceptionally close to bulk magnetization, boasting a value of 480 emu/cm³. Even at a lower substrate temperature of 260°C, the magnetization remains remarkably as high as 435 emu/cm^3.

The study of interface characteristics using Transmission Electron Microscopy revealed that the interface between Fe_3O_4 and ZnO remains geometrically flat when growth is executed at substrate temperatures below 400°C. However, this interface takes on a curvier form when growth is performed at 500°C, indicating thermally activated interdiffusion between the film and the substrate at higher temperatures. Further exploration of the effect of growth temperature using SIMS depth profiling demonstrated that a content of Zn can be detected in the Fe_3O_4 film when it is grown at 400°C films, while it's virtually absent in the 260°C films. Among the most important outcomes of our study, these results underscore the importance of our decision to lower the growth temperature, creating an abrupt interface both chemically and structurally,

and thereby effectively preventing interdiffusion, a critical consideration in the field of spintronics.

In addition to our achievements in the growth of Fe_3O_4, we succeeded also in the growth of pure wurtzite FeO (111) on ZnO(0001) by controlling the PLD target stoichiometry. This accomplishment opens up possibilities for leveraging FeO as an interfacial layer. The interplay between Fe_3O_4 and FeO presents exciting avenues for exploration in the field.

While depositing Fe_3O_4, the presence of FeO during the early stages of growth has been observed using *operando* RHEED analysis. Despite the fact that RHEED monitoring suggests the formation of FeO, further HR-STEM investigations confirm the absence of this compound at the interface by the end of the growth process, thereby validating the possibility of growing Fe_3O_4 directly on the ZnO substrate. However, we also explored the intentional growth of a 1 nm FeO layer at the interface between Fe_3O_4 and ZnO. HR-STEM images revealed that even the intentionally grown FeO is oxidized during the subsequent growth of Fe_3O_4. It may be necessary to employ a thicker FeO layer to stabilize an ultra-thin FeO layer at the interface. Interestingly, despite the absence of the grown FeO at the interface, we have observed its influence on the magnetic properties of the final Fe_3O_4 film. This influence is manifested in differences in magnetic anisotropy among various samples, underscoring the impact of FeO on the magnetic behavior of the thin films.

Furthermore, our exploration of substrate miscut (1°) orientation has revealed that it significantly impacts remanent magnetization. The $[10\bar{1}0]$ miscut orientation, in particular, exhibited the highest remanence at 272 emu/cm^3 (resulting in Mr/Ms = 60%), highlighting the importance of substrate orientation in engineering the magnetic behavior of Fe_3O_4 thin films.

Moreover, our advanced TEM measurements, including DF-TEM, high-resolution HAADF-STEM, and ADF-STEM imaging, have allowed for an in-depth analysis of the epitaxial growth of Fe_3O_4(111) on ZnO(0001). Through GPA analysis, we've provided compelling evidence of relaxed epitaxial growth, with strain relaxation occurring within a remarkably thin layer of less than 5 Å. This relaxation is facilitated by the formation of misfit dislocations at the Fe_3O_4/ZnO interface, showcasing a periodicity of 1.74 nm along the $[1\bar{1}0]$ direction.

Our investigation unveiled primarily two categories of defects: twin boundaries and antiphase boundaries. It is noteworthy that these boundaries may not always align with high-symmetry planes and can exhibit curvature or tilt relative to the growth axis. Additionally, apart from twin

and antiphase boundaries, we observed curved defects in the ADF-STEM plane-view observations that do not exhibit the crystallographic characteristics of antiphase boundaries.
We quantified a characteristic defect length per unit area from HAADF-STEM plane-view images, measuring 0.12 nm^{-1} for samples grown with the FeO template layer and 0.10 nm^{-1} for samples without it. The orientation and fraction of antiphase boundaries, relative to the estimated density of total defects, can differ between these two sample types.

In the context of these findings and as a natural complement to this work, further work should focus on a precise quantification of antiphase boundaries density and exploring the nature of magnetic coupling across twin boundaries, including an investigation of the atomic structure along TBs. Examining the orientation of the substrate miscut effect in available samples is also essential to deepen our understanding.

Magnetic imaging techniques like Magnetic Force Microscopy (MFM) or Nitrogen-Vacancy Center (NV-center) magnetic imaging would offer a deeper understanding of in-plane magnetic coupling between crystallographic domains defined by curved boundaries that differ from antiphase boundaries. Additionally, magnetoresistance measurements can establish the relationship between APB density and the electrical properties of the films.
To maximize the remanent magnetization of Fe_3O_4 and reduce APBs for efficient spin injection and detection, several avenues need exploration. This includes growing Fe_3O_4 on substrates with different orientations (a and m face of ZnO) and different miscut values and investigating the effect of a thicker FeO template layer on defect density, domain size, and magnetic coupling between domains.

Moreover, within the SPINOXIDE project framework, is envisaged the use of magneto-optical experiments to examine spin injection and detection efficiency in devices based on films grown during this thesis. The integration of Fe_3O_4 on ZnO quantum wells and nanowires is also a promising axis of research chosen in SPINOXIDE to extend electron spin coherence time at room temperature, offering new possibilities for advancing spintronics.

The findings cited above represent a significant step forward in SPINOXIDE project. They pave the way for the development of efficient spintronic devices with practical applications.

In closing, this research represents a weighty contribution to the field of spintronics, and it significantly advances our understanding of the epitaxial growth of Fe_3O_4 thin films on ZnO substrates.

Appendix

Measurement of the laser fluence

Determining the fluence of the laser at the surface of the target is a crucial aspect of the research methodology. This is achieved through the following procedure:

The initial step involves measuring the laser power at its output, which is accomplished using a partially reflecting lens in conjunction with a laser power meter. This lens is specifically designed to recover only a fraction of the laser beam's total power. Subsequently, the laser power is measured at the surface of the target, inside the PLD chamber. **Figure A.1** illustrates the relationship between the power measured at the target surface and the fraction of power measured at the laser output. In addition to measuring the power values, the laser spot surface is also taken for each measurement, typically using a thermo-sensitive paper (a silicon substrate also can be used for example) as seen in **Figure A.2**.

With these measurements, it is possible to calculate the fluence in units of joules per square centimeter (J/cm²). Fluence is determined by considering the laser power and the laser pulse duration (derived from the laser's frequency). This method ensures the precise and reliable determination of fluence values for our PLD experiments

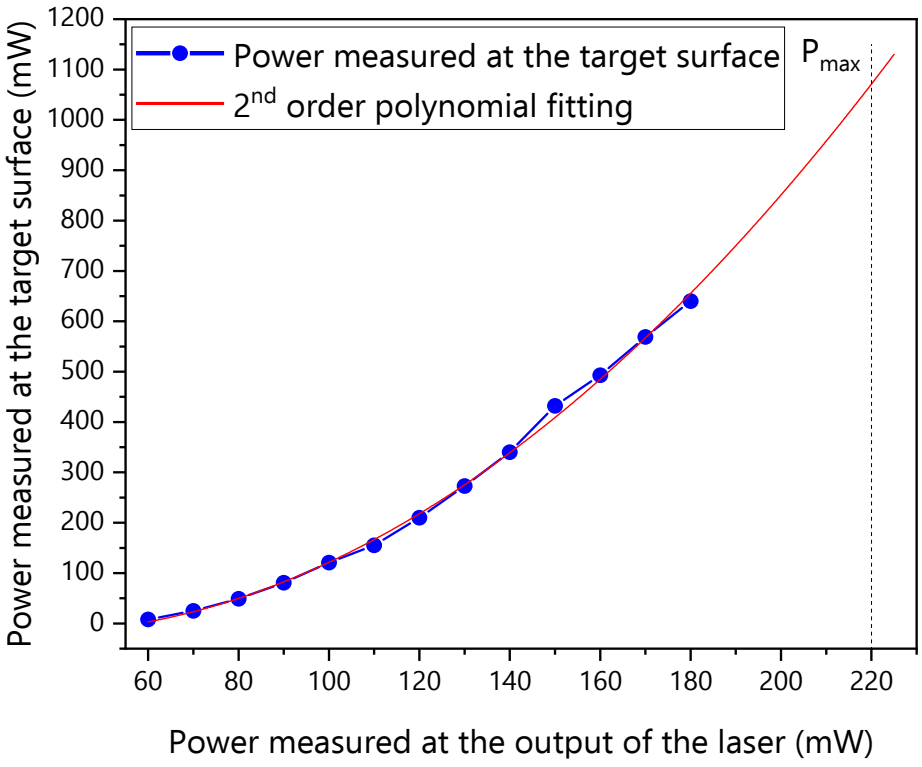

Figure A.1 *variation of the laser power at the target surface as function of the power measured at the laser output. This figure serves as power calibration curve*

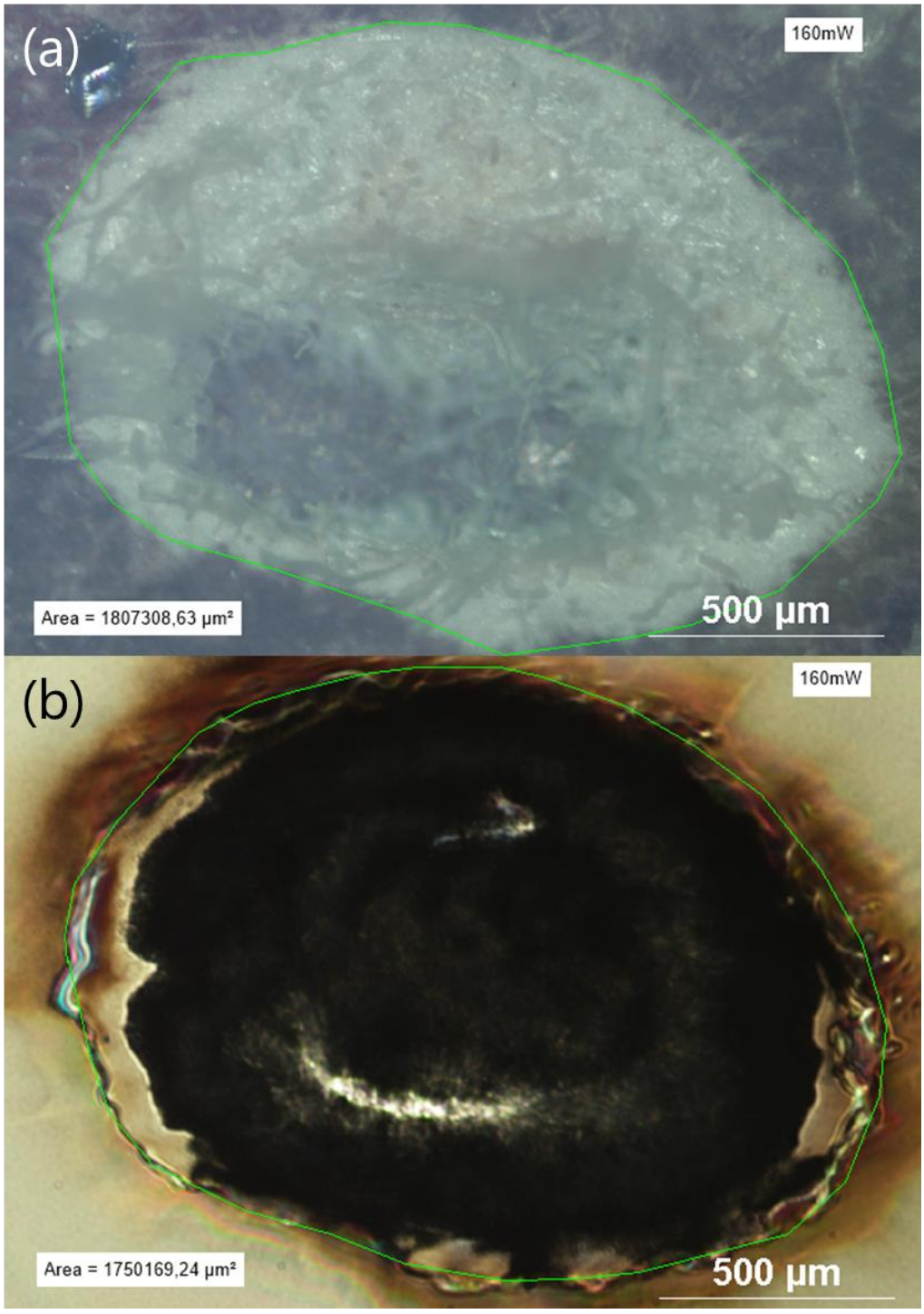

Figure A.2 *surface of the laser spot for (550mW) focused on (a) thermo-sensitive paper and (b) Si substrate*

Images used in the quantification of defects density

The ADF-STEM images used in 5.4.3 for the quantification of defect density are presented in **Figures A.3 - A8**.

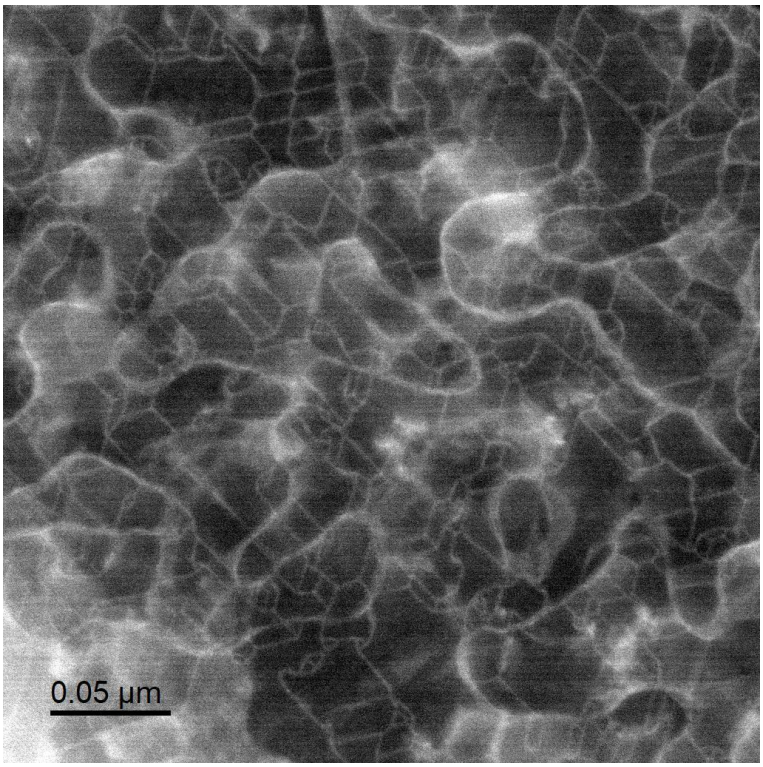

Figure A.3 *image 1 of the sample B1*

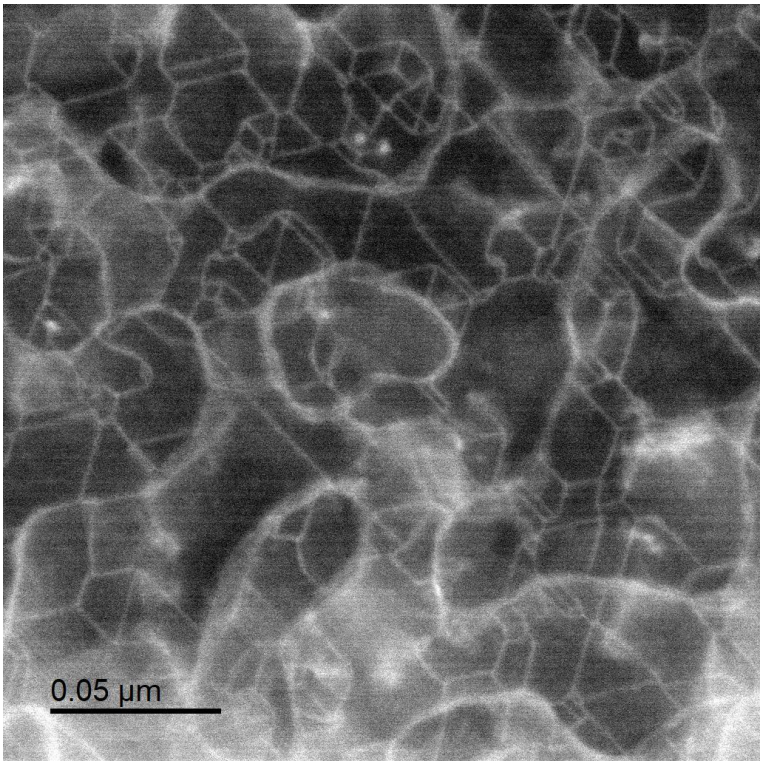

Figure A.4 *image 2 of the sample B1*

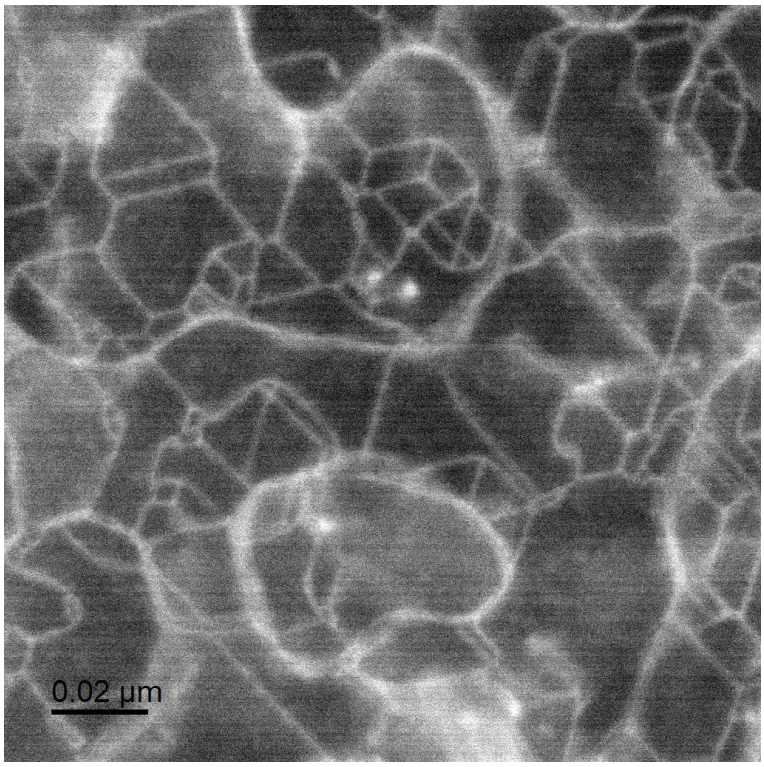

Figure A.5 *image 3 of the sample B1*

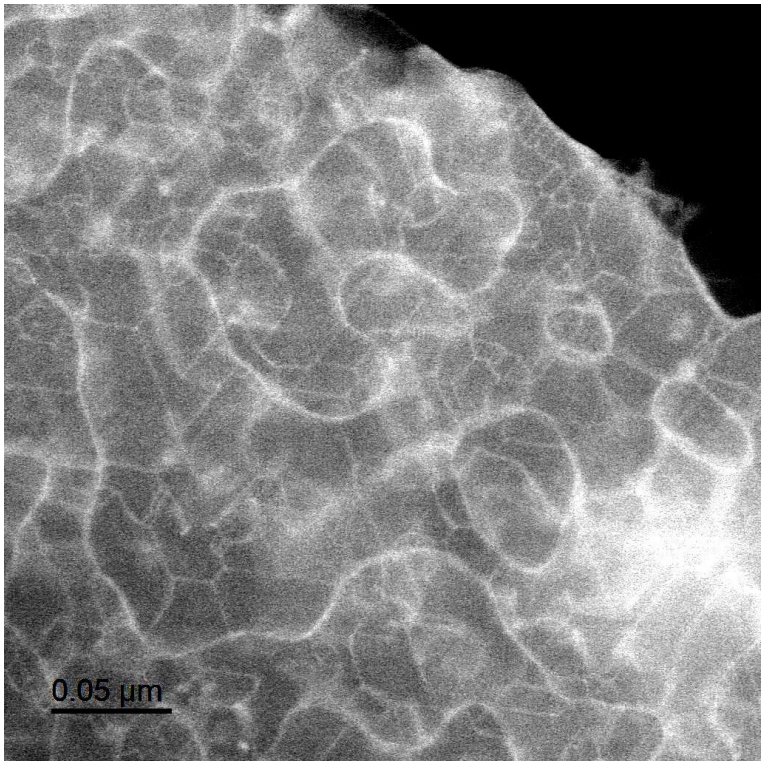

Figure A.6 *image 1' of the sample B2*

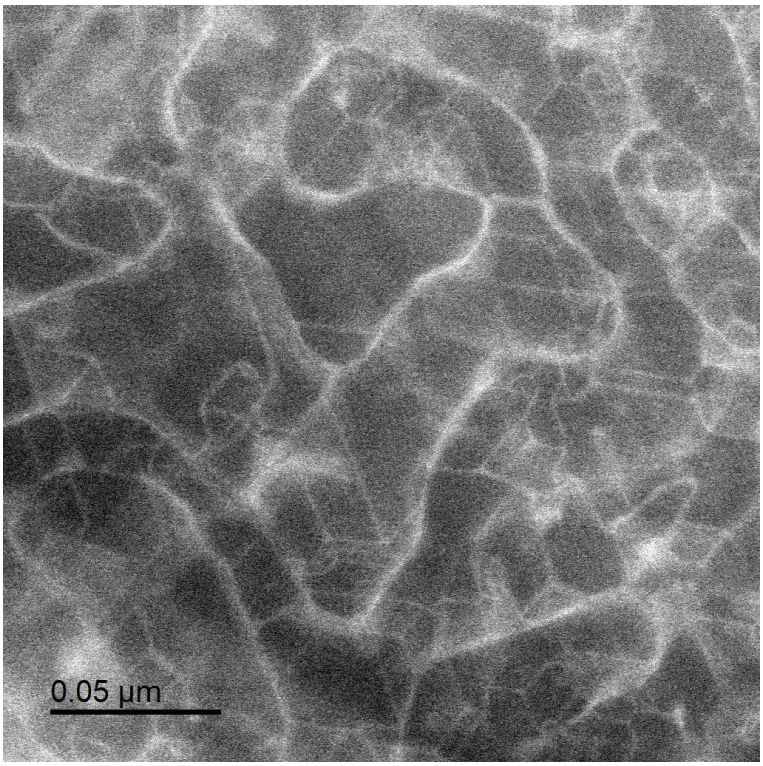

Figure A.7 *image 2' of the sample B2*

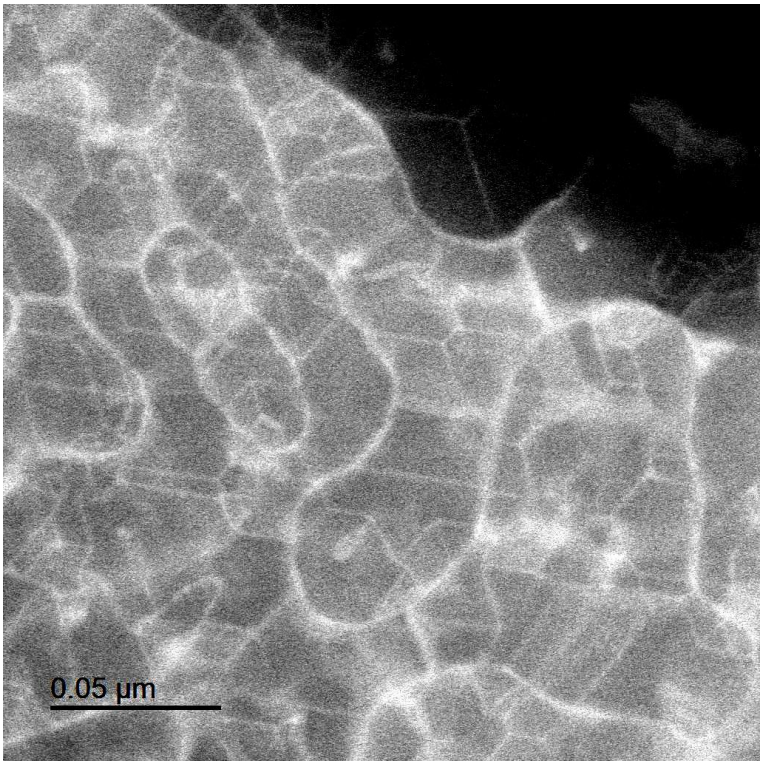

Figure A.8 *image 3' of the sample B2*

Bibliography

[1] E. Y. Tsymbal and I. Žutić, *Spintronics Handbook, Second Edition: Spin Transport and Magnetism: Volume Three: Nanoscale Spintronics and Applications*. CRC Press, 2019.

[2] H. Ohno *et al.*, '(Ga,Mn)As: A new diluted magnetic semiconductor based on GaAs', *Appl. Phys. Lett.*, vol. 69, no. 3, pp. 363–365, Jul. 1996, doi: 10.1063/1.118061.

[3] J. S. Dyck, Č. Drašar, P. Lošt'ák, and C. Uher, 'Low-temperature ferromagnetic properties of the diluted magnetic semiconductor $Sb_{2-x}Cr_xTe_3$', *Phys. Rev. B*, vol. 71, no. 11, p. 115214, Mar. 2005, doi: 10.1103/PhysRevB.71.115214.

[4] V. A. Kulbachinskii *et al.*, 'Ferromagnetism in new diluted magnetic semiconductor $Bi_{2-x}Fe_xTe_3$', *Physica B: Condensed Matter*, vol. 311, no. 3, pp. 292–297, Feb. 2002, doi: 10.1016/S0921-4526(01)00975-9.

[5] A. X. Gray *et al.*, 'Bulk electronic structure of the dilute magnetic semiconductor $Ga_{(1-x)}Mn_{(x)}As$ through hard X-ray angle-resolved photoemission', *Nat Mater*, vol. 11, no. 11, pp. 957–962, Nov. 2012, doi: 10.1038/nmat3450.

[6] G. Schmidt, 'Concepts for spin injection into semiconductors—a review', *J. Phys. D: Appl. Phys.*, vol. 38, no. 7, p. R107, Mar. 2005, doi: 10.1088/0022-3727/38/7/R01.

[7] C.-M. Hu, J. Nitta, A. Jensen, J. B. Hansen, and H. Takayanagi, 'Spin-polarized transport in a two-dimensional electron gas with interdigital-ferromagnetic contacts', *Phys. Rev. B*, vol. 63, no. 12, p. 125333, Mar. 2001, doi: 10.1103/PhysRevB.63.125333.

[8] S. Gardelis, C. G. Smith, C. H. W. Barnes, E. H. Linfield, and D. A. Ritchie, 'Spin-valve effects in a semiconductor field-effect transistor: A spintronic device', *Phys. Rev. B*, vol. 60, no. 11, pp. 7764–7767, Sep. 1999, doi: 10.1103/PhysRevB.60.7764.

[9] F. G. Monzon and M. L. Roukes, 'Spin injection and the local Hall effect in InAs quantum wells', *Journal of Magnetism and Magnetic Materials*, vol. 198–199, pp. 632–635, Jun. 1999, doi: 10.1016/S0304-8853(98)01205-0.

[10] S. H. Liang *et al.*, 'Large and robust electrical spin injection into GaAs at zero magnetic field using an ultrathin CoFeB/MgO injector', *Phys. Rev. B*, vol. 90, no. 8, p. 085310, Aug. 2014, doi: 10.1103/PhysRevB.90.085310.

[11] S. Ghosh *et al.*, 'Room-temperature spin coherence in ZnO', *Appl. Phys. Lett.*, vol. 86, no. 23, p. 232507, Jun. 2005, doi: 10.1063/1.1946204.

[12] Yu. S. Dedkov, U. Rüdiger, and G. Güntherodt, 'Evidence for the half-metallic ferromagnetic state of Fe_3O_4 by spin-resolved photoelectron spectroscopy', *Phys. Rev. B*, vol. 65, no. 6, p. 064417, Jan. 2002, doi: 10.1103/PhysRevB.65.064417.

[13] Ö. Özdemir and S. K. Banerjee, 'A preliminary magnetic study of soil samples from west-central Minnesota', *Earth and Planetary Science Letters*, vol. 59, no. 2, pp. 393–403, Jul. 1982, doi: 10.1016/0012-821X(82)90141-8.

[14] M. B. A. Jalil, S. G. Tan, S. B. Kumar, and S. Bae, 'Spin drift diffusion studies of magnetoresistance effects in current-perpendicular-to-plane spin valves with half-metallic insertions', *Phys. Rev. B*, vol. 73, no. 13, p. 134417, Apr. 2006, doi: 10.1103/PhysRevB.73.134417.

[15] K. Yang, D. H. Kim, and J. Dho, 'Schottky barrier effect on the electrical properties of Fe_3O_4/ZnO and Fe_3O_4/Nb : $SrTiO_3$ heterostructures', *J. Phys. D: Appl. Phys.*, vol. 44, no. 35, p. 355301, Sep. 2011, doi: 10.1088/0022-3727/44/35/355301.

[16] A. Müller *et al.*, 'Epitaxial growth of Fe_3O_4 thin films on ZnO and MgO substrates', *arXiv:0911.3572 [cond-mat]*, Nov. 2009, Accessed: Sep. 08, 2021. [Online]. Available: http://arxiv.org/abs/0911.3572

[17] ‘XXX. The structure of the spinel group of crystals: The London, Edinburgh, and Dublin Philosophical Magazine and Journal of Science: Vol 30, No 176’. Accessed: Jul. 24, 2023. [Online]. Available: https://www.tandfonline.com/doi/abs/10.1080/14786440808635400?journalCode=tphm17

[18] A. A. Claassen, ‘The scattering power of oxygen and iron for X-rays’, *Proc. Phys. Soc. London*, vol. 38, no. 1, p. 482, Jan. 1925, doi: 10.1088/1478-7814/38/1/348.

[19] J. Zemann, ‘Crystal structures, 2nd edition, Vol. 2 by R. W. G. Wyckoff’, *Acta Cryst*, vol. 19, no. 3, pp. 490–490, Sep. 1965, doi: 10.1107/S0365110X6500378X.

[20] M. A. Gilleo, ‘Superexchange Interaction Energy for Fe^{3+}-O^{2-}-Fe^{3+} Linkages’, *Phys. Rev.*, vol. 109, no. 3, pp. 777–781, Feb. 1958, doi: 10.1103/PhysRev.109.777.

[21] F. C. Voogt, T. Fujii, P. J. M. Smulders, L. Niesen, M. A. James, and T. Hibma, ‘NO_2-assisted molecular-beam epitaxy of Fe_3O_4, $Fe_{3-\delta}O_4$, and γ−Fe_2O_3 thin films on MgO(100)’, *Phys. Rev. B*, vol. 60, no. 15, pp. 11193–11206, Oct. 1999, doi: 10.1103/PhysRevB.60.11193.

[22] M. L. Néel, ‘Propriétés magnétiques des ferrites ; ferrimagnétisme et antiferromagnétisme’, *Ann. Phys.*, vol. 12, no. 3, pp. 137–198, 1948, doi: 10.1051/anphys/194812030137.

[23] A. Weiss, ‘John B. Goodenough: Magnetism and the Chemical Bond. Interscience Publishers. New York, London 1963. 393 Seiten, 89 Abbildungen. Preis: DM 95 s.’, *Berichte der Bunsengesellschaft für physikalische Chemie*, vol. 68, no. 10, pp. 996–996, 1964, doi: 10.1002/bbpc.19640681015.

[24] P. Atkins and J. de Paula, *Atkins’ Physical Chemistry*. OUP Oxford, 2010.

[25] M. C. Paul, ‘Molecular beam epitaxy and properties of magnetite thin films on semiconducting substrates’, doctoralthesis, Universität Würzburg, 2010.

[26] J.-B. Moussy, ‘From epitaxial growth of ferrite thin films to spin-polarized tunnelling’, *J. Phys. D: Appl. Phys.*, vol. 46, no. 14, p. 143001, Apr. 2013, doi: 10.1088/0022-3727/46/14/143001.

[27] B. H. Torrie, ‘Spin waves in magnetite at a temperature below the electronic ordering transition’, *Solid State Communications*, vol. 5, no. 9, pp. 715–717, Sep. 1967, doi: 10.1016/0038-1098(67)90356-0.

[28] C. M. Srivastava, G. Srinivasan, and N. G. Nanadikar, ‘Exchange constants in spinel ferrites’, *Phys. Rev. B*, vol. 19, no. 1, pp. 499–508, Jan. 1979, doi: 10.1103/PhysRevB.19.499.

[29] S. Krupička and P. Novák, ‘Chapter 4 Oxide spinels’, in *Handbook of Ferromagnetic Materials*, vol. 3, Elsevier, 1982, pp. 189–304. doi: 10.1016/S1574-9304(05)80090-2.

[30] E. De Grave, R. M. Persoons, R. E. Vandenberghe, and P. M. A. de Bakker, ‘Mössbauer study of the high-temperature phase of Co-substituted magnetites, $CoxFe_{3-x}O_4$. I. $x \leq 0.04$’, *Phys. Rev. B*, vol. 47, no. 10, pp. 5881–5893, Mar. 1993, doi: 10.1103/PhysRevB.47.5881.

[31] M. Uhl and B. Siberchicot, ‘A first-principles study of exchange integrals in magnetite’, *J. Phys.: Condens. Matter*, vol. 7, no. 22, p. 4227, May 1995, doi: 10.1088/0953-8984/7/22/006.

[32] P. G. Bercoff and H. R. Bertorello, ‘Exchange constants and transfer integrals of spinel ferrites’, *Journal of Magnetism and Magnetic Materials*, vol. 169, no. 3, pp. 314–322, May 1997, doi: 10.1016/S0304-8853(96)00748-2.

[33] D. J. Huang *et al.*, ‘Spin and Orbital Magnetic Moments of Fe_3O_4’, *Phys. Rev. Lett.*, vol. 93, no. 7, p. 077204, Aug. 2004, doi: 10.1103/PhysRevLett.93.077204.

[34] D. T. Margulies *et al.*, ‘Anomalous moment and anisotropy behavior in Fe_3O_4 films’, *Phys. Rev. B*, vol. 53, no. 14, pp. 9175–9187, Apr. 1996, doi: 10.1103/PhysRevB.53.9175.
[35] S. Chikazumi and S. H. Charap, *Physics of Magnetism*. Huntington, N.Y: Krieger Pub Co, 1978.
[36] E. J. Verwey, P. W. Haayman, and F. C. Romeijn, ‘Physical Properties and Cation Arrangement of Oxides with Spinel Structures II. Electronic Conductivity’, *The Journal of Chemical Physics*, vol. 15, no. 4, pp. 181–187, Nov. 2004, doi: 10.1063/1.1746466.
[37] P. Weiss and R. Forrer, ‘La saturation absolue des ferromagnétiques et les lois d’approche en fonction du champ et de la température’, *Ann. Phys.*, vol. 10, no. 12, pp. 279–372, 1929, doi: 10.1051/anphys/192910120279.
[38] C. H. Li, ‘Magnetic Properties of Magnetite Crystals at Low Temperature’, *Phys. Rev.*, vol. 40, no. 6, pp. 1002–1012, Jun. 1932, doi: 10.1103/PhysRev.40.1002.
[39] ‘Heat capacity and entropy of nonstoichiometric magnetite $Fe_{3(1-\delta)}O_4$: The thermodynamic nature of the Verwey transition’. Accessed: Jul. 20, 2023. [Online]. Available: https://journals.aps.org/prb/abstract/10.1103/PhysRevB.43.8461
[40] L. R. Bickford, ‘The Low Temperature Transformation in Ferrites’, *Rev. Mod. Phys.*, vol. 25, no. 1, pp. 75–79, Jan. 1953, doi: 10.1103/RevModPhys.25.75.
[41] R. W. Millar, ‘The heat capacities at low temperatures of “ferrous oxide,” magnetite and cuprous and cupric oxides’, *J. Am. Chem. Soc.*, vol. 51, no. 1, pp. 215–222, Jan. 1929, doi: 10.1021/ja01376a026.
[42] M. Iizumi and G. Shirane, ‘Crystal symmetry of the low temperature phase of magnetite’, *Solid State Communications*, vol. 17, no. 4, pp. 433–436, Aug. 1975, doi: 10.1016/0038-1098(75)90471-8.
[43] A. Kozłowski, P. Metcalf, Z. Kąkol, and J. M. Honig, ‘Electrical and magnetic properties of $Fe_{3-z}Al_zO_4$ ($z<0.06$)’, *Phys. Rev. B*, vol. 53, no. 22, pp. 15113–15118, Jun. 1996, doi: 10.1103/PhysRevB.53.15113.
[44] N. Guigue-Millot, N. Keller, and P. Perriat, ‘Evidence for the Verwey transition in highly nonstoichiometric nanometric Fe-based ferrites’, *Phys. Rev. B*, vol. 64, no. 1, p. 012402, Jun. 2001, doi: 10.1103/PhysRevB.64.012402.
[45] A. Yanase and K. Siratori, ‘Band Structure in the High Temperature Phase of Fe_3O_4’, *Journal of the Physical Society of Japan*, vol. 53, no. 1, pp. 312–317, 1984, doi: 10.1143/JPSJ.53.312.
[46] Z. Zhang and S. Satpathy, ‘Electron states, magnetism, and the Verwey transition in magnetite’, *Phys. Rev. B*, vol. 44, no. 24, pp. 13319–13331, Dec. 1991, doi: 10.1103/PhysRevB.44.13319.
[47] V. I. Anisimov, I. S. Elfimov, N. Hamada, and K. Terakura, ‘Charge-ordered insulating state of Fe_3O_4 from first-principles electronic structure calculations’, *Phys. Rev. B*, vol. 54, no. 7, pp. 4387–4390, Aug. 1996, doi: 10.1103/PhysRevB.54.4387.
[48] A. Bataille, ‘Etude des propriétés physiques des films de Fe_3O_4 et de la polarisation en spin à l’interface Fe_3O_4/gamma-Al_2O_3’, These de doctorat, Paris 11, 2005. Accessed: Jul. 12, 2023. [Online]. Available: https://www.theses.fr/2005PA112314
[49] W. E. Pickett and D. J. Singh, ‘Electronic structure and half-metallic transport in the $La_{1-x}Ca_xMnO_3$ system’, *Phys. Rev. B*, vol. 53, no. 3, pp. 1146–1160, Jan. 1996, doi: 10.1103/PhysRevB.53.1146.
[50] A. Chainani, T. Yokoya, T. Morimoto, T. Takahashi, and S. Todo, ‘High-resolution photoemission spectroscopy of the Verwey transition in Fe_3O_4’, *Phys. Rev. B*, vol. 51, no. 24, pp. 17976–17979, Jun. 1995, doi: 10.1103/PhysRevB.51.17976.

[51] J.-H. Park, L. H. Tjeng, J. W. Allen, P. Metcalf, and C. T. Chen, 'Single-particle gap above the Verwey transition in Fe_3O_4', *Phys. Rev. B*, vol. 55, no. 19, pp. 12813–12817, May 1997, doi: 10.1103/PhysRevB.55.12813.

[52] J. R. Cullen and E. R. Callen, 'Multiple Ordering in Magnetite', *Phys. Rev. B*, vol. 7, no. 1, pp. 397–402, Jan. 1973, doi: 10.1103/PhysRevB.7.397.

[53] M. Fonin, Yu. S. Dedkov, J. Mayer, U. Rüdiger, and G. Güntherodt, 'Preparation, structure, and electronic properties of Fe_3O_4 films on the Fe(110)/Mo(110)/Al_2O_3(11-20) substrate', *Phys. Rev. B*, vol. 68, no. 4, p. 045414, Jul. 2003, doi: 10.1103/PhysRevB.68.045414.

[54] G. Hu and Y. Suzuki, 'Negative Spin Polarization of Fe_3O_4 in Magnetite/Manganite-Based Junctions', *Phys. Rev. Lett.*, vol. 89, no. 27, p. 276601, Dec. 2002, doi: 10.1103/PhysRevLett.89.276601.

[55] J. G. Tobin, S. A. Morton, S. W. Yu, G. D. Waddill, I. K. Schuller, and S. A. Chambers, 'Spin resolved photoelectron spectroscopy of Fe_3O_4: the case against half-metallicity', *J. Phys.: Condens. Matter*, vol. 19, no. 31, p. 315218, Aug. 2007, doi: 10.1088/0953-8984/19/31/315218.

[56] M. Fonin, Y. S. Dedkov, R. Pentcheva, U. Rüdiger, and G. Güntherodt, 'Magnetite: a search for the half-metallic state', *J. Phys.: Condens. Matter*, vol. 19, no. 31, p. 315217, Aug. 2007, doi: 10.1088/0953-8984/19/31/315217.

[57] J. Y. T. Wei, N.-C. Yeh, R. P. Vasquez, and A. Gupta, 'Tunneling evidence of half-metallicity in epitaxial films of ferromagnetic perovskite manganites and ferrimagnetic magnetite', *Journal of Applied Physics*, vol. 83, no. 11, pp. 7366–7368, Jun. 1998, doi: 10.1063/1.367799.

[58] P. Seneor, A. Fert, J.-L. Maurice, F. Montaigne, F. Petroff, and A. Vaurès, 'Large magnetoresistance in tunnel junctions with an iron oxide electrode', *Appl. Phys. Lett.*, vol. 74, no. 26, pp. 4017–4019, Jun. 1999, doi: 10.1063/1.123246.

[59] J. M. Gaines *et al.*, 'An STM study of Fe_3O_4(100) grown by molecular beam epitaxy', *Surface Science*, vol. 373, no. 1, pp. 85–94, Feb. 1997, doi: 10.1016/S0039-6028(96)01145-4.

[60] Y. Gao, Y. J. Kim, S. A. Chambers, and G. Bai, 'Synthesis of epitaxial films of Fe_3O_4 and α-Fe_2O_3 with various low-index orientations by oxygen-plasma-assisted molecular beam epitaxy', *Journal of Vacuum Science & Technology A: Vacuum, Surfaces, and Films*, vol. 15, no. 2, pp. 332–339, Mar. 1997, doi: 10.1116/1.580488.

[61] Y. J. Kim, Y. Gao, and S. A. Chambers, 'Selective growth and characterization of pure, epitaxial α-Fe_2O_3(0001) and Fe_3O_4(001) films by plasma-assisted molecular beam epitaxy', *Surface Science*, vol. 371, no. 2–3, pp. 358–370, Feb. 1997, doi: 10.1016/S0039-6028(96)00999-5.

[62] T. Hibma *et al.*, 'Anti-phase domains and magnetism in epitaxial magnetite layers', *Journal of Applied Physics*, vol. 85, no. 8, pp. 5291–5293, Apr. 1999, doi: 10.1063/1.369857.

[63] E. Guiot, S. Gota, M. Henriot, M. Gautier-Soyer, and S. Lefebvre, 'Growth And Structure Of Nanometric Iron Oxide Films', *MRS Proc.*, vol. 524, p. 101, 1998, doi: 10.1557/PROC-524-101.

[64] A. V. Mijiritskii and D. O. Boerma, 'The (001) surface and morphology of thin Fe_3O_4 layers grown by O_2-assisted molecular beam epitaxy', *Surface Science*, vol. 486, no. 1–2, pp. 73–81, Jul. 2001, doi: 10.1016/S0039-6028(01)01064-0.

[65] J. F. Anderson, M. Kuhn, U. Diebold, K. Shaw, P. Stoyanov, and D. Lind, 'Surface structure and morphology of Mg-segregated epitaxial Fe_3O_4(001) thin films on MgO(001)', *Phys. Rev. B*, vol. 56, no. 15, pp. 9902–9909, Oct. 1997, doi: 10.1103/PhysRevB.56.9902.

[66] P. K. J. Wong *et al.*, 'Ultrathin Fe_3O_4 epitaxial films on wide bandgap GaN(0001)', *Phys. Rev. B*, vol. 81, no. 3, p. 035419, Jan. 2010, doi: 10.1103/PhysRevB.81.035419.
[67] Y. X. Lu, J. S. Claydon, Y. B. Xu, S. M. Thompson, K. Wilson, and G. van der Laan, 'Epitaxial growth and magnetic properties of half-metallic Fe_3O_4 on GaAs(100)', *Phys. Rev. B*, vol. 70, no. 23, p. 233304, Dec. 2004, doi: 10.1103/PhysRevB.70.233304.
[68] C. A. Kleint, H. C. Semmelhack, M. Lorenz, and M. K. Krause, 'Structural and magnetic properties of epitaxial magnetite thin films prepared by pulsed laser deposition', *Journal of Magnetism and Magnetic Materials*, vol. 140–144, pp. 725–726, Feb. 1995, doi: 10.1016/0304-8853(94)00821-3.
[69] S. Kale *et al.*, 'Film thickness and temperature dependence of the magnetic properties of pulsed-laser-deposited Fe_3O_4 films on different substrates', *Phys. Rev. B*, vol. 64, no. 20, p. 205413, Nov. 2001, doi: 10.1103/PhysRevB.64.205413.
[70] S. A. Krasnikov *et al.*, 'Oxidation effects in epitaxial Fe_3O_4 layers on MgO and $MgAl_2O_4$ substrates studied by X-ray absorption, fluorescence and photoemission', *Materials Science and Engineering: B*, vol. 109, no. 1–3, pp. 207–212, Jun. 2004, doi: 10.1016/j.mseb.2003.10.066.
[71] B. Carvello and L. Ranno, 'Transport properties of the Fe_3O_4/Nb:$SrTiO_3$ interface', *Journal of Magnetism and Magnetic Materials*, vol. 272–276, pp. 1926–1927, May 2004, doi: 10.1016/j.jmmm.2003.12.348.
[72] A. Hamie *et al.*, 'Investigation of high quality magnetite thin films grown on $SrTiO_3$(001) substrates by pulsed laser deposition', *Thin Solid Films*, vol. 525, pp. 115–120, Dec. 2012, doi: 10.1016/j.tsf.2012.10.076.
[73] M. Paul *et al.*, 'Surface structure, morphology, and growth mechanism of Fe_3O_4/ZnO thin films', *Journal of Applied Physics*, vol. 110, no. 7, p. 073519, Oct. 2011, doi: 10.1063/1.3644927.
[74] M. L. Paramês *et al.*, 'Magnetic properties of Fe_3O_4 thin films grown on different substrates by laser ablation', *Applied Surface Science*, vol. 253, no. 19, pp. 8201–8205, Jul. 2007, doi: 10.1016/j.apsusc.2007.02.134.
[75] P. Prieto, J. de la Figuera, L. Martín-García, J. E. Prieto, and J. F. Marco, 'Fourfold in-plane magnetic anisotropy of magnetite thin films grown on TiN buffered Si(001) by ion-assisted sputtering', *J. Mater. Chem. C*, vol. 4, no. 32, pp. 7632–7639, 2016, doi: 10.1039/C6TC02152B.
[76] S. K. Singh, S. Husain, A. Kumar, and S. Chaudhary, 'Effect of oxygen partial pressure on the density of antiphase boundaries in Fe_3O_4 thin films on Si(100)', *Journal of Magnetism and Magnetic Materials*, vol. 448, pp. 303–309, Feb. 2018, doi: 10.1016/j.jmmm.2017.07.082.
[77] J. F. Bobo *et al.*, 'Magnetic behavior and role of the antiphase boundaries in Fe_3O_4 epitaxial films sputtered on MgO(001)', *Eur. Phys. J. B*, vol. 24, no. 1, pp. 43–49, Nov. 2001, doi: 10.1007/s100510170020.
[78] X. Huang and J. Ding, 'The structure, magnetic and transport properties of Fe_3O_4 thin films on different substrates by pulsed laser deposition', *Journal of the Korean Physical Society*, vol. 62, no. 12, pp. 2228–2232, Jun. 2013, doi: 10.3938/jkps.62.2228.
[79] W. L. Zhou, K.-Y. Wang, C. J. O'Connor, and J. Tang, 'Granular growth of Fe_3O_4 thin films and its antiphase boundaries prepared by pulsed laser deposition', *Journal of Applied Physics*, vol. 89, no. 11, pp. 7398–7400, Jun. 2001, doi: 10.1063/1.1358831.
[80] R. Master, R. J. Choudhary, and D. M. Phase, 'Structural and magnetic properties of epitaxial Fe_3O_4/ZnO and ZnO/Fe_3O_4 bilayers grown on c-Al_2O_3 substrate', *Journal of Applied Physics*, vol. 108, no. 10, p. 103909, Nov. 2010, doi: 10.1063/1.3511348.
[81] M. L. Paramés, N. Popovici, P. M. Sousa, A. J. Silvestre, and O. Conde, 'Iron Oxide Thin Films Grown by Pulsed Laser Deposition', in *Recent Advances in Multidisciplinary*

Applied Physics, Elsevier, 2005, pp. 457–461. doi: 10.1016/B978-008044648-6.50073-2.
[82] A. Müller, 'Towards functional oxide heterostructures', doctoralthesis, Universität Würzburg, 2012.
[83] K. Ellmer, A. Klein, and B. Rech, Eds., *Transparent Conductive Zinc Oxide: Basics and Applications in Thin Film Solar Cells*, vol. 104. in Springer Series in Materials Science, vol. 104. Berlin, Heidelberg: Springer, 2008. doi: 10.1007/978-3-540-73612-7.
[84] M. W. Allen *et al.*, 'Polarity effects in the x-ray photoemission of ZnO and other wurtzite semiconductors', *Applied Physics Letters*, vol. 98, no. 10, p. 101906, Mar. 2011, doi: 10.1063/1.3562308.
[85] A. Mang, K. Reimann, and St. Rübenacke, 'Band gaps, crystal-field splitting, spin-orbit coupling, and exciton binding energies in ZnO under hydrostatic pressure', *Solid State Communications*, vol. 94, no. 4, pp. 251–254, Apr. 1995, doi: 10.1016/0038-1098(95)00054-2.
[86] O. Madelung, *Semiconductors — Basic Data*. Springer Science & Business Media, 2012.
[87] D. Look, 'Recent Advances in ZnO Materials and Devices', *Materials Science and Engineering B-Solid State Materials for Advanced Technology*, vol. 80, no. 1–3, pp. 383–387, Jan. 2001, doi: 10.1016/S0921-5107(00)00604-8.
[88] Ü. Özgür *et al.*, 'A comprehensive review of ZnO materials and devices', *Journal of Applied Physics*, vol. 98, no. 4, p. 041301, Aug. 2005, doi: 10.1063/1.1992666.
[89] S. B. Ogale, *Thin films and heterostructures for oxide electronics*. Springer Science & Business Media, 2005.
[90] E. V. Kalinina *et al.*, 'ZnO/AlGaN Ultraviolet Light Emitting Diodes', in *Zinc Oxide — A Material for Micro- and Optoelectronic Applications*, N. H. Nickel and E. Terukov, Eds., in NATO Science Series II: Mathematics, Physics and Chemistry. Dordrecht: Springer Netherlands, 2005, pp. 211–216. doi: 10.1007/1-4020-3475-X_18.
[91] 'Zinc Oxide Bulk, Thin Films and Nanostructures - 1st Edition'. Accessed: Jul. 24, 2023. [Online]. Available: https://shop.elsevier.com/books/zinc-oxide-bulk-thin-films-and-nanostructures/jagadish/978-0-08-044722-3
[92] N. J. Harmon, W. O. Putikka, and R. Joynt, 'Theory of electron spin relaxation in ZnO', *Phys. Rev. B*, vol. 79, no. 11, p. 115204, Mar. 2009, doi: 10.1103/PhysRevB.79.115204.
[93] D. T. Margulies *et al.*, 'Origin of the Anomalous Magnetic Behavior in Single Crystal Fe_3O_4 Films', *Phys. Rev. Lett.*, vol. 79, no. 25, pp. 5162–5165, Dec. 1997, doi: 10.1103/PhysRevLett.79.5162.
[94] S. Celotto, W. Eerenstein, and T. Hibma, 'Characterization of anti-phase boundaries in epitaxial magnetite films', *The European Physical Journal B - Condensed Matter*, vol. 36, no. 2, pp. 271–279, Nov. 2003, doi: 10.1140/epjb/e2003-00344-7.
[95] W. Eerenstein, T. T. M. Palstra, T. Hibma, and S. Celotto, 'Origin of the increased resistivity in epitaxial Fe_3O_4 films', *Phys. Rev. B*, vol. 66, no. 20, p. 201101, Nov. 2002, doi: 10.1103/PhysRevB.66.201101.
[96] X. W. Li, A. Gupta, G. Xiao, W. Qian, and V. P. Dravid, 'Fabrication and properties of heteroepitaxial magnetite (Fe_3O_4) tunnel junctions', *Applied Physics Letters*, vol. 73, no. 22, pp. 3282–3284, Nov. 1998, doi: 10.1063/1.122745.
[97] A. G. Fitzgerald and T. G. May, 'Defects in epitaxial ferrite films grown by chemical vapour deposition', *Thin Solid Films*, vol. 35, no. 2, pp. 201–213, Jun. 1976, doi: 10.1016/0040-6090(76)90257-1.
[98] A. Hamié, 'Hétérostructures à base de l'oxyde ferrimagnétique rendu semiconducteur $Fe_{2-x}Ti_xO_{3-\delta}$: vers des effets de polarisation en spin', These de doctorat, Versailles-St Quentin en Yvelines, 2011. Accessed: Feb. 22, 2023. [Online]. Available: https://www.theses.fr/2011VERS0028

[99] J.-B. Moussy *et al.*, 'Thickness dependence of anomalous magnetic behavior in epitaxial Fe_3O_4(111) thin films: Effect of density of antiphase boundaries', *Phys. Rev. B*, vol. 70, no. 17, p. 174448, Nov. 2004, doi: 10.1103/PhysRevB.70.174448.
[100] I. Yamaguchi *et al.*, 'Preparation of (111)-Oriented Epitaxial $Fe_{3-x}O4$ Films on α-Al_2O_3 (0001) Substrates by Coating-Pyrolysis Process Using Postepitaxial Topotaxy via (0001)-Oriented α-Fe_2O_3', *Journal of Solid State Chemistry*, vol. 163, no. 1, pp. 239–247, Jan. 2002, doi: 10.1006/jssc.2001.9398.
[101] K. P. McKenna *et al.*, 'Atomic-scale structure and properties of highly stable antiphase boundary defects in Fe_3O_4', *Nat Commun*, vol. 5, no. 1, p. 5740, Dec. 2014, doi: 10.1038/ncomms6740.
[102] H. Zijlstra, 'Coping with Brown's paradox: The pinning and nucleation of magnetic domain walls at antiphase boundaries', *IEEE Transactions on Magnetics*, vol. 15, no. 5, pp. 1246–1250, Sep. 1979, doi: 10.1109/TMAG.1979.1060313.
[103] B. Dieny, D. Givord, and J. M. B. Ndjaka, 'Original magnetization processes in the artificial ferrimagnet Y-Co/Gd-Co/Y-Co', *Journal of Magnetism and Magnetic Materials*, vol. 93, pp. 503–508, Feb. 1991, doi: 10.1016/0304-8853(91)90394-P.
[104] A. M. Bataille *et al.*, 'Characterization of antiphase boundary network in Fe_3O_4(111) epitaxial thin films: Effect on anomalous magnetic behavior', *Phys. Rev. B*, vol. 74, no. 15, p. 155438, Oct. 2006, doi: 10.1103/PhysRevB.74.155438.
[105] M. Grundmann, T. Böntgen, and M. Lorenz, 'Occurrence of Rotation Domains in Heteroepitaxy', *Phys. Rev. Lett.*, vol. 105, no. 14, p. 146102, Sep. 2010, doi: 10.1103/PhysRevLett.105.146102.
[106] L. D. Landau, E. M. Lifšic, L. P. Pitaevskij, and L. D. Landau, *Course of Theoretical Physics, Statistical Physics*, 3. ed., repr. in Course of theoretical physics / L. D. Landau and E. M. Lifshitz, no. 5. Amsterdam Heidelberg: Elsevier Butterworth Heinemann, 1980.
[107] M. Grundmann, 'Formation of epitaxial domains: Unified theory and survey of experimental results', *phys. stat. sol. (b)*, vol. 248, no. 4, pp. 805–824, Apr. 2011, doi: 10.1002/pssb.201046530.
[108] C. Chen *et al.*, 'Direct Determination of Atomic Structure and Magnetic Coupling of Magnetite Twin Boundaries', *ACS Nano*, vol. 12, no. 3, pp. 2662–2668, Mar. 2018, doi: 10.1021/acsnano.7b08802.
[109] A. Rizzi, B. N. E. Rösen, D. Freundt, Ch. Dieker, H. Lüth, and D. Gerthsen, 'Heteroepitaxy of β-$FeSi_2$ on Si by gas-source MBE', *Phys. Rev. B*, vol. 51, no. 24, pp. 17780–17794, Jun. 1995, doi: 10.1103/PhysRevB.51.17780.
[110] W. O'reilly, 'Estimation of the Curie Temperatures of Maghemite and Oxidized Titanomagnetites', *Journal of geomagnetism and geoelectricity*, vol. 20, no. 4, pp. 381–386, 1968, doi: 10.5636/jgg.20.381.
[111] J. M. D. Coey, Ed., 'Magnetic materials', in *Magnetism and Magnetic Materials*, Cambridge: Cambridge University Press, 2010, pp. 374–438. doi: 10.1017/CBO9780511845000.012.
[112] R. M. Bozorth, *Ferromagnetism*. D. Van Nostrand Company, 1953.
[113] D. Dijkkamp *et al.*, 'Preparation of Y-Ba-Cu oxide superconductor thin films using pulsed laser evaporation from high Tc bulk material', *Appl. Phys. Lett.*, vol. 51, no. 8, pp. 619–621, Aug. 1987, doi: 10.1063/1.98366.
[114] H. M. Smith and A. F. Turner, 'Vacuum Deposited Thin Films Using a Ruby Laser', *Appl. Opt.*, vol. 4, no. 1, p. 147, Jan. 1965, doi: 10.1364/AO.4.000147.
[115] A. Ohtomo and H. Y. Hwang, 'A high-mobility electron gas at the $LaAlO_3/SrTiO_3$ heterointerface', *Nature*, vol. 427, no. 6973, pp. 423–426, Jan. 2004, doi: 10.1038/nature02308.

[116] V. Garcia *et al.*, ‘Ferroelectric Control of Spin Polarization’, *Science*, vol. 327, no. 5969, pp. 1106–1110, Feb. 2010, doi: 10.1126/science.1184028.
[117] K. Mitamura, T. Honke, J. Ohta, A. Kobayashi, H. Fujioka, and M. Oshima, ‘Characteristics of InN grown directly on Al_2O_3 (0001) substrates by pulsed laser deposition’, *Journal of Crystal Growth*, vol. 311, no. 5, pp. 1316–1320, Feb. 2009, doi: 10.1016/j.jcrysgro.2008.12.015.
[118] S. Bauer *et al.*, ‘Structure Quality of $LuFeO_3$ Epitaxial Layers Grown by Pulsed-Laser Deposition on Sapphire/Pt’, *Materials*, vol. 13, no. 1, p. 61, Dec. 2019, doi: 10.3390/ma13010061.
[119] D. K. Shukla *et al.*, ‘Thin film growth of multiferroic $BiMn_2O_5$ using pulsed laser ablation and its characterization’, *J. Phys. D: Appl. Phys.*, vol. 42, no. 12, p. 125304, Jun. 2009, doi: 10.1088/0022-3727/42/12/125304.
[120] S. P. Balmuchu, E. Radhika, and P. Dobbidi, ‘The impact of oxygen partial pressure in modifying energy storage property of lanthanum doped multiferroic bismuth ferrite thin films deposited via pulsed laser deposition’, *Journal of Energy Storage*, vol. 71, p. 108179, Nov. 2023, doi: 10.1016/j.est.2023.108179.
[121] J. Dho, C. W. Leung, J. L. MacManus-Driscoll, and M. G. Blamire, ‘Epitaxial and oriented $YMnO_3$ film growth by pulsed laser deposition’, *Journal of Crystal Growth*, vol. 267, no. 3, pp. 548–553, Jul. 2004, doi: 10.1016/j.jcrysgro.2004.04.028.
[122] R. W. Dreyfus, ‘Mechanisms of laser ablation of monolayers as determined by laser-induced fluorescence measurements’, in *Laser Ablation Mechanisms and Applications*, J. C. Miller and R. F. Haglund, Eds., in Lecture Notes in Physics. New York, NY: Springer, 1991, pp. 209–212. doi: 10.1007/BFb0048372.
[123] Y. Nishikawa, K. Tanaka, and Y. Yoshida, ‘Morphology of Particles Generated from Thin Film by Excimer Laser Ablation’, *Journal of the Japan Institute of Metals*, vol. 55, no. 5, pp. 581–587, 1991, doi: 10.2320/jinstmet1952.55.5_581.
[124] H.-U. Krebs and O. Bremert, ‘Pulsed laser deposition of thin metallic alloys’, *Applied Physics Letters*, vol. 62, no. 19, p. 2341, Jun. 1998, doi: 10.1063/1.109412.
[125] J. C. Miller, Ed., *Laser Ablation: Principles and Applications*, vol. 28. in Springer Series in Materials Science, vol. 28. Berlin, Heidelberg: Springer, 1994. doi: 10.1007/978-3-642-78720-1.
[126] S. Fähler, M. Störmer, and H. U. Krebs, ‘Origin and avoidance of droplets during laser ablation of metals’, *Applied Surface Science*, vol. 109–110, pp. 433–436, Feb. 1997, doi: 10.1016/S0169-4332(96)00782-9.
[127] T. Scharf and H. U. Krebs, ‘Influence of inert gas pressure on deposition rate during pulsed laser deposition’, *Appl Phys A*, vol. 75, no. 5, pp. 551–554, Nov. 2002, doi: 10.1007/s00339-002-1442-4.
[128] S. Fa¨hler and H.-U. Krebs, ‘Calculations and experiments of material removal and kinetic energy during pulsed laser ablation of metals’, *Applied Surface Science*, vol. 96–98, pp. 61–65, Apr. 1996, doi: 10.1016/0169-4332(95)00466-1.
[129] P. E. Dyer, ‘Electrical characterization of plasma generation in KrF laser Cu ablation’, *Appl. Phys. Lett.*, vol. 55, no. 16, pp. 1630–1632, Oct. 1989, doi: 10.1063/1.102220.
[130] K. Sturm, S. Fähler, and H.-U. Krebs, ‘Pulsed laser deposition of metals in low pressure inert gas’, *Applied Surface Science*, vol. 154–155, pp. 462–466, Feb. 2000, doi: 10.1016/S0169-4332(99)00407-9.
[131] J. Chen *et al.*, ‘Tracing the origin of oxygen for $La_{0.6}Sr_{0.4}MnO_3$ thin film growth by pulsed laser deposition’, *J. Phys. D: Appl. Phys.*, vol. 49, no. 4, p. 045201, Dec. 2015, doi: 10.1088/0022-3727/49/4/045201.

[132] G. Koster, D. H. A. Blank, and G. A. J. H. M. Rijnders, ‘Oxygen in Complex Oxide Thin Films Grown by Pulsed Laser Deposition: a Perspective’, *J Supercond Nov Magn*, vol. 33, no. 1, pp. 205–212, Jan. 2020, doi: 10.1007/s10948-019-05276-5.
[133] C. W. Schneider *et al.*, ‘The origin of oxygen in oxide thin films: Role of the substrate’, *Applied Physics Letters*, vol. 97, no. 19, p. 192107, Nov. 2010, doi: 10.1063/1.3515849.
[134] J. A. Venables, G. D. T. Spiller, and M. Hanbucken, ‘Nucleation and growth of thin films’, *Rep. Prog. Phys.*, vol. 47, no. 4, p. 399, Apr. 1984, doi: 10.1088/0034-4885/47/4/002.
[135] C. Claeys and E. Simoen, Eds., *Extended Defects in Germanium*, vol. 118. in Springer Series in Materials Science, vol. 118. Berlin, Heidelberg: Springer Berlin Heidelberg, 2009. doi: 10.1007/978-3-540-85614-6.
[136] O. Auciello and J. Engemann, Eds., *Multicomponent and Multilayered Thin Films for Advanced Microtechnologies: Techniques, Fundamentals and Devices*. Dordrecht: Springer Netherlands, 1993. doi: 10.1007/978-94-011-1727-2.
[137] B. Berini, ‘Elaboration de couches minces de $SmFeO_3$ et $LaNiO_3$, de structure perovskite, par dépôt laser pulsé : études associées des transitions de phase à haute température par ellipsométrie spectropique in situ’, These de doctorat, Versailles-St Quentin en Yvelines, 2007. Accessed: Feb. 22, 2023. [Online]. Available: https://www.theses.fr/2007VERS0024
[138] M. A. Hafez, M. K. Zayed, and H. E. Elsayed-Ali, ‘Review: Geometric interpretation of reflection and transmission RHEED patterns’, *Micron*, vol. 159, p. 103286, Aug. 2022, doi: 10.1016/j.micron.2022.103286.
[139] S. Andrieu and P. Müller, *Les Surfaces solides : concepts et méthodes*. EDP Sciences, 2012.
[140] S. Hasegawa, ‘Reflection High-Energy Electron Diffraction’, in *Characterization of Materials*, John Wiley & Sons, Ltd, 2012, pp. 1–14. doi: 10.1002/0471266965.com139.
[141] B. D. Cullity, *Elements of X-ray Diffraction*. Addison-Wesley Publishing Company, 1956.
[142] R. Chierchia, ‘Strain and crystalline defects in epitaxial GaN layers studied by high-resolution X-ray diffraction’, *http://elib.suub.uni-bremen.de/diss/docs/00011449.pdf*, Jan. 2007.
[143] ‘Introduction to High resoultion X-ray diffraction’. Accessed: Apr. 24, 2023. [Online]. Available: http://www.geocities.ws/pranab_muduli/xrd.html
[144] J. F. Watts, J. Wolstenholme, and R. P. Webb, ‘Secondary Ion Mass Spectrometry’, in *Characterization of Materials*, E. N. Kaufmann, Ed., Hoboken, NJ, USA: John Wiley & Sons, Inc., 2012, p. com142. doi: 10.1002/0471266965.com142.
[145] S. Foner, ‘Versatile and Sensitive Vibrating-Sample Magnetometer’, *Review of Scientific Instruments*, vol. 30, no. 7, pp. 548–557, Jul. 1959, doi: 10.1063/1.1716679.
[146] ‘Magnétisme (Tome II)’, EDP Sciences. Accessed: May 03, 2023. [Online]. Available: https://laboutique.edpsciences.fr/produit/202/9782759801329/magnetisme-tome-ii
[147] R. P. Guertin and S. Foner, ‘Magnetometry’, in *Characterization of Materials*, E. N. Kaufmann, Ed., Hoboken, NJ, USA: John Wiley & Sons, Inc., 2012, p. com044.pub2. doi: 10.1002/0471266965.com044.pub2.
[148] P. Stamenov and J. M. D. Coey, ‘Sample size, position, and structure effects on magnetization measurements using second-order gradiometer pickup coils’, *Review of Scientific Instruments*, vol. 77, no. 1, p. 015106, Jan. 2006, doi: 10.1063/1.2149190.
[149] H. Kohl, ‘Transmission Electron Microscopy’, in *Encyclopedia of Nanotechnology*, B. Bhushan, Ed., Dordrecht: Springer Netherlands, 2012, pp. 2767–2780. doi: 10.1007/978-90-481-9751-4_383.

[150] M. J. Hÿtch, E. Snoeck, and R. Kilaas, ‘Quantitative measurement of displacement and strain fields from HREM micrographs’, *Ultramicroscopy*, vol. 74, no. 3, pp. 131–146, Aug. 1998, doi: 10.1016/S0304-3991(98)00035-7.
[151] B. Fultz and J. Howe, *Transmission Electron Microscopy and Diffractometry of Materials*. in Graduate Texts in Physics. Berlin, Heidelberg: Springer, 2013. doi: 10.1007/978-3-642-29761-8.
[152] M. J. Hÿtch, ‘Geometric phase analysis of high resolution electron microscope images’.
[153] J. J. P. Peters *et al.*, ‘Artefacts in geometric phase analysis of compound materials’, *Ultramicroscopy*, vol. 157, pp. 91–97, Oct. 2015, doi: 10.1016/j.ultramic.2015.05.020.
[154] M. Korytov, *Quantitative TEM Study of Nitride Semiconductors: Quantitative transmission electron microscopy study of III-nitride semiconductor nanostructures*. Editions universitaires europeennes, 2010.
[155] R. K. Gupta, K. Ghosh, and P. K. Kahol, ‘Transparent, conducting, and ferromagnetic multilayer films based on ZnO/Fe_3O_4 by pulsed laser deposition technique’, *Materials Letters*, vol. 64, no. 13, pp. 1487–1489, Jul. 2010, doi: 10.1016/j.matlet.2010.03.069.
[156] C. Suryanarayana and M. G. Norton, *X-Ray Diffraction: A Practical Approach*. Springer Science & Business Media, 2013.
[157] S. M. Suturin *et al.*, ‘Tunable polymorphism of epitaxial iron oxides in the four-in-one ferroic-on-GaN system with magnetically ordered α-, γ-, ε- Fe_2O_3 , and Fe_3O_4 layers’, *Phys. Rev. Materials*, vol. 2, no. 7, p. 073403, Jul. 2018, doi: 10.1103/PhysRevMaterials.2.073403.
[158] C. A. McCammon and L. Liu, ‘The effects of pressure and temperature on nonstoichiometric wüstite, Fe_xO: The iron-rich phase boundary’, *Phys Chem Minerals*, vol. 10, no. 3, pp. 106–113, Feb. 1984, doi: 10.1007/BF00309644.
[159] H. Yamada, M. Kawasaki, and Y. Tokura, ‘Epitaxial growth and valence control of strained perovskite $SrFeO_3$ films’, *Appl. Phys. Lett.*, vol. 80, no. 4, pp. 622–624, Jan. 2002, doi: 10.1063/1.1445805.
[160] P. Benzi, E. Bottizzo, and N. Rizzi, ‘Oxygen determination from cell dimensions in YBCO superconductors’, *Journal of Crystal Growth*, vol. 269, no. 2, pp. 625–629, Sep. 2004, doi: 10.1016/j.jcrysgro.2004.05.082.
[161] P. K. Gallagher, J. B. MacChesney, and D. N. E. Buchanan, ‘Mössbauer Effect in the System $SrFeO_{2.5–3.0}$’, *The Journal of Chemical Physics*, vol. 41, no. 8, p. 2429, Jul. 2004, doi: 10.1063/1.1726282.
[162] Y. Dumont *et al.*, ‘Tuning magnetic properties with off-stoichiometry in oxide thin films: An experiment with yttrium iron garnet as a model system’, *Phys. Rev. B*, vol. 76, no. 10, p. 104413, Sep. 2007, doi: 10.1103/PhysRevB.76.104413.
[163] A. P. Chen, F. Khatkhatay, W. Zhang, C. Jacob, L. Jiao, and H. Wang, ‘Strong oxygen pressure dependence of ferroelectricity in $BaTiO_3/SrRuO_3/SrTiO_3$ epitaxial heterostructures’, *Journal of Applied Physics*, vol. 114, no. 12, p. 124101, Sep. 2013, doi: 10.1063/1.4821643.
[164] E. Enriquez *et al.*, ‘Oxygen vacancy-driven evolution of structural and electrical properties in $SrFeO_{3–\delta}$ thin films and a method of stabilization’, *Appl. Phys. Lett.*, vol. 109, no. 14, p. 141906, Oct. 2016, doi: 10.1063/1.4964384.
[165] Z. Kąkol, J. Sabol, J. Stickler, and J. M. Honig, ‘Effect of low-level titanium(IV) doping on the resistivity of magnetite near the Verwey transition’, *Phys. Rev. B*, vol. 46, no. 4, pp. 1975–1978, Jul. 1992, doi: 10.1103/PhysRevB.46.1975.
[166] A. Kozłowski, P. Metcalf, Z. Kąkol, and J. M. Honig, ‘Electrical and magnetic properties of $Fe_{3–z}Al_zO_4$ (z <0.06)’, *Phys. Rev. B*, vol. 53, no. 22, pp. 15113–15118, Jun. 1996, doi: 10.1103/PhysRevB.53.15113.

[167] F. Walz, 'The Verwey transition - a topical review', *J. Phys.: Condens. Matter*, vol. 14, no. 12, pp. R285–R340, Apr. 2002, doi: 10.1088/0953-8984/14/12/203.
[168] A. A. Khan, 'X-ray determination of thermal expansion of zinc oxide', *Acta Cryst A*, vol. 24, no. 3, pp. 403–403, May 1968, doi: 10.1107/S0567739468000793.
[169] G. R. Holcomb, 'A review of the thermal expansion of magnetite', *Materials at High Temperatures*, vol. 36, no. 3, pp. 232–239, May 2019, doi: 10.1080/09603409.2018.1520953.
[170] C. Schlueter, M. Lübbe, A. M. Gigler, and W. Moritz, 'Growth of iron oxides on Ag(111) — Reversible Fe_2O_3/Fe_3O_4 transformation', *Surface Science*, vol. 605, no. 23, pp. 1986–1993, Dec. 2011, doi: 10.1016/j.susc.2011.07.019.
[171] J. Karunamuni, R. L. Kurtz, and R. L. Stockbauer, 'Growth of iron oxide on Cu(001) at elevated temperature', *Surface Science*, vol. 442, no. 2, pp. 223–238, Nov. 1999, doi: 10.1016/S0039-6028(99)00921-8.
[172] F. Bertram *et al.*, 'X-ray diffraction study on size effects in epitaxial magnetite thin films on MgO(0 0 1)', *J. Phys. D: Appl. Phys.*, vol. 45, no. 39, p. 395302, Sep. 2012, doi: 10.1088/0022-3727/45/39/395302.
[173] S. Gota, E. Guiot, M. Henriot, and M. Gautier-Soyer, 'Atomic-oxygen-assisted MBE growth of $\alpha-Fe_2O_3$ on $\alpha-Al_2O_3$ (0001): Metastable FeO(111)-like phase at subnanometer thicknesses', *Phys. Rev. B*, vol. 60, no. 20, pp. 14387–14395, Nov. 1999, doi: 10.1103/PhysRevB.60.14387.
[174] N. Spiridis *et al.*, 'Growth and electronic and magnetic structure of iron oxide films on Pt(111)', *Phys. Rev. B*, vol. 85, no. 7, p. 075436, Feb. 2012, doi: 10.1103/PhysRevB.85.075436.
[175] N. Spiridis *et al.*, 'Phonons in Ultrathin Oxide Films: 2D to 3D Transition in FeO on Pt(111)', *Phys. Rev. Lett.*, vol. 115, no. 18, p. 186102, Oct. 2015, doi: 10.1103/PhysRevLett.115.186102.
[176] L. W. Wangoh *et al.*, 'Mg^{2+} Diffusion-Induced Structural and Property Evolution in Epitaxial Fe_3O_4 Thin Films', *ACS Nano*, vol. 14, no. 11, pp. 14887–14894, Nov. 2020, doi: 10.1021/acsnano.0c04025.
[177] T. Pohlmann *et al.*, 'Time-resolved x-ray diffraction and photoelectron spectroscopy investigation of the reactive molecular beam epitaxy of Fe_3O_4 ultrathin films', *Phys. Rev. B*, vol. 105, no. 4, p. 045412, Jan. 2022, doi: 10.1103/PhysRevB.105.045412.
[178] F. Raouafi, C. Barreteau, M. C. Desjonquères, and D. Spanjaard, 'Energetics of stepped and kinked surfaces of Rh, Pd and Cu from electronic structure calculations', *Surface Science*, vol. 505, pp. 183–199, May 2002, doi: 10.1016/S0039-6028(02)01156-1.
[179] C. Misbah, O. Pierre-Louis, and Y. Saito, 'Crystal surfaces in and out of equilibrium: A modern view', *Rev. Mod. Phys.*, vol. 82, no. 1, pp. 981–1040, Mar. 2010, doi: 10.1103/RevModPhys.82.981.
[180] R. Fischer *et al.*, 'Material properties of high-quality GaAs epitaxial layers grown on Si substrates', *Journal of Applied Physics*, vol. 60, no. 5, pp. 1640–1647, Sep. 1986, doi: 10.1063/1.337253.
[181] Y. Sun *et al.*, 'Effects of substrate miscut on threading dislocation distribution in metamorphic GaInAs/AlInAs buffers', *J Mater Sci: Mater Electron*, vol. 25, no. 1, pp. 581–585, Jan. 2014, doi: 10.1007/s10854-013-1626-z.
[182] C. M. Rouleau, G. E. Jellison, and D. B. Beach, 'Influence of MgO substrate miscut on domain structure of pulsed laser deposited $Sr_xBa_{1-x}Nb_2O_6$ as characterized by x-ray diffraction and spectroscopic ellipsometry', *Appl. Phys. Lett.*, vol. 82, no. 18, pp. 2990–2992, May 2003, doi: 10.1063/1.1572464.

[183] S. K. Arora, R. G. S. Sofin, and I. V. Shvets, ‘Magnetoresistance enhancement in epitaxial magnetite films grown on vicinal substrates’, *Phys. Rev. B*, vol. 72, no. 13, p. 134404, Oct. 2005, doi: 10.1103/PhysRevB.72.134404.
[184] V. O. Golub *et al.*, ‘Influence of miscut direction on magnetic anisotropy of magnetite films grown on vicinal MgO (100)’, *Journal of Applied Physics*, vol. 107, no. 9, p. 09B108, May 2010, doi: 10.1063/1.3355890.
[185] P. Zaumseil, ‘High-resolution characterization of the forbidden Si 200 and Si 222 reflections’, *J Appl Crystallogr*, vol. 48, no. 2, pp. 528–532, Apr. 2015, doi: 10.1107/S1600576715004732.
[186] M. Renninger, ‘“Umweganregung”, eine bisher unbeachtete Wechselwirkungserscheinung bei Raumgitterinterferenzen’, *Z. Physik*, vol. 106, no. 3–4, pp. 141–176, Mar. 1937, doi: 10.1007/BF01340315.
[187] H. Cole, F. H. Chambers, and H. M. Dunn, ‘Simultaneous diffraction. Indexing unweganregung peaks in simple cases’, *Acta Cryst*, vol. 15, no. 2, pp. 138–144, Feb. 1962, doi: 10.1107/S0365110X62000353.
[188] M. Grundmann, M. Scheibe, M. Lorenz, J. Bläsing, and A. Krost, ‘X-ray multiple diffraction of ZnO substrates and heteroepitaxial thin films: Umweganregung in ZnO’, *Phys. Status Solidi B*, vol. 251, no. 4, pp. 850–863, Apr. 2014, doi: 10.1002/pssb.201350297.
[189] K.-C. Kim, S. K. Kim, J.-S. Kim, and S.-H. Baek, ‘Domain engineering of epitaxial (001) Bi2Te3 thin films by miscut GaAs substrate’, *Acta Materialia*, vol. 197, pp. 309–315, Sep. 2020, doi: 10.1016/j.actamat.2020.07.051.
[190] J. M. Ok *et al.*, ‘Twin-Domain Formation in Epitaxial Triangular Lattice Delafossites’, *ACS Appl. Mater. Interfaces*, vol. 13, no. 18, pp. 22059–22064, May 2021, doi: 10.1021/acsami.1c04169.
[191] F. Pailloux, R. Lyonnet, J.-L. Maurice, and J.-P. Contour, ‘Twinning and lattice distortions in the epitaxy of $La_{0.67}Sr_{0.33}MnO_3$ thin films on (001) $SrTiO_3$’, *Applied Surface Science*, vol. 177, no. 4, pp. 263–267, Jun. 2001, doi: 10.1016/S0169-4332(01)00218-5.
[192] M. Paul *et al.*, ‘Fe_3O_4/ZnO: A high-quality magnetic oxide-semiconductor heterostructure by reactive deposition’, *Appl. Phys. Lett.*, vol. 98, no. 1, p. 012512, Jan. 2011, doi: 10.1063/1.3540653.
[193] D. T. Margulies *et al.*, ‘Anomalous moment and anisotropy behavior in Fe_3O_4 films’, *Phys. Rev. B*, vol. 53, no. 14, pp. 9175–9187, Apr. 1996, doi: 10.1103/PhysRevB.53.9175.
[194] S. Brück *et al.*, ‘Magnetic and electronic properties of the interface between half metallic Fe_3O_4 and semiconducting ZnO’, *Appl. Phys. Lett.*, vol. 100, no. 8, p. 081603, Feb. 2012, doi: 10.1063/1.3687731.
[195] S. Alraddadi, W. Hines, T. Yilmaz, G. D. Gu, and B. Sinkovic, ‘Structural phase diagram for ultra-thin epitaxial Fe_3O_4 / MgO(001) films: thickness and oxygen pressure dependence’, *J. Phys.: Condens. Matter*, vol. 28, no. 11, p. 115402, Feb. 2016, doi: 10.1088/0953-8984/28/11/115402.
[196] S. K. Arora, R. G. S. Sofin, I. V. Shvets, and M. Luysberg, ‘Anomalous strain relaxation behavior of Fe_3O_4/MgO (100) heteroepitaxial system grown using molecular beam epitaxy’, *Journal of Applied Physics*, vol. 100, no. 7, p. 073908, Oct. 2006, doi: 10.1063/1.2349468.
[197] C. A. Kleint *et al.*, ‘Magnetic Properties of Epitaxial Fe_3O_4 Films’, *J. Phys. IV France*, vol. 07, no. C1, pp. C1-593-C1-594, Mar. 1997, doi: 10.1051/jp4:19971244.

[198] W. Eerenstein, T. T. M. Palstra, S. S. Saxena, and T. Hibma, 'Spin-Polarized Transport across Sharp Antiferromagnetic Boundaries', *Phys. Rev. Lett.*, vol. 88, no. 24, p. 247204, Jun. 2002, doi: 10.1103/PhysRevLett.88.247204.
[199] A. M. Bataille *et al.*, 'Characterization of antiphase boundary network in Fe_3O_4(111) epitaxial thin films: Effect on anomalous magnetic behavior', *Phys. Rev. B*, vol. 74, no. 15, p. 155438, Oct. 2006, doi: 10.1103/PhysRevB.74.155438.
[200] J. D. Wei *et al.*, 'Influence of the antiphase domain distribution on the magnetic structure of magnetite thin films', *Appl. Phys. Lett.*, vol. 89, no. 12, p. 122517, Sep. 2006, doi: 10.1063/1.2356308.
[201] A. V. Ramos *et al.*, 'Magnetotransport properties of Fe_3O_4 epitaxial thin films: Thickness effects driven by antiphase boundaries', *Journal of Applied Physics*, vol. 100, no. 10, p. 103902, Nov. 2006, doi: 10.1063/1.2386927.
[202] K. P. McKenna *et al.*, 'Atomic-scale structure and properties of highly stable antiphase boundary defects in Fe_3O_4', *Nat Commun*, vol. 5, no. 1, p. 5740, Dec. 2014, doi: 10.1038/ncomms6740.
[203] Z. Xu *et al.*, 'Structure and properties of Fe_3O_4 films grown on ZnO template via metal organic chemical vapor deposition', *Journal of Magnetism and Magnetic Materials*, vol. 385, pp. 257–264, Jul. 2015, doi: 10.1016/j.jmmm.2015.03.018.
[204] Y. Gao, Y. J. Kim, and S. A. Chambers, 'Preparation and characterization of epitaxial iron oxide films', *Journal of Materials Research*, vol. 13, no. 7, pp. 2003–2014, Jul. 1998, doi: 10.1557/JMR.1998.0281.
[205] H. Tian *et al.*, 'Interface-Induced Modulation of Charge and Polarization in Thin Film Fe_3O_4', *Adv. Mater.*, vol. 26, no. 3, pp. 461–465, Jan. 2014, doi: 10.1002/adma.201303329.
[206] N. Junqua and J. Grilhé, 'Surface strains and measurements of misfit dislocation density by diffraction methods in thin films on substrates', *Thin Solid Films*, vol. 250, no. 1, pp. 37–41, Oct. 1994, doi: 10.1016/0040-6090(94)90161-9.
[207] J. Hornstra, 'Dislocations, stacking faults and twins in the spinel structure', *Journal of Physics and Chemistry of Solids*, vol. 15, no. 3, pp. 311–323, Oct. 1960, doi: 10.1016/0022-3697(60)90254-7.
[208] R. Wang *et al.*, 'Twin boundary defect engineering improves lithium-ion diffusion for fast-charging spinel cathode materials', *Nat Commun*, vol. 12, no. 1, p. 3085, May 2021, doi: 10.1038/s41467-021-23375-7.
[209] B. Devouard, M. Posfai, X. Hua, D. A. Bazylinski, R. B. Frankel, and P. R. Buseck, 'Magnetite from magnetotactic bacteria; size distributions and twinning', *American Mineralogist*, vol. 83, no. 11-12_Part_2, pp. 1387–1398, Dec. 1998, doi: 10.2138/am-1998-11-1228.
[210] Y. Yang, X. W. Sun, B. K. Tay, J. X. Wang, Z. L. Dong, and H. M. Fan, 'Twinned Zn_2TiO_4 Spinel Nanowires Using ZnO Nanowires as a Template', *Advanced Materials*, vol. 19, no. 14, pp. 1839–1844, 2007, doi: 10.1002/adma.200700299.
[211] Y. Lin, A. G. Norman, W. E. McMahon, H. R. Moutinho, C.-S. Jiang, and A. J. Ptak, 'Single-crystalline aluminum grown on $MgAl_2O_4$ spinel using molecular-beam epitaxy', *Journal of Vacuum Science & Technology B*, vol. 29, no. 3, p. 03C128, Mar. 2011, doi: 10.1116/1.3570869.
[212] W. Eerenstein, T. T. M. Palstra, T. Hibma, and S. Celotto, 'Diffusive motion of antiphase domain boundaries in Fe_3O_4 films', *Phys. Rev. B*, vol. 68, no. 1, p. 014428, Jul. 2003, doi: 10.1103/PhysRevB.68.014428.
[213] M. Ziese and H. J. Blythe, 'Magnetoresistance of magnetite', p. 17.

[214] D. T. Margulies *et al.*, ‘Origin of the Anomalous Magnetic Behavior in Single Crystal Fe_3O_4 Films’, *Phys. Rev. Lett.*, vol. 79, no. 25, pp. 5162–5165, Dec. 1997, doi: 10.1103/PhysRevLett.79.5162.
[215] ‘Fiji: ImageJ’. Accessed: Jun. 01, 2023. [Online]. Available: https://fiji.sc/